



AFRL-RQ-WP-TR-2016-0004

MULTI-DISCIPLINARY COMPUTATIONAL AERODYNAMICS

Miguel R. Visbal

Aerodynamic Technology Branch
Aerospace Vehicles Division

JANUARY 2016
Final Report

Approved for public release; distribution unlimited.

See additional restrictions described on inside pages

STINFO COPY

AIR FORCE RESEARCH LABORATORY
AEROSPACE SYSTEMS DIRECTORATE
WRIGHT-PATTERSON AIR FORCE BASE, OH 45433-7541
AIR FORCE MATERIEL COMMAND
UNITED STATES AIR FORCE

NOTICE AND SIGNATURE PAGE

Using Government drawings, specifications, or other data included in this document for any purpose other than Government procurement does not in any way obligate the U.S. Government. The fact that the Government formulated or supplied the drawings, specifications, or other data does not license the holder or any other person or corporation; or convey any rights or permission to manufacture, use, or sell any patented invention that may relate to them.

This report was cleared for public release by the USAF 88th Air Base Wing (88 ABW) Public Affairs Office (PAO) and is available to the general public, including foreign nationals.

Copies may be obtained from the Defense Technical Information Center (DTIC) (<http://www.dtic.mil>).

AFRL-RQ-WP-TR-2016-0004 HAS BEEN REVIEWED AND IS APPROVED FOR PUBLICATION IN ACCORDANCE WITH ASSIGNED DISTRIBUTION STATEMENT.

*/Signature//

MIGUEL R. VISBAL, Program Engineer
Aerodynamic Technology Branch
Aerospace Vehicles Division
Aerospace Systems Directorate

//Signature//

JAMES M. HAAS, Branch Chief
Aerodynamic Technology Branch
Aerospace Vehicles Division
Aerospace Systems Directorate

This report is published in the interest of scientific and technical information exchange, and its publication does not constitute the Government's approval or disapproval of its ideas or findings.

*Disseminated copies will show “//Signature//” stamped or typed above the signature blocks.

REPORT DOCUMENTATION PAGE				<i>Form Approved OMB No. 0704-0188</i>
<p>The public reporting burden for this collection of information is estimated to average 1 hour per response, including the time for reviewing instructions, searching existing data sources, gathering and maintaining the data needed, and completing and reviewing the collection of information. Send comments regarding this burden estimate or any other aspect of this collection of information, including suggestions for reducing this burden, to Department of Defense, Washington Headquarters Services, Directorate for Information Operations and Reports (0704-0188), 1215 Jefferson Davis Highway, Suite 1204, Arlington, VA 22202-4302. Respondents should be aware that notwithstanding any other provision of law, no person shall be subject to any penalty for failing to comply with a collection of information if it does not display a currently valid OMB control number. PLEASE DO NOT RETURN YOUR FORM TO THE ABOVE ADDRESS.</p>				
1. REPORT DATE (DD-MM-YY) January 2016		2. REPORT TYPE Final	3. DATES COVERED (From - To) 01 October 2007 – 30 September 2015	
4. TITLE AND SUBTITLE MULTI-DISCIPLINARY COMPUTATIONAL AERODYNAMICS			5a. CONTRACT NUMBER In-house	5b. GRANT NUMBER
			5c. PROGRAM ELEMENT NUMBER 61102F	5d. PROJECT NUMBER 2307
			5e. TASK NUMBER N/A	5f. WORK UNIT NUMBER Q05N
6. AUTHOR(S) Miguel R. Visbal			7. PERFORMING ORGANIZATION NAME(S) AND ADDRESS(ES) Aerodynamic Technology Branch (AFRL/RQVA) Aerospace Vehicles Division Air Force Research Laboratory, Aerospace Systems Directorate Wright-Patterson Air Force Base, OH 45433-7541 Air Force Materiel Command, United States Air Force	
			8. PERFORMING ORGANIZATION REPORT NUMBER AFRL-RQ-WP-TR-2016-0004	
9. SPONSORING/MONITORING AGENCY NAME(S) AND ADDRESS(ES) Air Force Research Laboratory Aerospace Systems Directorate Wright-Patterson Air Force Base, OH 45433-7541 Air Force Materiel Command United States Air Force			10. SPONSORING/MONITORING AGENCY ACRONYM(S) AFRL/RQVA	11. SPONSORING/MONITORING AGENCY REPORT NUMBER(S) AFRL-RQ-WP-TR-2016-0004
12. DISTRIBUTION/AVAILABILITY STATEMENT Approved for public release; distribution unlimited.				
13. SUPPLEMENTARY NOTES PA Case Number: 88ABW-2016-0146; Clearance Date: 15 Jan 2016. This report also contains eight published journal articles.				
14. ABSTRACT High-fidelity simulation was employed to address several complex unsteady interactions important to future USAF air vehicles. The research described in this report was focused on three key elements: 1. Vortex interactions in formation flight. 2. Dynamic stall. 3. Plasma-based transition control.				
15. SUBJECT TERMS Vortex, interaction, streamwise, oriented, orbital motion, dynamic stall, pitching, laminar separation, actuation, plasma-based transition control, excrescence-induced, transition				
16. SECURITY CLASSIFICATION OF:		17. LIMITATION OF ABSTRACT: SAR	18. NUMBER OF PAGES 209	19a. NAME OF RESPONSIBLE PERSON (Monitor) Miguel R. Visbal 19b. TELEPHONE NUMBER (Include Area Code) N/A
a. REPORT Unclassified	b. ABSTRACT Unclassified	c. THIS PAGE Unclassified		

TABLE OF CONTENTS

Section	Page
List of Figures.....	ii
1. Summary.....	1
2. Introduction.....	2
3. Methodology	4
3.1 Fluid Dynamics Solver.....	4
3.2 Structural Solver.....	5
4. Results and Discussion.....	8
4.1 Streamwise-Oriented Vortex Interactions with Rigid and Flexible Wings.....	8
4.2 Gust Interactions and Dynamic Stall.....	10
4.3 Laminar Flow Control Using Simulated Plasma Actuators	12
5. Conclusions.....	15
6. References.....	16
Appendices: Published Papers	
Appendix A. Interaction of a Streamwise-oriented Vortex with a Wing	17
Appendix B. Unsteady Interactions of a Wandering Streamwise Oriented Vortex with a Wing	40
Appendix C. Numerical Simulations of Streamwise-Oriented Vortex/Flexible Wing Interactions	62
Appendix D. Streamwise-Oriented Vortex Interactions with a NACA0012 Wing....	89
Appendix E. Analysis of the Onset of Dynamic Stall Using High-Fidelity Large- Eddy Simulations.....	109
Appendix F. Control of Dynamic Stall on a Pitching Airfoil Using High-Frequency Actuation	134
Appendix G. Plasma-Based Flow Control for Delay of Excrescence-Generated Transition	159
Appendix H. Plasma-Based Control of Transition on a Wing with Leading-Edge Excrescence	184

LIST OF FIGURES

Figure 1: USAF Air Vehicle Driven Solutions and Challenges	3
Figure 2: Representative Flow Simulations Using High-Order Overset Solver <i>FDL3DI</i>	5
Figure 3: Representative Simulations of Complex Nonlinear Fluid-Structure Interactions Using the High-Fidelity Computational Framework.....	7
Figure 4: Multiple Modes of Interaction as a Function of Vortex Position in Formation Flight.....	9
Figure 5: Feedback Effect due to Wing Aero-elastic Deformation in Formation Flight.....	9
Figure 6: Suppression of Dynamic Stall Vortex over a Pitching Wing Employing High-Frequency Actuation	12
Figure 7: Delay of Excrescence-Induced Transition by Means of a Simulated Plasma Actuator	14

1. Summary

USAF future operations pose unprecedented challenges for air dominance, ISR and mobility solutions that must meet stringent requirements for energy efficiency and sustainability. To meet these challenges, insertion of new technologies are envisioned such as aggressive use of laminar flow, lightweight multi-functional highly flexible structures and close and extended formation flight. Unforeseen and difficult to control multidisciplinary interactions may arise due to large excursions in transition location and unsteady separation coupled to wing elastic response. These complex interactions are further exacerbated by encounters with flight-path disturbances, gusts or trailing vortices. The ability to discover and control these interactions is critical for achieving vehicle performance and for avoiding costly remedial fixes late in the design process. In this research, we have targeted canonical multi-disciplinary interactions employing physics-based high-fidelity simulations. Three main elements of the research are covered in this report, as outlined below.

- I. **Streamwise-Oriented Vortex Interactions with Rigid and Flexible Wings.** Several studies have been conducted to delineate various interaction regimes encountered in formation flight and to provide insight into the underlying physics of vortex-induced separation and buffeting, as well as into the role of structural compliance.
- II. **Gust Interactions and Dynamic Stall.** Aggressive use of laminar flow over lightweight structures for improved energy efficiency brings about the potential for unforeseen interactions excited by incoming gusts. Coupling of large excursion of transition location, unsteady separation and elastic response may severely impact vehicle dynamics. Results from a study of dynamic stall, as a model of gust interaction, are presented and a new flow control approach based on very high frequency actuation is proposed and evaluated.
- III. **Laminar Flow Control Using Simulated Plasma Actuators.** Laminar flow is a key enabler for increased range. Outer-mold-line (OML) disruptions are critical to design, manufacturing tolerances and operational damage/contamination. OML imperfections play also a crucial role in the development of laminar-flow-compatible high-lift systems. A study has been performed to investigate the impact of surface excrescences on the laminar-to-turbulent transition, as well as to explore plasma-based flow control approaches for transition delay.

2. Introduction

The Aerospace Systems Directorate in AFRL is focused on developing innovative air vehicles with unprecedented capabilities for future air dominance, mobility and reconnaissance (ISR). Besides being effective, these solutions must also meet more stringent requirements for energy efficiency and sustainability throughout their lifecycle. These simultaneous goals of capability, efficiency and sustainability, coupled to limited resources, drive the long-term development of these highly innovative revolutionary systems. As part of this paradigm, technological approaches such as extensive use of laminar flow, formation flight and lightweight multi-functional structures need serious consideration. The challenges are exacerbated by the broad range of vehicle configurations ranging from small unmanned air systems (SUAS) to large-scale high-altitude long-endurance (HALE) ISR platforms. The aforementioned technological approaches introduce a greater potential for unforeseen and difficult to predict multi-disciplinary effects (Figure 1) which, if not properly accounted for, can ultimately lead to limits on performance and to costly delays and design modifications.

Examples of potential multi-disciplinary effects where fundamental understanding is lacking include the following:

- Although lightweight laminar wings are desirable for energy efficiency, they are inherently more susceptible to incoming flow disruptions or gusts. In addition large excursions in transition location or the onset of unsteady separation may give rise to complex self-sustained oscillations of highly flexible structures. These represent a new realm of aeroelastic phenomena outside of the more classic transonic or stall flutter regimes. Risk mitigation in the fielding and operation of revolutionary platforms will demand discovery and understanding of adverse non-linear gust interactions, dynamic loads and flexible vehicle response. Advances in this front are essential for the development of improved control systems and mitigation strategies employing active flow and aeroelastic control.
- Both homogeneous or heterogeneous, close or extended formation flight are envisioned as a potential technology for reduced fuel consumption or improved range, critical to operations with limited forward presence. This approach, although promising, must overcome several hurdles for routine application. For instance, in extended flight at higher subsonic speed, transonic effects and shock-induced separation may be encountered. Preliminary analysis indicates that optimal vortex location for the trimmed aircraft lies inboard of the wing tip. This may induce complex vortex/surface interactions and buffeting. Coupling of non-linear flow phenomena near the wing tip with structural flexibility could result in a severe dynamic load environment and limit-cycle oscillations which will impact drag reduction and life cycle fatigue.
- Laminar flow is a key enabler for increased range. Outer-mold-line (OML) disruptions are critical to design, manufacturing tolerances and operational damage/contamination. OML imperfections play also a crucial role in the development of laminar-flow-compatible high-lift mobility systems. Given the potential benefits of laminar flow there is the need to investigate the impact of surface

excrescences on the laminar-to-turbulent transition process. Unavoidable surface imperfections also dictate the exploration and evaluation of novel plasma-based flow control approaches for transition delay.

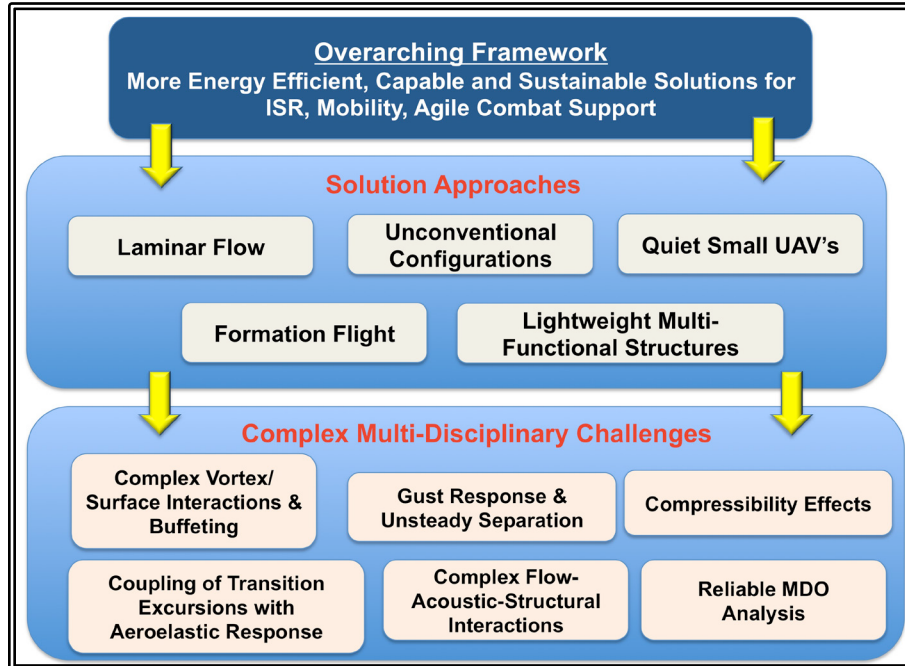


Figure 1: USAF Air Vehicle Driven Solutions and Challenges

The present project addresses several fundamental aspects of the previous challenges through the application of high-fidelity, multi-disciplinary simulation. Emphasis is placed on well-defined configurations that, while tractable, still embody the relevant physics of the problem. A commonality to all of the aforementioned interactions is the importance of fine-scale unsteady effects that cannot be predicted reliably by traditional low-fidelity turbulence modeling approaches. More advanced physics-based methodologies are required to capture boundary layer transition, unsteady separation and the ensuing dynamic loading. This high-end computational approach (described in Section 3) is a critical component of AFRL/RQ's comprehensive multi-fidelity and multi-disciplinary framework for vehicle design and analysis.

A portion of the research effort, described in more detail in Section 4, is comprised of three main elements: (a) streamwise-oriented vortex interactions with rigid and flexible wings, (b) unsteady separation and dynamic stall, and (c) laminar flow control using simulated plasma-based actuators.

3. Methodology

3.1 Fluid Dynamics Solver

A crucial element in the simulation of fine-scale unsteady features inherent in transitional and turbulent flows is highly accurate algorithms. Under previous AFOSR sponsorship, the team has developed and demonstrated a unique, robust and versatile high-fidelity computational framework, which has proven extremely successful for the prediction and manipulation of a broad range of complex unsteady flows. Although a detailed algorithmic description is not provided in this report, key attributes embodied in the computational solver (*FDL3DI*) are summarized as follows:

- The approach is applicable to general sets of conservation equations including the full compressible Navier-Stokes, Euler and electromagnetic equations[1-3]
- A hierarchy of viscous flow simulations is possible extending from Reynolds-averaged (RANS) to large-eddy and direct numerical simulations (LES, DNS). A hybrid RANS/LES approach is also incorporated [4].
- Highly accurate spatial discretization is provided by means of 6th-order compact schemes augmented with up to 10th-order spectrally based Pade-type low-pass filter operators [5]. The former component is critical for capturing fine-scale transitional features and acoustic propagation. The latter element enforces stability at poorly resolved high wave numbers without dissipating energy in the resolved portion of the spectrum (as shown schematically in Fig. 2a).
- The previous algorithmic components are key for what is referred to as a high-order implicit large-eddy simulation (ILES) approach [6, 7], which offers a more robust and efficient alternative to standard dynamic sub-grid-scale (SGS) models (also incorporated into the solver [8]). In Ref. [9], a comparison of ILES and a dynamic Smagorinsky SGS model is provided for transitional flow past a wing section. It was determined that the addition of the dynamic SGS model did not significantly affect the time-mean or statistical flow quantities. It should be emphasized that in transitional regions of the flow, the present approach corresponds to a *high-order DNS*. This aspect is critical to capturing transitional features and in this regard the method is superior to low-order SGS techniques. The present high-order ILES methodology has been proven to be quite effective for a broad range of mixed transitional and turbulent flows.
- Time marching is accomplished employing either explicit 4th-order Runge-Kutta schemes or an implicit second-order Beam-Warming scheme with sub-iterations [5].
- Careful attention to the treatment of the metric derivatives and the Geometric Conservation Law (GCL) [5] ensures higher-order accuracy on curvilinear, deforming and moving grids as required for instance in fluid-structure interactions
- For flows containing shock waves, an adaptive filtering procedure and hybrid compact/upwind spatial differencing schemes are integrated which retain high accuracy in smooth regions while capturing sharp interfaces [10,11].
- The framework has been extended to complex geometries through incorporation of the overset mesh technique implemented using high-order interpolation across overlapping meshes [12].

- The solver is fully parallelized for effective use on modern DoD High-Performance Computing platforms employing thousands of cores while retaining excellent scalability.

The previous computational framework has been demonstrated for a number of complex unsteady flows as illustrated pictorially in Fig. 2. A subset of these configurations include canonical turbulent benchmark cases [6,7], airfoils and wings in unsteady motion [13-15], plasma-based control of transitional and turbulent flows [16,17], separated flows around laser turrets [4] and a full unmanned combat air vehicle [18].

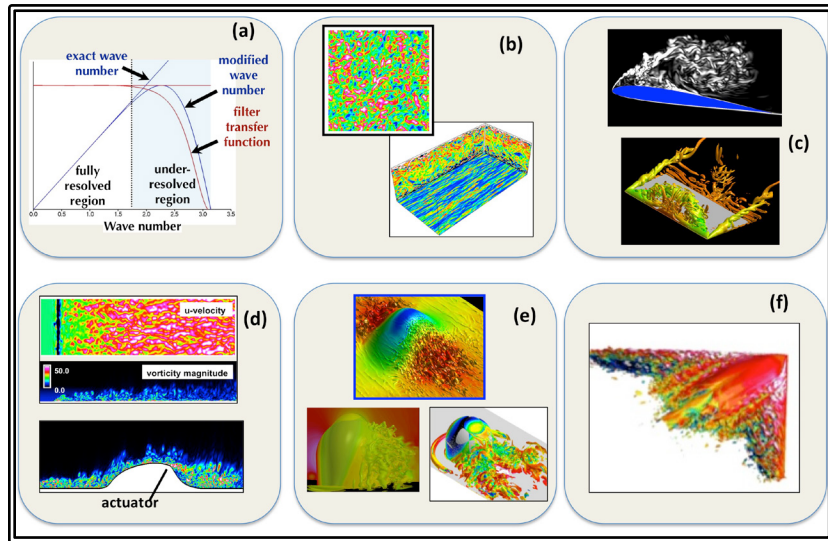


Figure 2: Representative Flow Simulations Using High-Order Overset Solver *FDL3DI*

3.2 Structural Solver

The Air Force identified need for more energy efficient aircraft requires the development of lightweight and therefore more flexible structural design concepts. These inherently flexible systems will be more susceptible to complex fluid/structure interactions resulting from such issues as gust encounters and unsteady vortex encounters due to formation flight. To address the critical issues associated with the fundamental fluid/structure interactions inherent in the design of these flexible systems, several different nonlinear structural models of increasing fidelity have been coupled in the ***FDL3DI*** framework to create a high-fidelity aeroelastic computational capability. These structural models are summarized as follows:

- A nonlinear 2-DOF model for pitching and plunging of a rigid airfoil has been coupled with ***FDL3DI*** as a representative model for a three-dimensional bending-torsion wing response. The model can take on varying levels of complexity from a general nonlinear form where higher order nonlinearities are retained to a linear version based on the assumption of small-amplitude oscillations [19].

- For highly flexible but more structurally conventional wing designs a geometrically-nonlinear structural dynamics model based on an asymptotic approach to the equations governing the dynamics of a general 3-D anisotropic slender solid is employed. The equations of motion are approximated by the recursive solution of a linear 2-D problem at each cross section, and a 1-D geometrically-nonlinear beam problem along the reference line. This structural model has been implemented in the University of Michigan’s Nonlinear Active Beam Solver (UM/NLABS) [20,21].
- A nonlinear P-version Mixed Reissner-Mindlin plate finite-element model with *higher-order* capabilities [22] has also been developed and coupled into the **FDL3DI** framework. The kinematical assumptions for this model are based on Mindlin’s hypothesis that fibers normal to the plate remain straight and do not change length. The ability of this model to predict large structural deflections provides an attractive alternative for structural designs that vary from the more standard wing designs addressed by the NLABS model.

The coupling of these structural solvers with the fluid mechanics equations comes through the imposed loads and the structural deflections. The aerodynamic mesh is deformed to account for the surface deflection using a simple algebraic method described in Ref. [23]. For the three-dimensional geometries and more complex structural layouts a one-to-one matching of the structural mesh and the surface mesh for the fluid is not always possible. More sophisticated approaches such as thin plate splines or local bilinear interpolation are employed. Complete synchronization of the equation sets is accomplished via sub-iterations.

These computational aeroelastic solvers have been validated and applied to a variety of fluid/structure interaction problems as seen in Figure 3. Figure 3a portrays results from the exploration of limit cycle oscillations for delta wing configurations [24,25]. In Figs. 3b,c acoustic interactions and shock-wave impingement on flexible panels were investigated [26,27]. Figures 3d-f show computations for transitional flows over flexible plunging wings [15] and membrane wings [28-30] with applications to small unmanned air systems.

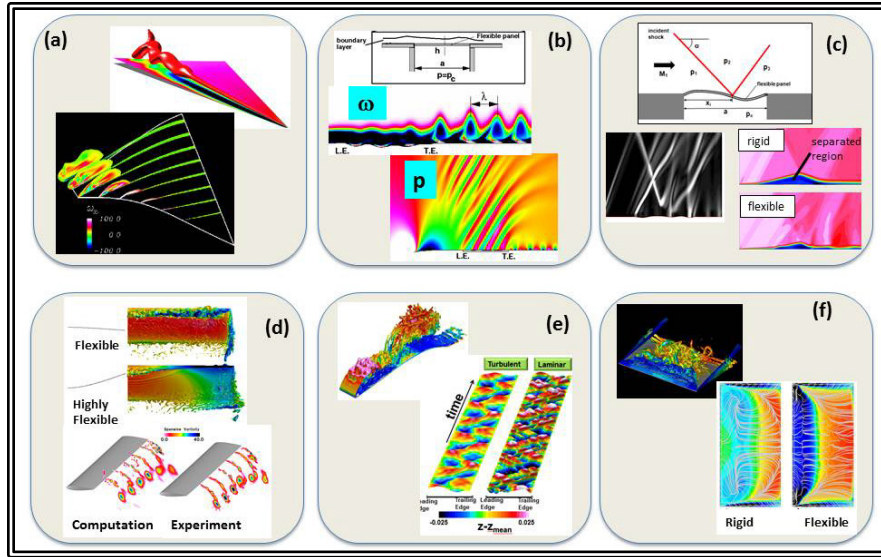


Figure 3: Representative Simulations of Complex Nonlinear Fluid-Structure Interactions Using the High-Fidelity Computational Framework

4. Results and Discussion

4.1 Streamwise-Oriented Vortex Interactions with Rigid and Flexible Wings

Formation flight of aircrafts has long been understood to provide significant benefits in aerodynamic performance [32-37]. With proper positioning, a trailing aircraft can capture the upwash from the tip vortex left in the wake of a lead aircraft. The result is a forward-tilted lift vector that provides increased lift and a reduction in induced drag, which can lead to significant energy savings. Close formation flight has historically been limited by safety concerns arising from the high speed and proximity of adjacent aircraft. Fortunately, technological advances in positioning and guidance systems along with collision avoidance systems are making it possible for military and commercial aircraft to fly in closer proximity to take advantage of close formation flight. Unfortunately, close formation flight can also produce undesirable effects including vortex buffeting [38] which may lead to structural fatigue. For close-in formations, it is important to understand the complex unsteady interactions of the streamwise-oriented vortices with a follower wing.

In the course of this project, significant progress has been achieved in the characterization of several aspects of streamwise-oriented vortex interactions with rigid and flexible wings. The results are described in detail in Appendices A-D. In Appendix A, several interaction regimes are characterized as a function of vortex relative spanwise position. As shown in Figure 4, these range from an outboard case in which a vortex dipole is formed which self-propels vertically upwards with implications for multiple formations, to a fully-inboard scenario where the increased induced effective angle attack enhances separation and unloads the tip region. There is also a rapid reversal in rolling moment as the vortex moves inboard with implications for trim and responsive roll control. The effects of an imposed incoming vortex wandering on the interaction are studied in Appendix B. The impact of vortex vertical offset and wing flexibility is detailed in Appendix C. As shown in Figure 5, the flow is highly unsteady and includes a spiraling instability or breakdown of the incident vortex. For a high aspect ratio wing the deformation is dominated by a primary bending mode. Therefore wing deformation will result to first order in a vertical shift in vortex position. With increased wing flexibility it was discovered that the spiral instability penetrates further upstream (see Figure 5) and buffeting on the wing is enhanced. This is a new feedback effect associated with coupling of the vortex instabilities with the wing pressure field. Finally, in Appendix D, results are extended to a NACA 0012 wing configuration at higher Reynolds number.

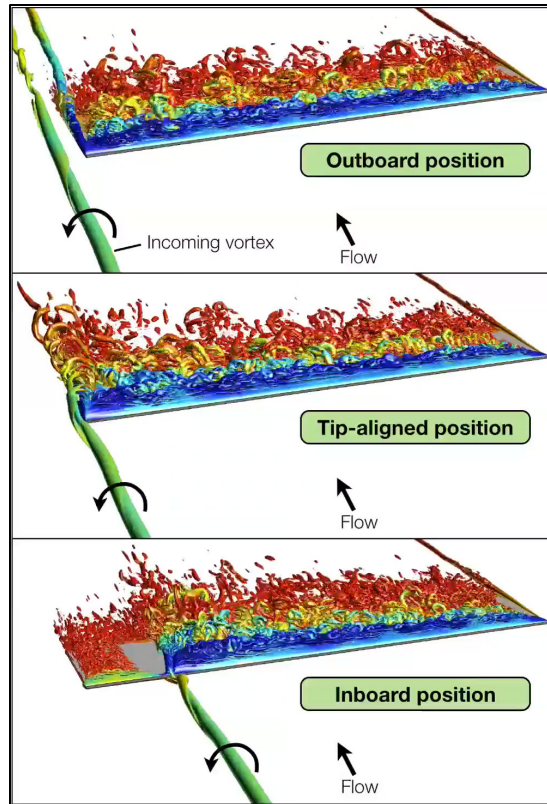


Figure 4: Multiple Modes of Interaction as a Function of Vortex Position in Formation Flight

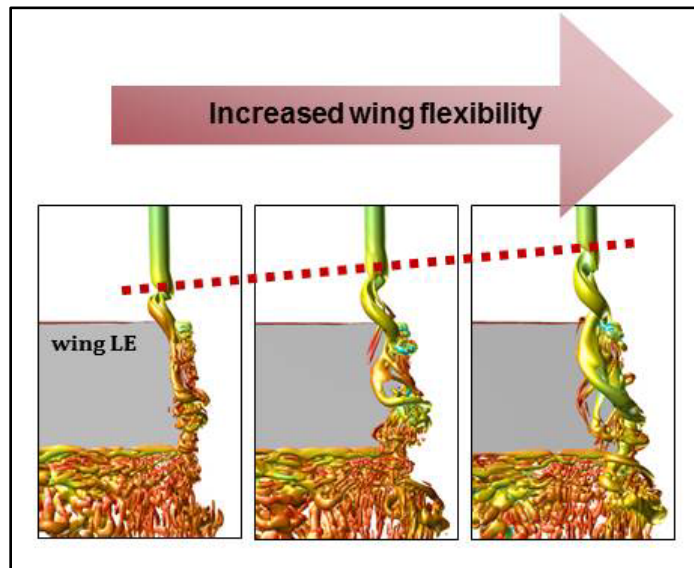


Figure 5: Feedback Effect due to Wing Aero-elastic Deformation in Formation Flight

4.2 Gust Interactions and Dynamic Stall

Maneuvering wings subjected to large excursions in effective angle of attack exhibit the phenomenon referred to in general as dynamic stall. Dynamic stall is characterized by a transient delay in separation (relative to the static situation) followed by the abrupt onset of unsteady separation which culminates in the formation of a large-scale dynamic stall vortex (DSV). The angular lag in separation in conjunction with the DSV-induced suction promotes a transiently elevated aerodynamic lift. However, as the DSV is shed and propagates along the wing it induces sudden and difficult to predict variations in aerodynamic forces and pitching moment which severely impact controllability, vibrations, structural integrity and noise generation. Dynamic stall is found in a broad range of engineering applications including retreating blades of helicopter rotors in forward flight, maneuvering aircraft and wind turbines. It is also important in severe wing-gust encounters where large excursions in effective angle of attack may be generated over a wing in nominal steady flight. For the extensive body of literature on the subject, the reader is referred to several comprehensive reviews addressing various aspects of this complex phenomenon. These include the works of McCroskey [40] Carr [41], Ekaterinaris and Platzer [42], Visbal [43] and Carr and Chandrasekhara [44].

Over a broad range of flow conditions and kinematics, the gross characteristics of dynamic stall are by now well established. For instance, the presence of a coherent DSV which forms near the leading edge and then convects along the airfoil inducing large overshoots in the aerodynamic loads is universally observed for a wide range of Reynolds numbers. However, the detailed underlying viscous mechanisms which precede the emergence of the DSV are not yet fully understood. This task is hindered not only by the inherently complex unsteady boundary-layer behavior but also by the presence of several interrelated flow effects, including compressibility, transition, type and rate of motion and leading-edge geometry. Although suitably-calibrated RANS methodologies will continue to be employed for design purposes, they cannot be expected to be truly predictive given the complex flow physics at play near the leading edge. In particular, they are of limited value for probing the detailed viscous mechanisms, for exploring active flow sensing and control strategies and for characterizing noise generation.

In order to provide insight into the viscous mechanisms during the onset of unsteady separation and dynamic stall vortex formation, a transiently pitching airfoil was studied numerically employing high-fidelity large-eddy simulations. The primary case considered consists of a SD7003 airfoil section at a freestream Mach number 0.1 and chord Reynolds number 500,000. The airfoil is pitched about its quarter-chord axis at a nominally constant non-dimensional rate of 0.05 from a small initial incidence to a high angle of attack beyond the onset of dynamic stall. The unsteady flow was studied in detail with emphasis on characterizing the unsteady boundary layer behavior which precedes the formation of the dynamic stall vortex. Details are provided in Appendix E, and only salient findings are briefly discussed below.

As the wing is pitched, the transition location propagates forward along the airfoil upper surface and forms a laminar separation bubble (LSB) which contracts significantly with increasing incidence. Downstream of the LSB, a turbulent boundary layer is

observed whose thickness increases with angle of attack while the flow remains effectively attached and body-conforming. The accompanying expansion around the leading edge promotes very low surface pressures and a local Mach number four times higher than the freestream value. During these early stages, the normal force increases linearly albeit with a reduced slope relative to steady inviscid theory reflecting the lag in circulation build-up around the airfoil. The pitching moment is also shifted to a lower value due to rotation-induced camber effects. Beyond a critical incidence, the contracted LSB breaks down and a sudden collapse of leading-edge suction ensues. A very abrupt separation of the turbulent boundary layer at the DSV inception point is also observed. The rapid appearance of reversed flow allows the turbulent boundary-layer vorticity to coalesce into a nascent dynamic stall vortex. As the DSV increases in strength, it induces very high values of reversed flow velocity underneath. This reversed flow subsequently detaches due to the high vortex-induced pressure gradient forming a secondary separation region. The shear layer emanating from the leading-edge is also displaced away from the wing due to the growing DSV. This feeding sheet exhibits discrete Kelvin-Helmholtz type sub-structures which undergo pairing and subsequent breakdown due to spanwise instabilities. Maximum surface pressure fluctuations are observed near the leading edge resulting in significant acoustic radiation. These fluctuations, associated with the LSB, decrease in magnitude as the shear layer moves away from the wall. The aforementioned unsteady boundary layer behavior appears to be in agreement with available experimental observations, even some obtained at higher Reynolds number. It is clear that at least for the conditions considered, the LSB plays a critical role both in establishing the propagation of transition along the pitching airfoil, as well as in the collapse of suction and subsequent DSV emergence. The importance of the LSB has significant implications for the quantitative prediction of the phenomenon. It remains to be seen if Reynolds-averaged approaches can be calibrated to reproduce the abrupt nature of LSB bursting and suction collapse.

The role of the laminar separation bubble in the initiation of dynamic stall, as well as its natural high frequency fluctuations motivated a new flow control approach employing very high-frequency pulsed actuation. This was imparted through a zero-net mass flow blowing/suction slot located on the airfoil lower surface just downstream of the leading edge. Details and evaluation of this flow control strategy are given in Appendix F. A significant delay in the onset of dynamic stall was demonstrated for the pulsed forcing at high frequencies both for ramp and oscillatory pitching motions. As shown in Figure 6 for a light dynamic stall case, flow actuation is capable of maintaining an effectively attached flow during the entire pitching cycle and inhibits the formation of large-scale leading-edge and shear-layer vortical structures. For deep dynamic stall, control is also found to be very effective in eliminating leading-edge separation and the subsequent DSV. Nonetheless, trailing-edge separation eventually occurs at high incidence during the downstroke. For both cases, actuation provided a significant reduction in the cycle-averaged drag, and in the force and moment fluctuations. In addition, the negative (unstable) net-cycle pitch damping found in the baseline cases was eliminated. The flow control benefits demonstrated so far in this study should serve as motivation for additional computational and experiments investigations employing plasma-based devices or other means of high-frequency actuation.

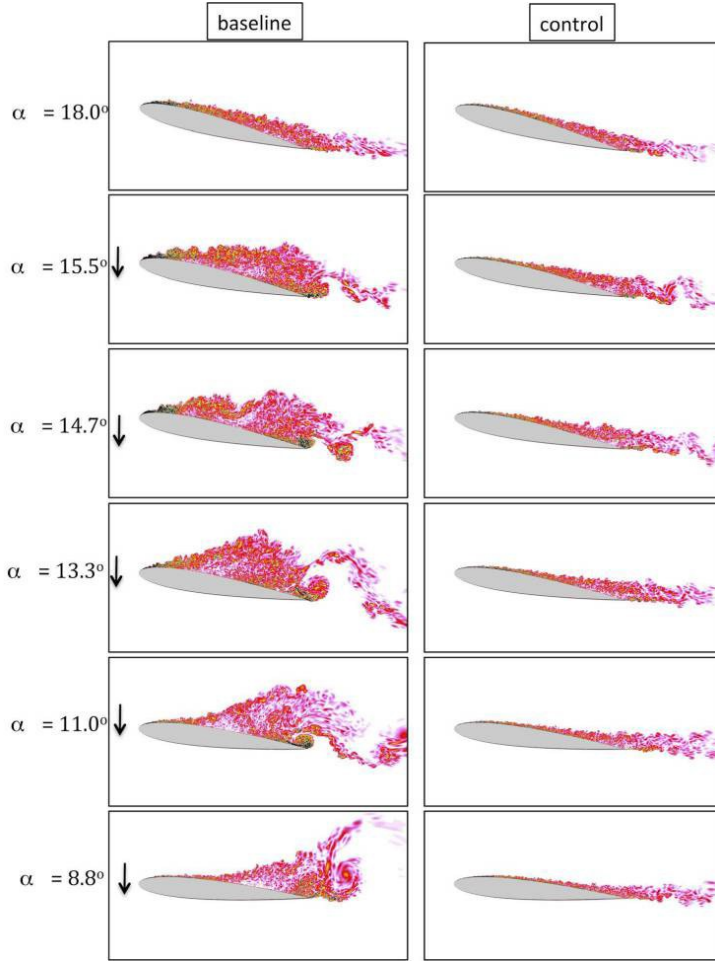


Figure 6: Suppression of Dynamic Stall Vortex over a Pitching Wing Employing High-Frequency Actuation

4.3 Laminar Flow Control Using Simulated Plasma Actuators

Drag reduction is one of the principal considerations in the design and construction of unmanned air systems (UAS) and high altitude long endurance (HALE) vehicles. Such platforms are primarily used for intelligence, surveillance, and reconnaissance missions, which require long range and/or long endurance operations. Laminar flow configurations for these applications offer a substantial reduction in drag, leading directly to lower fuel consumption, greater energy efficiency, longer range, larger payloads, or increased flight times. Because of these benefits, laminar arrangements are also being considered for new mobility and strike platforms. There are three main components to consider in the production and deployment of modern laminar flow vehicles. First, the design process must account for flight Reynolds number and sweep angles of high lift systems, and the growth of crossflow disturbances. Second, fabrication of aerodynamic surfaces must honor tolerances required for maintaining laminar flow by minimizing surface steps, skin seams, and three dimensional excrescences. Third, operational effects, resulting in leading-edge modification, must be overcome.

Under this project, numerical simulations were carried out to explore flow control that delays transition generated by excrescence on a plate-like geometry in subsonic flow. Details of the study are given in Appendix G. Both forward-facing and rearward-facing steps of small roughness height are considered in the simulations. These are representative of joints and other surface imperfections on wing sections that disrupt laminar flow, thereby increasing skin friction and drag. Dielectric barrier discharge (DBD) plasma-based flow control is employed to delay transition and increase the extent of the laminar flow region. Solutions are obtained to the Navier-Stokes equations that were augmented by source terms used to characterize the body force imparted by a plasma actuator on the fluid. A simple phenomenological model provided these forces resulting from the electric field generated by the plasma. Very small-amplitude numerical forcing is applied to generate perturbations, which are amplified by the geometric disturbances and result in transition, similar to the physical situation. Both continuous and pulsed operation of actuators is investigated. Features of the flowfields are described in Appendix G, and comparisons are provided between the baseline and control cases. It is found that use of plasma actuators can maintain laminar flow for the entire length of the computational domain, resulting in a reduction of the integrated drag by up to 70%.

The previous work on flat plates was extended to the more realistic case of a laminar wing section, as described in detail in Appendix H. Large-eddy simulations (LES) were carried out to investigate plasma-based flow control to delay transition generated by excrescence on the leading edge of a wing. The wing airfoil section has a geometry that is representative of modern reconnaissance air vehicles, and has an appreciable region of laminar flow at design conditions. Modification of the leading edge, which can be caused by the accumulation of debris, insect impacts, microscopic ice crystal formation, damage, or structural fatigue, may result in premature transition and an increase in drag. A dielectric barrier discharge (DBD) plasma actuator, located downstream of the excrescence, is employed to mitigate transition, decrease drag, and increase energy efficiency. Solutions were generated for both uniform and distributed excrescence geometries, as well as for the clean wing configuration without leading-edge modification. As shown in Figure 7, it was found that plasma control can re-establish the laminar flow region lost to excrescence-generated transition, and reduce integrated configuration drag by up to 25%.

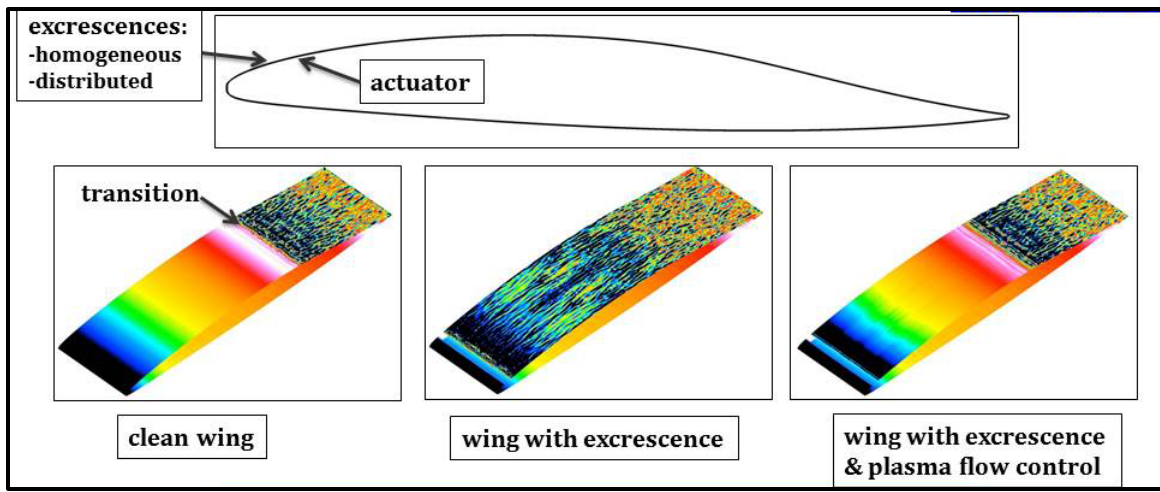


Figure 7: Delay of Excrescence-Induced Transition by Means of a Simulated Plasma Actuator

5. Conclusions

High-fidelity simulation was employed to address several complex unsteady interactions important to future USAF air vehicles. The research was focused on three key elements as outlined below:

1. Vortex interactions in formation flight.

This work elucidated the complex unsteady flow structure engendered by the interaction of a streamwise-oriented vortex with a wing. Several flow regimes were identified as a function of relative vortex position, as well as the corresponding effect on rolling moment. The effect of vortex wandering on the flow structure was described including the self-induced orbital motion of the vortex core upstream of the wing. Wing flexibility was found to increase buffeting due primarily to the shifting of the vortex axis to regions of higher adverse pressure gradient which in turn enhanced vortex spiral instabilities.

2. Dynamic stall.

The problem of dynamic stall for a pitching wing was studied as a model of parallel gust encounters. For the first time, a detailed analysis was presented of the unsteady separation process preceding dynamic stall vortex formation. The role of transition and of a highly-contracted laminar separation bubble near the leading edge was elucidated. This understanding led to a new flow control strategy based on very high frequency actuation. This control approach was found to be highly effective in suppressing dynamic stall for a pitching wing.

3. Plasma-based transition control.

The use of simulated plasma-based flow control in order to delay excrescence-induced premature transition was explored. Plasma actuation, located downstream of a canonical surface protuberance, was found to be promising for delaying transition to turbulence over a wing resulting in significant drag reduction.

6. References

1. Visbal, M. R. and Gaitonde, D.V., "High-Order Accurate Methods for Complex Unsteady Subsonic Flows", *AIAA Journal*, 37(10): 1231-1239, October 1999.
2. Visbal, M. and Gaitonde, D., "Very High-Order Spatially Implicit Schemes for Computational Acoustics on Curvilinear Meshes," *Journal of Computational Acoustics*, Vol. 9, No. 4, 2001
3. White, M. and Visbal, M., "Using Filters to Design Absorbing Boundary Conditions", *IEEE Transactions on Magnetics*, V. 4, No. 2, Mar. 2004, pp. 961-964.
4. Morgan, P. and Visbal, M., "Hybrid RANS/LES Simulation Investigating Control of Flow Over a Turret," *Journal of Aircraft* Vol. 49, No. 6, pp. 1700-1717, 2012.
5. Visbal, M. and Gaitonde, D., "On the Use of Higher-Order Finite-Difference Schemes on Curvilinear and Deforming Meshes," *J. of Comp. Physics*, Vol. 185, 2002.
6. Visbal, M.R., Morgan, P.E. and Rizzetta, D. P., "An Implicit LES Approach Based on High-Order Compact Differencing and Filtering Schemes (Invited)", AIAA 2003-4098, June, 2003.
7. Visbal, M. and Rizzetta, D., "Large-Eddy Simulation on Curvilinear Grids Using Compact Differencing and Filtering Schemes," *ASME Journal of Fluids Engineering*, Vol. 124, 2002.
8. Rizzetta, D., Visbal, M., and Blaisdell, G., "A time-implicit high-order compact differencing and filtering scheme for large-eddy simulation," *International Journal for Numerical Methods in Fluids*, Vol. 42, pp. 665–693, 2003.
9. Garmann, D. J., Visbal, M. R., and Orkwis, P. D., "Comparative study of implicit and sub-grid-scale model large-eddy simulation techniques for low-Reynolds number airfoil applications", *International Journal for Numerical Methods in Fluids*, Vol. 71, No. 12, 2013.
10. Visbal, M. and Gaitonde, D., "Shock Capturing Using Compact-Difference-Based Methods," AIAA Paper 2005-1265, Jan. 2005.
11. Rizzetta, D. P., Visbal, M. R., and Gaitonde, D. V., "Large-Eddy Simulation of Supersonic Compression-Ramp Flow by a High-Order Method," *AIAA Journal*, Vol. 39, No. 12, Dec. 2001.
12. Sherer, S. and Visbal, M., "Multi-resolution implicit large eddy simulations using a high-order overset-grid approach," *International Journal for Numerical Methods in Fluids*, Vol. 55, pp. 455–482, 2007.
13. Visbal, M. R., "High-Fidelity Simulations of Transitional Flows past a Plunging Airfoil", *AIAA Journal*, Vol. 47, No. 11, 2009.
14. Visbal, M., "Numerical Investigation of Deep Dynamic Stall of a Plunging Airfoil," *AIAA Journal*, Vol. 49, No. 10, 2011.
15. Gordnier, R. E., Chimakurthi, S. K., Cesnik, C.E.S., and Attar, P.J., "High-Fidelity Computations of a Flapping Wing with Spanwise Flexibility", *Journal of Fluids and Structures*", accepted for publication.
16. Visbal, M., "Strategies for Control of Transitional and Turbulent Flows Using Plasma-Based Actuators," *Int. J. of Computational Fluid Dynamics*, Vol. 24, No.7, August 2010.

17. Rizzetta, D. P., and Visbal, M. R., "Large-Eddy Simulation of Plasma-Based Turbulent Boundary-Layer Separation Control," *AIAA Journal*, Vol. 48, No. 12, Dec. 2010, pp. 2660-2793-2810.
18. Sherer, S.E., Visbal, M.R., Gordnier, R.E., Yilmaz, T.O., Rockwell, D.O., "1303 Unmanned Combat Air Vehicle Flowfield Simulations and Comparison to Experimental Data", *AIAA Journal of Aircraft*, Vol. 48, No.3, May-June 2011.
19. Golubev, V. V., Dreyer, B. D. and Hollenshade, T. M., "High-Accuracy Viscous Simulations of Gust-Airfoil Nonlinear Aeroelastic Interactions", AIAA-2009-4200, June, 2009.
20. Palacios, R. and Cesnik, C. E. S., "Cross-Sectional Analysis of Non-homogenous Anisotropic Active Slender Structures", *AIAA Journal* Vol. 43 No. 12, pp. 2624-2638, 2005.
21. Palacios, R. and Cesnik, C. E. S., "A Geometrically Nonlinear Theory of Active Composite Beams with deformable Cross Sections", *AIAA Journal* Vol. 46 No. 2, pp. 439-450, 2008.
22. Attar, P. J. and Gordnier, R. E., "Aeroelastic Modeling Using a Geometrically Nonlinear P-Version Mixed Reissner-Mindlin Plate Element", AIAA-2007-2318, April 2007.
23. Melville, R., Morton, S. and Rizzetta, D., "Implementation of a Fully-Implicit Aeroelastic Navier-Stokes Solver," AIAA 1997-2039, June, 1997.
24. Gordnier, R. E. and Visbal, M. R., "Computation of the Aeroelastic Response of a Flexible Delta Wing at High Angles of Attack," *Journal of Fluids and Structures*, Vol. 19, 2004, pp 758-800.
25. Attar, P.J. and Gordnier, R.E., "Aeroelastic Prediction of the Limit Cycle Oscillations of a Cropped Delta Wing," *Journal of Fluids and Structures*, Vol. 22, 2006, pp. 45-58
26. Visbal, M. R. and Gordnier, R. E., "Numerical simulation of the interaction of a transitional boundary layer with a 2-D flexible panel in the subsonic regime," *Journal of Fluids and Structures*, Vol. 19, 2004, pp. 881-903.
27. Visbal, M. R., "On the interaction of an oblique shock on a flexible panel", *Journal of Fluids and Structures*, Vol. 30, April 2012, pp. 219-225.
28. Gordnier, R. E., "High fidelity computational simulation of a membrane wing airfoil," *Journal of Fluids and Structures*, Vol. 25, pp 897-917, 2009.
29. Gordnier, R. E., "Implicit LES Simulations of a Low Reynolds Number Flexible Membrane Wing Airfoil," AIAA-2009-579, January 2009.
30. Gordnier, R.E. and Attar, P. J., "Impact of Flexibility on an Aspect Ratio Two Membrane Wing", FEDSM2012-72296, July 2012.
31. Gal, E. and Levy, R., "The Geometric Stiffness of Triangular Composite-Materials Shell Elements," *Computers and Structures*, Vol. 83, 2005, pp. 2318-2333.
32. Lissaman, S., Shollenberger, C. A., "Formation Flight of Birds, *Science* 168, 1003-1005. 1970.
33. Hummel, D., "Aerodynamic Aspects of Formation Flight in Birds," *Journal of Theoretical Biology*, Vol. 104, 1983, pp. 321-347.
34. Hummel, D., "Formation Flight as an Energy Saving Mechanism," *Israel Journal of Zoology*, Vol. 41, 1995.
35. Beukenberg, M. and Hummel, D., "Aerodynamics, Performance and Control of Airplanes in Formation Flight," CAS paper 90-5.9.3, 1990.

36. Ning, S. A., Flanzer, T.C., Kroo, I.M., "Aerodynamic Performance of Extended Formation Flight," AIAA Paper 2010-1240, 48th Aerospace Meeting. Orlando, FL, Jan 2010.
37. Kless, J., Aftosmis, M., Ning, A. and Nemec, M., "Inviscid Analysis of Extended Formation Flight," ICCFD7-4306, 7th Int. Conference on Computational Fluid Dynamics (ICCFD7), July 9-13, 2012.
38. R. Gordnier and M. Visbal, Numerical Simulation of the Impingement of a Streamwise Vortex on a Plate, *Int. J. of Computational Fluid Dynamics*, Vol. 12, 1999.
39. Martin, M., Carpenter, A. and Saric, W., "Swept Wing Laminar Flow Control Studies Using Cessna Test O-2A Aircraft, AIAA Paper 2008-1636, 2008.
40. McCroskey, J., "Unsteady Airfoils", *Annual Rev. Fluid Mech.*, 14:285–311, 1982.
41. Carr, L., "Progress in Analysis and Prediction of Dynamic Stall," *Journal of Aircraft*, 25(1): 6–17, 1988.
42. Ekaterinaris, J. and Platzer, M., "Computational Prediction of Airfoil Dynamic Stall," *Progress in Aerospace Sciences*, 33:759–846, 1997.
43. Visbal, M., "On some physical aspects of airfoil dynamic stall". In J. Miller and D. Telionis, editors, *Proceedings of the International Symposium on Non-Steady Fluid Dynamics*, volume 92. American Society of Mechanical Engineers, 1990.
44. Carr, L. and Chandrasekhara, M., "Compressibility Effects on Dynamic Stall," *Progress in Aerospace Sciences*, 32:523-573, 1996.

APPENDIX A

Interaction of a streamwise-oriented vortex with a wing

Daniel J. Garmann* and Miguel R. Visbal †

Air Force Research Laboratory, Wright-Patterson AFB, OH 45433

This work examines the interaction of a streamwise-oriented vortex impinging upon a wing for applications in formation flight. An analytically defined vortex superimposed on a free-stream is convected toward an aspect-ratio-six ($AR = 6$) wing oriented at an angle of $\alpha = 4^\circ$ and Reynolds number of $Re = 20,000$ in order to characterize the unsteady loading and induced vortex separation. Several spanwise positions of the vortex are analyzed and three distinct flow regimes are found. When the vortex is positioned outboard of, but in close proximity to, the wingtip, it pairs with the tip vortex to form a dipole that propels itself away from the plate due to its self-induced velocity and diffuses slowly. When the incoming vortex is aligned with the wingtip, the incident and tip vortex feeding sheets interact quite strongly and become entrained in the circulation of the opposite structure, which diminishes the coherence of both vortices into the wake. Finally, when the incident vortex is positioned inboard of the wingtip, the vortex bifurcates in the time-mean sense with portions convecting below and above the wing. The increased effective angle of attack inboard of impingement enhances the three-dimensional recirculation region created by the separated boundary layer off the leading edge which draws fluid from the incident vortex inboard and diminishes its impact on the outboard section of the wing. The slight but remaining downwash present outboard of impingement reduces the effective angle of attack in that region resulting in a small separation bubble on either side of the wing in the time-mean solution effectively unloading the tip outboard of impingement. All incident vortex positions provide substantial increases in the wing's lift-to-drag ratio; however, significant sustained rolling moments also result. As the vortex is brought inboard, the rolling moment diminishes and eventually switches sign, indicating that small changes in vortex position can cause dramatic moment variations, which will require dynamic and responsive control systems.

I. Introduction

Formation flight of aircraft and birds has long been understood to provide significant benefits in aerodynamic performance. With proper positioning, trailing aircraft can capture the upwash from the tip vortex left in the wake of a lead aircraft. The result is a forward-tilted lift vector that provides increased lift and a reduction in induced drag, which can lead to significant energy savings.¹ Close formation flight has historically been limited by safety concerns arising from the high speed and proximity of adjacent aircraft. Fortunately, technological advances in positioning and guidance systems along with collision avoidance systems are making it possible for military and commercial aircraft to fly in closer proximity to take advantage of close formation flight. This does not come without cost, however. Close formation flight can also produce undesirable effects including strong or unsteady vortex buffeting leading to structural fatigue or a net downwash from improper positioning of the wake vortex during capture. For close-in formations, it is important to understand the complex interactions of the streamwise-oriented vortices with a follower wing.

Analysis of the benefits of formation flight employing classic aerodynamic theory was provided in a series of papers by Hummel^{2,3,4} wherein citations to earlier seminal work can also be found. Recently, Ning et al.⁵ performed an investigation of several factors affecting the benefits and feasibility of extended formation flight for three aircraft in canonical echelon and V-type arrangements. These factors included wake roll-up, vortex core size, vortex decay and gust effects. Kless et al.⁶ provided a computational inviscid flow analysis of

*Research Aerospace Engineer; Ohio Aerospace Institute; AIAA Senior Member.

†Technical Area Lead; AIAA Fellow.

This material is declared a work of the U.S. Government and is not subject to copyright protection in the United States.

several aspects of extended formation flight with consideration of optimal incident vortex location, roll trim effects and transonic flow effects. Despite advances in the understanding, prediction and demonstration of the benefits of formation flight, significant challenges still require further investigation before this technology becomes a viable and safe operational capability.

The interaction of a streamwise vortex with an aerodynamic surface can engender a broad range of difficult-to-predict unsteady phenomena that will impact drag and lift performance as well as the unsteady loading or buffeting experienced by the wing. These effects are expected to be crucial for more aggressive close-in and heterogeneous aircraft formations. For instance, the strong adverse local pressure gradients imposed by a vortex in close proximity to a wing can induce unsteady separation over a portion of the wing. This may lead to increased drag, reduced lift and ill-behaved rolling moments, which will induce additional trim penalties and impose further requirements on control systems. These direct vortex/surface interactions cannot necessarily be avoided since improved aerodynamic performance may dictate formation arrangements in which the incident vortex impinges inboard of the wing tip, i.e. the wings are overlapped in the spanwise direction. In fact, this is not only observed in natural overlapped close formation flight,^{2,3} but also in the inviscid extended formation study of Ref. 6 wherein optimal trimmed impingement and zero rolling moment states were found to correspond to incident vortex positions inboard of the wing tip. In the tandem wing experiments of Inasawa et al.,⁷ maximum advantage of lift-to-drag ratio was also observed when the wings were overlapped in the spanwise direction.

Either a single vortex or systems of streamwise-oriented vortices are known to exhibit a rich dynamics. Long wavelength,⁸ short wavelength (elliptical) and spiral breakdown⁹ constitute examples of potential outcomes which may affect the evolution of a trailing vortex and its interaction with aerodynamic surfaces encountered in its path. Furthermore, axial vortices may also exhibit spiral sub-structures generated during their roll-up process.^{10,11} These instabilities and unsteady features can result in additional sources of buffeting upon impingement on a trailing wing. To further compound the problem, either deliberate or unanticipated motions of the leading aircraft will induce perturbations that propagate downstream and provide another degree of uncertainty in predicting and harnessing potential benefits of the interaction. In multiple-aircraft formation flight, this uncertainty is likely to increase as one proceeds to the rear of the formation array.

Another unresolved critical aspect of the problem is the modification of the incident vortex and its instability modes generated by the process of impingement on the follower wing. For anticipated streamwise separation distances this feedback will most likely be limited to a region of upstream influence in front of the wing. Nonetheless coupling of vortex instabilities with the unsteady separation is in general not well understood and could give rise to a resonant behavior with significant impact on the vortex/surface interaction.

In this work, an investigation of a streamwise-oriented vortex impinging upon a finite-span wing is provided. An analytically defined vortex is superimposed into a free-stream and convected towards a wing in order to characterize the unsteady loading and induced vortex separation from formation flight conditions. The simplified vortex/wing configuration allows many vortex positions, strengths, and sizes to be readily examined without the need for detailed simulation of a lead wing, making it an ideal problem for careful study of the vortex impingement problem. The size and strength of the vortex could be adjusted to represent different lead aircraft planforms along with the relative position of the vortex to the follower wing, so their effects on aerodynamic performance can be determined. In this work, only vortex spanwise position is varied to highlight impingement location effects.

II. Governing equations

The governing equations for the current work are the compressible, three-dimensional Navier-Stokes equations. After a general time-dependent transformation from Cartesian coordinates (x, y, z, t) to computational space (ξ, η, ζ, τ) , these equations can be written in strong conservation form¹² as follows:

$$\frac{\partial}{\partial \tau} \left(\frac{\mathbf{U}}{J} \right) + \frac{\partial \mathbf{F}}{\partial \xi} + \frac{\partial \mathbf{G}}{\partial \eta} + \frac{\partial \mathbf{H}}{\partial \zeta} = \frac{1}{\text{Re}} \left[\frac{\partial \mathbf{F}_v}{\partial \xi} + \frac{\partial \mathbf{G}_v}{\partial \eta} + \frac{\partial \mathbf{H}_v}{\partial \zeta} \right] \quad (1)$$

where the solution vector is

$$\mathbf{U} = [\rho, \rho u, \rho v, \rho w, \rho E]^T \quad (2)$$

and the inviscid flux vectors are

$$\mathbf{F} = \frac{1}{J} \begin{bmatrix} \rho U \\ \rho u U + \xi_x p \\ \rho v U + \xi_y p \\ \rho w U + \xi_z p \\ (\rho E + p) U - \xi_t p \end{bmatrix}, \mathbf{G} = \frac{1}{J} \begin{bmatrix} \rho V \\ \rho u V + \eta_x p \\ \rho v V + \eta_y p \\ \rho w V + \eta_z p \\ (\rho E + p) V - \eta_t p \end{bmatrix}, \mathbf{H} = \frac{1}{J} \begin{bmatrix} \rho W \\ \rho u W + \zeta_x p \\ \rho v W + \zeta_y p \\ \rho w W + \zeta_z p \\ (\rho E + p) W - \zeta_t p \end{bmatrix} \quad (3)$$

In these expressions, $J = \partial(\xi, \eta, \zeta, \tau) / \partial(x, y, z, t)$ is the Jacobian of the transformation, u , v , and w are the Cartesian velocity components, ρ is the density, p is the pressure, U , V , and W are the contravariant velocities given as

$$\begin{aligned} U &= \xi_t + \xi_x u + \xi_y v + \xi_z w \\ V &= \eta_t + \eta_x u + \eta_y v + \eta_z w \\ W &= \zeta_t + \zeta_x u + \zeta_y v + \zeta_z w \end{aligned} \quad (4)$$

and the internal energy, E , is

$$E = \frac{T}{(\gamma - 1) M_\infty^2} + \frac{1}{2} (u^2 + v^2 + w^2) \quad (5)$$

where T is the temperature and M_∞ is the free-stream Mach number. The viscous fluxes, \mathbf{F}_v , \mathbf{G}_v , and \mathbf{H}_v , written in indicial notation are

$$\mathbf{F}_v = \frac{1}{J} \begin{bmatrix} 0 \\ \xi_{x_i} \sigma_{i1} \\ \xi_{x_i} \sigma_{i2} \\ \xi_{x_i} \sigma_{i3} \\ \xi_{x_i} (u_j \sigma_{ij} - \Theta_i) \end{bmatrix}, \mathbf{G}_v = \frac{1}{J} \begin{bmatrix} 0 \\ \eta_{x_i} \sigma_{i1} \\ \eta_{x_i} \sigma_{i2} \\ \eta_{x_i} \sigma_{i3} \\ \eta_{x_i} (u_j \sigma_{ij} - \Theta_i) \end{bmatrix}, \mathbf{H}_v = \frac{1}{J} \begin{bmatrix} 0 \\ \zeta_{x_i} \sigma_{i1} \\ \zeta_{x_i} \sigma_{i2} \\ \zeta_{x_i} \sigma_{i3} \\ \zeta_{x_i} (u_j \sigma_{ij} - \Theta_i) \end{bmatrix} \quad (6)$$

The components of the stress tensor and heat flux vector are given as

$$\sigma_{ij} = \mu \left(\frac{\partial \xi_k}{\partial x_j} \frac{\partial u_i}{\partial \xi_k} + \frac{\partial \xi_k}{\partial x_i} \frac{\partial u_j}{\partial \xi_k} - \frac{2}{3} \delta_{ij} \frac{\partial \xi_l}{\partial x_k} \frac{\partial u_k}{\partial \xi_l} \right) \quad (7)$$

and

$$\Theta_i = - \left[\frac{1}{(\gamma - 1) M_\infty^2} \right] \left(\frac{\mu}{Pr} \right) \frac{\partial \xi_j}{\partial x_i} \frac{\partial T}{\partial \xi_j} \quad (8)$$

where μ is the dynamic viscosity, γ is the ratio of specific heats, and $x_i (\equiv x, y, z)$, $\xi_i (\equiv \xi, \eta, \zeta)$ and $u_i (\equiv u, v, w)$ for $i = 1, 2, 3$. Stokes' hypothesis is assumed for the bulk viscosity coefficient ($\lambda = -2/3\mu$), and the governing equations are also supplemented with the perfect gas equation, $p = \rho T / \gamma M_\infty^2$, Sutherland's viscosity law, and a constant Prandtl number ($Pr = 0.72$ for air). All flow variables are normalized by their respective free-stream counterparts, except for pressure, which is scaled by twice the dynamic pressure, $\rho_\infty U_\infty^2$. The reference length is the wing chord, c .

This set of equations corresponds to the *unfiltered* Navier-Stokes equations and is used without change in laminar, transitional or fully turbulent regions of the flow for the ILES procedure. Unlike the standard LES approach, no additional subgrid-scale (SGS) model or heat flux terms are appended. Instead, a high-order, low-pass filter operator, which will be discussed later, is applied to the conserved variables during the solution of the standard Navier-Stokes equations. This highly-discriminating, Padé-type filter selectively dampens only the evolving, poorly resolved high-frequency content of the solution.^{13, 14} The filtering regularization procedure provides an attractive alternative to the use of standard SGS models, and has been found to yield suitable results for several turbulent and transitional flows on LES level grids.¹⁵ A reinterpretation of this ILES approach in the context of an Approximate Deconvolution Model¹⁶ has been provided by Matthew *et al.*¹⁷ With sufficient spatial resolution, the ILES technique is effectively a direct numerical simulation (DNS).

III. Numerical Procedure

All simulations were performed with the extensively validated high-order, Navier-Stokes flow solver, *FDL3DI*.^{18,19} In this code, the governing equations are discretized through a finite-difference approach with all spatial derivatives obtained using high-order compact-differencing schemes.²⁰ The spatial derivative of any scalar quantity, ϕ , such as a metric, flux component, or flow variable, is obtained along a coordinate line in computational space by solving the following tridiagonal system:

$$\alpha \phi'_{i-1} + \phi'_i + \alpha \phi'_{i+1} = a \left(\frac{\phi_{i+1} - \phi_{i-1}}{2} \right) + b \left(\frac{\phi_{i+2} - \phi_{i-2}}{4} \right) \quad (9)$$

where proper choice of the coefficients, α , a , and b , provides up to sixth-order spatial accuracy. At boundary points, higher-order, one-sided formulae are utilized that retain the tridiagonal form of the scheme.^{18,19} For all the computations presented in this work, the interior coefficients are $\alpha = 1/3$, $a = 14/9$, and $b = 1/9$, which correspond to a sixth-order accurate, compact scheme. The boundary point and first off-boundary point use fourth- and fifth-order compact schemes, respectively.

The derivatives of the inviscid fluxes are obtained by forming the fluxes at the nodes and differentiating each component with the compact differencing scheme. Viscous terms are obtained by first computing the derivatives of the primitive variables and then constructing the components of the viscous fluxes at each node and differentiating by a second application of the same scheme.

In order to eliminate spurious components of the solution, a high-order, low-pass spatial filtering operator^{18,21} is applied to the conserved variables along each transformed coordinate direction one time after each time step or sub-iteration. If a typical component of the solution vector is denoted by ϕ , filtered values $\hat{\phi}$ at interior points in computational space satisfy,

$$\alpha_f \hat{\phi}_{i-1} + \hat{\phi}_i + \alpha_f \hat{\phi}_{i+1} = \sum_{n=0}^N a_n \left(\frac{\phi_{i-n} + \phi_{i+n}}{2} \right) \quad (10)$$

where proper choice of the coefficients, (a_0, a_1, \dots, a_N) , provides a $2N^{th}$ -order formula on a $2N + 1$ point stencil. The filtering technique is based on templates proposed in References 20 and 22, and the coefficients, along with representative filter transfer functions, can be found in References 19 and 21. The parameter, α_f , is left as a free variable in order to provide limited control of the cutoff frequency of the low-pass filter operator. Typical values are in the range: $0.3 \leq \alpha_f \leq 0.49$. For the near-boundary points, the filtering strategies described in References 18 and 21 are used. For transitional and turbulent flows, the high-fidelity spatial algorithmic components provide an effective implicit LES (ILES) approach in lieu of traditional SGS models, as demonstrated in References 13 and 14 and more recently in Ref. 15. All computations presented in this work utilized an eighth-order accurate interior filter with a coefficient of $\alpha_f = 0.40$ for targeted dissipation.

Time marching of the governing equations is achieved through the iterative, implicit approximately-factored integration method of Beam and Warming²³ and supplemented with the use of Newton-like sub-iterations to achieve second-order accuracy^{13,14} and reduce errors due to factorization, linearization, diagonalization, and explicit application of boundary conditions.²⁴ The block-tridiagonal form of the algorithm can be written in delta form as

$$\begin{aligned} & \left[\left(\frac{1}{J} \right)^{p+1} + \phi^i \Delta\tau \delta_\xi^{(2)} \left(\frac{\partial \mathbf{F}^p}{\partial \mathbf{U}} - \frac{1}{\text{Re}} \frac{\partial \mathbf{F}_v^p}{\partial \mathbf{U}} \right) \right] J^{p+1} \times \\ & \left[\left(\frac{1}{J} \right)^{p+1} + \phi^i \Delta\tau \delta_\eta^{(2)} \left(\frac{\partial \mathbf{G}^p}{\partial \mathbf{U}} - \frac{1}{\text{Re}} \frac{\partial \mathbf{G}_v^p}{\partial \mathbf{U}} \right) \right] J^{p+1} \times \\ & \left[\left(\frac{1}{J} \right)^{p+1} + \phi^i \Delta\tau \delta_\zeta^{(2)} \left(\frac{\partial \mathbf{H}^p}{\partial \mathbf{U}} - \frac{1}{\text{Re}} \frac{\partial \mathbf{H}_v^p}{\partial \mathbf{U}} \right) \right] \Delta \mathbf{U} \\ & = -\phi^i \Delta\tau \left[\left(\frac{1}{J} \right)^{p+1} \frac{(1+\phi) \mathbf{U}^p - (1+2\phi) \mathbf{U}^n + \phi \mathbf{U}^{n-1}}{\Delta\tau} + \mathbf{U}^p \left(\frac{1}{J} \right)_\tau^p + \right. \\ & \quad \left. \delta_\xi \left(\mathbf{F}^p - \frac{1}{\text{Re}} \mathbf{F}_v^p \right) + \delta_\eta \left(\mathbf{G}^p - \frac{1}{\text{Re}} \mathbf{G}_v^p \right) + \delta_\zeta \left(\mathbf{H}^p - \frac{1}{\text{Re}} \mathbf{H}_v^p \right) \right] \end{aligned} \quad (11)$$

where \mathbf{U}^p is the p^{th} approximation to \mathbf{U} at the $n+1$ time level and $\Delta\mathbf{U} = \mathbf{U}^{n+1} - \mathbf{U}^p$. For the first iteration $\mathbf{U}^p = \mathbf{U}^n$, and as $p \rightarrow \infty$, $\mathbf{U}^p \rightarrow \mathbf{U}^{n+1}$. The block-tridiagonal form of Eq. (11) is further simplified through the diagonalization of Pulliam and Chaussee,²⁵ and fourth-order, nonlinear dissipation terms^{26,27} are also appended to the implicit operator to augment stability, although these are not shown in Eq. (11) for clarity. Second-order finite differencing is used in the implicit operator, while high-order compact differencing is employed in the residual. Iteration drives the left-hand-side to zero, so only the high-order spatial error of the residual remains.

IV. Details of the computations

A. Geometry and vortex model

An analytically defined vortex is superimposed on a free-stream at the inflow boundary and convected toward a wing as shown in Fig. 1. The rectangular wing has an aspect ratio of six ($AR = b/c = 6$) and a thickness of $t = 0.03c$ and is oriented at an angle of attack of $\alpha = 4^\circ$ relative to the free-stream. Preliminary computations, which are not presented here, showed that the vortex deflects upward as it approaches the wing and could convect completely over the upper side when positioned at or above the leading edge in the vertical direction due to the accelerating flow over the lifting body. To prevent this and enable a more pronounced impact with the wing for this study, the incident vortex is positioned under the leading edge such that its axis intersects with the mid-chord of the wing ($\Delta z = 0.035$) in the vertical direction. Several spanwise positions of the incoming vortex are examined corresponding to $\Delta y = -0.25, 0.00, 0.25, 0.50$, and 1.00 . The first position is outboard of the wingtip, the second is tip-aligned, and the others are all inboard of the tip.

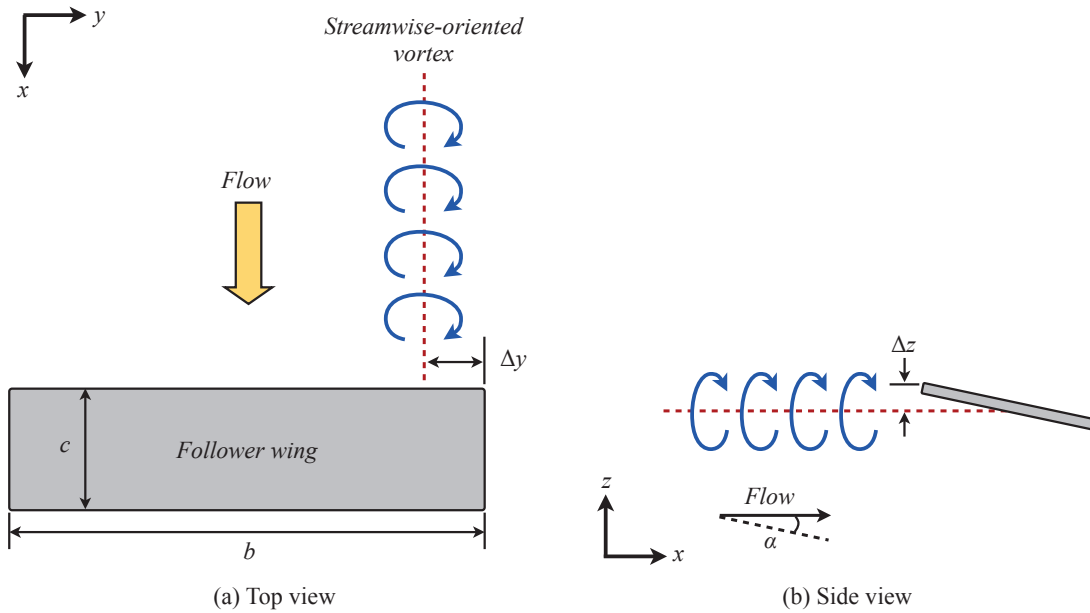


Figure 1: Configuration of a streamwise-oriented vortex impinging on a wing; (a) Top view, (b) Side view

In order to model a trailing vortex from a lead wing, a Batchelor²⁸ or q -vortex vortex is superimposed into the incoming flow upstream of the wing. This vortex is described analytically as

$$u_r(r) = 0 \quad (12)$$

$$u_\theta(r) = \frac{\Gamma_0}{2\pi r} \left(1 - e^{-(r/r_0)^2} \right) \quad (13)$$

$$u_x(r) = 1 - \Delta u e^{-(r/r_0)^2} \quad (14)$$

where u_r , u_θ , and u_x correspond to the radial, circumferential, and axial velocities, respectively, Γ_0 is the

vortex circulation, r_0 is a measure of the vortex radius, and Δu is the axial velocity deficit in the vortex core. Rather than circulation, the swirl parameter, q , is used to specify the strength of the vortex. This parameter is defined as

$$q = \frac{\Gamma_0}{2\pi r_0 \Delta u} \approx 1.567 \frac{V_0}{\Delta u} \quad (15)$$

where V_0 is the maximum circumferential velocity. This shows that q is a measure of the relative tangential and axial velocity intensities.²⁹ The circumferential velocity recast in terms of q becomes

$$u_\theta(r) = \frac{q \Delta u}{r/r_0} \left(1 - e^{-(r/r_0)^2} \right) \quad (16)$$

A stability criterion for the q -vortex was established by Leibovich and Stewartson³⁰ to prevent amplification of small-wave perturbations at any r . This restriction is given as

$$\sigma^2(r) = \frac{2u_\theta(r)u'_\theta - u_\theta(u_\theta^2/r^2 - u'^2_\theta - u'^2_x)}{(r u'_\theta - u_\theta)^2 + (r u'_x)^2} < 0 \quad (17)$$

Substitution of Eqs. (14) and (16) into the stability criterion leads to a lower bound prediction on the swirl parameter of $q \geq \sqrt{2}$ to maintain stability of the vortex. All values of q in this work are taken in the stable range to prevent the vortex from becoming susceptible to breakdown before interacting with the wing.

For the cases presented here, the swirl parameter is selected as $q = 2.0$ and the axial velocity deficit is $\Delta u = 0.4 U_\infty$ to achieve a maximum circumferential velocity of $V_0 = 0.5 U_\infty$. The vortex core radius is set as $r_0 = 0.1c$, and the Reynolds number based on wing chord and free-stream velocity is selected as $Re = 20,000$. Each of these parameters has been selected based on vortex profiles documented within the literature by the Euler computations of Kless *et al.*⁶ and the experiments of Inasawa *et al.*⁷ in which a lead wing was actually tested and the wake was analyzed. The estimated values for the maximum circumferential velocity and its radial location are listed in Table 1 along with details of the lead wing geometry and orientation. The maximum velocity radial location, $r_{u_{\max}}$, is related to the core radius by $r_{u_{\max}} \approx 1.1209 r_0$, leading to the choice of $r_0/c = 0.1$ for the current study, which falls in between the values from References 6 and 7.

Table 1: Vortex profiles from the literature

Reference	Solution method	Lead wing	V_0/U_∞	$r_{u_{\max}}/c$
Kless <i>et al.</i> ⁶	Euler computations	NACA0012, AR=8, $\alpha \approx 4^\circ$, $C_L = 0.55$	0.10	≈ 0.20
Inasawa <i>et al.</i> ⁷	Experiments	NACA23012, AR=5, $\alpha = 8^\circ$	0.5	≈ 0.05

B. Computational mesh and boundary conditions

The imposed vortex problem requires the use of a nested mesh system that utilizes Chimera overset³¹ with high-order interpolation³² in order to make it tractable for LES. The configuration consists of six near-body stretched Cartesian meshes protruding normal to the rectangular wing with increased stretching away from the surface. Once a nominal spacing has been achieved, the near-body grids cease and a coarser background mesh continues to the farfield boundaries located 30-50 chords from the wing. A separate, higher-resolution mesh is overset into the background mesh to maintain the integrity of the streamwise-oriented vortex as it convects towards the wing from the inflow boundary. A depiction of the near-field, nested mesh system is presented in Fig. 2. The farfield boundaries actually extend much farther away from the wing, but only the near-body domain is shown for clarity. Additionally, the wing is oriented at an angle of $\alpha = 4^\circ$ and the mesh is analytically deformed near the surface using a exponential decay weighting function to maintain normal gridlines at the boundary while keeping the mid-field overlap regions undisturbed away from the wing. This allows multiple wing orientations to be readily available by merely deforming the mesh rather than completely regenerating the discretized domain, although, only one orientation is considered in this study.

The inflow boundary is positioned 10 chords ahead of the wing, and the analytically defined vortex is imposed there. All other farfield boundaries are prescribed as outflow conditions, which in conjunction

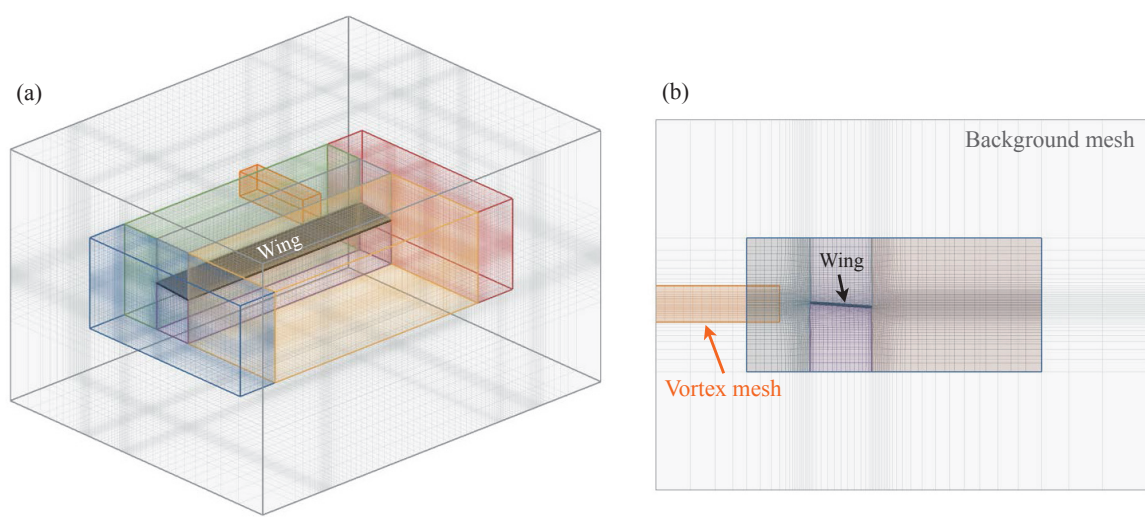


Figure 2: Depiction of the near-field nested mesh configuration; (a) Full view, (b) Side view

C. Effects of spatial resolution

In order to examine the spatial resolution required for the current problem, three geometrically similar meshes have been created with successive levels of refinement: fine, medium (75%), and coarse (50%). Specific details of these grids are listed in Table 2 including the number of surface points across the chord (n_ξ), span (n_η), and thickness (n_ζ) along with the minimum spacing in each direction. In these cases, the incident vortex is prescribed at a constant spanwise position aligned with the wingtip ($\Delta y = 0$) and inline with the midchord of the wing in the vertical direction ($\Delta z = 0.035$).

Table 2: Details of the computational grids

Mesh	Surface elements			Total grid points	Minimum spacing		
	n_ξ	n_η	n_ζ		Normal	Streamwise	Spanwise
Coarse	136	408	34	64,747,539	1.47×10^{-4}	7.35×10^{-4}	7.35×10^{-4}
Medium	154	461	39	91,880,552	1.30×10^{-4}	6.49×10^{-4}	6.49×10^{-4}
Fine	170	510	43	123,755,401	1.18×10^{-4}	5.88×10^{-4}	5.88×10^{-4}

The flow structure from the time-mean solution of all resolutions is shown in Fig. 3(a) through iso-surfaces of Q-criterion along with the instantaneous aerodynamic loading for ten convective times in Fig. 3(b). The different resolutions produce virtually the same instantaneous aerodynamic loading with no significant deviations from the mean. The flow structure of the incident and tip vortex interaction also shows almost no change with increased grid refinement whereby the incident vortex becomes entrained by the upwash of the tip vortex and is diverted over the suction side of the wing. The opposite-signed vortices drain one another as their feeding sheets interact; however, there is almost no interaction with the time-averaged vortex cores themselves as they remain coherent and distinct. After a chord of travel in the streamwise direction, both vortices are almost completely dissipated. The higher resolution meshes do show slightly more structure in the time-mean solution in the region of reattachment from the leading edge vortex; however, these smaller scales do not appear to impact the incident and tip vortex interaction. Additionally, the time-mean loads are listed in Table 3, where it is seen that the various resolutions produce nearly identical forces and moments

with only minor differences that are a few percent of the fine mesh values. With so few differences in flow structure and instantaneous loading, the *medium* mesh is confidently chosen for the remainder of this study.

Table 3: Mean aerodynamic loads for the different spatial resolutions

Mesh	C_L	C_D	$C_{M,c/4}$	C_x
Coarse	0.573	0.078	-0.031	0.202
Medium	0.574	0.078	-0.033	0.201
Fine	0.562	0.077	-0.027	0.204

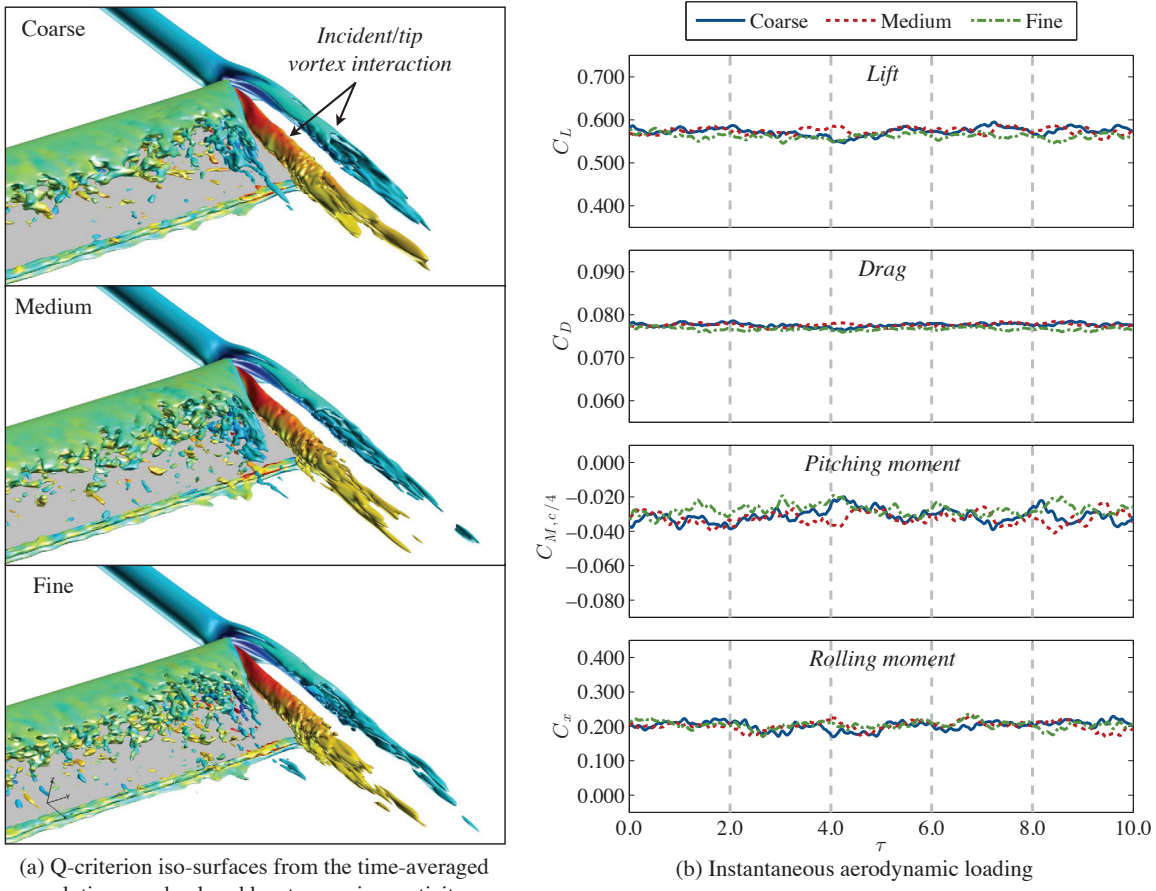


Figure 3: Effect of spatial resolution on the time-mean flow structure and instantaneous loading; (a) Iso-surfaces of time-mean Q-criterion, (b) Instantaneous lift, drag, pitching moment, and rolling moment coefficients

V. Results

In this section, simulations of the superimposed vortex positioned at several spanwise locations are presented. In all cases, the solution was advanced for 20 convective times to eliminate spurious transients associated with the startup and to allow the incident vortex to convect past the wing and establish the flow. Ten more convective times were then simulated to collect time-mean and statistical information. The dimensionless time step was selected as $\Delta\tau = 0.0001$ to provide ample temporal resolution.

A. Description of the three-dimensional flow structure

Snapshots of the instantaneous flow structure are shown in Fig. 4 through iso-surfaces of Q-criterion ($Q = 15$). The baseline case is shown in (a) along with all the incident vortex positions (b-f) corresponding to $\Delta y = -0.25, 0.00, 0.25, 0.50$, and 1.00 , respectively. Additionally, the time-mean flow structure is provided in Fig. 5 for $Q = 5$. Note that the orientations in these figures are different to expose the interesting features. When the incident vortex is positioned just outboard of the wingtip (b), its core remains mostly intact as it convects past the tip vortex. The two structures pair to form a vortex dipole that propels itself upward, away from the plate, due to their self-induced velocity. Although the two structures remain distinct and coherent, their interaction causes the vortex cores to become susceptible to spiraling disruptions downstream of the wing, which can be seen in the instantaneous flow of Fig. 4(b).

When the incident vortex is, instead, aligned directly with the wingtip (c), it is drawn to the upper side of the wing from the accelerating flow over the leading edge and tip of the wing, and its outer shear layer interacts very strongly with the feeding sheet of the tip vortex. Finger-like substructures develop from the interaction and become entrained into the tip vortex, which has reversed-signed vorticity. While neither vortex core is discernible in the instantaneous flow, the conglomeration of all the small scales in the time-mean solution shows two distinct and coherent cores that remain intact across the wing. However, with the disruption of their feeding sheets and entrainment of opposite-signed vorticity, both structures start to lose their coherency in the wake.

Finally, when the incoming vortex is positioned inboard of the wingtip (d-f), yet another, completely different regime is encountered. The upstream influence of the wing promotes spiraling disruptions in the incident vortex that wind in a direction opposite the sense of rotation of the vortex as pointed out in the instantaneous flow of Figures 4(d₁-f₁). As they approach the wing, these structures reorient from streamwise to plate-normal and are pinched off by the leading edge and attach to the wing surface, alternating from the upper to lower surface as the vortex spirals. A quantitative measure of the undulation is provided in Fig. 6 by the energy spectra computed from the time-histories of the velocity fluctuations measured at a probe that was positioned in the boundary layer off the upper surface of the wing ($\Delta\eta = 0.001c$) at the mid-chord and aligned with the vortex impingement. A distinct peak is found in the energy spectra at a reduced frequency of $f = 1.1$, which corresponds to the alternating interaction of the vortex with the upper surface. Further details on this complex unsteady interaction are left for future studies. Turning back to the time-mean solution of Fig. 5, the alternating lower/upper surface interaction appears as a vortex bifurcation with portions of the incoming vortex convecting over the upper and lower surfaces of the wing. Downwash now present on the most outboard section of the wing reduces the effective angle of attack there causing the flow to mostly attach and essentially suppressing the tip vortex formation. An almost identical separation bubble is present on the upper and lower wing surfaces in the time-mean solution (shown in inset Fig. 5(f₁) for $\Delta y = -1.0$) highlighting the drop in effective angle of attack. The other inboard positions have similar features, and are therefore, not shown in detail.

Next, the incident vortex is dissected and shown through contours of time-mean streamwise vorticity in Fig. 7 as it interacts with the wing. The view is directed from a downstream location towards the inflow boundary, and the incoming vortex in each image has negatively-signed (blue) vorticity. The slices start from $0.5c$ upstream of the wing and end $1.5c$ into the wake. The inboard positions, (d) and (e), have been excluded in this figure since they are very similar to (f). The vortex dipole is seen very clearly in (b) when the incoming vortex is positioned just outboard of the wingtip. The tip vortex is much larger than the baseline case and is propelled upward slightly, away from the wing surface due to the induced velocity of the pair. Both structures persist into the wake without noticeable decay. For the tip-aligned case (c), the tip and incident vortex cores are distinct, and the tip vortex (or conglomeration of the smaller scales associated with the tip vortex) is larger than that of the baseline and outboard-positioned cases. The two structures are still evident $1.5c$ downstream, but they experience a loss of strength and coherency as they continue to interact. Finally, with all inboard positions of the incident vortex (f), the bifurcation is quite evident along with the suppression of the tip vortex. The integrity of the incident vortex is lost as it convects downstream following its interaction with the three-dimensional recirculation region where flow is drawn inboard, and the streamwise vorticity is reoriented to the spanwise direction.

In Fig. 8, the surface-restricted streamlines are pictured on the suction and pressure sides of the wing. Here, we can see the slightly inboard-directed streamlines on the suction side of the wing for cases (d-f) near the impingement location from the vortex interacting with its reflected image in the surface. On the underside, the lower portion of the bifurcated vortex also interacts with its image, and the induced velocity

Table 4: Integrated surface pressure fluctuations

Δy	Pressure side ($\times 10^{-3}$)	Suction side ($\times 10^{-3}$)
No vortex	0.02	3.76
-0.25	0.02	4.75
0.00	0.03	4.80
0.25	0.05	4.30
0.50	0.11	3.65
1.00	0.22	3.30

is directed outboard. In all cases, the reattachment line on the suction side of the wing (approximately shown with a dotted line) moves towards the trailing edge due to the increased separation from the upwash of the incident vortex. For all inboard positions (d-f), the increased effective angle of attack enhances the recirculation region created by the separated boundary layer inboard of impingement that closely resembles the flow over the corner of a wing at much higher angles of attack in a freestream, which have been simulated and shown in detail by Visbal and Garman³³ for lower aspect-ratio wings. The incident vortex becomes entrained in this three-dimensional region and fluid is drawn inboard, thereby diminishing but not completely eliminating its impact on the outboard section of the wing. The three-dimensional streamlines over the suction side of the wing are depicted in Fig. 9. These images show, perhaps more clearly, the enhancement of the recirculation region that draws the fluid towards mid-span and the reduced impact outboard of impingement. It is interesting to note the almost self-similarity about these recirculation regions with inboard vortex position that appears to pin the flow near impingement and effectively reduces the usable aspect ratio of the wing. This process should eventually saturate for large enough span. Only slight downwash remains near the wingtip, but it is significant enough to substantially reduce separation on the upper side of the wing outboard of impingement. The reduced effective angle of attack also causes the flow on the underside to separate as well indicated by the separation bubble seen in the surface-restricted streamlines in Fig. 8(f) denoted by (2). Additionally, cases (e) and (f) show a line of convergence oriented chordwise on the underside that corresponds with a region of minor separation due to an eruption of secondary vorticity from the surface as highlighted in Fig. 10 for $\Delta y = 1.00$.

Next, the time-averaged surface pressure near the impingement location is shown in Fig. 11 along with the surface-restricted streamlines for each case. The incident vortex induces larger separated regions that provide more suction over a larger chordwise extent of the wing. The outboard (b) and tip-aligned (c) positions both reveal a stronger imprint of the tip vortex in the surface pressure (denoted as (1)) as a result of the strengthened tip vortex feeding sheet from the upwash of the incident vortex that is in close proximity. Alternatively, the incident vortex, when positioned inboard (d-f), does not enhance the tip vortex, but instead, it suppresses its formation by reducing the effective angle of attack outboard of impingement. This results in two small separation bubbles on the upper and lower surfaces with nearly equivalent suction for the inboard positions examined.

Contours of the mean-squared fluctuations of pressure, $\overline{p'p'}$, on the surface are displayed in Fig. 12, and the mean values integrated over the wing are listed in Table 4. On the suction side, all cases produce fluctuations across a wider chordwise extent over the baseline simulation. As the vortex is moved inboard, the mean fluctuations in Table 12 decrease on the suction side from the growing region of attached flow present outboard of the impingement location with the two farthest inboard positions, $\Delta y = 0.5$ and 1.0, achieving mean fluctuations below the baseline wing. Alternatively, the underside fluctuations, although much smaller than the upper side values, increase with vortex inboard position from the portion of the bifurcated incident vortex traveling across the pressure side and disturbing the otherwise attached boundary layer. There are also fluctuations associated with reattachment of the outboard separation bubbles on either sides of the wing as one would expect.

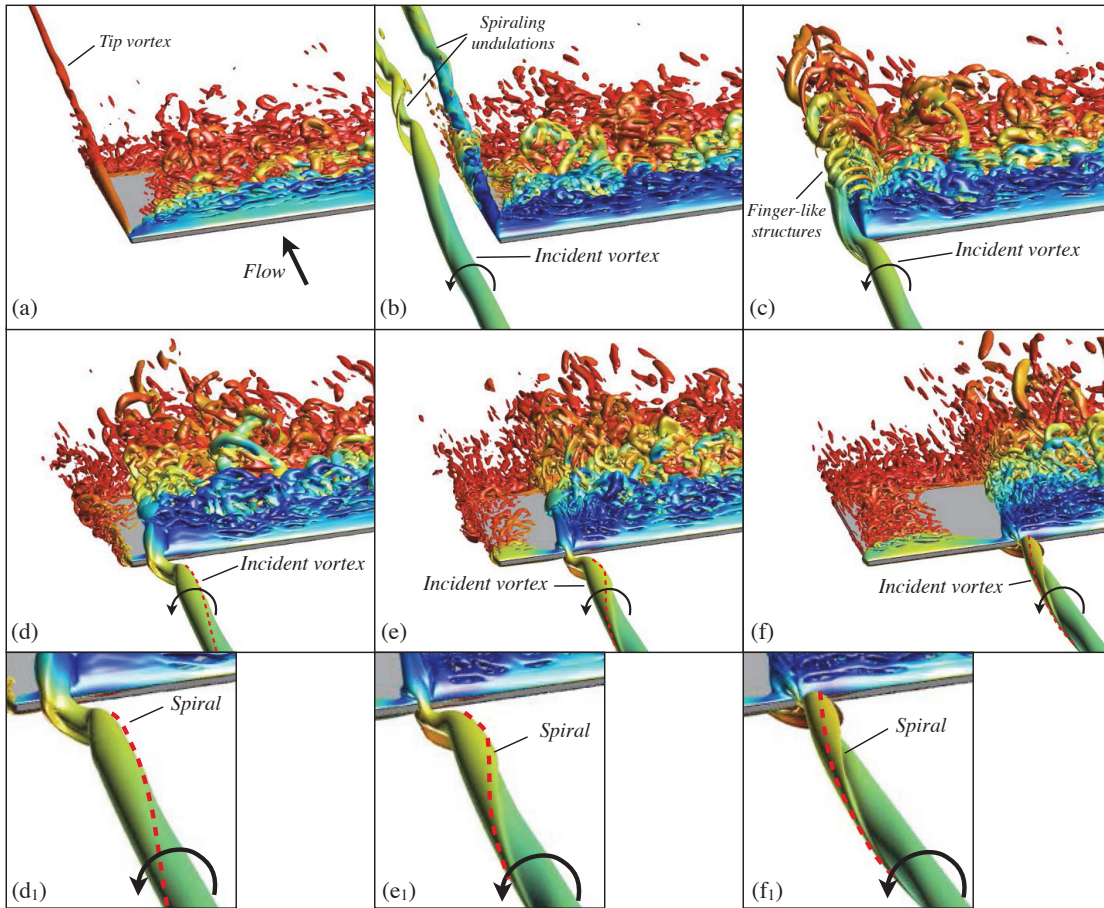


Figure 4: Instantaneous iso-surfaces of Q-criterion ($Q = 15$); (a) No vortex, (b) $\Delta y = -0.25$, (c) $\Delta y = 0.00$, (d) $\Delta y = 0.25$, (e) $\Delta y = 0.50$, (f) $\Delta y = 1.00$; Additional details of the impingement are provided as insets for (d), (e), and (f) denoted with subscript 1

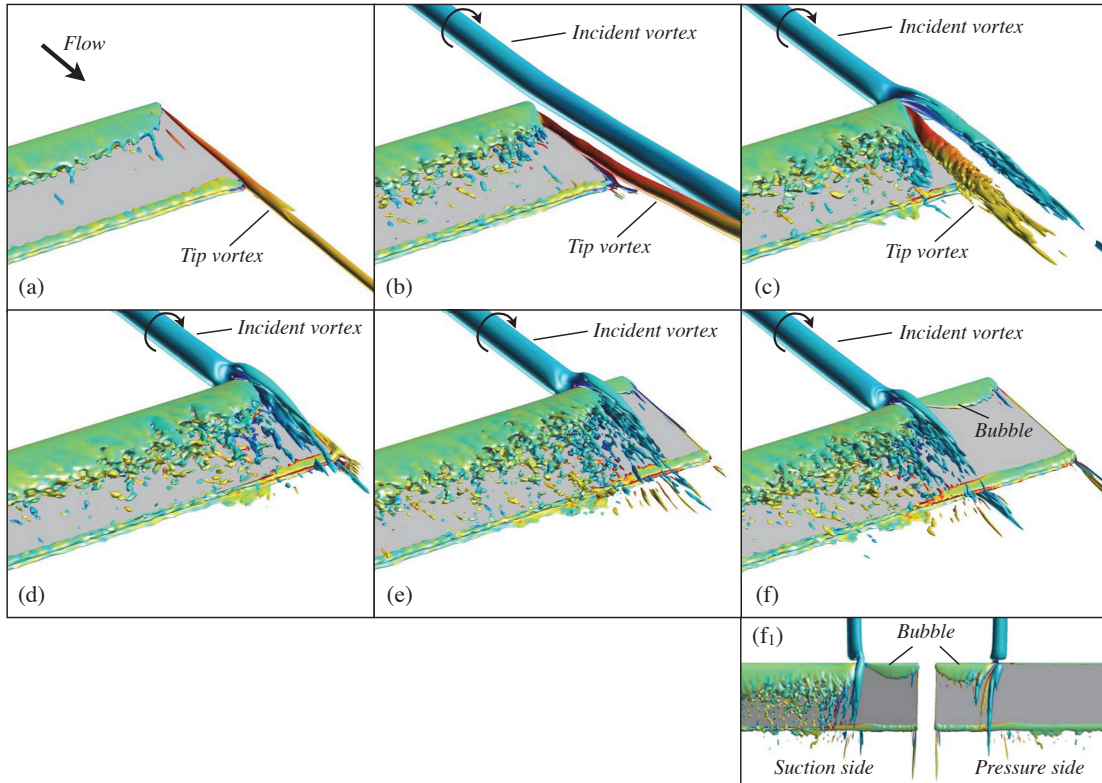


Figure 5: Time-averaged iso-surfaces of Q-criterion ($\bar{Q} = 5$); (a) No vortex, (b) $\Delta y = -0.25$, (c) $\Delta y = 0.00$, (d) $\Delta y = 0.25$, (e) $\Delta y = 0.50$, (f) $\Delta y = 1.00$

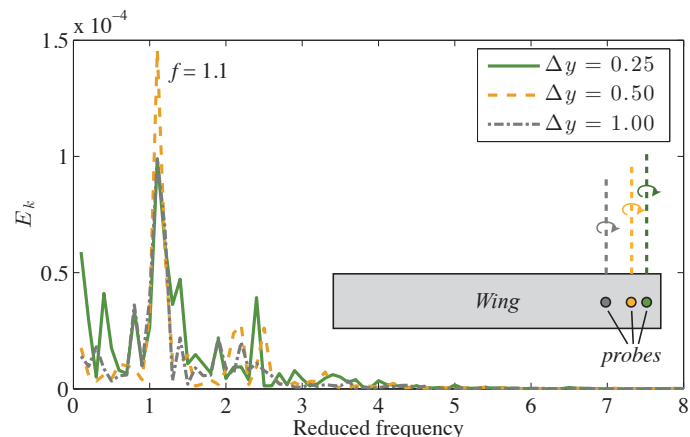


Figure 6: Spectra of the turbulent kinetic energy, E_k , measured at the mid-chord of the wing and inline with the incoming vortex

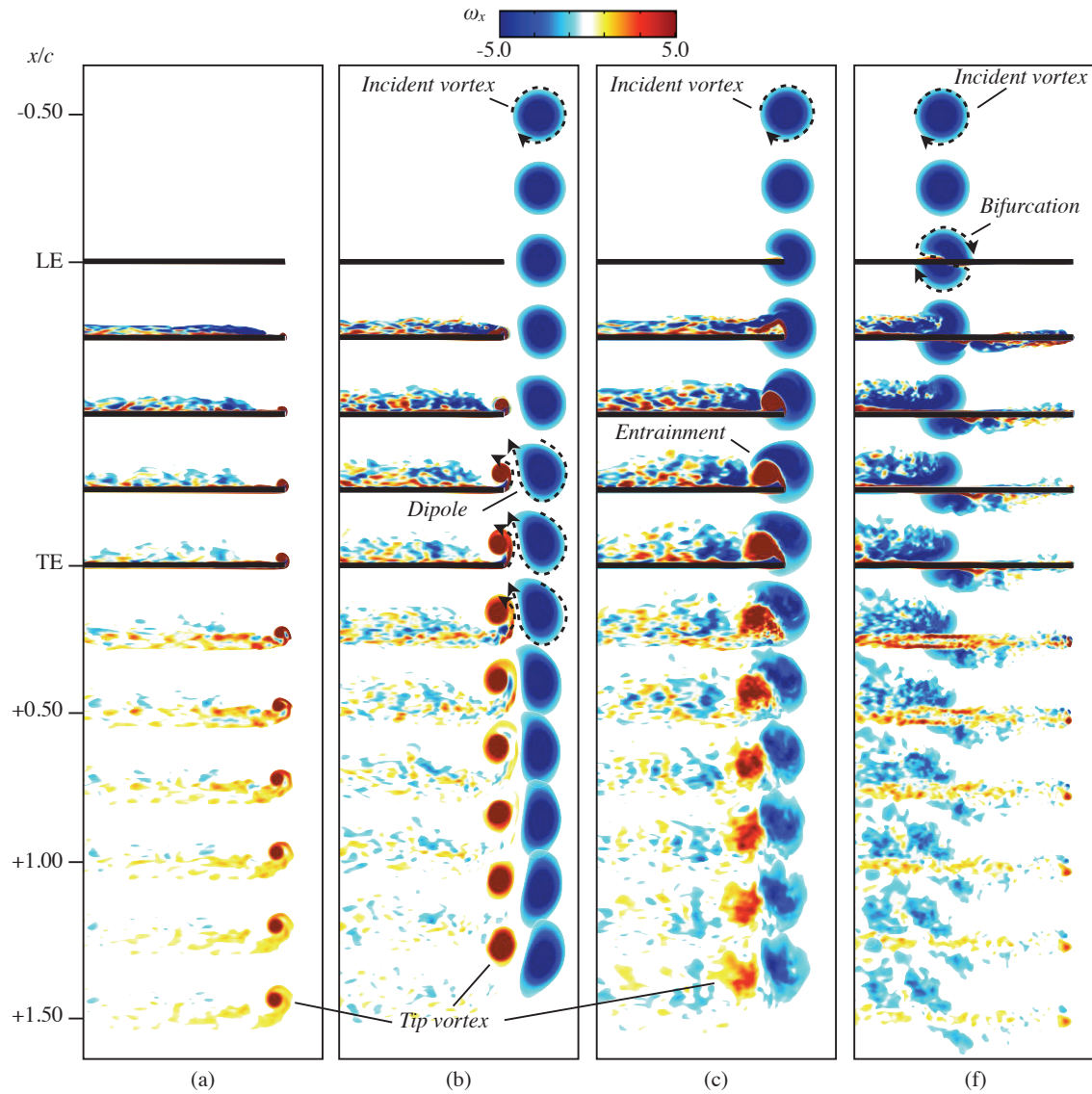


Figure 7: Time-mean streamwise vorticity contours dissecting the incident vortex near the wingtip; (a) No vortex, (b) $\Delta y = -0.25$, (c) $\Delta y = 0.00$, (f) $\Delta y = 1.00$; (d) and (e) have been excluded due to their similarity with (f)

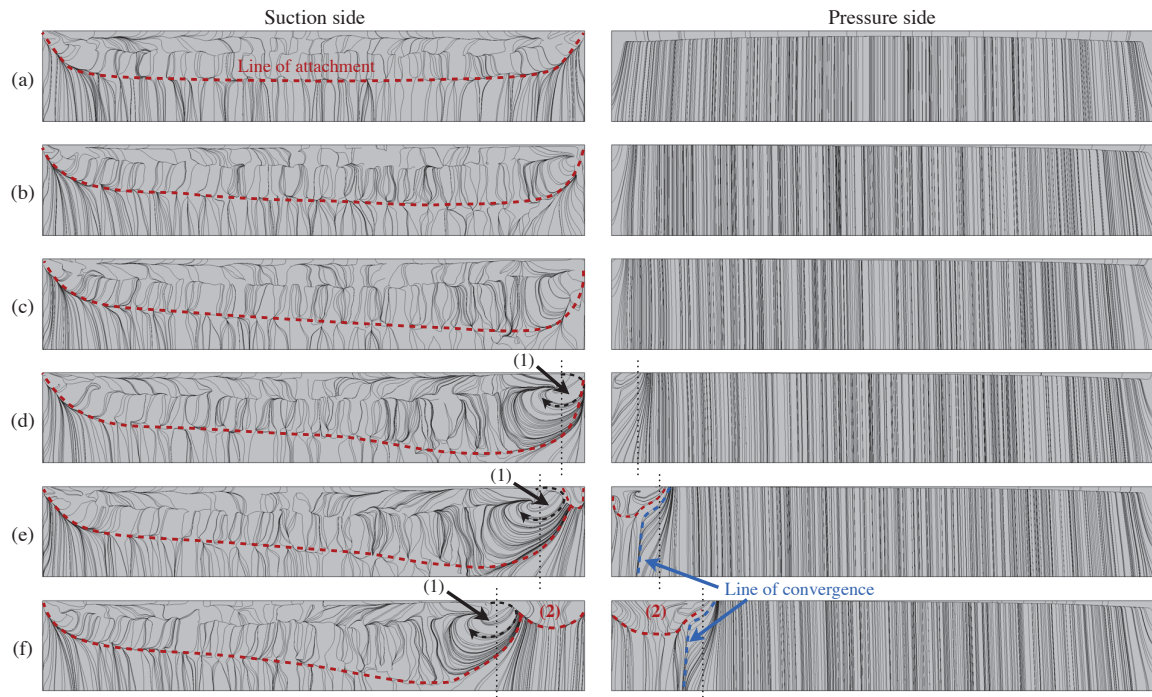


Figure 8: Surface-restricted streamlines from the time-mean solution; (a) No vortex, (b) $\Delta y = -0.25$, (c) $\Delta y = -0.25$, (d) $\Delta y = 0.25$, (e) $\Delta y = 0.50$, (f) $\Delta y = 1.00$

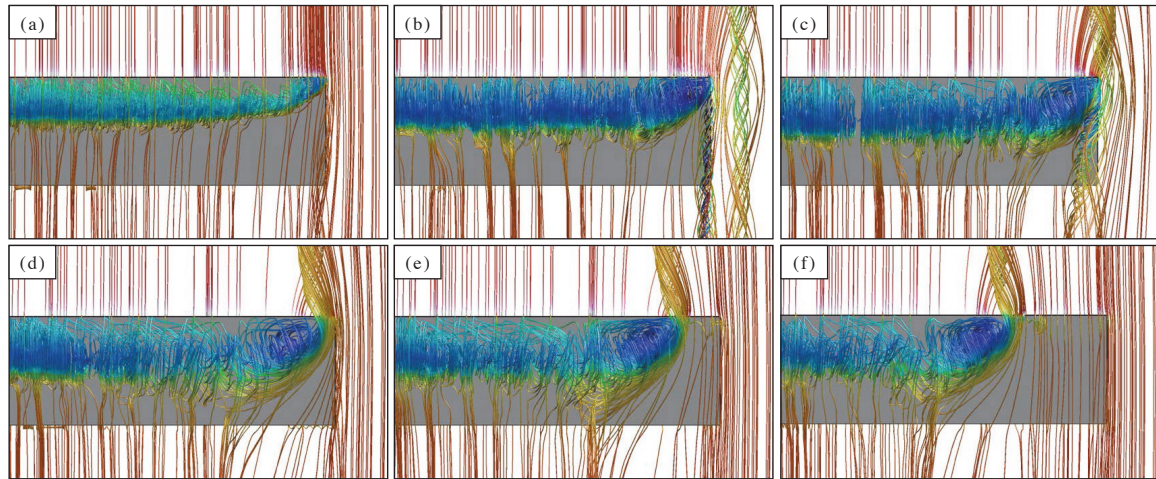


Figure 9: Three-dimensional streamlines over the suction side of the wing; (a) No vortex, (b) $\Delta y = -0.25$, (c) $\Delta y = -0.25$, (d) $\Delta y = 0.25$, (e) $\Delta y = 0.50$, (f) $\Delta y = 1.00$

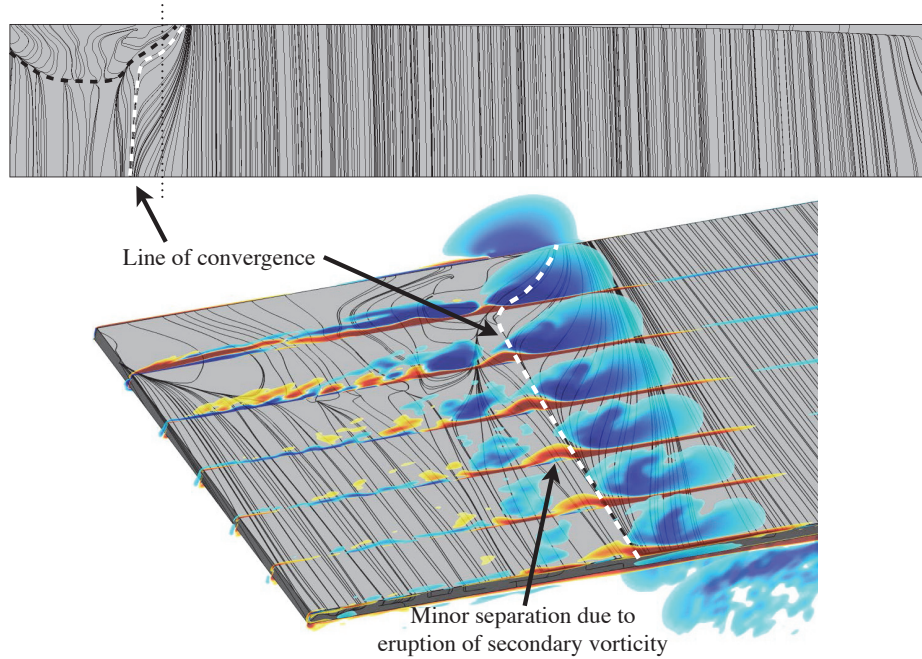


Figure 10: Contours of streamwise vorticity showing the separation on the underside of the wing for $\Delta y = 1.00$

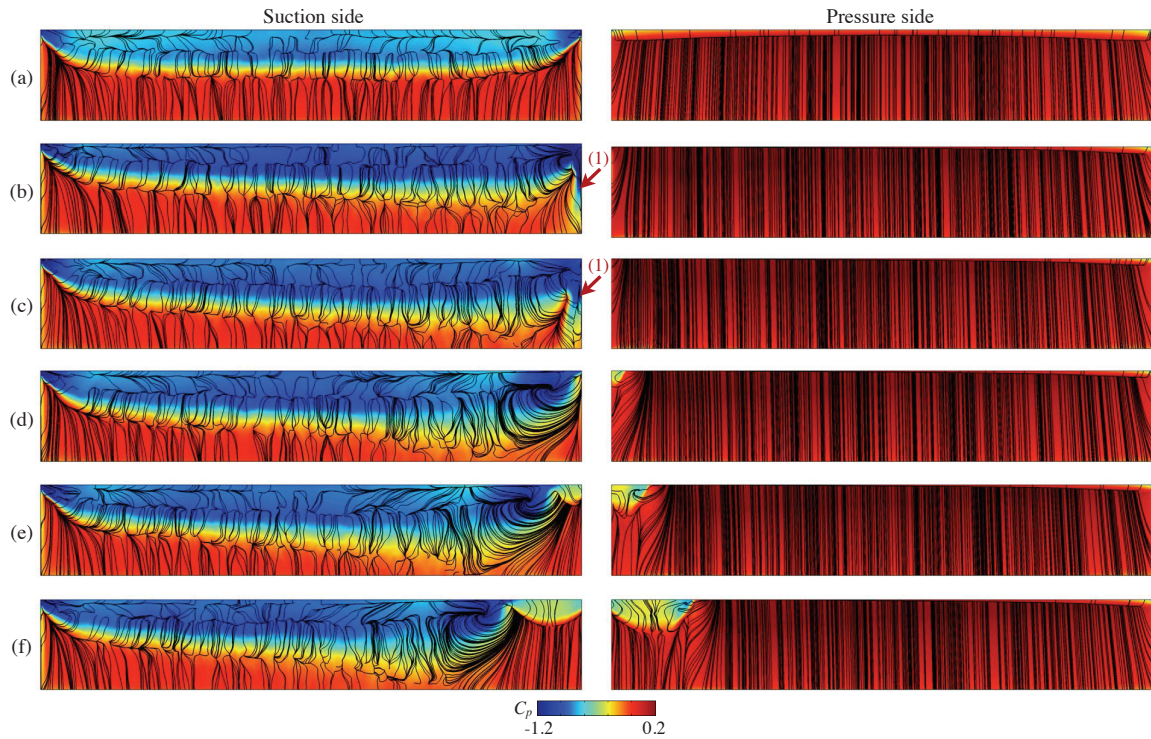


Figure 11: Contours of surface pressure; (a) No vortex, (b) $\Delta y = -0.25$, (c) $\Delta y = 0.00$, (d) $\Delta y = 0.25$, (e) $\Delta y = 0.50$, (f) $\Delta y = 1.00$

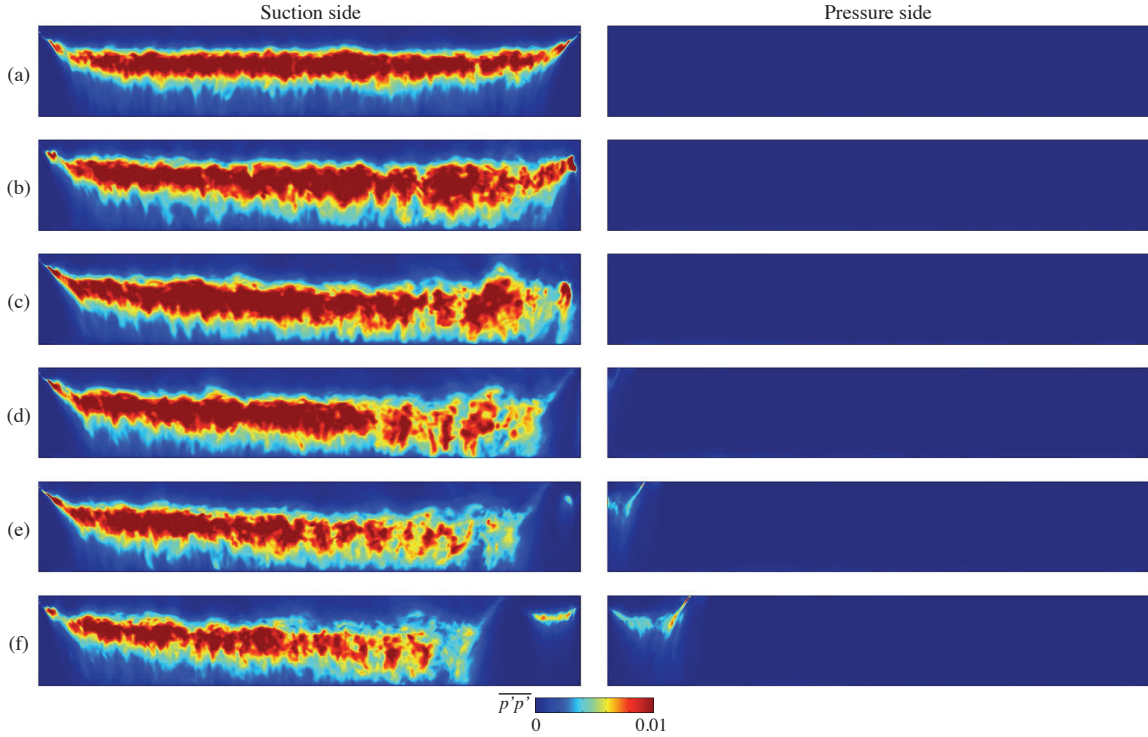


Figure 12: Contours of mean-squared fluctuations of surface pressure; (a) No vortex, (b) $\Delta y = -0.25$, (c) $\Delta y = 0.00$, (d) $\Delta y = 0.25$, (e) $\Delta y = 0.50$, (f) $\Delta y = 1.00$

B. Aerodynamic loads

Figure 13(a) details the instantaneous force and moment histories over ten convective times of the incident vortex interaction for the vortex positions shown in Fig. 13(b). The baseline case is also shown with no incoming vortex. For all incident vortex locations, sustained increases are observed in the lift and drag coefficients with no significant variations from their respective means. The pitching moment, $C_{M,c/4}$, decreases to become more pitch-down and shows some temporal variation most likely due to fluctuations in the larger separated region. The rolling moment coefficient, C_x , highlights a different behavior, however. As the impingement location is moved inboard of the tip, the rolling moment decreases and eventually switches from positive to negative for $\Delta y = 1.0$.

The time-mean aerodynamic loads and moments are plotted in Fig. 14, and the individual values are listed in Table 5 for each spanwise position of the incident vortex. The baseline wing produces mean pitching and rolling moments that are essentially zero. In all cases, there is a substantial augmentation of lift and drag over the baseline wing with the peak loads achieved when the incident vortex is aligned with the wingtip ($\Delta y = 0.00$). This is also true with the lift-to-drag ratio, which achieves up to a 35% increase over the baseline wing when the incident vortex is aligned with the tip. The loss of lift as the the vortex moves inboard is attributed to the unloading of the tip outboard of impingement, which had been described previously and shown in the surface pressure from Fig. 11. The pitching moment, $C_{M,c/4}$, is pitch-down for all cases, but is significantly higher in magnitude with an incoming vortex, although it does not vary dramatically with spanwise position of the incident vortex position. This, again, highlights the increased separation induced by the upwash of the vortex that moves the aerodynamic center farther downstream of the quarter-chord position. The rolling moment, on the other hand, shows significant changes with spanwise position of the incident vortex and even changes sign as the vortex moves inboard from $\Delta y = 0.5$ to 1.0 as a result of the unloaded tip. This indicates that although the tip-aligned case may be optimal for maximum achievable lift-to-drag ratio, a more inboard position may be more suitable for optimal trimming of the aircraft to reduce or even eliminate rolling moment while still seeing benefits in aerodynamic performance.

Table 5: Time-mean aerodynamic loads

	No vortex	$\Delta y = -0.25$		$\Delta y = 0.00$		$\Delta y = 0.25$		$\Delta y = 0.50$		$\Delta y = 1.00$	
		Value	% diff	Value	% diff	Value	% diff	Value	% diff	Value	% diff
C_L	0.349	0.542	55.2%	0.574	64.4%	0.560	60.3%	0.530	51.8%	0.477	36.6%
C_D	0.064	0.076	19.7%	0.078	21.8%	0.076	19.3%	0.074	16.3%	0.071	11.2%
C_M	-0.001	-0.020	-	-0.032	-	-0.033	-	-0.033	-	-0.026	-
C_x	0.001	0.182	-	0.201	-	0.152	-	0.069	-	-0.062	-
L/D	5.483	7.112	29.7%	7.400	35.0%	7.367	34.4%	7.156	30.5%	6.738	22.9%

The sectional lift distribution across the span for each incident vortex position is shown in Fig. 15(a). Significant increases are observed across the entirety of the wing for each case when compared to the baseline wing with a peak encountered just inboard of the impingement location where the maximum swirl velocity occurs. The inboard positions all show the tip unloaded outboard of impingement, which was discussed earlier. The effective angle attack variation based on the prescribed inflow of the incident vortex is plotted in Fig. 16(a) and is computed as

$$\alpha_{\text{eff}} = \alpha + \tan^{-1}(w/u_x) \quad (18)$$

where $\alpha = 4^\circ$ is the geometric angle of attack of the wing, and w and u_x are the vertical and axial velocities of the incoming vortex, respectively. The vertical velocity is given as $w = (y - y_c)u_\theta/r$ where y is the spanwise position, y_c is the vortex impingement location, and u_θ is the circumferential velocity. Assuming the lift is proportional to the effective angle of attack by inviscid theory, the lift distribution can be rescaled by $\alpha/\alpha_{\text{eff}}$ as demonstrated in Fig. 16(b) for the outboard-positioned incident vortex, where the effective angle of attack is well behaved and below 20° . The other positions do not collapse to the baseline case when scaled the same way indicating that inviscid theory does not hold for the tip-aligned and inboard-positioned incoming vortices. While the side of the wing opposite of impingement may see gains due to inviscid arguments, the enhancement of the recirculation region from the separated boundary layer near impingement, the reoriented spanwise flow, and the unloading of the wingtip is a viscous and highly three-dimensional process that is not properly represented by inviscid theory.

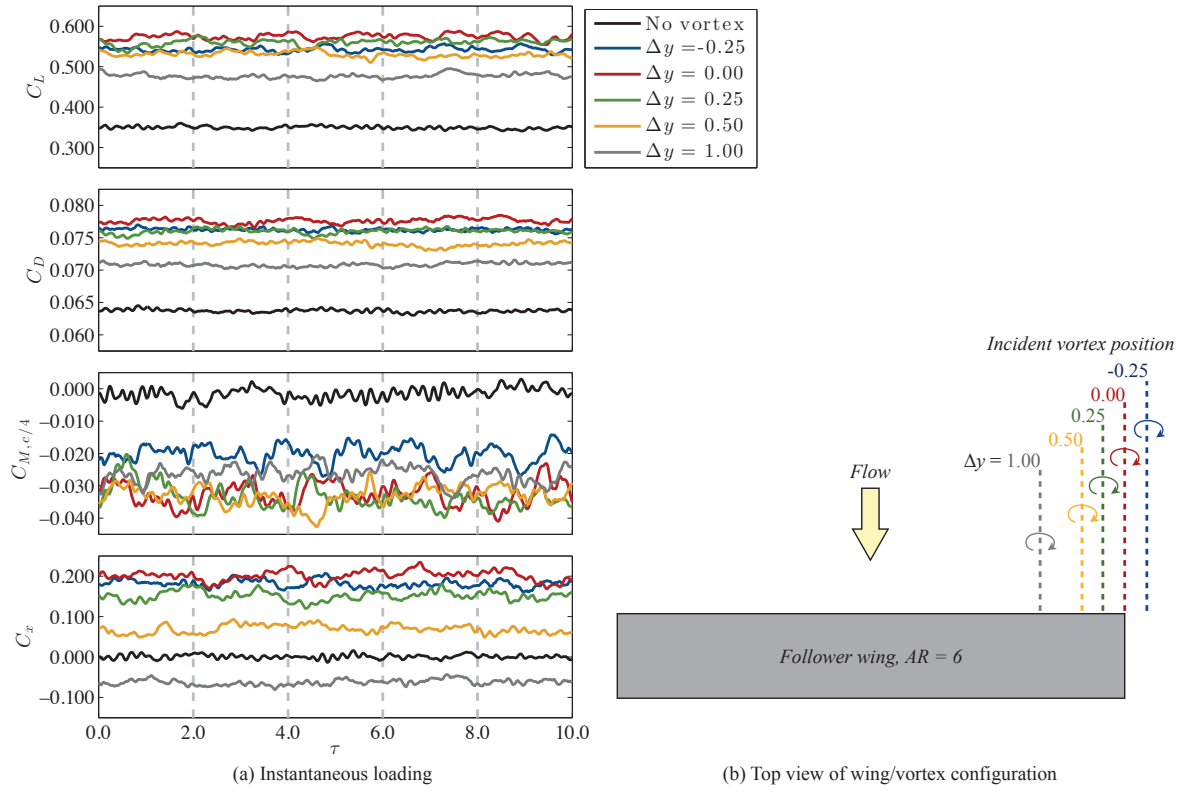


Figure 13: Instantaneous aerodynamic loading for various incident vortex positions; (a) Instantaneous lift, drag, pitching moment, and rolling moment coefficients, (b) Top view of the wing/vortex configuration

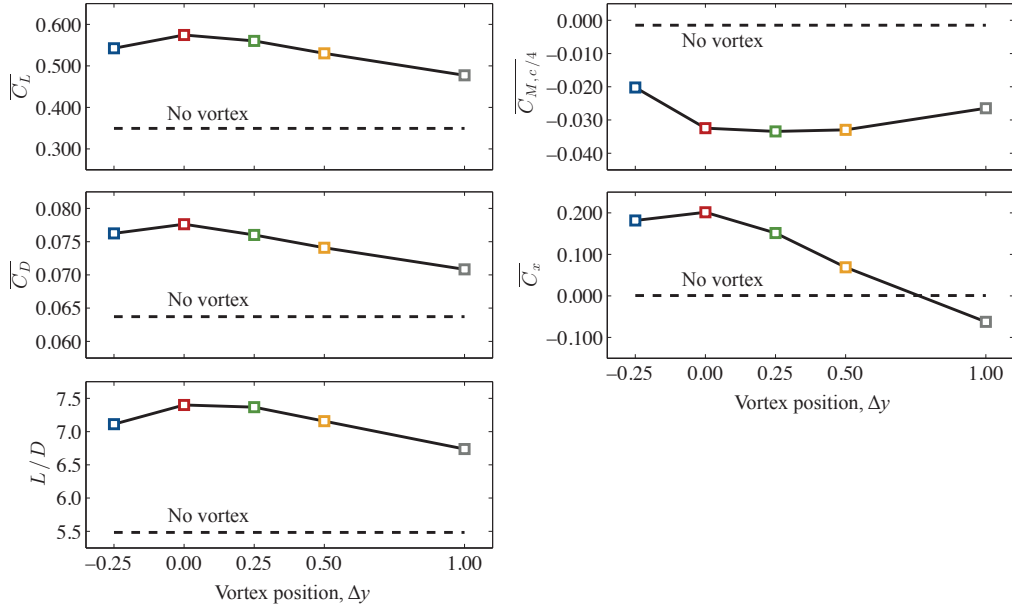


Figure 14: Time-mean lift, drag, pitching and rolling moment coefficients, and lift-to-drag ratio for various incident vortex spanwise positions. The loads for the baseline case with no incident vortex are also shown (dashed lines)

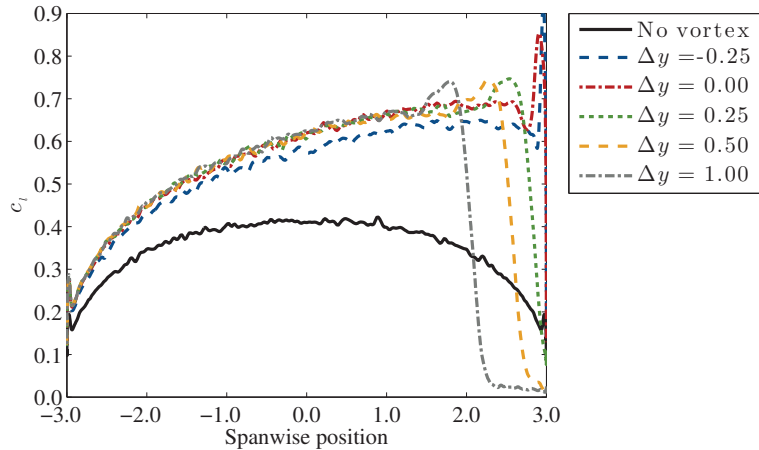


Figure 15: Time-mean distribution of sectional lift coefficient for various incident vortex locations

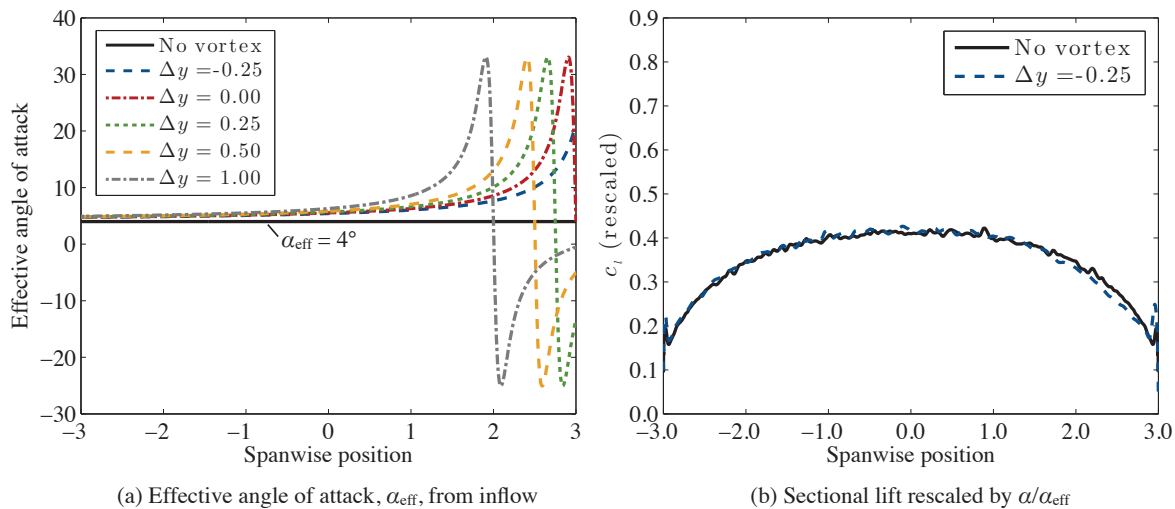


Figure 16: Time-mean effective angle of attack (a) and the sectional lift coefficient rescaled by $\alpha/\alpha_{\text{eff}}$ for the outboard-positioned incident vortex (b)

VI. Conclusions

High-fidelity simulations have been conducted of a streamwise-oriented vortex impinging upon a wing, representative of formation flight. An aspect-ratio-six wing oriented at an angle of $\alpha = 4^\circ$ was simulated at a Reynolds number of $Re = 20,000$ with an analytically-defined vortex superimposed in the freestream. Several spanwise positions of the incoming vortex were analyzed and three distinct flow behaviors were observed. When the vortex is positioned outboard of, but in close proximity to, the wingtip, it forms a dipole with the tip vortex that propels itself upward, away from the plate, from its induced velocity and persists into the wake. When the incident vortex is aligned with the wingtip, the incident and tip vortex feeding sheets interact quite strongly and become entrained in the circulation of the opposite structure, which causes both vortices to lose their coherency as they convect downstream. Finally, when the incident vortex is positioned inboard of the wingtip, the upstream influence of the wing promotes spiraling disruptions in the incoming vortex that wind in a direction opposite the sense of the vortex rotation. The winding vortex reorients from streamwise to vertical as it approaches the leading edge before pinching off and attaching

to the wing surface, alternating from the upper to lower side. A discrete reduced frequency of $f = 1.1$ was found in the turbulent kinetic energy near the impingement location that corresponds to the spiraling undulation of the vortex. In the time-mean sense, the incident vortex bifurcates with portions convecting over the upper and lower sides of the wing. The upwash from the incoming vortex increases the effective angle of attack inboard of impingement, which enhances the three-dimensional recirculation region created by the separated boundary layer off the leading edge of the wing. Fluid is then drawn inboard from the incident vortex, thereby diminishing, but not completely eliminating, its impact on the outboard section of the wing. The slight downwash remaining outboard of impingement reduces the effective angle of attack resulting in small separation bubbles on either side of the wing as the flow separates over the leading edge and quickly reattaches near the quarter-chord location. The nearly symmetric formation on the upper and lower surfaces effectively unloads the wingtip outboard of impingement, which reduces lift, drag, and the incurred rolling moment. Additionally, the tip vortex is virtually suppressed for these cases. The different inboard positions create an almost self-similar flow pattern that enhances the recirculation region, pins the flow near impingement, and essentially reduces the usable aspect ratio of the wing by unloading the tip. This viscous and highly three-dimensional process should eventually saturate with large enough span.

All incident vortex positions provide substantial increases in the wing's lift-to-drag ratio; however, significant sustained rolling moments also result. As the vortex is brought inboard, the rolling moment diminishes and eventually switches sign, indicating that small changes in vortex position can cause dramatic moment variations. The large sensitivity of the rolling moment to impingement location is the motivation for future studies to examine the interaction of a wing with a wandering vortex. Small perturbations in the incident vortex spanwise position will be introduced to represent the unsteady motion of a lead wing's trailing vortex possibly due to atmospheric turbulence, aircraft wandering, or crow-instability effects, for instance. Large fluctuations in the loading will require a responsive control system to dynamically trim the aircraft and could potentially lead to increased fatiguing of the wing structure that could potentially mitigate the advantages of formation flying.

Acknowledgements

This work is supported in part by AFOSR under a task monitored by Dr. D. Smith and also by a grant of HPC time from the DoD HPC Shared Resource Centers at AFRL and ERDC.

References

- ¹Lissaman, P. B. S. and Shollenberger, C. A., "Formation Flight of Birds," *Science*, Vol. 168, No. 3934, May 1970, pp. 1003-1005.
- ²Hummel, D., "Aerodynamic Aspects of Formation Flight in Birds," *Journal of Theoretical Biology*, Vol. 104, No. 3, 1983, pp. 321-347.
- ³Hummel, D., "Formation Flight as an Energy-Saving Mechanism," *Israel Journal of Zoology*, Vol. 41, No. 3, 1995, pp. 261-278.
- ⁴Beukenberg, M. and Hummel, D., "Aerodynamics, Performance and Control of Airplanes in Formation Flight," *Proceedings of the 17th Congress of the International Council of the Aeronautical Sciences*, Vol. 2, September 1990, pp. 1777-1794.
- ⁵Ning, S. A., Flanzer, T. C., and Kroo, I. M., "Aerodynamic Performance of Extended Formation Flight," AIAA Paper 2010-1240, AIAA, 2010.
- ⁶Kless, J., Aftosmis, M. J., Ning, S. A., and Nemec, M., "Inviscid Analysis of Extended-Formation Flight," *AIAA Journal*, Vol. 51, No. 7, July 2013.
- ⁷Inasawa, A., Mori, F., and Asai, M., "Detailed Observations of Interactions of Wingtip Vortices in Close-Formation Flight," *Journal of Aircraft*, Vol. 49, No. 1, January-February 2012.
- ⁸Crow, S. C., "Stability Theory of a Pair of Training Vortices," *AIAA Journal*, Vol. 8, 1970, pp. 2172-2179.
- ⁹Gordnier, R. E. and Visbal, M. R., "Numerical Simulation of the Impingement of Streamwise Vortex on a Plate," *International Journal for Computational Fluid Dynamics*, Vol. 12, No. 1, 1999, pp. 49-66.
- ¹⁰Visbal, M. and Gordnier, R., "On the Structure of the Shear Layer Emanating from a Swept Leading Edge at Angle of Attack," AIAA Paper 2003-4016, AIAA, 2003.
- ¹¹Richez, A., Le Pape, A., Costes, M., and Gavéraux, R., "Zonal Detached-Eddy Simulation (ZDES) of the three-dimensional stalled flow around a finite span wing," AIAA Paper 2012-3281, AIAA, 2012.
- ¹²Tannehill, J., Anderson, D., and Pletcher, R., "Computational Fluid Mechanics and Heat Transfer," *Series in computational and physical processes in mechanics and thermal sciences*, Taylor & Francis, 2nd ed., 1997.
- ¹³Visbal, M. and Rizzetta, D., "Large-Eddy Simulation on Curvilinear Grids Using Compact Differencing and Filtering Schemes," *Journal of Fluids Engineering*, Vol. 124, 2002, pp. 836-847.

¹⁴Visbal, M., Morgan, P., and Rizzetta, D., "An Implicit LES Approach Based on High-Order Compact Differencing and Filtering Schemes," AIAA Paper 2003-4098, AIAA, June 2003.

¹⁵Garmann, D., Visbal, M., and Orkwis, P., "Comparative study of implicit and subgrid-scale model large-eddy simulation techniques for low-Reynolds number airfoil applications," *International Journal for Numerical Methods in Fluids*, Vol. 71, No. 12, 2013, pp. 1546–1565.

¹⁶Stolz, S. and Adams, N., "An Approximate Deconvolution Procedure for Large-Eddy Simulation," *Physics of Fluids*, Vol. 11, No. 7, 1999, pp. 1699–1701.

¹⁷Matthew, J., Lechner, R., Foysi, H., Sesterhenn, J., and Friedrich, R., "An Explicit Filtering Method for LES of Compressible Flows," *Physics of Fluids*, Vol. 15, No. 8, 2003, pp. 2279–2289.

¹⁸Visbal, M. and Gaitonde, D., "High-Order Accurate Methods for Complex Unsteady Subsonic Flows," *AIAA Journal*, Vol. 37, No. 10, 1999, pp. 1231–1239.

¹⁹Gaitonde, D. and Visbal, M., "High-Order Schemes for Navier-Stokes Equations: Algorithm and Implementation into FDL3DI," Technical Report AFRL-VA-WP-TR-1998-3060, Air Force Research Laboratory, Wright-Patterson AFB, 1998.

²⁰Lele, S., "Compact Finite Difference Schemes with Spectral-like Resolution," *Journal of Computational Physics*, Vol. 103, No. 1, 1992, pp. 16–42.

²¹Gaitonde, D. and Visbal, M., "Further Development of a Navier-Stokes Solution Procedure Based on Higher-Order Formulas," AIAA Paper 99-0557, AIAA, 1999.

²²Alpert, P., "Implicit Filtering in Conjunction with Explicit Filtering," *Journal of Computational Physics*, Vol. 44, No. 1, 1981, pp. 212–219.

²³Beam, R. and Warming, R., "An Implicit Factored Scheme for the Compressible Navier-Stokes Equations," *AIAA Journal*, Vol. 16, No. 4, 1978, pp. 393–402.

²⁴Rizzetta, D., Visbal, M., and Morgan, P., "A High-Order Compact Finite-Difference Scheme for Large-Eddy Simulation of Active Flow Control (Invited)," AIAA Paper 2008-526, AIAA, 2008.

²⁵Pulliam, T. and Chaussee, D., "A Diagonal Form of an Implicit Approximate-Factorization Algorithm," *Journal of Computational Physics*, Vol. 17, No. 10, 1981, pp. 347–363.

²⁶Jameson, A., Schmidt, W., and Turkel, E., "Numerical Solutions of the Euler Equations by Finite Volume Methods Using Runge-Kutta Time Stepping Schemes," AIAA Paper 1981-1259, AIAA, 1981.

²⁷Pulliam, T., "Artificial Dissipation Models for the Euler Equations," *AIAA Journal*, Vol. 24, No. 12, Dec. 1986, pp. 1931–1940.

²⁸Batchelor, G., "Axial Flow in trailing line vortices," *Journal of Fluid Mechanics*, Vol. 20, No. 4, 1964, pp. 645–658.

²⁹Jacquin, L. and Pantano, C., "On the persistence of trailing vortices," *Journal of Fluid Mechanics*, Vol. 471, November 2002, pp. 159–168.

³⁰Leibovich, S. and Stewartson, K., "A sufficient condition for the instability of columnar vortices," *Journal of Fluid Mechanics*, Vol. 126, January 1983, pp. 335–356.

³¹Steger, J., Dougherty, F., and Benek, J., "A Chimera Grid Scheme," *Advances in Grid Generation*, edited by K. Ghia and U. Ghia, Vol. 5, American Society of Mechanical Engineers, 1983, pp. 59–69.

³²Sherer, S. and Scott, J., "High-Order Compact Finite-Difference Methods on General Overset Grids," *Journal of Computational Physics*, Vol. 210, No. 2, 2005, pp. 459–496.

³³Visbal, M. and Garmann, D., "Flow structure above stationary and oscillating low-aspect-ratio wings," *Proceedings of the ASME 2012 Fluids Engineering Division Summer Meeting*, No. FEDSM2012-72405, American Society of Mechanical Engineers, 2012, pp. 1593–1605.

APPENDIX B

Unsteady Interactions of a Wandering Streamwise-Oriented Vortex with a Wing

Daniel J. Garmann* and Miguel R. Visbal †

Air Force Research Laboratory, Wright-Patterson AFB, OH 45433

The unsteady interactions of wandering streamwise-oriented vortex impinging upon a finite wing are examined using high-fidelity numerical simulation. The incident vortex is prescribed analytically upstream of an aspect-ratio-six wing and is defined with a sinusoidal variation in its spanwise position. Two wandering amplitudes are considered, $a_y = 0.25$ and 0.5 chords (c), oscillating around a mean location measured $0.25c$ inboard of the wingtip at a Strouhal number of $St = fc/U_\infty = 0.2$. The imposed lateral motion of the vortex spatially evolves as it approaches the wing by inclining relative to its initial horizontal trajectory and also diminishing in amplitude. Just ahead of the wing, both wandering amplitudes are reduced by 36%, and the horizontal trajectories inclined by nearly 38° and 53° , respectively, for the initial wandering amplitudes of $0.5c$ and $0.25c$. This streamwise development of the incident vortex path has implications on the subsequent interaction with the wing, as the wing's streamwise position relative to the vortex self-induced motion dictates how the surface will be impacted. The vertical offset of the vortex core was also shown to drive an eventual pinch-off at the wing's leading edge with an alternating attachment to the upper and lower surfaces, which then evolved into a horseshoe-like structure before coalescing into a ring vortex and convecting into the wake. This is in contrast to the pinch-off experienced by a stationary vortex impacting a wing, which is driven by a spiraling instability in the vortex core induced by the upstream influence of the wing that reorients the vortex ahead of the leading edge. The wandering vortices examined here exhibited no signs of the same spiraling undulation. This finding may prevent conclusions about the flow structure engendered by a stationary vortex impingement from being generalized to the more dynamic wandering vortex interaction. Despite the differing pinch-off mechanisms, the unsteady loading experienced by the wing is shown to fall within the bounds of the time-mean loading of the stationary impinging vortices.

I. Introduction

Columnar vortices impacting a surface can be separated into three classes of interactions: (1) parallel, (2) normal, or (3) streamwise (perpendicular) vortex-body encounters with an excellent and extensive review of each of these interactions provided by Rockwell.¹ While the unsteady physics of the first two vortex representations have been well-documented, considerably less attention has been paid to streamwise-oriented vortex-body interactions; in particular, to the unsteady, three-dimensional nature of the vortex and how it relates to the induced loading on a finite wing as would be encountered in tubomachinery blade-row interactions or formation flight, for example. Even less understood are the implications of a wandering vortex impinging upon a wing that not only dynamically shifts from the upstream influence of the wing, but also from atmospheric turbulence, aircraft wandering, or crow-instability effects, to name a few. The fundamental unsteady interactions of a wandering vortex impacting a finite wing are the focus of this paper.

Either a single vortex or systems of streamwise-oriented vortices are known to exhibit a rich dynamics. Long wavelength,² short wavelength (elliptical) and spiral breakdown³ constitute examples of potential outcomes that may affect the evolution of a streamwise-oriented vortex and its interaction with aerodynamic surfaces encountered in its path. Furthermore, axial vortices may also exhibit spiral sub-structures generated during their roll-up process.^{4,5} These instabilities and unsteady features can result in additional sources

*Research Aerospace Engineer. Ohio Aerospace Institute. AIAA Senior Member.

†Technical Area Leader. AIAA Fellow.

This material is declared a work of the U.S. Government and is not subject to copyright protection in the United States.

of buffeting while impinging upon a finite wing. To further compound the problem, either deliberate or unanticipated motions of the incident vortex can provide another degree of uncertainty in the predicted flow structure, even experimentally. Heyes *et al.*⁶ for example, discuss the difficulties in extracting reliable measurements from wandering vortices and demonstrate how vortex wandering effects must be corrected to prevent false conclusions from being drawn about the vortex structure, i.e. breakdown. These difficult-to-predict unsteady phenomena engendered by the vortex/surface interaction will impact the unsteady loading or buffeting experienced by the wing. Another unresolved critical aspect of the problem is the modification of the incident vortex and its instability modes generated by the process of impingement upon the wing. This feedback will most likely be limited to a region of upstream influence in front of the wing. Nonetheless coupling of vortex instabilities with the unsteady separation is in general not well understood and could give rise to a resonant behavior with significant impact on the vortex/surface interaction.

Streamwise-oriented vortex/wing interactions in the context of formation flight, which has long been understood to provide significant benefits in aerodynamic performance, have been analyzed in a series of papers by Hummel^{7,8} and Beukenberg and Hummel⁹ using classic aerodynamic theory, wherein citations to earlier seminal work can also be found. With proper positioning, trailing aircraft can capture the upwash from the tip vortex left in the wake of a lead aircraft. The result is a forward-tilted lift vector that provides increased lift and a reduction in induced drag and can lead to significant energy savings.¹⁰ Recently, Ning *et al.*¹¹ performed an investigation of several factors affecting the benefits and feasibility of extended formation flight for three aircraft in canonical echelon and V-type arrangements. These factors included wake roll-up, vortex core size, vortex decay and gust effects. Kless *et al.*¹² provided a computational inviscid flow analysis of several aspects of extended formation flight with consideration of optimal incident vortex location, roll trim effects and transonic flow effects. Vortex meandering induced from wind-tunnel unsteadiness, atmospheric turbulence, crow instability, or upstream feedback from the surface,¹³ can also pose a problem for reliable wake capturing in this context, wherein significant deviation of the impacting vortex core can lead to unintended separation or unsteady loading. Despite advances in the understanding, prediction and demonstration of the benefits of formation flight, significant challenges still require further investigation before this technology becomes a viable and safe operational capability.

The recent high-fidelity numerical studies of Barnes *et al.*¹⁴ and Garman and Visbal¹⁵ have investigated the unsteady interactions of a streamwise-oriented vortex impinging upon a finite wing. In the former, two aspect-ratio-six flat plate wings, arranged in tandem, were simulated at a Reynolds number of 30,000 as a generic problem of formation flight-like conditions. Several spanwise positions and incidence angles of the lead wing were varied for both rigid and flexible follower wings in an effort to engender the most significant aeroelastic response. The resulting flow structure with outboard-positioning yielded vortex dipole-like pairing between the incident and tip vortices, while more inboard locations presented a time-mean bifurcation of the incident vortex. It was concluded from the unsteady loading that lead-wing wandering may be a more dominant driver of structural response. Additionally, wing compliance led to substantial repositioning and stabilizing effect of the incident vortex.

In the latter work of Garman and Visbal,¹⁵ the lead wing was neglected and, instead, an analytically-defined vortex was superimposed in the freestream and convected towards a finite wing. This was in an effort to gain greater control over the strength, size, position, and stability of the incident vortex as a canonical problem of streamwise-oriented vortex/surface interactions. The imposed vortex actually compares quite well to an enlarged trailing vortex from Barnes *et al.*,¹⁴ which was chosen to exacerbate the unsteady interaction. To that end, three distinct flow regimes were found: When the vortex was positioned outboard of, but in close proximity to, the wingtip, it paired with the tip vortex to form a dipole that propelled itself away from the plate due to its self-induced velocity and diffused slowly. When the incoming vortex was aligned with the wingtip, the incident and tip vortex feeding sheets interacted quite strongly and become entrained in the circulation of the opposite structure, which diminished the coherence of both vortices into the wake. Finally, when the incident vortex was positioned inboard of the wingtip, the vortex bifurcated in the time-mean sense with portions convecting above and below the wing. The increased effective angle of attack inboard of impingement enhanced the three-dimensional recirculation region created by the separated boundary layer off the leading edge which draws fluid from the incident vortex inboard and diminishes its impact on the outboard section of the wing. The slight but remaining downwash present outboard of impingement reduced the effective angle of attack in that region resulting in a small separation bubble on either side of the wing in the time-mean solution that effectively unloaded the tip outboard of impingement. All incident vortex positions provided substantial increases in the wing's lift-to-drag ratio; however, significant sustained rolling

moments also resulted. As the vortex was brought inboard, the rolling moment diminished and eventually switched sign, indicating that small changes in vortex position can cause dramatic variations in the unsteady loading.

The purpose of this paper is to build upon a previous study by the current authors¹⁵ that examined the interactions of a streamwise-oriented vortex with a wing at several fixed spanwise impingement locations. In this work, however, the incident vortex is prescribed with perturbations in its spanwise position to represent vortex meandering as a means of examining the changes in unsteady loading of the wing and large-scale vortex-induced separation from relatively small fluctuations in the incident vortex position. An analytically-defined vortex superimposed in a freestream is convected towards a wing to provide a canonical problem of perpendicular vortex/surface interactions. This allows fundamental understanding of the unsteady interaction in the absence of the many interrelated and complicated effects such as atmospheric turbulence, crow-instability, etc. that can potentially lead to vortex distortion and breakdown.

II. Governing equations

The governing equations for the current work are the compressible, three-dimensional Navier-Stokes equations. After a general time-dependent transformation from Cartesian coordinates (x, y, z, t) to computational space (ξ, η, ζ, τ) , these equations can be written in strong conservation form¹⁶ as follows:

$$\frac{\partial}{\partial \tau} \left(\frac{\mathbf{U}}{J} \right) + \frac{\partial \mathbf{F}}{\partial \xi} + \frac{\partial \mathbf{G}}{\partial \eta} + \frac{\partial \mathbf{H}}{\partial \zeta} = \frac{1}{Re} \left[\frac{\partial \mathbf{F}_v}{\partial \xi} + \frac{\partial \mathbf{G}_v}{\partial \eta} + \frac{\partial \mathbf{H}_v}{\partial \zeta} \right] \quad (1)$$

where the solution vector is

$$\mathbf{U} = [\rho, \rho u, \rho v, \rho w, \rho e]^T \quad (2)$$

and the inviscid flux vectors are

$$\mathbf{F} = \frac{1}{J} \begin{bmatrix} \rho U \\ \rho u U + \xi_x p \\ \rho v U + \xi_y p \\ \rho w U + \xi_z p \\ (\rho e + p) U - \xi_t p \end{bmatrix}, \quad \mathbf{G} = \frac{1}{J} \begin{bmatrix} \rho V \\ \rho u V + \eta_x p \\ \rho v V + \eta_y p \\ \rho w V + \eta_z p \\ (\rho e + p) V - \eta_t p \end{bmatrix}, \quad \mathbf{H} = \frac{1}{J} \begin{bmatrix} \rho W \\ \rho u W + \zeta_x p \\ \rho v W + \zeta_y p \\ \rho w W + \zeta_z p \\ (\rho e + p) W - \zeta_t p \end{bmatrix} \quad (3)$$

In these expressions, $J = \partial(\xi, \eta, \zeta, \tau) / \partial(x, y, z, t)$ is the Jacobian of the transformation, and the metrics are $\xi_t = \partial \xi / \partial t$ and $\xi_x = \partial \xi / \partial x$, for example, with similar definitions for the other terms; u , v , and w are the Cartesian velocity components, ρ is the density, and p is the pressure. The contravariant velocities, U , V , and W , are

$$\begin{aligned} U &= \xi_t + \xi_x u + \xi_y v + \xi_z w \\ V &= \eta_t + \eta_x u + \eta_y v + \eta_z w \\ W &= \zeta_t + \zeta_x u + \zeta_y v + \zeta_z w \end{aligned} \quad (4)$$

and the specific internal energy, e , is

$$e = \frac{T}{\gamma(\gamma-1) M_\infty^2} + \frac{1}{2} (u^2 + v^2 + w^2) \quad (5)$$

where T is the temperature, γ is the ratio of specific heats, and M_∞ is the freestream Mach number. For the sake of brevity, the viscous fluxes, \mathbf{F}_v , \mathbf{G}_v , and \mathbf{H}_v , are not shown, but they are provided in Ref. 16, for instance.

The governing equations are also supplemented with the perfect gas equation, $p = \rho T / \gamma M_\infty^2$, and Sutherland's viscosity law. A constant Prandtl number ($Pr = 0.72$ for air) is assumed along with Stokes' hypothesis for the bulk viscosity coefficient ($\lambda = -2/3\mu$). All flow variables are normalized by their respective freestream counterparts, except for pressure, which is scaled by twice the dynamic pressure, $\rho_\infty U_\infty^2$. The reference length is taken as the wing chord, c .

This set of equations corresponds to the *unfiltered* Navier-Stokes equations and is used without change in laminar, transitional or fully turbulent regions of the flow for the ILES procedure. Unlike the standard LES approach, no additional subgrid-scale (SGS) model or heat flux terms are appended. Instead, a high-order,

low-pass filter operator, which will be discussed later, is applied to the conserved variables during the solution of the standard Navier-Stokes equations. This highly-discriminating, Padé-type filter selectively damps only the high-frequency components of the solution, that are often times under-resolved by the mesh.¹⁷ The filtering regularization procedure provides an attractive alternative to the use of standard SGS models, and has been found to yield suitable results for several turbulent and transitional flows on LES level grids.¹⁸ A reinterpretation of this ILES approach in the context of an Approximate Deconvolution Model¹⁹ has been provided by Mattheq *et al.*²⁰ For low Reynolds numbers and/or high spatial resolutions, the ILES approach is effectively direct numerical simulation (DNS).

III. Numerical procedure

All simulations were performed with the extensively validated high-order, Navier-Stokes flow solver, *FDL3DI*.^{21,22} In this code, the governing equations are discretized through a finite-difference approach with all spatial derivatives obtained using high-order compact-differencing schemes.²³ The spatial derivative of any scalar quantity, ϕ , such as a metric, flux component, or flow variable, is obtained along a coordinate line in computational space by solving the following tridiagonal system:

$$\alpha \phi'_{i-1} + \phi'_i + \alpha \phi'_{i+1} = a \left(\frac{\phi_{i+1} - \phi_{i-1}}{2} \right) + b \left(\frac{\phi_{i+2} - \phi_{i-2}}{4} \right) \quad (6)$$

where proper choice of the coefficients, α , a , and b , provides up to sixth-order spatial accuracy. At boundary points, higher-order, one-sided formulae are utilized that retain the tridiagonal form of the scheme.^{21,22} For all the computations presented in this work, the interior coefficients are $\alpha = 1/3$, $a = 14/9$, and $b = 1/9$, which correspond to a sixth-order accurate, compact scheme. The boundary point and first off-boundary point use fourth- and fifth-order compact schemes, respectively.

The derivatives of the inviscid fluxes are obtained by forming the fluxes at the nodes and differentiating each component with the compact differencing scheme. Viscous terms are obtained by first computing the derivatives of the primitive variables and then constructing the components of the viscous fluxes at each node and differentiating by a second application of the same scheme.

In order to eliminate spurious components of the solution, a high-order, low-pass spatial filtering operator^{22,24} is applied to the conserved variables along each transformed coordinate direction one time after each time step or sub-iteration. If a typical component of the solution vector is denoted by ϕ , filtered values $\hat{\phi}$ at interior points in computational space satisfy,

$$\alpha_f \hat{\phi}_{i-1} + \hat{\phi}_i + \alpha_f \hat{\phi}_{i+1} = \sum_{n=0}^N a_n \left(\frac{\phi_{i-n} + \phi_{i+n}}{2} \right) \quad (7)$$

where proper choice of the coefficients, (a_0, a_1, \dots, a_N) , provides a $2N^{th}$ -order formula on a $2N + 1$ point stencil. The filtering technique is based on templates proposed by Lele²³ and Alpert;²⁵ The coefficients, along with representative filter transfer functions, can be found in the works of Gaitonde and Visbal.^{21,24} The parameter, α_f , is left as a free variable in order to provide limited control of the cutoff frequency of the low-pass filter operator. Typical values are in the range: $0.3 \leq \alpha_f \leq 0.49$. For the near-boundary points, the filtering strategies described in Refs. 22 and 24 are used. For transitional and turbulent flows, the high-fidelity spatial algorithmic components provide an effective implicit LES (ILES) approach in lieu of traditional SGS models, as demonstrated in Refs. 17 and 26, and more recently by Garmann *et al.*¹⁸ All computations presented in this work utilized an eighth-order accurate interior filter with a coefficient of $\alpha_f = 0.40$ for targeted dissipation.

Time marching of the governing equations is achieved through the iterative, implicit approximately-factored integration method of Beam and Warming²⁷ and supplemented with the use of Newton-like sub-iterations to achieve second-order accuracy^{17,26} and reduce errors due to factorization, linearization, diagonalization, and explicit application of boundary conditions.²⁸ The block-tridiagonal form of the algorithm

can be written in delta form as

$$\begin{aligned}
 & \left[\left(\frac{1}{J} \right)^{p+1} + \phi^i \Delta\tau \delta_\xi^{(2)} \left(\frac{\partial \mathbf{F}^p}{\partial \mathbf{U}} - \frac{1}{Re} \frac{\partial \mathbf{F}_v^p}{\partial \mathbf{U}} \right) \right] J^{p+1} \times \\
 & \left[\left(\frac{1}{J} \right)^{p+1} + \phi^i \Delta\tau \delta_\eta^{(2)} \left(\frac{\partial \mathbf{G}^p}{\partial \mathbf{U}} - \frac{1}{Re} \frac{\partial \mathbf{G}_v^p}{\partial \mathbf{U}} \right) \right] J^{p+1} \times \\
 & \left[\left(\frac{1}{J} \right)^{p+1} + \phi^i \Delta\tau \delta_\zeta^{(2)} \left(\frac{\partial \mathbf{H}^p}{\partial \mathbf{U}} - \frac{1}{Re} \frac{\partial \mathbf{H}_v^p}{\partial \mathbf{U}} \right) \right] \Delta \mathbf{U} \\
 & = -\phi^i \Delta\tau \left[\left(\frac{1}{J} \right)^{p+1} \frac{(1+\phi)\mathbf{U}^p - (1+2\phi)\mathbf{U}^n + \phi\mathbf{U}^{n-1}}{\Delta\tau} + \mathbf{U}^p \left(\frac{1}{J} \right)_\tau^p + \right. \\
 & \quad \left. \delta_\xi \left(\mathbf{F}^p - \frac{1}{Re} \mathbf{F}_v^p \right) + \delta_\eta \left(\mathbf{G}^p - \frac{1}{Re} \mathbf{G}_v^p \right) + \delta_\zeta \left(\mathbf{H}^p - \frac{1}{Re} \mathbf{H}_v^p \right) \right]
 \end{aligned} \tag{8}$$

where \mathbf{U}^p is the p^{th} approximation to \mathbf{U} at the $n+1$ time level and $\Delta \mathbf{U} = \mathbf{U}^{n+1} - \mathbf{U}^p$. For the first iteration $\mathbf{U}^p = \mathbf{U}^n$, and as $p \rightarrow \infty$, $\mathbf{U}^p \rightarrow \mathbf{U}^{n+1}$. The block-tridiagonal form of Eq. (8) is further simplified through the diagonalization of Pulliam and Chaussee,²⁹ and fourth-order, nonlinear dissipation terms^{30,31} are also appended to the implicit operator to augment stability, although these are not shown in Eq. (8) for clarity. Second-order finite differencing is used in the implicit operator, while high-order compact differencing is employed in the residual. Iteration drives the left-hand-side to zero, so only the high-order spatial error of the residual remains.

IV. Details of the computations

A. Geometry and vortex model

An analytically defined vortex is superimposed on a freestream and convected toward a wing as shown in Fig. 1. The rectangular wing has an aspect ratio of six ($AR = b/c = 6$) and a thickness of $t = 0.03c$ and is oriented at an angle of attack of $\alpha = 4^\circ$ relative to the freestream. The flat plate was selected as a starting point for this canonical study since it is a generic surface that is easily modeled and manufactured. A more streamlined, airfoil cross-section is planned for future studies at higher Reynolds numbers and will certainly be of interest; however, at the Reynolds number considered here, $Re = 20,000$, a streamlined body would not separate as it would at higher values, which further promotes the choice of a flat plate, which guarantees separation off the leading edge.

The incident vortex is selected as a Batchelor or q -vortex vortex,³² which provides a simple model with known stability properties. The vortex is superimposed into the incoming flow upstream of the wing and is described analytically as

$$u_r(r) = 0 \tag{9}$$

$$u_\theta(r) = \frac{\Gamma_0}{2\pi r} \left(1 - e^{-(r/r_0)^2} \right) \tag{10}$$

$$u_x(r) = 1 - \Delta u e^{-(r/r_0)^2} \tag{11}$$

where u_r , u_θ , and u_x correspond to the radial, circumferential, and axial velocities, respectively, Γ_0 is the vortex circulation, r_0 is a measure of the vortex radius, and Δu is the axial velocity deficit in the vortex core. Rather than circulation, the swirl parameter, q , is used to specify the strength of the vortex. This parameter is defined as

$$q = \frac{\Gamma_0}{2\pi r_0 \Delta u} \approx 1.567 \frac{V_0}{\Delta u} \tag{12}$$

where V_0 is the maximum circumferential velocity. This shows that q is a measure of the relative tangential and axial velocity intensities.³³ The circumferential velocity recast in terms of q becomes

$$u_\theta(r) = \frac{q \Delta u}{r/r_0} \left(1 - e^{-(r/r_0)^2} \right) \tag{13}$$

The radius, r , in the above equations is defined as

$$r = \sqrt{(y - y_c(\tau))^2 + (z - z_c)^2} \quad (14)$$

where $(y_c(\tau), z_c)$ is the vortex center in a $x =$ constant inflow plane. The spanwise position, $y_c(\tau)$, is set as a function of time as

$$y_c(\tau) = y_{\text{tip}} - \Delta y + a_y \sin(2\pi St \tau) \quad (15)$$

to allow the incident vortex to propagate with an oscillating impingement location on the wing. The initial vortex spanwise position measured inboard of the wingtip, $y_{\text{tip}} - \Delta y$ as indicated in Fig. 1, a_y is the perturbation amplitude, and $St = fc/U_{\text{ref}}$ is the Strouhal number of the imposed vortex motion.

A stability criterion for the q-vortex was established by Leibovich and Stewartson³⁴ to prevent amplification of small-wave perturbations at any r . This restriction is given as

$$\sigma^2(r) = \frac{2u_\theta(r u'_\theta - u_\theta)(u_\theta^2/r^2 - u'_\theta^2 - u_x'^2)}{(r u'_\theta - u_\theta)^2 + (r u'_x)^2} < 0 \quad (16)$$

Substitution of Eqs. (11) and (13) into the stability criterion leads to a lower bound prediction on the swirl parameter of $q \geq \sqrt{2}$ to maintain stability of the vortex.

For the cases presented here, the swirl parameter is selected as $q = 2.0$ to prevent the vortex from breaking down prior to its interaction with the wing. To achieve a maximum circumferential velocity of $V_0 = 0.5 U_\infty$, the axial velocity deficit is chosen as $\Delta u = 0.4 U_\infty$. The vortex core radius is set as $r_0 = 0.1c$, and the Reynolds number based on wing chord and freestream velocity is selected as $Re = 20,000$ to ensure tractability for LES. Each of these parameters has been selected based on the previous work by the current authors¹⁵ and vortex profiles documented within the literature by the Euler computations of Kless *et al.*¹² and the experiments of Inasawa *et al.*³⁵ in which a lead wing was actually tested and the wake was analyzed. The estimated values for the maximum circumferential velocity and its radial location are listed in Table 1 along with details of the lead wing geometry and orientation. The maximum velocity radial location, $r_{u_{\max}}$, is related to the core radius of the Q-vortex by $r_{u_{\max}} \approx 1.121 r_0$, leading to the choice of $r_0/c = 0.1$ for the current study, which falls in between the values appearing in the reported literature. It should also be noted that the chosen parameters yield a vortex that mimics the nature of the trailing vortex generated by the flat plate wing at an angle of attack, only with around twice the strength and core radius as indicated in Fig. 2. Here, the tip vortex profile was extracted 1.5c behind the flat plate wing oriented at $\alpha = 4^\circ$ in a free stream, and values for a q-vortex were found to match quite closely to the physically generated tip vortex. The chosen vortex for this study with nearly twice the swirl strength and core radius is also plotted for comparison. Although the larger and stronger vortex is used to exacerbate the surface interaction, similar flow structure was observed between the prior studies by Garmann and Visbal¹⁵ of the analytically-defined vortex and that of Barnes *et al.*,¹⁴ where the tip vortex was generated by a wing.

The wandering vortex is centered around a position of $\Delta y = 0.25c$ from the wingtip and oscillates at a Strouhal number of $St = 0.2$, resulting in a spatial wavelength of $\lambda = 5c$. Two wandering amplitudes are considered, $a_y = 0.50c$ and $0.25c$, corresponding to 0.1λ , and 0.05λ , respectively. These extents were chosen to fall within the range of stationary impinging vortices examined in Ref. 15. In that study, stationary vortices positioned just outboard, tip-aligned, and inboard of the wingtip resulted in three distinct flow regimes as detailed previously in the introduction. Therefore, it was desirable in the current work for the wandering vortices to traverse those possible regimes. Additionally, the reference Mach number in all cases is set as $M_{\text{ref}} = 0.1$ to avoid effects of compressibility, which are left for future studies.

Reference	Solution method	Lead wing	V_0/U_∞	$r_{u_{\max}}/c$
Kless <i>et al.</i> ¹²	Euler computations	NACA0012, AR=8, $\alpha \approx 4^\circ$	0.10	≈ 0.20
Inasawa <i>et al.</i> ³⁵	Experiments	NACA23012, AR=5, $\alpha = 8^\circ$	0.5	≈ 0.05

Table 1: Vortex profiles from the literature

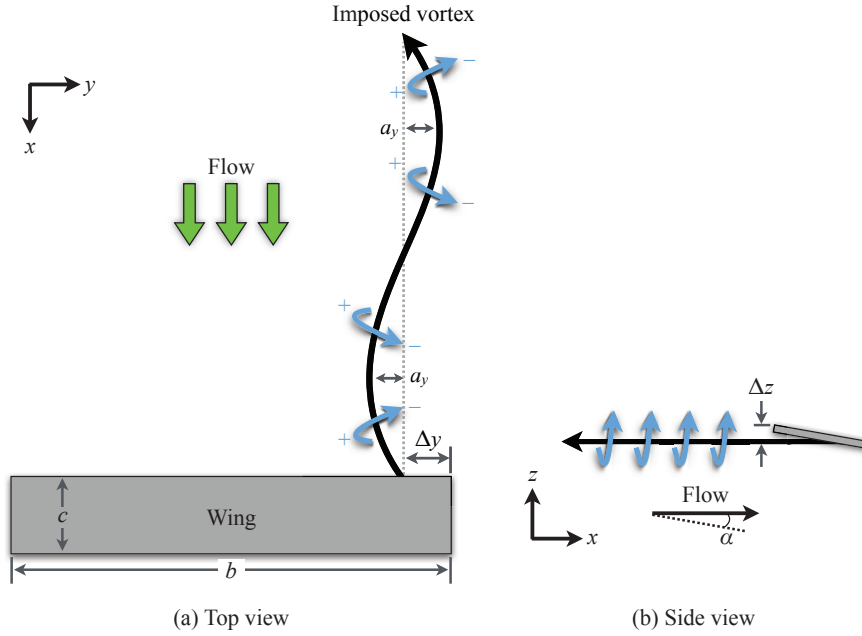


Figure 1: Wandering streamwise-oriented vortex/wing configuration: (a) Top view, (b) Side view

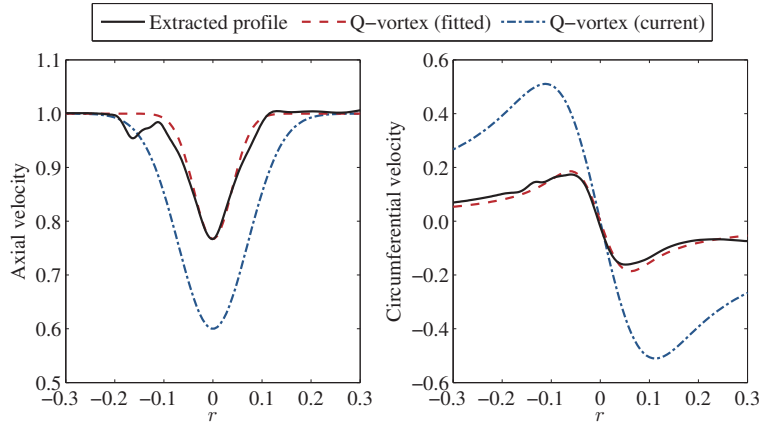


Figure 2: Matching of a q-vortex to the tip vortex of a flat plate wing. Extracted profile is taken 1.5c downstream of a flat plate wing in a free stream oriented at $\alpha = 4^\circ$. A fitted q-vortex is shown along with the vortex used in this study with twice the swirl strength and core radius.

B. Computational mesh and boundary conditions

A nested mesh system that utilizes Chimera overset³⁶ with high-order interpolation³⁷ has been created to discretize the domain around the wing. The configuration consists of six near-body stretched Cartesian meshes protruding normal to the rectangular wing with increased stretching away from the surface. Once a nominal spacing has been achieved, the near-body grids cease and a coarser background mesh continues to the farfield boundaries located 30-50 chords from the wing. A separate, higher resolution mesh is overset into the background mesh to maintain the integrity of the streamwise-oriented vortex as it convects towards the wing from the inflow boundary. A depiction of the nearfield, nested mesh system is presented in Fig. 3. The farfield boundaries actually extend much farther away from the wing, but only the near-body domain is shown for clarity. Additionally, the wing is oriented at an angle of $\alpha = 4^\circ$ and the mesh is analytically

deformed near the surface using a exponential decay weighting function to maintain normal gridlines at the boundary while keeping the mid-field overlap regions undisturbed away from the wing. This allows multiple wing orientations to be readily available by merely deforming the mesh rather than completely regenerating the discretized domain; although, only one orientation is considered in this study, i.e. $\alpha = 4^\circ$.

The inflow boundary is positioned 10 chords ahead of the wing, and the analytically defined vortex is imposed there with a variable center position. All other farfield boundaries are prescribed as outflow conditions, which in conjunction with the increased grid-stretching and high-order filtering, provides a buffer-like treatment that prevents reflections from corrupting the interior of the domain. The wing surface is set as a no-slip, adiabatic wall enforced by a fourth-order-accurate, zero-normal pressure gradient.

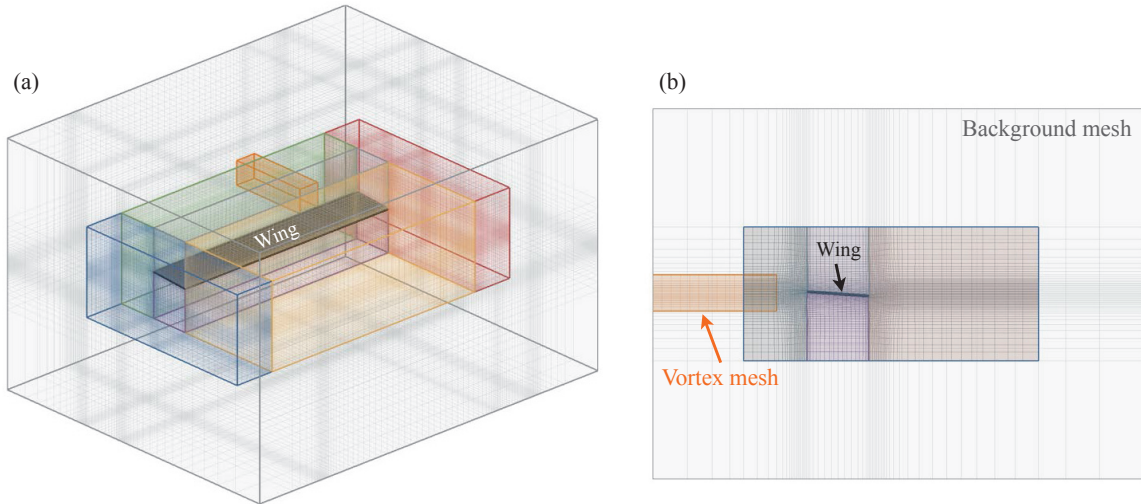


Figure 3: Depiction of the nearfield nested mesh configuration; (a) Full view, (b) Side view; Note that the farfield mesh actually extends 30-50 chords from the wing, but only the nearfield is shown for clarity

C. Effects of spatial resolution

In order to examine the spatial resolution required for the current problem, three geometrically similar meshes have been created with successive levels of refinement: fine, medium (75%), and coarse (50%). Specific details of these grids are listed in Table 2 including the number of surface elements across the chord (n_ξ), span (n_η), and thickness (n_ζ) along with the minimum spacing in each direction. In these cases, the incident vortex mean position on the inflow boundary is prescribed at $\Delta y = 0.25c$ inboard of the wingtip in the spanwise direction, and it oscillates laterally with an amplitude of $a_y = 0.5c$ and Strouhal number of $St = 0.2$. In the vertical direction, the vortex is positioned inline with the midchord of the wing ($\Delta z = 0.035$), which was shown in a previous study¹⁵ to allow a stationary vortex to collide head-on with the wing's leading edge. The domain is initialized with freestream conditions everywhere, except at the inflow boundary, where the wandering vortex is prescribed. The flow then evolves for 20 convective times to washout spurious transients generated from the startup and to allow the incident vortex to propagate up to and past the body and establish the nearly periodic structure. The next 40 convective times (8 vortex cycles) are then used to collect the phase-averaged solutions. In terms of wall-units, the normal, streamwise, and spanwise average spacings on the wing's upper surface are less than 0.06, 3.8, and 6.6, respectively, which are all within the acceptable ranges of well-resolved LES. The time step is selected as $\Delta\tau = 0.0001$, which leads to an average time step in wall units of $\Delta\tau^+ < 0.036$ on the wing's upper surface for each mesh. This should provide ample temporal resolution based on the study of Choi and Moin³⁸ that showed $\Delta\tau^+ < 0.4$ allowed for proper resolution of the relevant scales for turbulent channel flow.

Figure 4 depicts the phase-averaged flow structure of the impacting vortex near its outermost position for each resolution. With only 8 phases, many of the smaller scales associated with the separated boundary layer off the leading edge are still quite evident as they have not been averaged away, especially as the resolution is increased. Despite these smaller features, the overall structure of the incident vortex propagating over the

upper side of the wing and interacting with the separated region is well-resolved by each mesh, with very few differences visible among the various solutions. The instantaneous and phase-averaged aerodynamic loads are presented in Fig. 5(a) and (b), respectively, for each spatial resolution. Each mesh provides nearly the same unsteady force response throughout the eight cycles of the vortex motion with only slight deviations from the fine solution. In the phase-averaged representations, the periodic force histories almost collapse with increased resolution. For this reason, the medium resolution is confidently selected for the remainder of this study.

Although the spatial resolution was only examined for one realization of the incident vortex, the other case in this work is prescribed with a lower wandering amplitude, $a_y = 0.25$, which should require less resolution to maintain its integrity throughout the domain. Therefore, the chosen medium resolution should also be sufficient for the lower amplitude wandering vortex.

Mesh	Surface elements			Total grid points	Minimum spacing		
	n_ξ	n_η	n_ζ		Normal	Streamwise	Spanwise
Coarse	124	461	31	62,026,474	1.61×10^{-4}	8.07×10^{-4}	8.07×10^{-4}
Medium	140	520	35	89,192,973	1.43×10^{-4}	7.14×10^{-4}	7.14×10^{-4}
Fine	154	571	39	115,614,544	1.30×10^{-4}	6.49×10^{-4}	6.49×10^{-4}

Table 2: Details of the computational domains

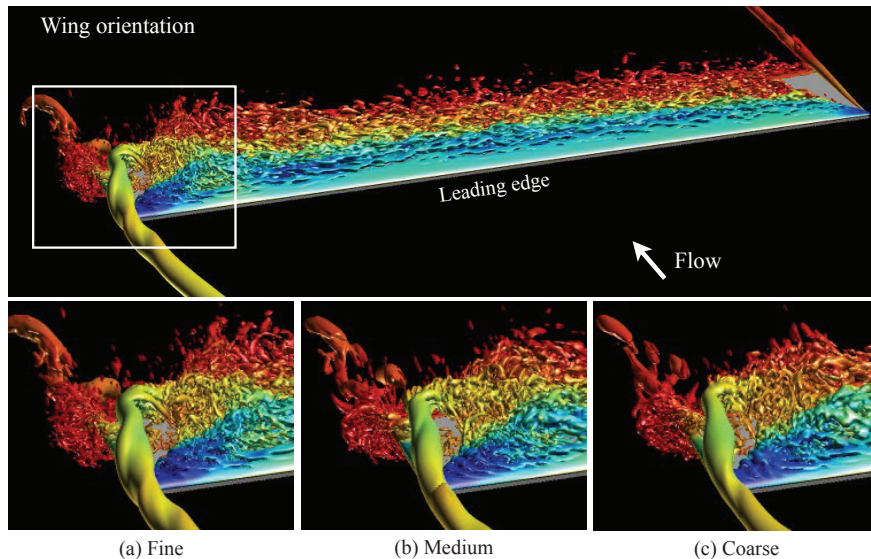


Figure 4: Isosurfaces of Q-criterion from the (a) fine, (b) medium, and (c) coarse resolution, phase-averaged solutions

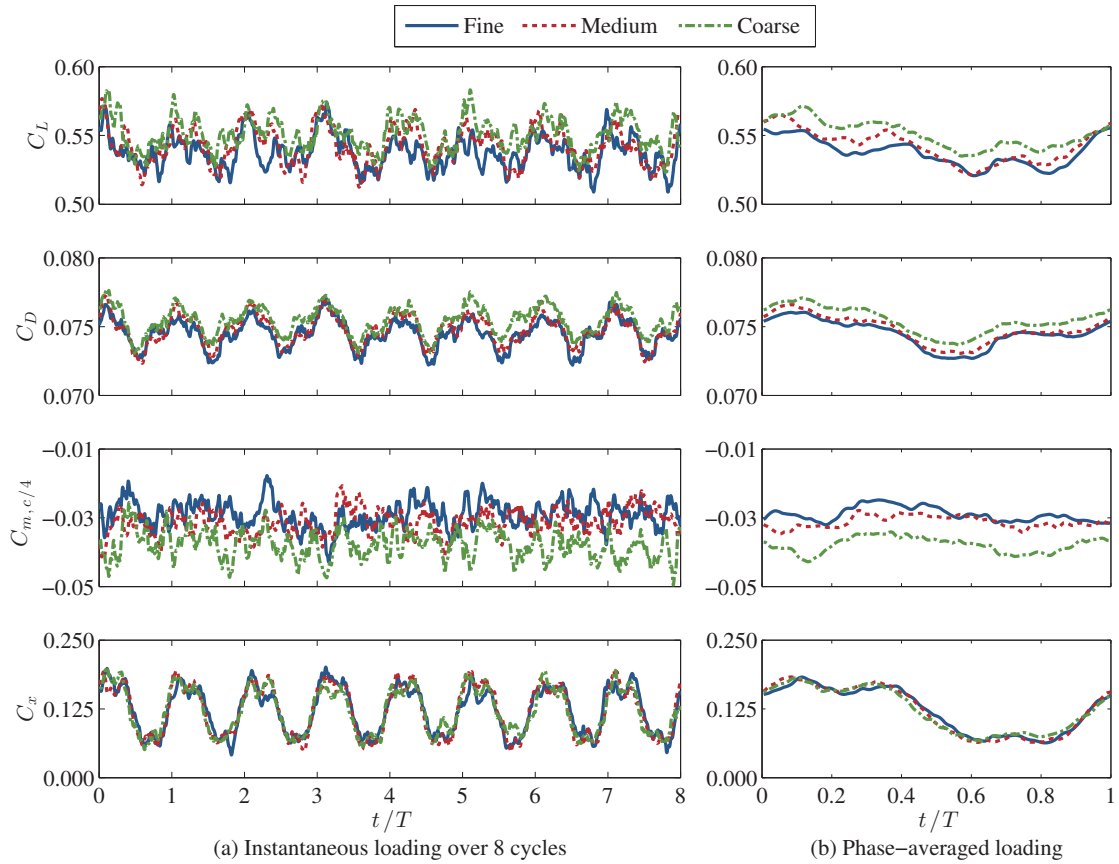


Figure 5: Instantaneous and phase-averaged lift, drag, pitching moment, and rolling moment coefficients over eight cycles of the vortex motion for $a_y = 0.5c$

V. Results

In this section, two simulations of wandering vortex/surface interactions are presented. The incident vortices are initially positioned at $\Delta y = 0.25$ inboard of the wingtip and forced to oscillate laterally at a Strouhal number of $St = 0.2$ with amplitudes of $a_y = 0.50c$ and $0.25c$, respectively. In both cases, the solution is advanced for 20 convective times to eliminate spurious transients associated with the startup and to allow the incident vortex to convect from the inflow boundary past the wing and to establish the mostly periodic interaction. Forty more convective times are then simulated to collect a phase-averaged solution over eight cycles of the vortex motion.

A. Description of the three-dimensional flow structure

As the streamwise-oriented vortex moves laterally, an alternating vertical displacement of the vortex core spatially evolves under self-induction depicted by the Q-criterion isosurfaces in Fig. 6 for $a_y = 0.5$. An upward deflection results at the outboard-most extent of the vortex core, while a downward displacement ensues at the inboard-most position. The imposed and induced displacements lead to a tilted traversing plane as the vortex reaches the leading edge as shown in the path traces of Fig. 7. Here, the vortex path is tracked in planes $10c$ upstream (inflow boundary), $5c$ upstream, and $0.5c$ upstream of the wing. The planar trajectories for both wandering vortices incline with respect to the initial lateral motion as they approach the wing while also diminishing in amplitude. This promotes an interaction in both cases where the vortex is positioned above the upper surface at its outboard-most extent and moves under the wing as it progresses inboard. The amplitudes and incline angles measured at each plane are listed in Table 3. Interestingly, for both wandering amplitudes, the vortex loses 20% of its initial amplitude after convecting $5c$ (one wavelength) and reduces by another 16% just before reaching the leading edge. The incline angles differ between the two cases, with the larger amplitude trajectory rotating to 12° and 31° at $5c$ and $0.5c$ upstream of the wing, respectively. The smaller initial amplitude trajectory inclines more dramatically to 15° and 45° , respectively, at the same upstream locations. In both cases, the resulting interaction with the wing is then dependent upon the wing's streamwise location relative to the self-induced motion of the vortex core that spatially develops as it convects. For the cases examined here, only one streamwise location of the wing is considered, but other positions are of interest for future studies, along with wandering vortex studies in the absence of a wing to examine the self-induced and evolving vertical displacement.

In Figures 8 and 9, the progression of the incident vortex impingement along the leading edge is shown for $a_y = 0.50c$ and $0.25c$, respectively, through isosurfaces of total pressure, which are used to highlight the overall vortex structure while masking the smaller scales. The flow above the wing is shown in (a), while the underside is visualized in (b) for the same phases. For both wandering amplitudes, the incident vortex is completely above the wing surface at its outboard-most position (1); however, as it travels inboard (1-5), it also descends vertically causing it to pinch off at the leading edge (pointed out in 3a) as the low pressure isosurface spills onto the underside of the wing for the remainder of its inboard progression. Similarly, on the return stroke to the tip (phases 6-10), the vortex is propelled upward from its self-induced velocity and pinches off again at the leading edge (pointed out in 7b), but this time, as it erupts onto the upper surface.

Location	$a_y = 0.50c$		$a_y = 0.25c$	
	Amplitude	Incline	Amplitude	Incline
Inflow	0.50	0°	0.25	0°
Upstream $5.0c$	0.41	12°	0.20	15°
Upstream $0.5c$	0.32	31°	0.16	45°

Table 3: Incident vortex wandering amplitude and incline angles measured at several planes upstream of the wing's leading edge

Turning back to the inboard progression and pinch-off at phase 3, the remaining structure on the upper surface is quickly entrained into the separated boundary layer off the leading edge. On the underside, the vortex anchors itself to the surface and connects with the newly-formed and growing separated region near the wingtip. The upstream portion of the vortex continues to convect past the separated region on the underside, while maintaining its connection, resulting in a horseshoe-like vortex, the evolution of which is

seen very clearly in the Q-criterion isosurfaces of Fig. 10. When the vortex pinches off again between phases 7 and 8 as the low-pressure isosurface spills over to the upper side, the horseshoe-like vortex coalesces into a ring structure and convects into the wake. A similar evolution is encountered on the upper surface of the wing as the vortex traverses outboard, which is overlaid in Figures 8 and 9, although the horseshoe structure is less coherent as it is drawn into the large separated region inboard of impingement. It is interesting to note that while the pinch-off and alternating surface attachment of the incident vortex does resemble the stationary inboard vortices impinging upon a wing from Ref. 15, the mechanism differs between the stationary and wandering vortex interactions. For the stationary cases, the upstream influence of the wing induces a spiraling instability in the vortex core that reorients the vortex ahead of the wing, leading to the pinch-off. In contrast, the wandering vortices examined here exhibit no signs of this same spiraling undulation. Instead, the pinch off is driven by the large-scale, self-induced vertical displacement of the vortex core. This finding has potential implications when generalizing conclusions about the flow structure engendered by a stationary vortex impingement to the more dynamic problem of a wandering vortex.

Figure 11 depicts the surface pressure and surface-restricted streamlines on the upper and lower sides of the wing for both wandering cases. A transparent isosurface of total pressure ($p_0/p_{0,\text{ref}} = 0.997$) is overlaid to show the corresponding vortex structure at each phase. Near the beginning and end of the cycle (phases 2 and 10), both wandering amplitudes lead to incident vortices positioned above the wing surface that allow a low-profile, tip vortex to form whose imprint is seen as a region of low pressure encompassed by an attachment line along the wingtip (indicated in 10). At all other phases, the tip vortex is suppressed as described in the previous study¹⁵ with inboard-positioned stationary vortices. With $a_y = 0.50c$, the incident vortex is farther outboard, slightly beyond the wingtip, inducing a stronger tip vortex. This momentary state parallels the result of a stationary tip-aligned incident vortices of Ref. 15. For both wandering cases, the upper side position of the incident vortex also enhances the three-dimensional recirculation region off the wing's leading edge, which also resembles the inboard-positioned, stationary vortex cases of Ref. 15. The corresponding strong suction diminishes in phase 4 as the incident vortex pinches off and spills over to the underside of the wing, causing the underside boundary layer separation, indicated by the small region of suction along the leading edge, outboard of impingement, which is much like the enhanced recirculation region formed on the upper side. The surface-restricted streamlines also show a complicated swirling pattern accompanied by a convergence line from the separation induced by the legs of the horseshoe vortex that was discussed earlier. Once the incident vortex fully returns to the upper side past phase 8, the imprint of the recirculation region on the upper side quickly increases in size and strengthens while the underside flow reattaches.

B. Analysis of the unsteady loading

The aerodynamic loads phase-averaged over the wandering cycle are plotted in Fig. 12(a). The time-mean loads from Ref. 15 for stationary incident vortices positioned at $\Delta y = -0.25c, 0.25c$, and $1.00c$ are also plotted for reference. These positions are measured inboard of the wingtip with the negative value corresponding to a location outboard of the wingtip. They also bracket the extents of the wandering cases examined here, whose positions vary between $\Delta y = 0.25c \pm 0.5c$. Near its outboard-most position ($t/T = 0$), the wandering vortex allows for the most efficiently loaded span along the wing, while still enhancing the three-dimensional recirculation from the separated boundary layer near the tip, resulting in the highest magnitudes of the lift, drag, pitching moment, and rolling moment coefficients. Alternatively, around the most inboard extent ($t/T = 0.5$), the wing is least-efficiently loaded due to the inboard impingement of the vortex and the formation of two similarly-sized separation bubbles on either side of the wing that effectively unload the region near the wingtip. For both cases, the phase-averaged loads fall within the time-mean values of the stationary vortices positioned at or near the maximum extents of the wandering vortex. This is despite the inherently different pinch-off mechanism between the examined stationary and wandering vortices.

The frequency spectra of the instantaneous loads is provided in Fig. 12(b) as a measure of the unsteadiness in the forces. The most dominant mode corresponds to the imposed wandering frequency of the incident vortex, $St = 0.2$, which is clearly seen in the lift, drag, and rolling moment spectra for both cases with the power level scaling with wandering amplitude, a_y . The wandering frequency is not as evident in the pitching moment, where the power in that mode is on the order of the signal noise. This is not surprising since the pitching moment shows very little sensitivity to the incident vortex spanwise position. In the other spectra, significant power is also present at $St = 0.4$ and 0.6 , which correspond to the first two harmonics of the wandering frequency; although both harmonics are much less pronounced and are not present in all of the

spectra for $a_y = 0.25c$. To analyze these modes further for $a_y = 0.50c$, the frequency spectra of the surface pressure is computed on both sides of the wing, and the power level in the dominant modes, $St = 0.2, 0.4$, and 0.6 , is displayed in Fig. 13. This image shows how the signal amplitude is distributed across the wing for these frequencies and how far the vortex-induced fluctuations persist inboard. In all three modes, the majority of the power is concentrated near the impingement location; however, significant content in the first mode also extends to the midspan on the upper surface, which highlights the incident vortex being drawn into the separated region from the recirculation zone off the leading edge. The spotty concentrations on the opposite side of the wing in all modes correspond to the broadband power present in the transitional modes past attachment of the leading edge separation. On the underside, the concentrations remain near impingement except for a narrow band of higher amplitude along the leading edge in the dominant mode, $St = 0.2$, indicating that the unsteady fluctuations of the wandering vortex do not remain entirely local to the impingement area even on the underside. The remainder of the lower surface is relatively undisturbed as the flow remains laminar.

Additionally, the time-mean and fluctuating loads are listed in Table 4 for the two wandering cases along with the stationary vortex positioned at the mean position of $\Delta y = 0.25$. The mean lift and rolling moment coefficients both experience decreases with increased wandering amplitude. However, they also show an initial reduction in the accompanying fluctuating quantities for $a_y = 0.25c$, but rise again for $a_y = 0.50c$ with the rolling moment fluctuations outpacing the stationary case by almost a factor of two.

a_y	C_L		C_D		C_M		C_X	
	Mean	RMS ($\times 10^4$)	Mean	RMS ($\times 10^5$)	Mean	RMS ($\times 10^4$)	Mean	RMS ($\times 10^3$)
0.50	0.542	3.385	0.075	2.613	-0.031	0.916	0.122	1.123
0.25	0.549	2.707	0.075	1.980	-0.034	1.373	0.136	0.548
0.00	0.560	3.863	0.076	1.873	-0.033	1.866	0.152	0.590

Table 4: Mean aerodynamic loads and corresponding fluctuations for the two wandering cases ($a_y = 0.50c$ and $0.25c$) and the stationary vortex¹⁵ ($a_y = 0.0c$) all around the center position of $\Delta y = 0.25$ inboard of the wingtip.

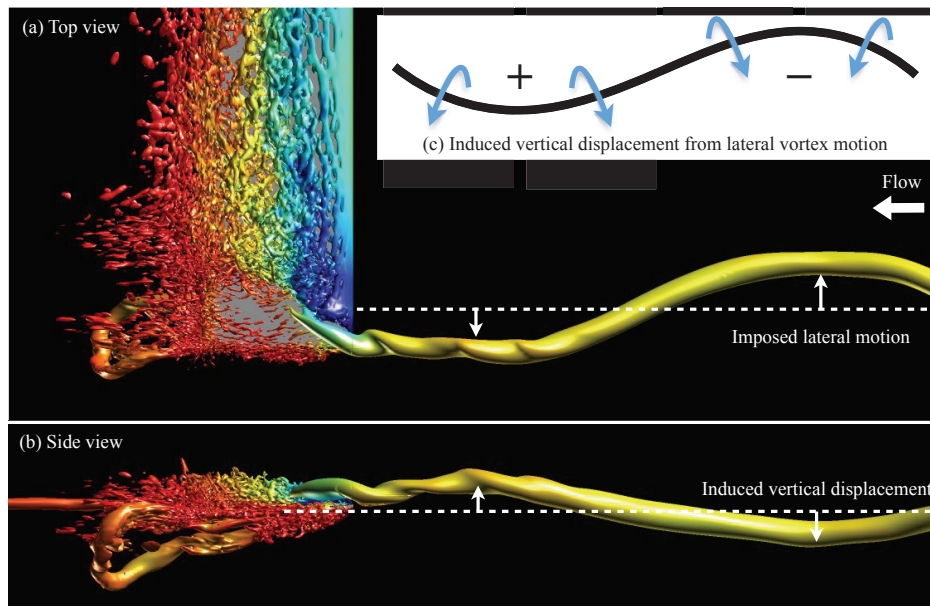


Figure 6: Isosurface of Q-criterion from the phase-averaged solution highlighting the imposed lateral motion and the vortex-induced vertical displacement

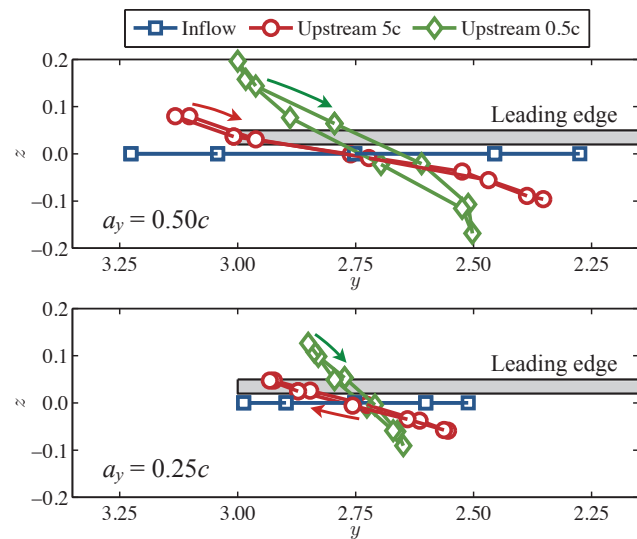


Figure 7: Traces of the incident vortex path on several planes upstream of the wing's leading edge; View is directed towards the leading edge from an upstream location.

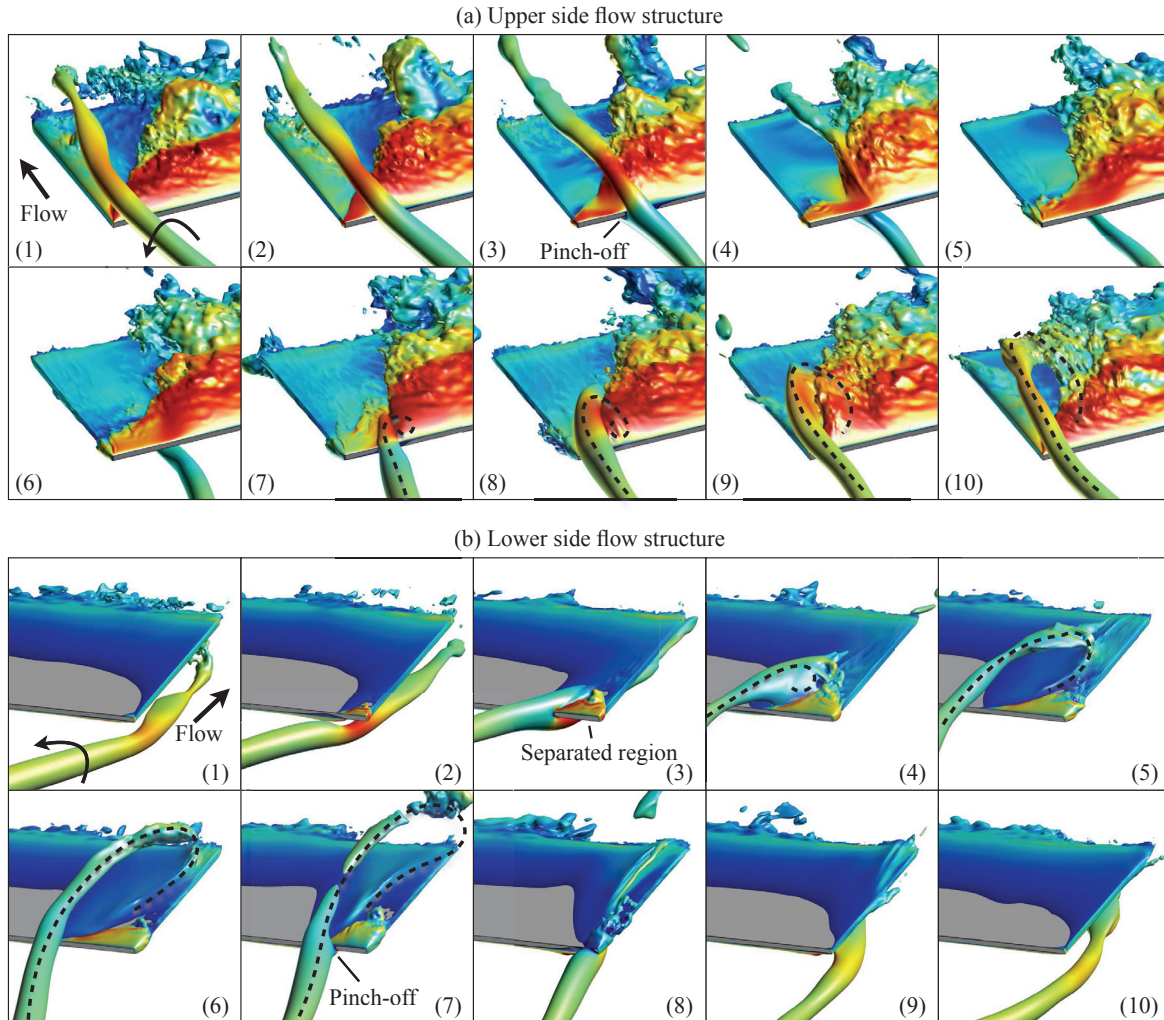


Figure 8: Isosurfaces of total pressure ($c_p/c_{p0} = 0.995$) colored by streamwise velocity showing the inboard progression of the impinging vortex near the wingtip for $a_y = 0.50c$

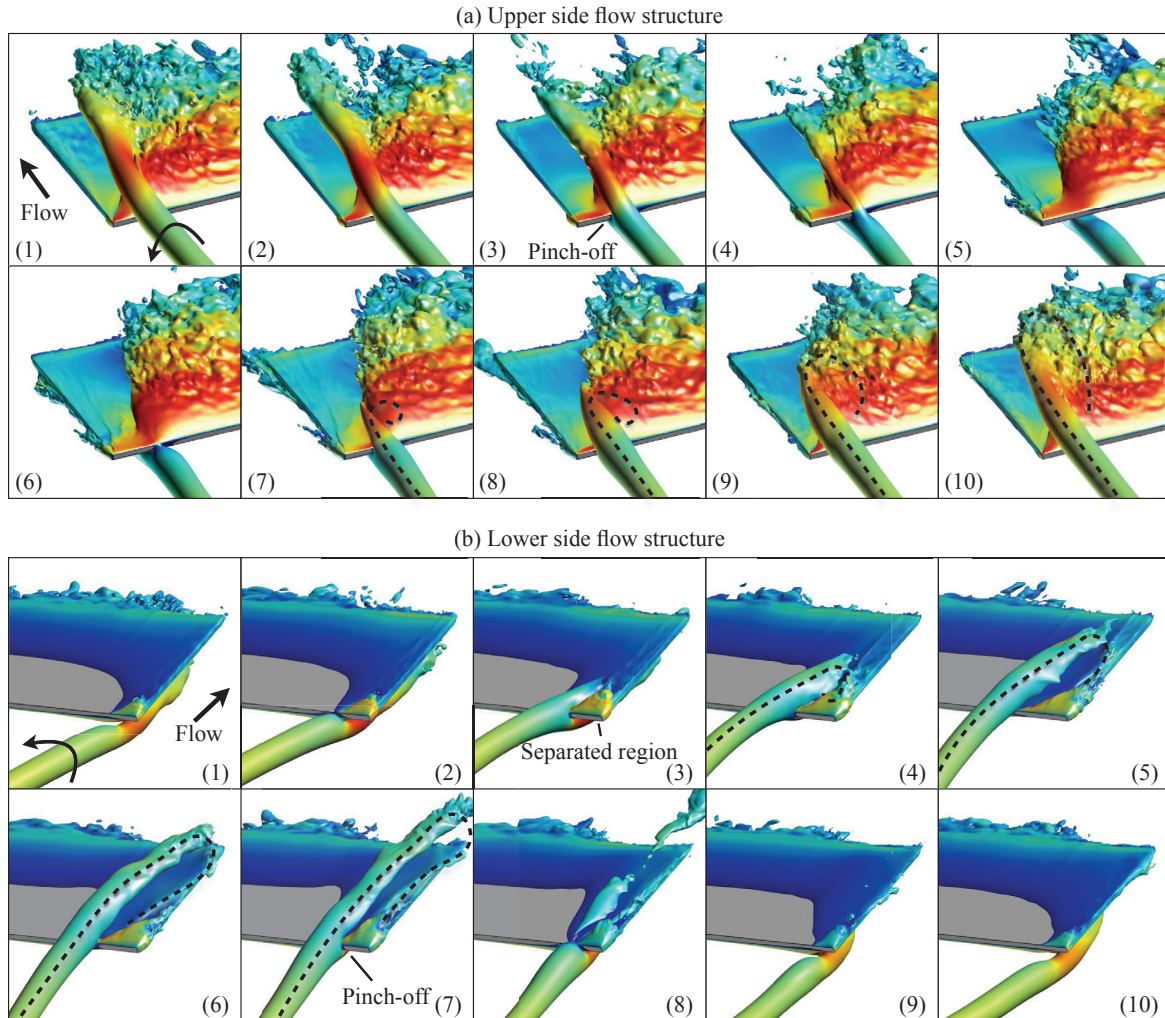


Figure 9: Isosurfaces of total pressure ($c_p/c_{p0} = 0.995$) colored by streamwise velocity showing the inboard progression of the impinging vortex near the wingtip for $a_y = 0.25c$

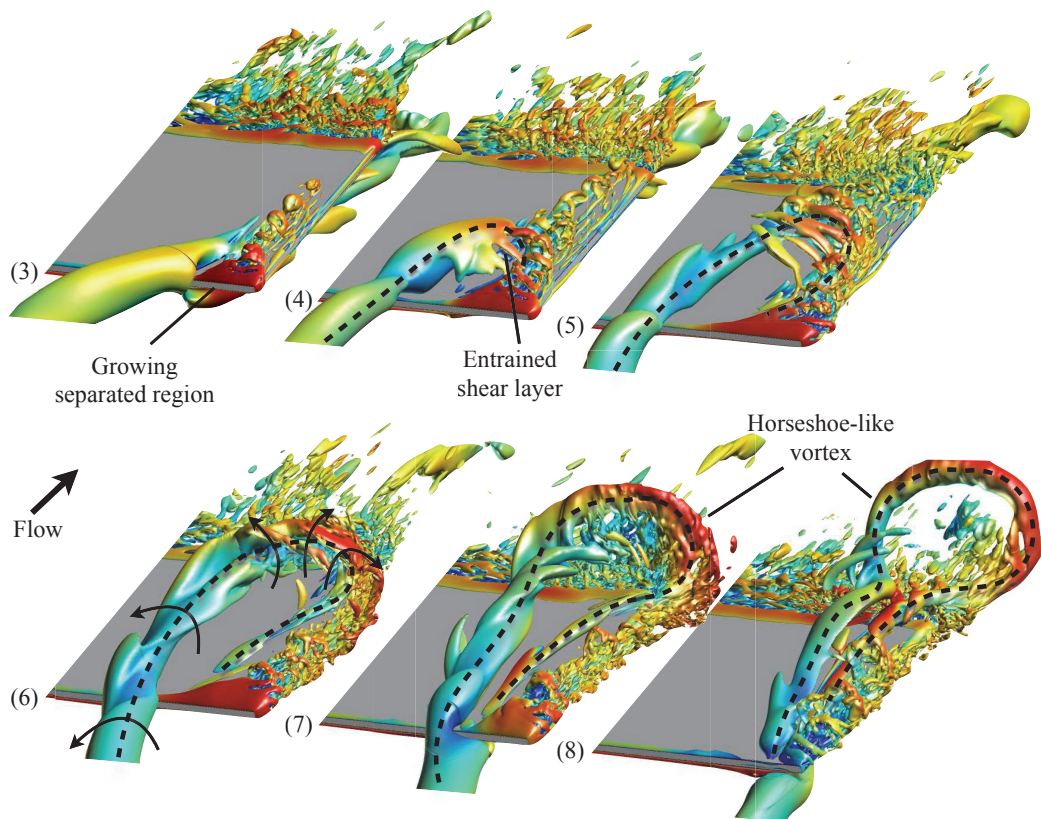


Figure 10: Isosurfaces of Q-criterion ($Q = 10$) depicting the vortex structure on the underside of the wing for phases (3-8) of the incident vortex with $a_y = 0.50c$

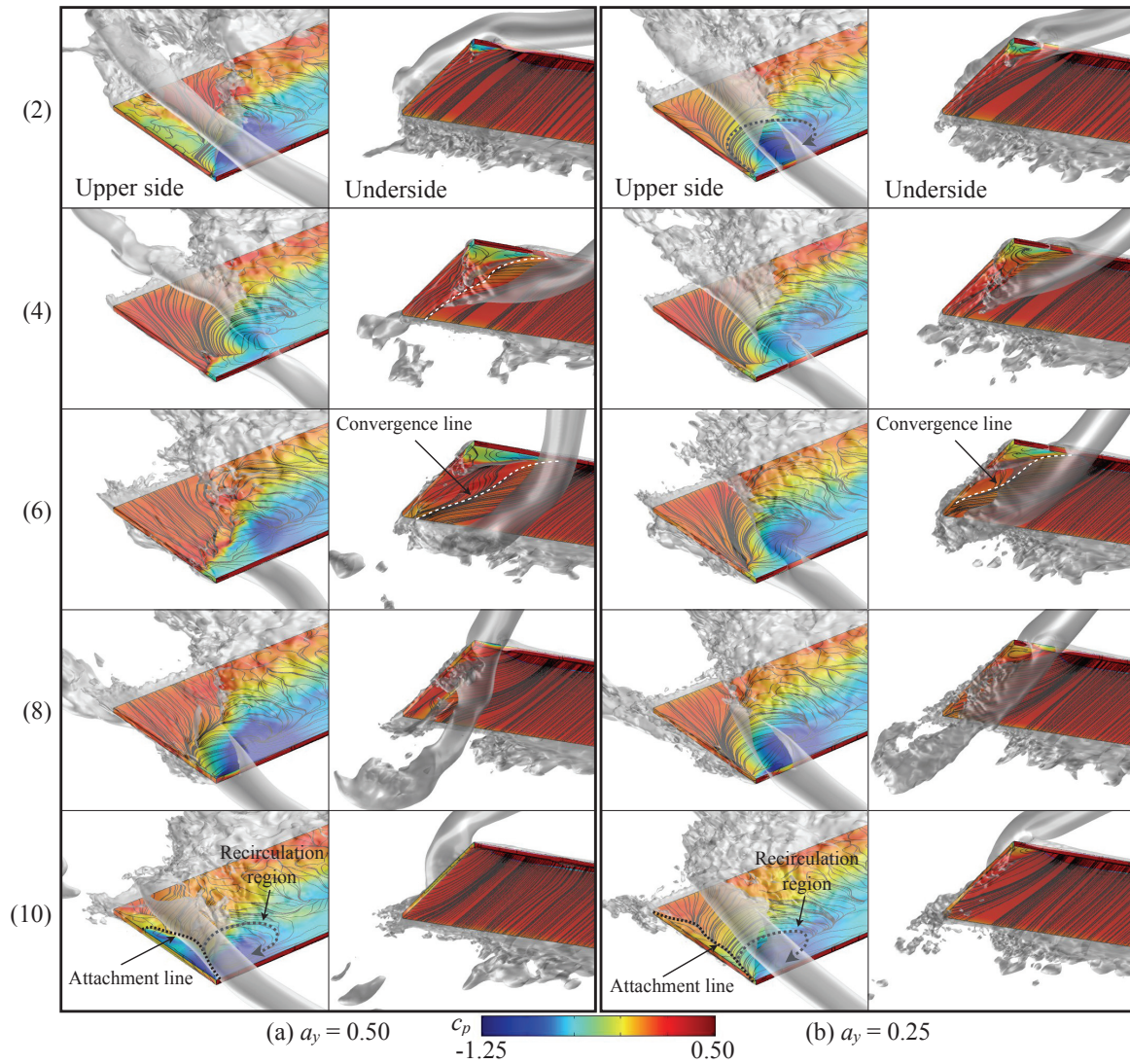


Figure 11: Surface pressure and surface-restricted streamlines on the upper and lower sides of the wing near impingement for wandering amplitudes of (a) $a_y = 0.50c$ and (b) $a_y = 0.25c$. A transparent isosurface of total pressure ($c_p/c_{p0} = 0.997$) is also overlaid to show the vortex structure at each phase

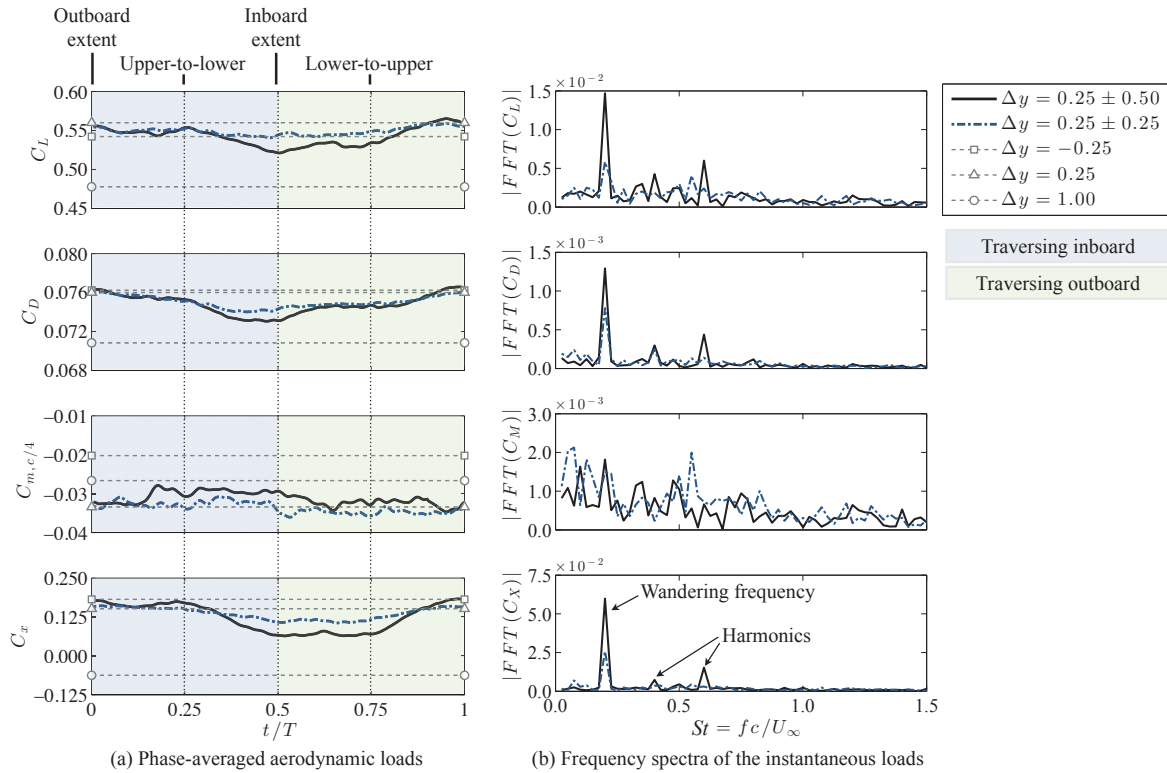


Figure 12: Phase-averaged aerodynamic loads (a) and the accompanying frequency spectra of the instantaneous loads (b) from the wandering vortex/wing interactions; Two wandering cases of $a_y = 0.25c$ and $0.5c$ are depicted about their mean positions at $0.25c$ inboard from the wingtip. The time-mean forces from the stationary vortex impingement cases for $\Delta y = -0.25$, 0.25 , and 1.00 from Ref. 15 are also shown in (a) for reference. The outboard and inboard extents of the wandering vortex are pointed out along with the instances when the vortex transitions from the upper-to-lower or lower-to-upper surfaces.

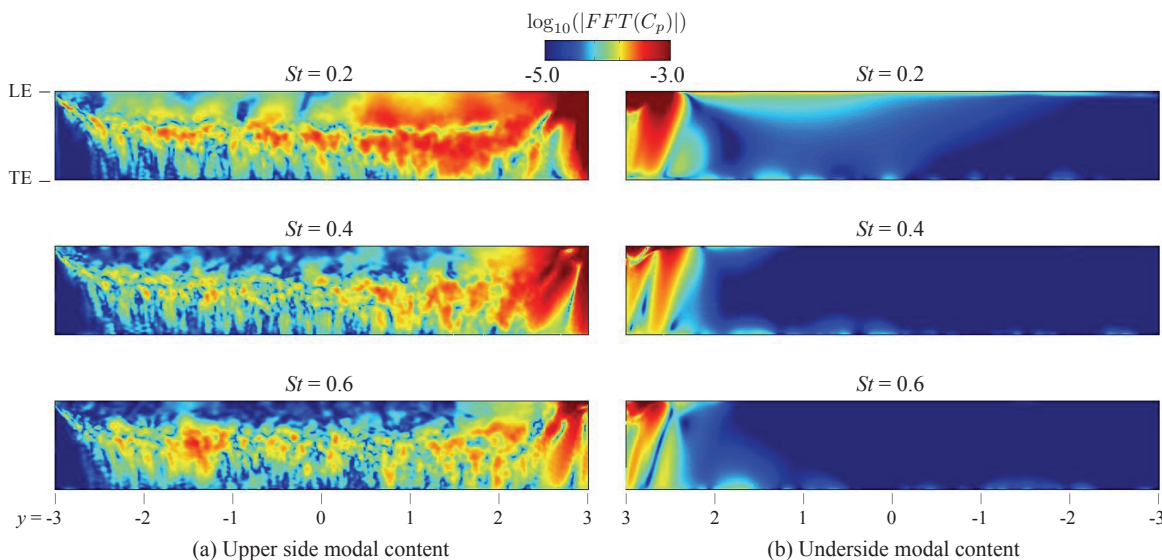


Figure 13: Power content in the dominant modes of the surface pressure spectra from the (a) upper side and (b) underside of the wing for $a_y = 0.50c$

VI. Conclusions

In this study, the unsteady interactions of wandering streamwise-oriented vortex impinging upon a finite wing were examined using high-fidelity numerical simulation. An incident vortex was prescribed analytically upstream of an aspect-ratio-six wing and was defined with a sinusoidal variation in its spanwise position as a canonical problem for examining the vortex-body interaction in the absence of freestream turbulence, crow instability, and lead wing influences. The mean position of the vortex was set at 0.25 chords inboard of the wingtip and oscillated at a Strouhal number of $St = fc/U_\infty = 0.2$, corresponding to a spatial wavelength of five chords. Two wandering amplitudes were considered, $a_y = 0.50c$ and $0.25c$, to traverse the impingement locations examined in a previous study of stationary incident vortices.

Most notably, the imposed lateral motion of the vortex spatially evolved as it approached the wing by inclining relative to its initial horizontal trajectory and also diminishing in amplitude. Just ahead of the wing, both wandering amplitudes were reduced by 36% and the horizontal trajectory inclined by nearly 31° and 45° , respectively, for the initial wandering amplitudes of $0.5c$ and $0.25c$. This streamwise development of the incident vortex path has implications on the subsequent interaction with the wing, as the wing's streamwise position relative to the vortex self-induced motion dictates the trajectory that the vortex will follow as it impacts the surface. For the cases examined here, only one streamwise location of the wing was considered, but other positions are of interest for future studies, along with wandering vortex studies in the absence of a wing to examine the self-induced and evolving vertical displacement.

The vertical offset of the vortex core was also shown to drive an eventual pinch-off and alternating attachment to the upper and lower surfaces, which then evolved into a horseshoe-like structure before coalescing into a ring vortex and convecting into the wake. This is in contrast to the pinch-off experienced by a stationary vortex impacting a wing, which is driven by a spiraling instability in the vortex core induced by the upstream influence of the wing that reorients the vortex ahead of the leading edge. The wandering vortices examined here exhibited no signs of the same spiraling undulation. This finding may prevent conclusions about the flow structure engendered by a stationary vortex impingement from being generalized to the more dynamic wandering vortex interaction.

Despite the differing mechanisms of pinch-off and surface attachment, the unsteady loading experienced by the wing with either wandering vortices were bracketed by the mean loads for the stationary impinging vortices positioned at or near the wandering extents. The temporal energy spectra of the surface pressure was also analyzed, and the unsteady fluctuations induced by the incident vortex were shown to propagate beyond the local interaction region towards the wing's midspan as a result of the impacting vortex being drawn into the separated region off the upper surface.

Acknowledgements

This work is supported in part by AFOSR under a task monitored by Dr. D. Smith and also by a grant of HPC time from the DoD HPC Shared Resource Centers at AFRL and ERDC.

References

- ¹Rockwell, D., "Vortex-body interactions," *Annual Review of Fluid Mechanics*, Vol. 30, 1998, pp. 199–229.
- ²Crow, S. C., "Stability Theory of a Pair of Training Vortices," *AIAA Journal*, Vol. 8, 1970, pp. 2172–2179.
- ³Gordnier, R. E. and Visbal, M. R., "Numerical Simulation of the Impingement of Streamwise Vortex on a Plate," *International Journal for Computational Fluid Dynamics*, Vol. 12, No. 1, 1999, pp. 49–66.
- ⁴Visbal, M. and Gordnier, R., "On the Structure of the Shear Layer Emanating from a Swept Leading Edge at Angle of Attack," AIAA Paper 2003-4016, AIAA, 2003.
- ⁵Richez, A., Le Pape, A., Costes, M., and Gavéraiaux, R., "Zonal Detached-Eddy Simulation (ZDES) of the three-dimensional stalled flow around a finite span wing," AIAA Paper 2012-3281, AIAA, 2012.
- ⁶Heyes, A. L., Jones, R. F., and Smith, D. A. R., "Wandering of wing-tip vortices," *12th International Symposium on Application of Laser Techniques to Fluid Mechanics*, Lisbon, Portugal, July 2004.
- ⁷Hummel, D., "Aerodynamic Aspects of Formation Flight in Birds," *Journal of Theoretical Biology*, Vol. 104, No. 3, 1983, pp. 321–347.
- ⁸Hummel, D., "Formation Flight as an Energy-Saving Mechanism," *Israel Journal of Zoology*, Vol. 41, No. 3, 1995, pp. 261–278.
- ⁹Beukenberg, M. and Hummel, D., "Aerodynamics, Performance and Control of Airplanes in Formation Flight," *Proceedings of the 17th Congress of the International Council of the Aeronautical Sciences*, Vol. 2, September 1990, pp. 1777–1794.
- ¹⁰Lissaman, P. B. S. and Shollenberger, C. A., "Formation Flight of Birds," *Science*, Vol. 168, No. 3934, May 1970, pp. 1003–1005.
- ¹¹Ning, S. A., Flanzer, T. C., and Kroo, I. M., "Aerodynamic Performance of Extended Formation Flight," AIAA Paper 2010-1240, AIAA, 2010.
- ¹²Kless, J., Aftosmis, M. J., Ning, S. A., and Nemec, M., "Inviscid Analysis of Extended-Formation Flight," *AIAA Journal*, Vol. 51, No. 7, July 2013.
- ¹³Jacquin, L., Fabre, D., and Geffroy, P., "The properties of a transport aircraft wake in the extended near field: an experimental study," AIAA Paper 2001-1038, AIAA, 2001.
- ¹⁴Barnes, C. J., Visbal, M. R., and Gordnier, R. E., "Investigation of aeroelastic effects in streamwise-oriented vortex/wing interactions," AIAA Paper 2014-1281, AIAA, 2014.
- ¹⁵Garmann, D. and Visbal, M., "Interaction of a streamwise-oriented vortex with a wing," AIAA Paper 2014-1282, AIAA, 2014.
- ¹⁶Tannehill, J., Anderson, D., and Pletcher, R., "Computational Fluid Mechanics and Heat Transfer," *Series in computational and physical processes in mechanics and thermal sciences*, Taylor & Francis, 2nd ed., 1997.
- ¹⁷Visbal, M. and Rizzetta, D., "Large-Eddy Simulation on Curvilinear Grids Using Compact Differencing and Filtering Schemes," *Journal of Fluids Engineering*, Vol. 124, 2002, pp. 836–847.
- ¹⁸Garmann, D., Visbal, M., and Orkwis, P., "Comparative study of implicit and subgrid-scale model large-eddy simulation techniques for low-Reynolds number airfoil applications," *International Journal for Numerical Methods in Fluids*, Vol. 71, No. 12, 2013, pp. 1546–1565.
- ¹⁹Stolz, S. and Adams, N., "An Approximate Deconvolution Procedure for Large-Eddy Simulation," *Physics of Fluids*, Vol. 11, No. 7, 1999, pp. 1699–1701.
- ²⁰Matthew, J., Lechner, R., Foysi, H., Sesterhenn, J., and Friedrich, R., "An Explicit Filtering Method for LES of Compressible Flows," *Physics of Fluids*, Vol. 15, No. 8, 2003, pp. 2279–2289.
- ²¹Gaitonde, D. and Visbal, M., "High-Order Schemes for Navier-Stokes Equations: Algorithm and Implementation into FDL3DI," Technical Report AFRL-VA-WP-TR-1998-3060, Air Force Research Laboratory, Wright-Patterson AFB, 1998.
- ²²Visbal, M. and Gaitonde, D., "High-Order Accurate Methods for Complex Unsteady Subsonic Flows," *AIAA Journal*, Vol. 37, No. 10, 1999, pp. 1231–1239.
- ²³Lele, S., "Compact Finite Difference Schemes with Spectral-like Resolution," *Journal of Computational Physics*, Vol. 103, No. 1, 1992, pp. 16–42.
- ²⁴Gaitonde, D. and Visbal, M., "Further Development of a Navier-Stokes Solution Procedure Based on Higher-Order Formulas," AIAA Paper 99-0557, AIAA, 1999.
- ²⁵Alpert, P., "Implicit Filtering in Conjunction with Explicit Filtering," *Journal of Computational Physics*, Vol. 44, No. 1, 1981, pp. 212–219.
- ²⁶Visbal, M., Morgan, P., and Rizzetta, D., "An Implicit LES Approach Based on High-Order Compact Differencing and Filtering Schemes," AIAA Paper 2003-4098, AIAA, June 2003.
- ²⁷Beam, R. and Warming, R., "An Implicit Factored Scheme for the Compressible Navier-Stokes Equations," *AIAA Journal*, Vol. 16, No. 4, 1978, pp. 393–402.
- ²⁸Rizzetta, D., Visbal, M., and Morgan, P., "A High-Order Compact Finite-Difference Scheme for Large-Eddy Simulation of Active Flow Control (Invited)," AIAA Paper 2008-526, AIAA, 2008.
- ²⁹Pulliam, T. and Chaussee, D., "A Diagonal Form of an Implicit Approximate-Factorization Algorithm," *Journal of Computational Physics*, Vol. 17, No. 10, 1981, pp. 347–363.
- ³⁰Jameson, A., Schmidt, W., and Turkel, E., "Numerical Solutions of the Euler Equations by Finite Volume Methods Using Runge-Kutta Time Stepping Schemes," AIAA Paper 1981-1259, AIAA, 1981.
- ³¹Pulliam, T., "Artificial Dissipation Models for the Euler Equations," *AIAA Journal*, Vol. 24, No. 12, Dec. 1986, pp. 1931–1940.
- ³²Batchelor, G., "Axial Flow in trailing line vortices," *Journal of Fluid Mechanics*, Vol. 20, No. 4, 1964, pp. 645–658.
- ³³Jacquin, L. and Pantano, C., "On the persistence of trailing vortices," *Journal of Fluid Mechanics*, Vol. 471, November 2002, pp. 159–168.

³⁴Leibovich, S. and Stewartson, K., "A sufficient condition for the instability of columnar vortices," *Journal of Fluid Mechanics*, Vol. 126, January 1983, pp. 335–356.

³⁵Inasawa, A., Mori, F., and Asai, M., "Detailed Observations of Interactions of Wingtip Vortices in Close-Formation Flight," *Journal of Aircraft*, Vol. 49, No. 1, January–February 2012.

³⁶Steger, J., Dougherty, F., and Benek, J., "A Chimera Grid Scheme," *Advances in Grid Generation*, edited by K. Ghia and U. Ghia, Vol. 5, American Society of Mechanical Engineers, 1983, pp. 59–69.

³⁷Sherer, S. and Scott, J., "High-Order Compact Finite-Difference Methods on General Overset Grids," *Journal of Computational Physics*, Vol. 210, No. 2, 2005, pp. 459–496.

³⁸Choi, H. and Moin, P., "Effects of the Computational Time Step on Numerical Solutions of Turbulent Flow," *Journal of Computational Physics*, Vol. 113, No. 1, 1994, pp. 1–4.

APPENDIX C

Numerical Simulations of Streamwise-Oriented Vortex/Flexible Wing Interactions

Caleb J. Barnes,* Miguel R. Visbal,†

AFRL/RQVA, Wright-Patterson AFB, OH 45433, United States

George P. Huang,‡

Wright State University, Dayton, OH 45435, United States

In this work, both rigid and flexible wings are subjected to a numerically imposed streamwise-oriented vortex and the unsteady flow, aerodynamic loading, and structural dynamics are evaluated. Impingement of the streamwise vortex on the rigid wing produces a spiraling instability in the vortex just upstream of the leading-edge. This helical flow disruption, which alternates between the upper and lower surfaces is shown to provide a source of unsteady loading. In response, the flexible wings exhibit oscillations about a time-mean vertical deflection at sub-harmonics of the incident vortex instability. The spiraling undulations of the vortex are exacerbated with decreasing rigidity which is shown to be influenced by the time-mean deflection of the wing rather than feedback effects from the dynamic response. Evaluation of several vertical offsets of the incident vortex on rigid wings reveals a strong dependency between vertical positioning and unsteady behavior of the incident vortex. For instance, direct impingement or a negative vertical offset can produce strong adverse pressure gradients that form as a direct consequence of vortex-surface interaction. The resulting deceleration of the axial velocity contributes to the formation of helical instabilities and potentially invoke spiral breakdown in more severe conditions. Conversely, a positive vertical offset removes the helical instability by placing the streamwise vortex inline with a favorable pressure gradient produced by flow accelerating over the leading-edge. However, pressure gradients associated with separation and stall downstream have the potential to introduce suction-side instability. While the vertical offset is typically less important than the lateral positioning in terms of aerodynamic benefits, it can have a significant impact on the flow unsteadiness with important considerations for formation flying.

I. Introduction

Recent trends in aviation tend towards learning how to fly more efficiently. One such approach is the recapture of energy lost in trailing vortices via formation flying. Essentially, the upwash component of the swirling flow can be used to reorient the lift vector forward on a follower wing¹ thereby reducing power requirements. The benefit of this vortex-surface interaction has been thoroughly explored in a number of seminal works using inviscid aerodynamic theory,¹⁻⁴ become a well-known energy-saving mechanism in the biological community,^{3,5-7} and more recently demonstrated as a viable and practical approach in aviation through a number of flight tests.^{4,8-14} However, several factors are not well-understood and must be addressed before this approach becomes commonplace. For instance, vortex buffeting can be detrimental to structural integrity and ultimately lead to catastrophic failure or have implications for ride comfort¹⁵ in the less extreme case.

Due to the level of complexity and computational cost, a bulk of what is known on formation flight aerodynamics is based on numerous potential flow solutions available.¹⁶⁻²³ In the last several years, formation flying has reemerged as a topic of interest. For instance, Inasawa *et al.*²⁴ modeled two rectangular NACA

*Student Researcher, Computational Sciences Branch, AFRL/RQVA, AIAA Student Member.

†Technical Area Leader, Computational Sciences Branch, AFRL/RQVA, AIAA Fellow.

‡Chair, Department of Mechanical and Materials Engineering, Wright State University. AIAA Associate Fellow.

23012 airfoil sections in a wind tunnel and observed the time-mean flow structure and behavior of wingtip vortex encounters. Improvements in computational resources have begun to facilitate more detailed numerical analysis of the complex multi-body problem. Ning *et al.*²⁵ addressed issues for wings in extended-formation (longitudinal spacing greater than ten spans) configurations including the effects of wake roll-up, core size, decay and gusts. Kless *et al.*²⁶ used a vortex propagation model to explore the inviscid effects of vortex positioning, impact of roll-trim penalties, and transonic flow effects on a full aircraft.

The impingement of a trailing vortex on a follower wing can be categorized under the broader classification as a streamwise vortex-body interaction where much of the literature on this topic is well-summarized in the review by Rockwell.²⁷ Much of the past work elaborates on the tendency for a broken-down vortex to elicit a buffeting response on aircraft fins. For instance, Ref. [28] shows mutual interaction between spiral-mode breakdown of the incident vortex and three-dimensional flow separation. Essentially, these works underscore the potential for formation flying to result in unsteady aerodynamics and describe potential outcomes of the vortex-surface interaction. Additionally, long-wavelength (Crow)²⁹ and short-wavelength (elliptical) instabilities that can develop in the trailing vortex are likely to influence buffeting upon interaction with a follower wing.

While all the literature to date provides a significant understanding of the problem at hand, the affluent dynamics associated with trailing vortices are not well-understood in the context of tandem wings. Inviscid and/or unsteady analysis is incapable of accounting for highly important effects that can be elicited in streamwise-oriented vortex encounters. In fact, several studies have shown discrepancies^{19,30–32} between experiment and potential flow solutions attributed to viscous effects. Recent efforts by the authors and colleagues have served to illuminate some of the detailed flow physics associated with streamwise-oriented vortex interactions and changes in the lateral positioning. For instance Barnes *et al.*³³ used numerical simulations of the full, viscous, unsteady Navier-Stokes equations to explore the detailed interaction between wings in a close homogeneous formation. While the presence of an incident vortex significantly impacts the flow structure and provides an aerodynamic benefit, a highly non-linear interaction between the incident and tip vortices was demonstrated to influence the bending moment and impact wake evolution. A congruent study by Garmann and Visbal³⁴ subjected the wing to a much stronger interaction which resulted in wider variation in rolling moment with the lateral position and elicited a helical disruption in the incident vortex.

Further complicating the problem, increasing energy efficiency trends may tend toward higher aspect ratios and lighter-weight wing structures. Thus, an increased flexibility may introduce risk associated with structural response in conjunction with the vortex/surface interaction. The impact of a streamwise-vortex impinging on light-weight, compliant structures is not well-understood and could range from static deformations in the simplest case to more hazardous dynamic response. Therefore, it will be greatly beneficial to explore and understand the coupling between wing deformation, unsteady separation, and vortex feedback of compliant wings in the presence of a streamwise-oriented vortex.

While formation flying involves the interaction of one aircraft traveling in the wake of another, resolving multiple bodies in a high-fidelity computational analysis is computationally expensive and complicates analysis of the global interactions that may occur. Instead, the current paper utilizes a numerically generated streamwise vortex superimposed upstream in order to simplify the otherwise complex problem and clarify fundamental effects that may occur as a result of the streamwise vortex interaction. The focus of the present work is intended to extend the findings of Ref. [33] by subjecting rigid and flexible wings to the vortex investigated in Ref. [34]. A stronger interaction, relevant to a heterogenous formation, is likely to elicit more vibrant aeroelastic effects. Both wing flexibility and vertical positioning of the incident vortex along with their influence on unsteady fluid dynamics are explored in this work. High-fidelity numerical techniques are applied using the extensively validated research code *FDL3DI* coupled with geometrically non-linear mixed Reissner-Mindlin plate elements.

II. Methodology

II.A. Aerodynamics Solver

II.A.1. Governing equations

The full unsteady Navier-Stokes equations are cast in strong conservation form and transferred from Cartesian coordinates (x, y, z, t) in the physical domain to the computation domain in curvilinear coordinates

(ξ, η, ζ, τ) .^{35,36} The system of equations are non-dimensionalized and written in vector form as,

$$\frac{\partial}{\partial \tau} \left(\frac{\mathbf{U}}{J} \right) + \frac{\partial \mathbf{F}_I}{\partial \xi} + \frac{\partial \mathbf{G}_I}{\partial \eta} + \frac{\partial \mathbf{H}_I}{\partial \zeta} = \frac{1}{Re} \left[\frac{\partial \mathbf{F}_v}{\partial \xi} + \frac{\partial \mathbf{G}_v}{\partial \eta} + \frac{\partial \mathbf{H}_v}{\partial \zeta} \right] \quad (1)$$

where the vector of conservative variables is given as

$$\mathbf{U} = \begin{bmatrix} \rho & \rho u & \rho v & \rho w & \rho E \end{bmatrix}^T \quad (2)$$

and $J = \partial(\xi, \eta, \zeta, \tau)/\partial(x, y, z, t)$ is the transformation Jacobian.³⁷

The inviscid flux vectors are given by

$$\mathbf{F}_I = \frac{1}{J} \begin{bmatrix} \rho U \\ \rho u U + \xi_x p \\ \rho v U + \xi_y p \\ \rho w U + \xi_z p \\ (\rho E + p)U - \xi_t p \end{bmatrix}, \mathbf{G}_I = \frac{1}{J} \begin{bmatrix} \rho V \\ \rho u V + \eta_x p \\ \rho v V + \eta_y p \\ \rho w V + \eta_z p \\ (\rho E + p)V - \eta_t p \end{bmatrix}, \mathbf{H}_I = \frac{1}{J} \begin{bmatrix} \rho W \\ \rho u W + \zeta_x p \\ \rho v W + \zeta_y p \\ \rho w W + \zeta_z p \\ (\rho E + p)W - \zeta_t p \end{bmatrix} \quad (3)$$

where

$$\begin{aligned} U &= \xi_t + \xi_x u + \xi_y v + \xi_z w \\ V &= \eta_t + \eta_x u + \eta_y v + \eta_z w \\ W &= \zeta_t + \zeta_x u + \zeta_y v + \zeta_z w \end{aligned} \quad (4)$$

are the contravariant velocities and

$$E = \frac{T}{(\gamma - 1)M_\infty^2} + \frac{1}{2}(u^2 + v^2 + w^2) \quad (5)$$

is the internal energy. Here the quantities u , v , and w are the Cartesian velocity components, ρ is the density, p is pressure, and T is temperature.

The viscous flux vectors are given by

$$\mathbf{F}_v = \frac{1}{J} \begin{bmatrix} 0 \\ \xi_x \tau_{i1} \\ \xi_x \tau_{i2} \\ \xi_x \tau_{i3} \\ \xi_x (u_j \tau_{ij} - \Theta_i) \end{bmatrix}, \mathbf{G}_v = \frac{1}{J} \begin{bmatrix} 0 \\ \eta_x \tau_{i1} \\ \eta_x \tau_{i2} \\ \eta_x \tau_{i3} \\ \eta_x (u_j \tau_{ij} - \Theta_i) \end{bmatrix}, \mathbf{H}_v = \frac{1}{J} \begin{bmatrix} 0 \\ \zeta_x \tau_{i1} \\ \zeta_x \tau_{i2} \\ \zeta_x \tau_{i3} \\ \zeta_x (u_j \tau_{ij} - \Theta_i) \end{bmatrix} \quad (6)$$

in indicial notation where the stress tensor (τ_{ij}) and heat flux vector (Θ_i) are given by

$$\tau_{ij} = \mu \left(\frac{\partial \xi_k}{\partial x_j} \frac{\partial u_i}{\partial \xi_k} + \frac{\partial \xi_k}{\partial x_i} \frac{\partial u_j}{\partial \xi_k} - \frac{2}{3} \delta_{ij} \frac{\partial \xi_l}{\partial x_k} \frac{\partial u_k}{\partial \xi_l} \right) \quad (7)$$

and

$$\Theta_i = - \left[\frac{1}{(\gamma - 1)M_\infty^2} \right] \left(\frac{\mu}{Pr} \right) \frac{\partial \xi_j}{\partial x_i} \frac{\partial T}{\partial \xi_j} \quad (8)$$

Here M_∞ , μ , and γ are the freestream Mach number, dynamic viscosity, and ratio of specific heats respectively. Additionally, Stoke's hypothesis was used for the bulk viscosity coefficient where $\lambda = -2/3\mu$ and the perfect gas relationship $p = \rho T/\gamma M_\infty^2$ was assumed. The Prandtl number (Pr) is chosen as a constant value of $Pr = 0.72$ for air and $M_\infty = 0.1$. Each of the flow variables are scaled by the freestream values except pressure which is non-dimensionalized by $\rho_\infty u_\infty^2$ while length scales are normalized by the chord length. Sutherland's law and the perfect gas law are used to close the Navier-Stokes equations.

The above form of the Navier-Stokes equations is *unfiltered* and used to solve laminar, transitional, and turbulent flow regions without change using an implicit large-eddy (ILES) simulation procedure. The ILES procedure does not require sub-grid-scale (SGS) models or additional heat flux terms required by the standard large-eddy-simulation (LES) approach. Alternatively, a high-order, low-pass Padé-type filter is applied to

the conserved variables of the standard Navier-Stokes equations. This operator is highly-discriminating and selectively damps only the poorly resolved high-frequency content of the solution.^{38,39} The filtering regularization procedure provides an effective alternative to the use of SGS models and has been validated extensively for several canonical turbulent flows. A re-interpretation of this ILES approach in the context of an Approximate Deconvolution Model⁴⁰ has been presented by Mathew *et al.*⁴¹ As the grid resolution increases or Reynolds number decreases, the ILES approach is effectively direct numerical simulation (DNS).

II.A.2. Numerical procedure

The high-order Navier-Stokes solver *FDL3DI* is used for all aerodynamic simulations in the present study.^{42,43} Here, spatial derivatives are discretized using high-order compact-differencing schemes.⁴⁴ The computations in this work utilize a sixth-order stencil. High-order one-sided formulas are used at the boundaries that retain the tri-diagonal form.^{42,43} Derivatives of the inviscid fluxes are obtained by determining the fluxes at the nodal locations and differentiating each component with the compact differencing scheme. Viscous terms are obtained by computing the primitive variable derivatives and then constructing the components of the viscous flux vectors. The components of the viscous fluxes are then differentiated by a second application of the same compact scheme.

In order to eliminate spurious components of the solution, a high-order, low-pass spatial filtering technique^{42,45} is incorporated that is based on templates proposed in Refs. [44] and [46]. With proper choice of coefficients, it provides a $2N^{th}$ -order formula on a $2N + 1$ point stencil. These coefficients, along with representative filter transfer functions, can be found in Refs. [43] and [45]. The filter is applied to the conserved variables along each transformed coordinate direction once after each time step or sub-iteration. An 8th-order filter is used for the interior points in the present work. For the near-boundary points, the filtering strategies described in Refs. [42] and [45] are used. For transitional and turbulent flows, the high-fidelity spatial algorithmic components provide an effective implicit LES approach in place of traditional SGS models, as demonstrated in Refs. [38] and [39] and more recently in Ref. [47].

Finally, time accurate solutions are obtained using the implicit, approximate-factorization of Beam and Warming⁴⁸ including the diagonalization of Pulliam and Chaussee.⁴⁹ Errors can occur due to factorization, linearization, diagonalization, and explicit specification of boundary conditions.⁵⁰ Therefore, temporal accuracy is maintained through the use of Newton-like sub-iterations where three sub-iterations per time step have been found to be sufficient. It will be described later that this sub-iteration process plays an important role in coupling the aerodynamic and structural solutions.

II.B. Structural Dynamics Solver

The structural portion of the aeroelastic simulations is handled using a nonlinear p-version mixed Reissner-Mindlin plate element.⁵¹ Kinematical assumptions are based on Mindlin's hypothesis that fibers normal to the mid-plane remain straight and do not change length. The x , y , and z deflections ($\mathbf{u} = \{u, v, w\}^T$) are given by

$$\begin{aligned} u &= \hat{u} + z \left(\theta - \frac{1}{6} (\theta^3 + \theta \psi^2) \right) \\ v &= \hat{v} + z \left(\psi - \frac{1}{6} (\theta^2 \psi + \psi^3) \right) \\ w &= \hat{w} - \frac{1}{2} z (\theta^2 + \psi^2) \end{aligned} \quad (9)$$

where the values of θ and ψ describe the rotations of fibers normal to the mid-plane and \hat{u} , \hat{v} , and \hat{w} are the components of the mid-plane deflections denoted by \mathbf{u}_m .

The principal of minimum potential energy is applied for the bending and membrane energy while the Hellinger-Reissner principle is used to handle the shear energy. The potential energy functional, including viscous structural damping ($\mathbf{F}_{damp} = c\dot{\mathbf{u}}$), nonconservative surface traction (Φ), body loads (\mathbf{b}), and concentrated forces (\mathbf{F}) can be written as

$$\begin{aligned} \Pi(\mathbf{u}, \mathbf{Q}) &= \int_{\Omega} \left(\frac{1}{2} \boldsymbol{\epsilon}^T \mathbf{N} + \frac{1}{2} \boldsymbol{\kappa}^T \mathbf{M} - \frac{1}{2} \mathbf{Q}^T \mathbf{C}_s^{-1} \mathbf{Q} + \right. \\ &\quad \left. \boldsymbol{\gamma}^T \mathbf{Q} - \mathbf{u}_m^T \mathbf{b} - \mathbf{u}^T \Phi - \mathbf{D}^T \mathbf{F} + \mathbf{u}_m^T h c \dot{\mathbf{u}}_m + \boldsymbol{\Lambda}^T \frac{c h^3}{12} \dot{\boldsymbol{\Lambda}} \right) d\Omega \end{aligned} \quad (10)$$

where the vector $\boldsymbol{\Lambda} = [\theta, \psi, 0]^T$, and \mathbf{D} are the displacements. Shear, bending, and membrane stress resultant vectors are represented by \mathbf{Q} , \mathbf{M} , and \mathbf{N} respectively. The vectors $\boldsymbol{\epsilon}$, $\boldsymbol{\kappa}$, and $\boldsymbol{\gamma}$ correspond to the bending,

membrane, and shear strains respectively. Applying Hamilton's principle to Eqn. 10 results in

$$\int_{t_0}^{t_1} \left[\int_{\Omega} \left(\rho h \delta \mathbf{u}_m^T \ddot{\mathbf{u}}_m + I_p \delta \boldsymbol{\Lambda}^T \ddot{\boldsymbol{\Lambda}} + \delta \boldsymbol{\epsilon}^T \mathbf{N} + \delta \boldsymbol{\kappa}^T \mathbf{M} - \delta \mathbf{Q}^T \mathbf{C}_s^{-1} \mathbf{Q} + \delta \mathbf{Q}^T \boldsymbol{\gamma}^T + \delta \boldsymbol{\gamma}^T \mathbf{Q} \right) d\Omega \right] dt = \int_{t_0}^{t_1} \left[\int_{\Omega} \left(h \delta \mathbf{u}_m^T \mathbf{b} + \delta \mathbf{u}_m^T \Phi + z \delta \boldsymbol{\Lambda}^T \Phi - \delta \mathbf{u}_m^T h c \dot{\mathbf{u}}_m - \delta \boldsymbol{\Lambda}^T \frac{ch^3}{12} \dot{\boldsymbol{\Lambda}} \right) d\Omega + \delta \mathbf{D}^T \mathbf{F} \right] dt \quad (11)$$

A linear relationship between the stress resultants and strain vectors is established through the assumption of a linear isotropic plate in the current work. A mixed element approach is used in the plate element model where the hierarchical shape functions of Szabó and Babuška⁵² are used for displacements and rotations and Legendre polynomials are used to interpolate the shear stress variables.

Second-order time integration of the discrete equation is accomplished using the implicit Hilber-Hughes-Taylor (HHT) method in conjunction with a Newton-Raphson predictor-corrector algorithm resulting in a linear system of equations. This system is solved using a parallel sparse multifrontal solver. The HHT method introduces a small degree of numerical damping in order to facilitate unconditional stability in time integration. Compared to Newmark schemes, HHT damping is better constrained to the higher-frequency modes⁵³ which are of little interest in the current problem. The full Green tensor and a three term approximation of the rotation tensor is used to approximate the bending, membrane, and shear strain vectors as described in Ref. [51]. Further details of the structural element model can be found in Ref. [54].

II.C. Aerodynamic and Structural Coupling

A key part of any aeroelastic computation is an accurate coupling between the fluid and structural components of the model. Aerodynamic forces are passed from the fluid mesh to the structural model while displacements are returned from the structural solver and imposed on the fluid grid. Because the structural and fluid meshes may not necessarily coincide, interpolation between the two is necessary. In the present work, interpolation is accomplished using the finite element shape functions.

Additionally, the aerodynamic mesh must be capable of deforming with the structure. A simple algebraic method presented in Ref. [55] is used to deform the aerodynamic mesh in accordance with the structural deformation. Grid velocities are determined using second order temporal differencing of the position vector as shown in Eqn. 12 below.

$$\frac{\partial \mathbf{x}_j^{n+1}}{\partial t} = \frac{3\mathbf{x}_j^{n+1} - 4\mathbf{x}_j^n + \mathbf{x}_j^{n-1}}{2\Delta t} \quad (12)$$

Furthermore, loose temporal coupling between the aerodynamic and structural models can adversely affect solution integrity.⁵⁶ In order to eliminate this time lag, the two physics models can be implicitly coupled during the sub-iteration procedure. Here, aerodynamic forces and structural displacements are interchanged at each sub-iteration, completely synchronizing both models and preserving second order temporal accuracy.

III. Details of the computations

III.A. Geometric and vortex definitions

Previously,³³ the influence of streamwise-oriented vortices was investigated in the context of a homogeneous formation for aspect-ratio $AR = 6$ wings at a $\alpha = 5^\circ$ angle of attack and chord-based Reynolds number of $Re_c = 30,000$. This article extends the previous work by exploring the interaction with stronger vortical features that may occur in heterogeneous formations while maintaining the same operating conditions for the follower wing. In this case, the leader-wing trailing vortex is created by imposing a Batchelor or q-vortex⁵⁷ upstream as shown in Fig. 1. This vortex is described analytically in cylindrical coordinates by defining the radial, circumferential, and axial velocities as

$$u_r(r) = 0 \quad (13)$$

$$u_\theta(r) = \frac{q_0 \Delta u}{r/r_0} \left(1 - e^{-(r/r_0)^2} \right) \quad (14)$$

$$u_x(r) = 1 - \Delta u e^{-(r/r_0)^2} \quad (15)$$

respectively where r_0 is a measure of the vortex radius, Δu is the maximum axial velocity deficit, and q_0 is the initial swirl parameter defined by

$$q_0 \approx 1.567V_0/\Delta u \quad (16)$$

where V_0 is the maximum tangential velocity. For the cases explored in this article, the initial swirl is chosen to be $q_0 = 2$ and the axial velocity deficit is $\Delta u = 0.4U_\infty$ resulting in a maximum circumferential velocity of $V_0 \approx 0.5U_\infty$. A similar vortex definition was successfully applied by Garmann and Visbal³⁴ at a lower Reynolds number and angle of attack for a rigid wing.

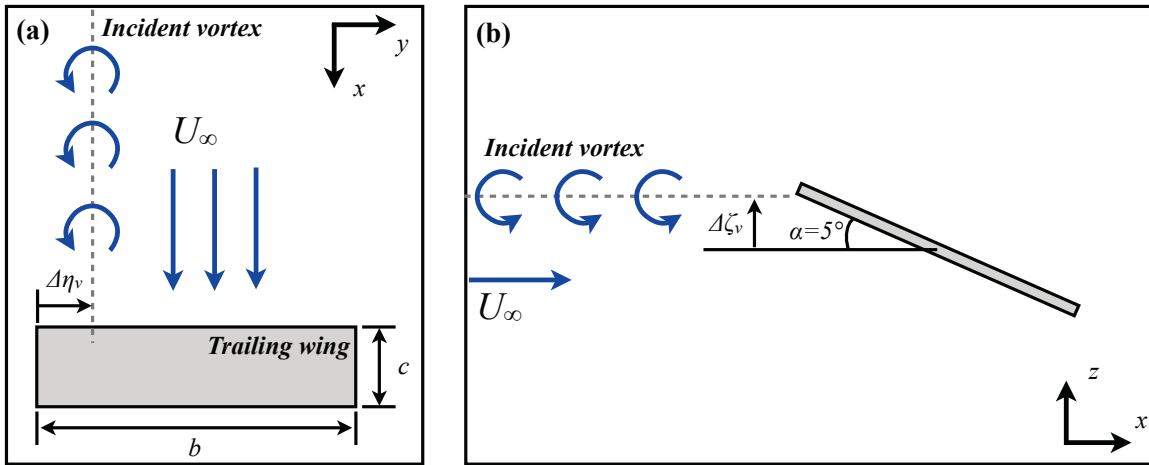


Figure 1: Configuration for streamwise-oriented vortex impingement; (a) top view, (b) side view

There are a number of benefits motivating the choice of using a numerically generated vortex in the present study. Namely, this approach provides greater control of the vortex size, strength, and positioning and is more feasible for parametric exploration. Secondly, isolating the vortex from other wake structures will help to clarify the complex unsteady effects that may result from a wing interacting with a trailing vortex. For reference, Fig. 2 depicts velocity profiles for the current and previous works³³ as a point of comparison. A q-vortex using values for q_0 , Δu , and r_0 obtained from Ref. [33] is also shown and demonstrates this vortex definition is fairly representative of the trailing vortex generated in the case of tandem wings.

As in Ref [33], the wing in this case is a rectangular flat plate with squared-off corners, aspect-ratio of $AR = 6$, and thickness of $t/c = 0.03$ operating at a $\alpha = 5^\circ$ angle of attack and Reynolds number of $Re_c = 30,000$. The positioning of the vortex is described by the parameters $\Delta\eta_v$, shown in Fig. 1(a), which defines the lateral positioning relative to the ‘inboard’ wingtip and $\Delta\zeta_v$, shown in Fig. 1(b), which describes the vertical positioning relative to the midchord. Both of these quantities are non-dimensional with respect to the chord length. While lateral positioning of the incident vortex was explored in previous works,^{33,34} vertical positioning will be investigated in greater detail. Every case presented in this paper uses a lateral position of $\Delta\eta_v = 0.25$ for the incident vortex while $\Delta\zeta_v$ varies from -0.25 to $+0.1$.

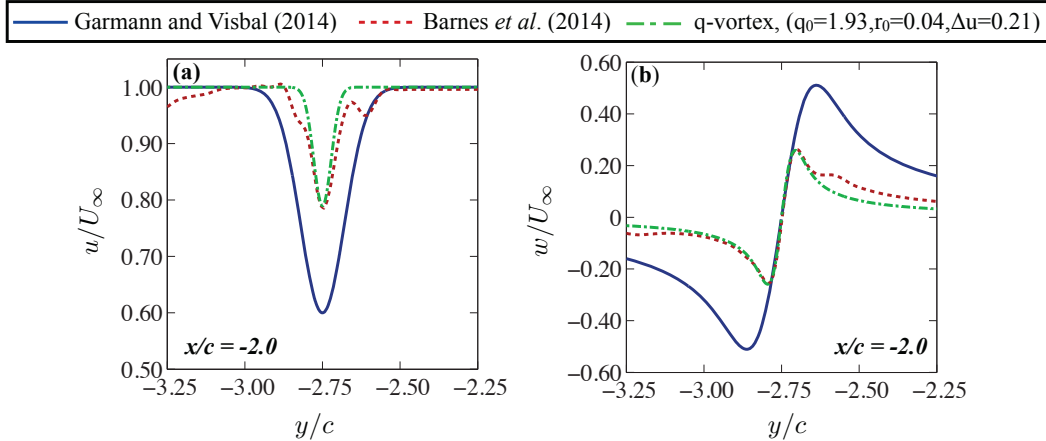


Figure 2: Time-mean (a) streamwise and (b) tangential velocity profiles for the current³⁴ and previous³³ vortices compared with a q-vortex similar to the trailing vortex in Ref.[33].

III.B. Computational mesh and boundary conditions

In order to facilitate efficient use of computational resources for the current large-aspect-ratio wing case, a nested grid configuration is convenient to efficiently discretize the computational domain. This topology, which is demonstrated in Fig. 3, consists of 16 total grids in order to properly model the detailed fluid physics in the region of interest and preserve the incident vortex generated at the boundary. The first set of blocks consists of a series of nearfield grids which wrap around the wing surface depicted by the dark red region in Fig. 3 and is designed to resolve the transitional flow structure near the wing body. The near-wing grid system is composed of leading-edge, trailing-edge, upper, lower and two tip grid regions. The described multiple grid configuration is applied in order to accommodate high-order stencils at the squared-off corners of the flat plate wing and includes a four-point coincident overlap between adjacent meshes eliminating the need for high-order interpolation within this set.

An additional block serves to preserve the incident vortex as it propagates from the farfield boundary where it is generated, shown in Fig. 3 in gray. This region is constructed using the same point distribution as the nearfield group. Finally, each of these blocks is wrapped in a farfield system which is coarsened to roughly 2/3 the number of points as that of the nearfield and vortex meshes and rapidly stretched to the farfield boundary. Communication between the farfield and nearfield groups is non-coincident and therefore Chimera overset⁵⁸ methodology with high-order interpolation⁵⁹ is employed. Grid point clustering is maintained in the farfield blocks in order to minimize volume ratios in the overlap regions. Modifications to the spacing parameters $\Delta\eta_v$ and $\Delta\zeta_v$ can be made by simply shifting the vortex grid position while changes in angle of attack can be accomplished through a local grid deformation in the nearfield group.

Boundary conditions for the described configuration are applied in the following manner. The solid boundaries at the wing surfaces employ a no slip condition where surface velocities are imposed at the corresponding surface grid points. In addition, third-order adiabatic ($\partial T/\partial n = 0$) and zero normal pressure gradient ($\partial P/\partial n = 0$) conditions are applied. The freestream velocity and incoming vortex are imposed on the upstream farfield boundary with first-order extrapolation of pressure. All other farfield boundaries employ first-order extrapolation of the primitive variables with the exception of pressure which is set to the free stream value. In addition to the described farfield conditions, the high-order, low-pass filter is used in conjunction with rapidly stretching the mesh outside the region of interest which serves as a buffer for spurious reflections. Energy not supported as the mesh expands is reflected in the form of high-frequency modes which are eliminated by the highly discriminating filter in a manner similar to that described in Ref. [60].

The finite element mesh used for the structural portion of the computations, shown in Fig. 4, is comprised of a two-dimensional plate model located at the wing midplane where all elements are uniformly spaced. Boundary conditions for the structural model consist of constraining all degrees of freedom for element nodes along the wing midspan. This approach is intended to model fixed-free wings mounted to an aircraft body.

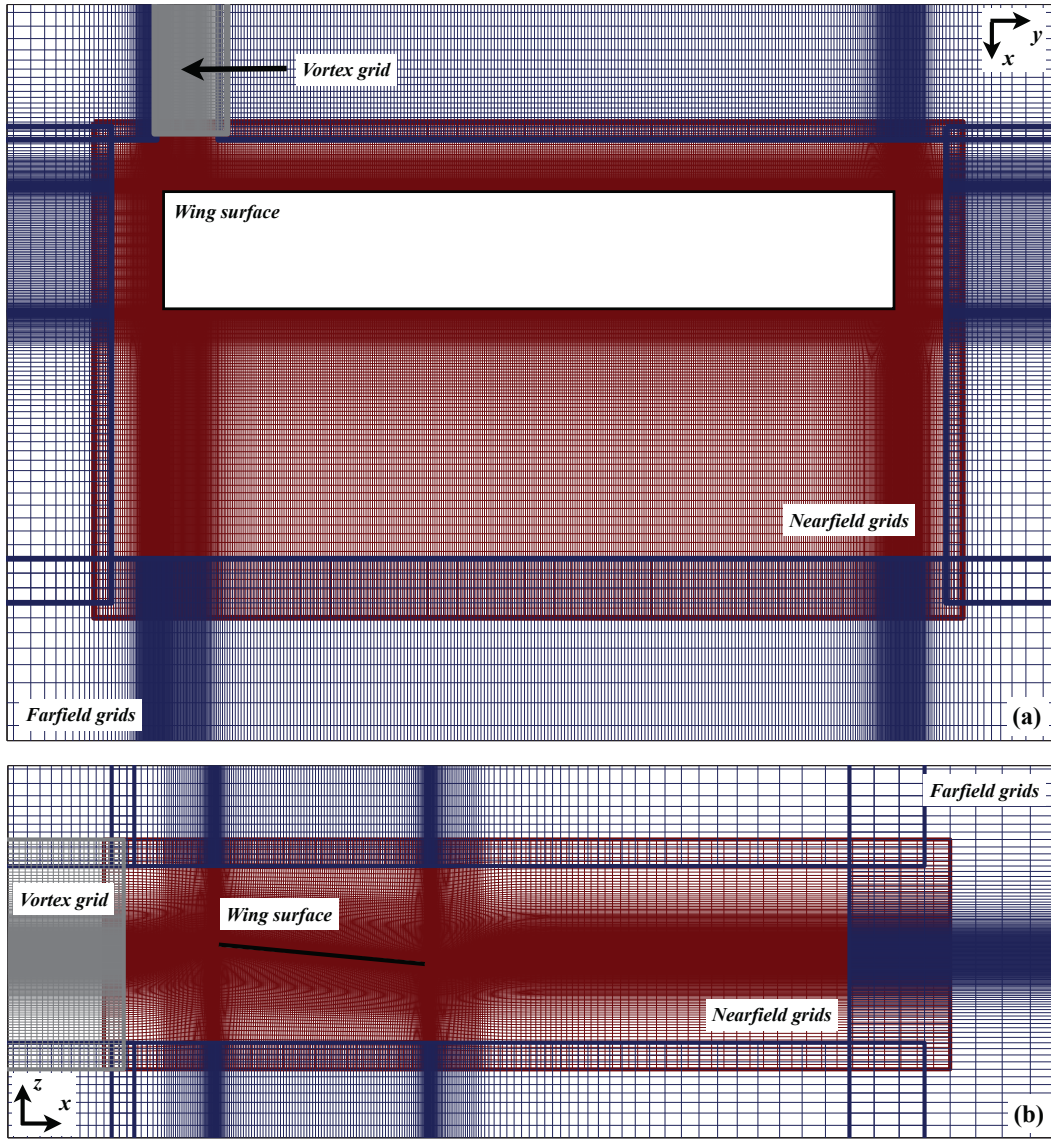


Figure 3: Overset multi-wing grid system used where (a) shows a top-view and (b) portrays a sideview.

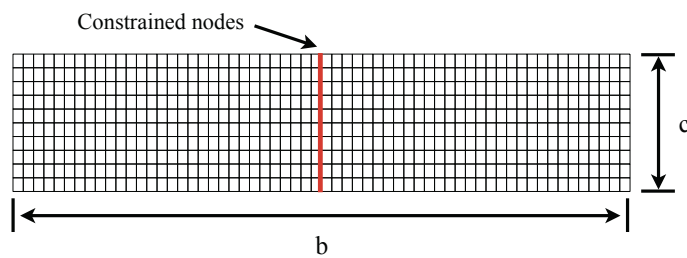


Figure 4: Structural element grid

IV. Results

Each of the rigid cases presented were initially run for 20 convective times allowing for the elimination of startup transients and the propagation of the incident vortex past the wing. The computations were then run for an additional $\tau = 10$ convective times allowing for the collection of time-mean and statistical quantities. Each of the aeroelastic computations were initialized from the previously completed rigid cases and run for an additional $\tau = 20$ in order for the flow field to return to an equilibrium state and provide sufficient temporal resolution for the collection of turbulence statistics. Each of the simulations presented utilizes a nondimensional time step of $\Delta\tau = 0.0001$ in order to provide sufficient temporal resolution for the fine-scale flow structure.

IV.A. Effect of grid resolution

In order to evaluate the effect of grid resolution, computations were performed on several grids for the baseline rigid case ($\Delta\eta_v = 0.25$, $\Delta\zeta_v = 0.0$). Both coarsened and refined versions of the baseline mesh system described in the previous section were constructed and presented here for comparison. Relevant dimensions of each grid system are given in Table 1 and Table 2 provides the time-mean aerodynamic loads. Observation of the time-averaged lift, drag, and moment coefficients demonstrates little change between any given levels of resolution with the exception of rolling moment. These results portray excellent agreement between the two finest grids. Convergence of these integrated quantities with increasing refinement provides confidence in the resolution of the present computations.

Figures 5(a) and (b) portray streamwise and vertical velocity profiles across the vortex core respectively upstream of the wing leading-edge. All grids produce indistinguishable results demonstrating the capability of the current grid system to preserve the streamwise vortex integrity. As with the integrated time-mean forces an excellent agreement between all cases demonstrates the incident vortex is preserved for each grid. Additionally, the instantaneous and time-mean flow structure of the vortex encounter for each mesh is shown in Figs. 5(c) and (d) respectively using an iso-surface of Q-criterion.⁶¹ This parameter is defined by the second invariant of the velocity gradient tensor where a positive value indicates that rotation dominates strain and shear. Here, the same qualitative behavior is observed for all three cases demonstrating independence of general flow structure to successive refinement. Observation of the selected quantities relevant to the current study demonstrates exceptional confidence in solutions for the *mid* level grid which is used in all subsequent computations.

Finally, the effect of grid resolution on the structural model was evaluated by separately loading the finite element mesh using the time-mean surface forces from the baseline fluid mesh and observing the static deflection. In this case, the time-mean surface loads were interpolated to the structural model using the same methodology described for the aeroelastic solution procedure and the resulting deformation and surface loading is depicted in Fig. 6(a). Three structural meshes with uniformly spaced elements were investigated in this section and dimensions for each are shown in Table 3. Nodal vertical deflections are recorded for both the inboard and outboard wingtips taken at the midchord in Table 4. Additionally, grid work is computed for the three cases which is defined here as the summation of the dot product of nodal deflections and loads, $W_{grid} = \sum_i (\mathbf{u}_m \cdot \mathbf{R})_i$. This calculation provides an integrated value for evaluation of deformations on the entire structural model. For each quantity presented differences between successive levels of refinement are on the order of 0.01%.

Additionally, the structural mesh dynamics were evaluated by subjecting the plate to an initial vertical acceleration as shown in Fig. 6(b) using the same time step of the aeroelastic analysis in order to elicit and compare the first bending and twisting modes of deformation. The frequency spectra of bending and twisting deformations at the wingtip, shown in Fig. 6(c), demonstrates that identical frequencies are predicted by each mesh. Therefore, the *coarse* structural mesh was deemed sufficient for use in the aeroelastic computations. It should be noted that frequencies depicted for this isolated case are not likely to be representative of those experienced in a coupled fluid-structure interaction in which the wing may experience viscous damping due external loading.

Table 1: Grid refinement details

Grid	Num. points	Δz_s	$\Delta x_{s,max}$	$\Delta y_{s,max}$	C_D	C_L	$C_{M,y(c/4)}$	$C_{M,x}$
Coarse	30,180,770	1.90×10^{-4}	0.82×10^{-2}	2.55×10^{-2}	0.093	0.653	-0.063	-0.131
Mid	59,671,456	1.51×10^{-4}	0.90×10^{-2}	2.02×10^{-2}	0.091	0.631	-0.045	-0.136
Fine	88,859,180	1.32×10^{-4}	1.04×10^{-2}	1.76×10^{-2}	0.090	0.633	-0.045	-0.140

Table 2: Lead-wing time-averaged forces

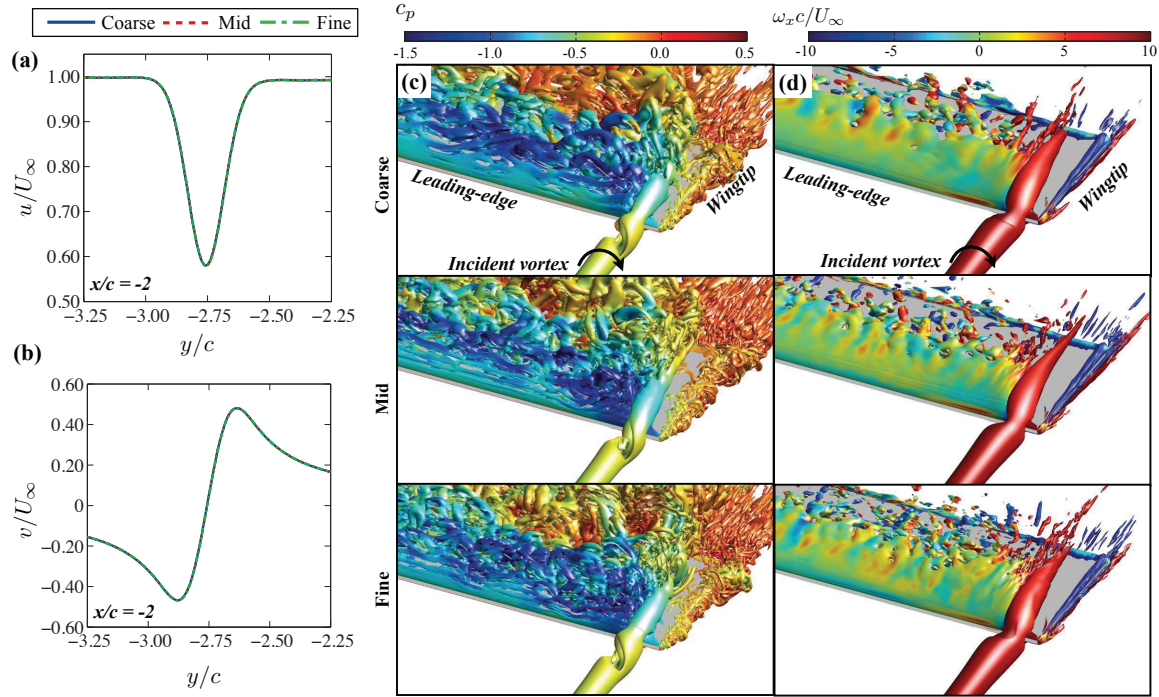


Figure 5: Effects of grid resolution for a (a) streamwise velocity and (b) tangential velocity across the vortex core, (c) iso-surface of instantaneous Q-criterion, and (d) iso-surface of time-averaged Q-criterion ($Q = 5$) for a vortex/rigid wing interaction

Table 3: Structural mesh dimensions

Grid	Dimensions	Grid size
Coarse	10×60	600
Mid	14×86	1204
Fine	20×120	2400

Table 4: Wing tip deflections and grid work

Grid	\hat{w}_{outer}/c	\hat{w}_{inner}/c	$W_{grid}[N \cdot m]$
Coarse	4.661×10^{-2}	6.630×10^{-2}	4.781×10^{-3}
Mid	4.661×10^{-2}	6.631×10^{-2}	4.782×10^{-3}
Fine	4.662×10^{-2}	6.632×10^{-2}	4.783×10^{-3}

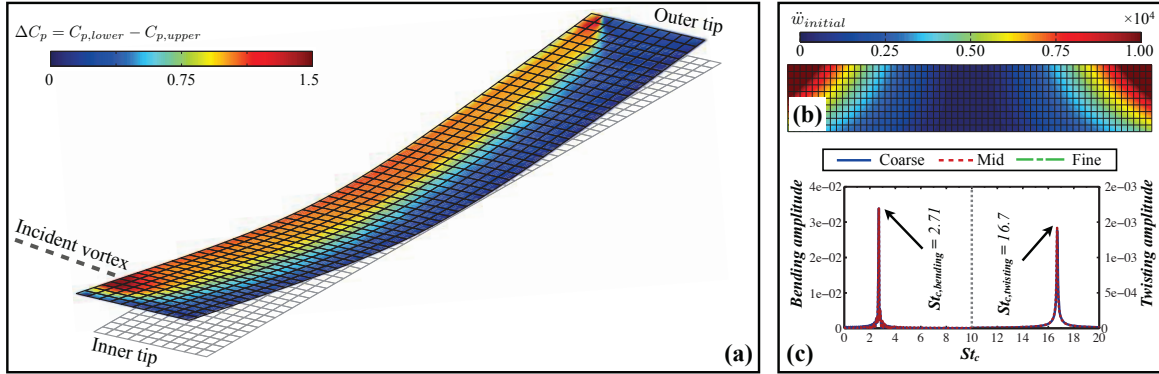


Figure 6: (a) Surface pressure difference contours on the deformed coarse structural mesh. Deformations are exaggerated for visualization purposes, (b) initial acceleration for dynamic analysis, and (c) Fourier analysis of bending and twisting deformations

IV.B. Effect of flexibility

In this section the influence of the described vortex, positioned at $\Delta\zeta_v = 0.0$, is evaluated on wings with specified levels of flexibility and compared to a rigid wing. Two compliant wings are evaluated where the *flexible* structure has an elastic modulus of $E = 69[MPa]$ and the *highly flexible* wing is half the nominal value, $E = 34.5[MPa]$. The density, poisson's ratio, and thickness of both these plate models are chosen to be $\rho_s = 2700[kg/m^3]$, $\nu = 0.30$, and $t/c = 0.01$ respectively. Finally, the characteristic length was defined as $c = 0.1[m]$. For reference, the flexible wing is representative of a thin aluminum plate. These particular choices are both tractable for LES computations and reproducible in ongoing experimental studies. Figure 7 provides notation that will be used throughout this section, namely the convention of referring to the vortex encounter side of the wing as the 'inboard wingtip' and the opposite side as the 'outboard wingtip'.

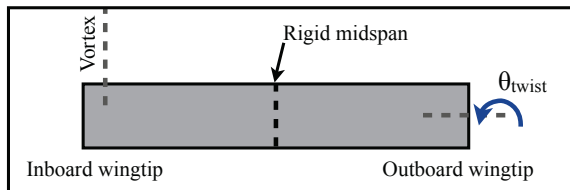


Figure 7: General notation for flexible cases

IV.B.1. Compliant wing deformations

The wing deformations are explored in this section in order to provide insight into the influence of a streamwise-oriented vortex on the dynamics of the flexible structures. A time-history of vertical displacements at the wingtip midchords is depicted in Fig. 8(a) over ten convective times. For both the flexible and highly flexible cases the inboard wingtip (vortex-encounter side) exhibits a pronounced dynamic response compared to the essentially static displacements at the outboard wingtip. Fourier analysis of the spanwise bending deformations, shown in Fig. 8(b) clarifies the dominant frequency components for each case. For the highly flexible wing, a single clearly defined frequency is elucidated at a non-dimensional frequency of $St_c = fc/U_\infty = 0.46$ whereas the flexible wing exhibits two additional values of $St_c = 0.91$ and 0.23 which are essentially harmonics and sub-harmonics respectively of the single frequency observed for the highly flexible wing.

A time-history of twisting deformations at both wingtips is provided in Fig. 8(c) in which the flexible and highly flexible wings demonstrate small amplitude high-frequency components and larger-amplitude low-frequency components of twisting on the inboard side. The larger-amplitude frequencies of the twisting deformations, computed using Fourier analysis of the twisting deformations shown in Fig. 8(d), directly correspond to those observed for the bending deformations at $St_c = 0.46$ indicating the dynamic response

is largely driven by unsteadiness in the flow field rather than excitation of structural modes. An additional higher dominant frequency of $St = 4.43$ is observed on the outboard wingtip for the flexible wing and consistent with those observed by Barnes *et al.*³³ As in the previous work, these oscillations appear to be a coupling between shear-layer instabilities on the lower outboard surface which are largely suppressed by the upwash from the incident vortex on the inboard side.

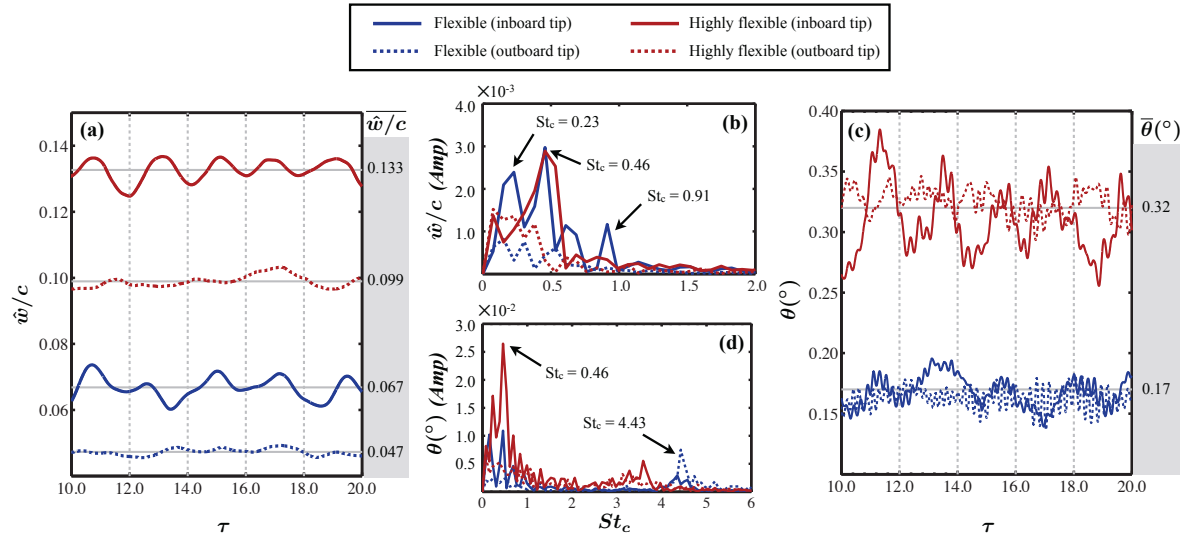


Figure 8: (a) Time-history of wingtip deformations, (b) Fourier analysis of wingtip deformations, (c) wingtip twisting time-history, and (d) Fourier analysis of wingtip twisting

IV.B.2. Flow structure

An iso-surface of instantaneous Q-criterion is shown for each of the rigid, flexible, and highly flexible wings in Fig. 9. For the *rigid* case, the incident vortex is positioned inline with the wing mid chord, $\Delta\zeta_v = 0.0$, but tends upward with flow acceleration over the leading-edge as it approaches the wing and impinges on the leading-edge. A helical instability in the vortex core is observed to occur upstream of the leading-edge which spirals in a sense opposite the rotation of the vortical flow indicative of hydrodynamic instability. Observation of the instantaneous flow reveals that this spiraling instability alternates between the upper and lower surfaces contributing to streamwise vortical components on both sides of the wing. These contributions appear as a bifurcated vortex in the time-mean flow shown in Fig. 10. The rigid case, to be discussed in greater detail later, is comparable to the similar computations presented by Garman and Visbal.³⁴ However, spiraling instabilities in the current work are more pronounced compared to the former due to the higher angle of attack and Reynolds exacerbating the underlying mechanisms that induce these instabilities. Interestingly, the dominant frequency of the spiral instability for the rigid case is approximately $St_c = 0.98$ —roughly double the frequency observed in the structural response.

The *flexible* wing, in which the inboard wingtip oscillates about a time-mean vertical deflection of $\hat{w} = 0.07c$, places the incident vortex predominantly on the pressure-side. Consequently, the spiraling instability spends more time along the pressure surface of the wing which is reflected in the time-mean iso-surface of Q-criterion in Fig. 10. It can also be noted that the instability in the vortex core is more pronounced in this case and begins further upstream indicating wing compliance promotes the instability of the incident vortex. Furthermore, a secondary spiraling vortical structure appears in the instantaneous Q-criterion iso-surfaces indicative of higher-mode helical instability. Beneath the wing, Fig. 9(b), the two spirals wind about each other and result in a complex interaction with the wing surface.

A further decrease in structural rigidity, as in the case of the *highly flexible* wing, results in a $\hat{w} = 0.13c$ time-mean vertical deflection of the inboard wingtip placing the incident vortex further below the leading-edge. The instabilities described in the previous cases advance further upstream and become more pronounced as reflected in Fig. 9. In fact, the secondary spiral is more obvious in this case. In the time-mean flow of Fig. 10 the upper surface component of the bifurcation is significantly diminished.

Although the form of the spiraling behavior for each wing appears much like spiral-breakdown of longitudinal vortices, it is not breakdown in the strict sense defined by Leibovich.⁶² Namely, flow reversal is absent and no stagnation points develop in the vortex core. Rather, the unsteady behavior is driven by hydrodynamic instabilities directly as a consequence of interaction with the wing. Clearly, the present analysis captures a significant influence of flexibility on the unsteady fluid dynamics in a streamwise-oriented vortex encounter. Two aspects of the aeroelastic response can contribute to this pronounced influence on the incident vortex. First, the time-mean spanwise bending deflection of the inboard wingtip effectively repositions the incident vortex relative to the wing surface, shown in Fig. 11, which could result in a very different vortex-surface interaction. Secondly, the small-amplitude low-frequency oscillations of the dynamic response have the potential to produce a feedback effect on the incident vortex. For instance, Gursul and Xie⁶³ demonstrated the breakdown of a leading-edge vortex over a delta wing can be particularly sensitive to lower-frequency oscillations of a fin. Uncertainty as to which of these two aspects dominates in the present flow motivates the evaluation of several vertical positions of the incident vortex on a rigid wing and presented in a later section of this article. This analysis will help to decouple the upstream influence of static bending and dynamic response.

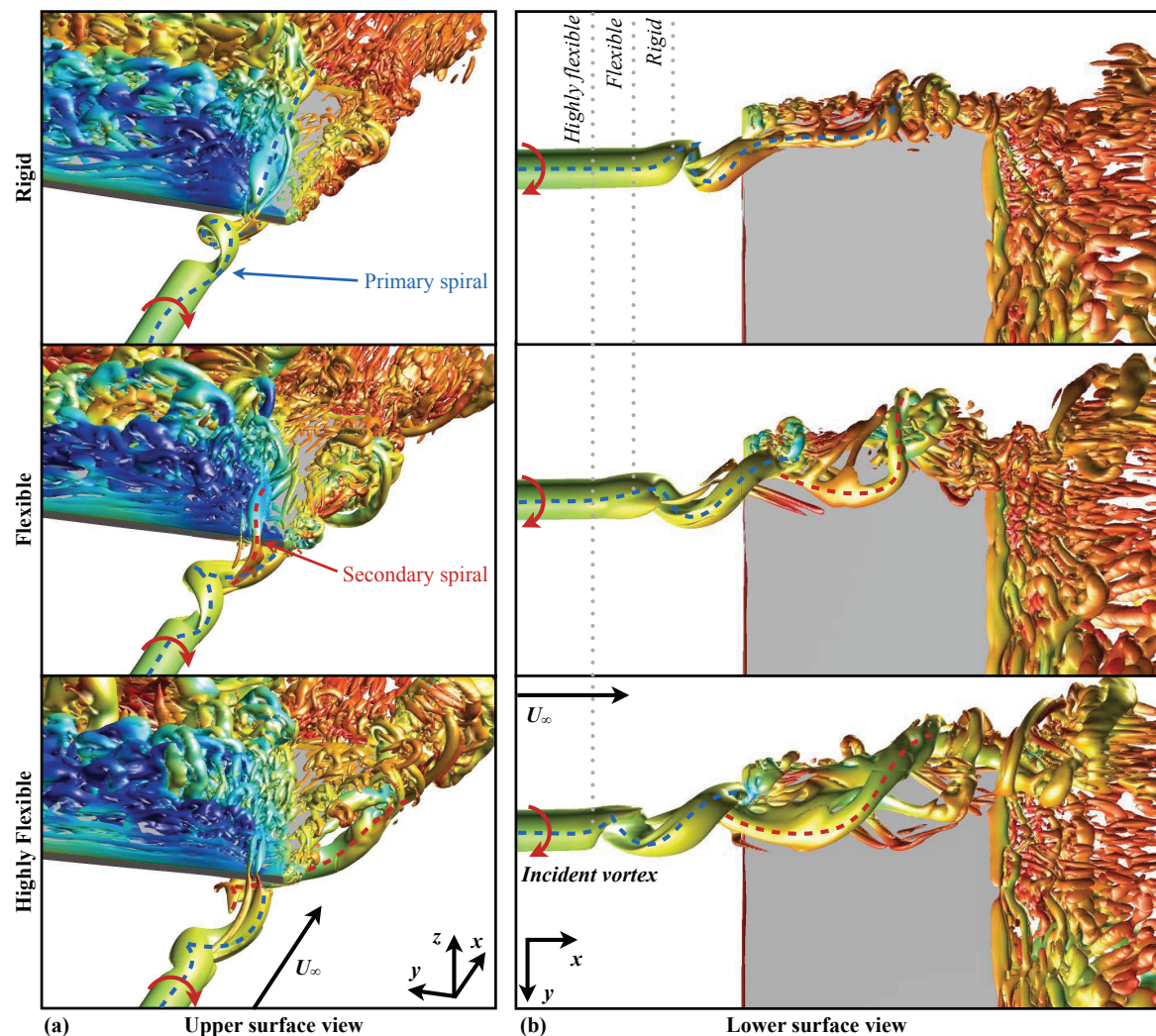


Figure 9: Iso-surfaces of instantaneous Q-criterion for rigid and flexible wings ($Q = 15$). Dotted lines roughly locate the beginning of instability

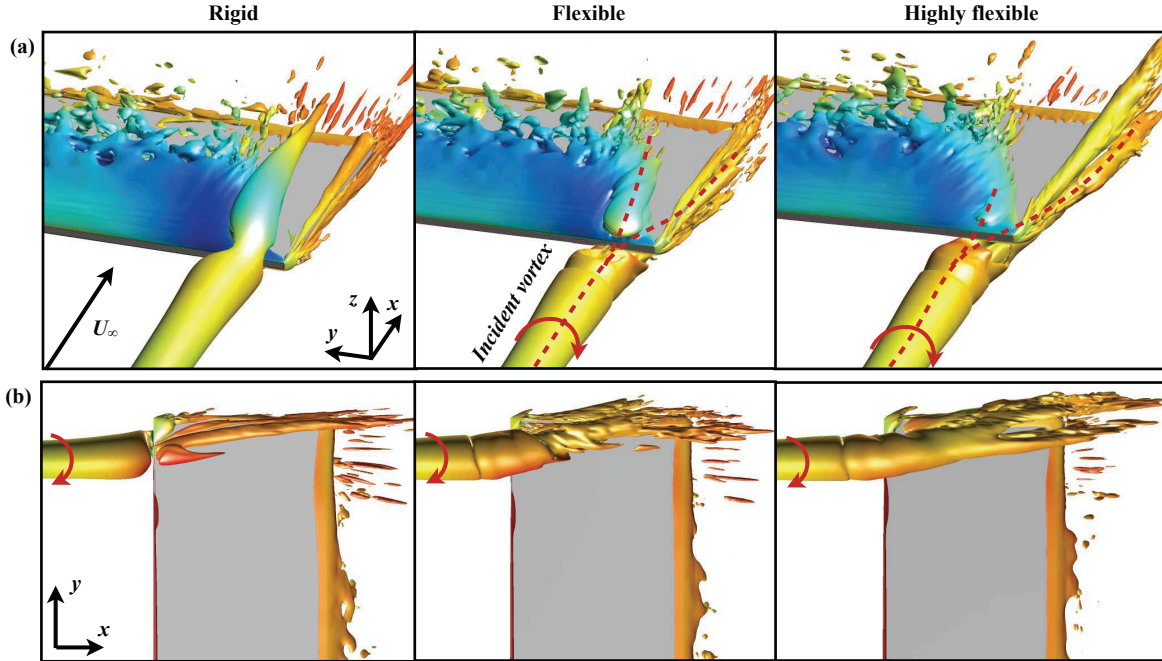


Figure 10: Iso-surfaces of time-mean Q-criterion for rigid and flexible wings ($Q = 5$) where (a) shows a top view and (b) portrays a bottom view

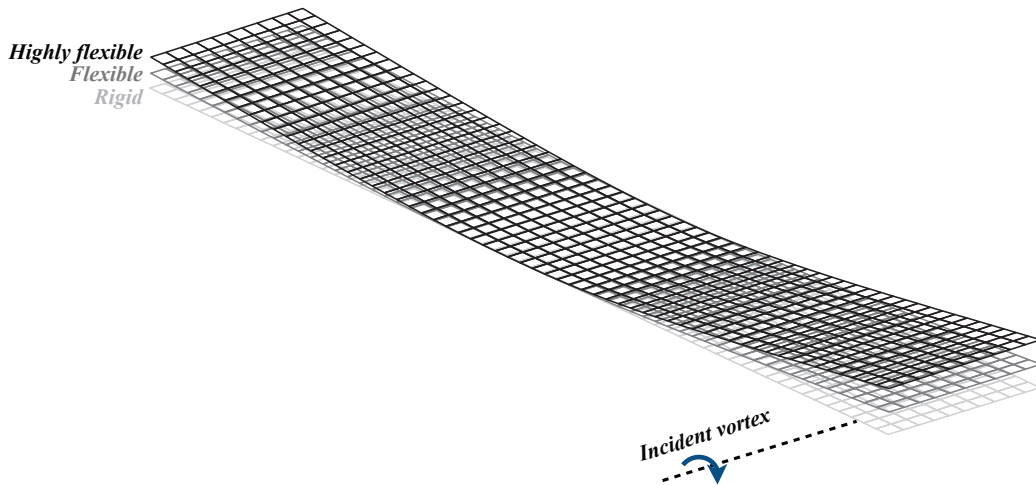


Figure 11: Position of incident vortex relative to rigid and flexible wings where time-mean deformations are exaggerated by a factor of $\times 2$ for clarity

IV.B.3. Aerodynamic loads

The time-mean aerodynamic loads for the rigid, flexible, and highly flexible cases are provided in Table 5 and compared to an identical wing without an incident vortex. An enhanced lift and lift-to-drag ratio compared to the isolated wing is apparent in all three cases. However, the benefit decreases with increasing flexibility. This effect can be explained by two factors. First, spanwise bending reorients the wing such that forces normal to the surface result in a small side force component effectively diminishing the contribution to lift. Secondly, moving the vortex away from the wing surface is likely to have an influence on the aerodynamic benefits. The lift coefficient per unit length is plotted along the span length in Fig 12(a). As can be expected,

a significant enhancement in the lift coefficient is observed along the span compared to lift distribution of the isolated wing. Additionally, a locally enhanced region of lift appears just inboard from the incident vortex related to strengthened recirculation on the upper surface and strong upwash from the incident vortex for the rigid case. This effect is absent for the flexible wings due to diminished swirl on the upper surface as a consequence of the vertical offset induced by the time-mean spanwise bending.

Observation of the rolling moment coefficient, C_{M_x} , demonstrates the tendency for the asymmetrical lift distribution to produce a significant rolling moment which is highest for the flexible wing. Most notably, the mean-squared fluctuations of rolling moment indicate unsteady loading in the flexible case is much stronger than that found for the rigid and highly flexible wings. Two possible sources help to explain this increased level of unsteadiness. The first is non-circulatory forces related to acceleration of the dynamically bending wing. Secondly, the vertical positioning of the incident vortex can be expected to influence the unsteady loading which may be most pronounced for the specific displacement provided by the flexible wing. Clearly, flexibility can elicit strong unsteady loading which would have serious implications for the fatigue-life of aerodynamic structures.

Finally, Fourier analysis of the unsteady loading, Fig. 12(b), demonstrates several dominant frequencies of interest. First, the frequency spectra for all values portrays a clearly defined peak at $St_c = 0.46$ for the rigid and flexible wings and an additional lower frequency of $St_c = 0.23$ for the flexible wing in the rolling moment which directly corresponds to the fluctuations previously observed in the bending deformations.

Table 5: Time-mean aerodynamic loads for rigid and flexible wings

	C_D		C_L		L/D		C_{M_x}		$C_{M_{x,rms}}$	
	Value	% diff.	Value	% diff.	Value	% diff.	Value		Value	
No vortex (rigid)	0.077	-	0.433	-	5.65	-	0.002	9.8×10^{-3}		
Rigid	0.091	+17.8%	0.631	+45.7%	6.96	+23.7%	-0.136	12.9×10^{-3}		
Flexible	0.092	+19.6%	0.637	+47.2%	6.92	+23.1%	-0.140	22.3×10^{-3}		
Highly flexible	0.094	+22.6%	0.651	+50.3%	6.89	+22.6%	-0.125	12.1×10^{-3}		

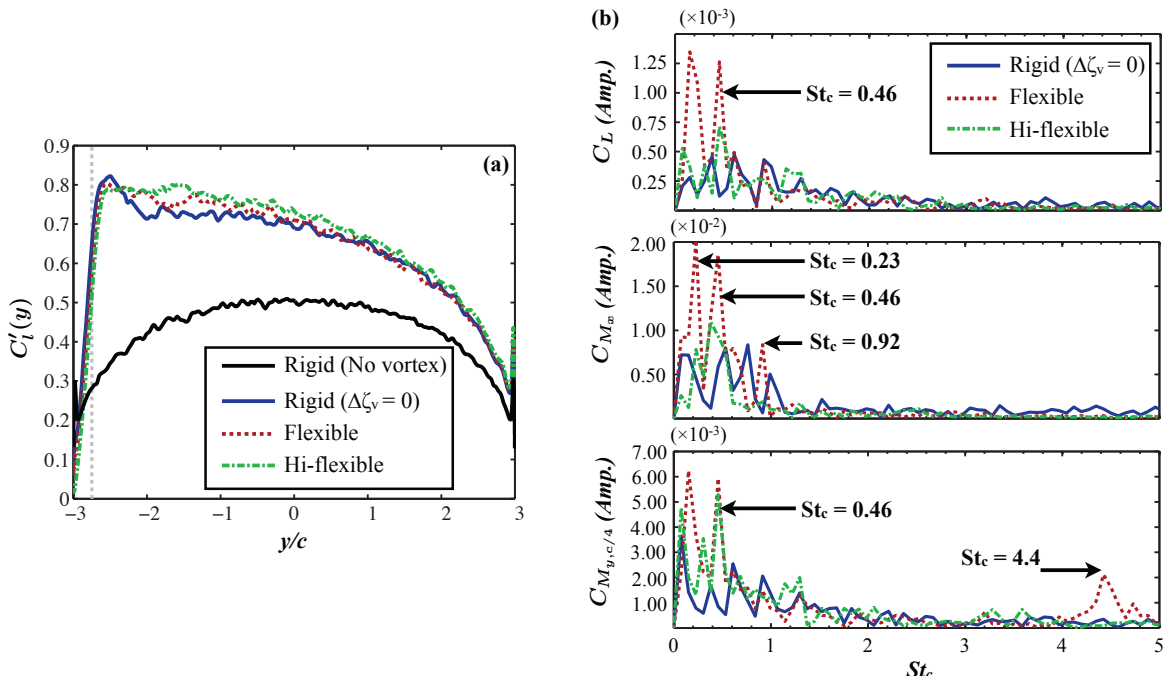


Figure 12: (a) Time-mean lift coefficient per unit span and (b) Fourier analysis of aerodynamic loads for rigid and flexible wings

IV.C. Effect of vertical positioning on rigid wings

A previous detailed numerical analysis on streamwise-vortex interactions with a wing under similar conditions³⁴ investigated the interaction of the current vortex definition for several *lateral* positions. Qualitatively, many of the behaviors between the previous and present cases are remarkably similar particularly in the time-mean flow and are well described in the antecedent work. Complimenting the previous article, this section explores several *vertical* positions, Fig. 13(a), of the incident vortex on a *rigid* wing and focuses on the changes to the baseline flow topology imposed by vertical positioning. The goal of this evaluation is two-fold. First, it separates the static and dynamic aeroelastic effects of the flexible cases and secondly provides further understanding on the effect of vortex positioning and vortex-surface interaction. It should be noted that in the baseline rigid case, $\Delta\eta_v = -0.25$ $\Delta\zeta_v = 0$, the spiraling disruptions in the vortex observed by Garmann and Visbal³⁴ have evolved into a helical instability as a result of the higher Reynolds number and angle of attack. Some of the mechanisms influencing this instability are addressed in the following discussion.

Figures 13(b) and (c) portray several views of the instantaneous flow structure using an iso-surface of Q-criterion at several vertical positions. Compared to the baseline $\Delta\zeta_v = 0.0$ case, placing the incident vortex beneath the wing, as in $\Delta\zeta_v = -0.1$, demonstrates advanced instability in the vortex core remarkably similar in nature to that observed for the highly flexible wing. Notable similarities in the flow structure include the appearance of both a primary and secondary spiral and an upstream advancement in the onset of the helical instability. In order to provide a more direct comparison, Fig. 15 shows a snapshot of the instantaneous flow structure along the lower surface for both the *rigid* $\Delta\zeta_v = -0.1$ and *highly flexible* $\Delta\zeta_v = 0.0$ cases at a comparable instant in time. The $\hat{w}/c = 0.13$ time-mean vertical deflection of the highly flexible wing is comparable to the vertical offset of $\Delta\zeta_v = -0.1$. Both the flow structure and onset of helical instability are markedly similar demonstrating the relative positioning of the vortex is the primary destabilizing mechanism in the aeroelastic cases rather than dynamic feedback from wing oscillations. Vertical offset demonstrates a tendency to influence the stability of the incident vortex and hence the unsteady fluid dynamics and loading. In a time-mean sense, an iso-surface of Q-criterion, shown in Fig. 14, portrays a diminished upper surface component of the time-mean bifurcation and an expansion of the incident vortex as it approaches the leading-edge associated with unsteadiness in the vortex core.

Remarkably, moving the incident vortex upward to $\Delta\zeta_v = +0.1$ elicits a completely different behavior in which the vortex, now primarily traversing the suction-surface, tends to maintain its coherency. Indeed, the structure of the time-mean flow is, as depicted in Fig. 14, markedly comparable to the instantaneous over the front section of the wing. This observation further supports the thesis that vertical positioning can have significant influence on the general unsteadiness in streamwise vortex interactions. Moving toward the trailing-edge, the laminar vortex begins to exhibit transitional features in the instantaneous flow denoted by (1) in Fig. 13(b).

Statistical data was collected in the shear layer off the lower surface of the wing and in line with the incident vortex at the mid chord shown in Fig. 16(a). Frequency spectra of pressure fluctuations are shown in Fig. 16(b) which portray the dominant frequencies in the unstable vortex. For both $\Delta\zeta_v = 0.0$ and -0.1 the dominant frequency is near $St_c \approx 1$ corresponding with fluctuations of the primary spiral observed in instantaneous frames of motion. Additional clearly defined peaks are observed for both cases at harmonics of the fundamental frequency indicating higher modes of hydrodynamic instability not clearly portrayed in the discussion so far. Detailed analysis of the complex instabilities implied by frequency spectra will be left for future analysis.

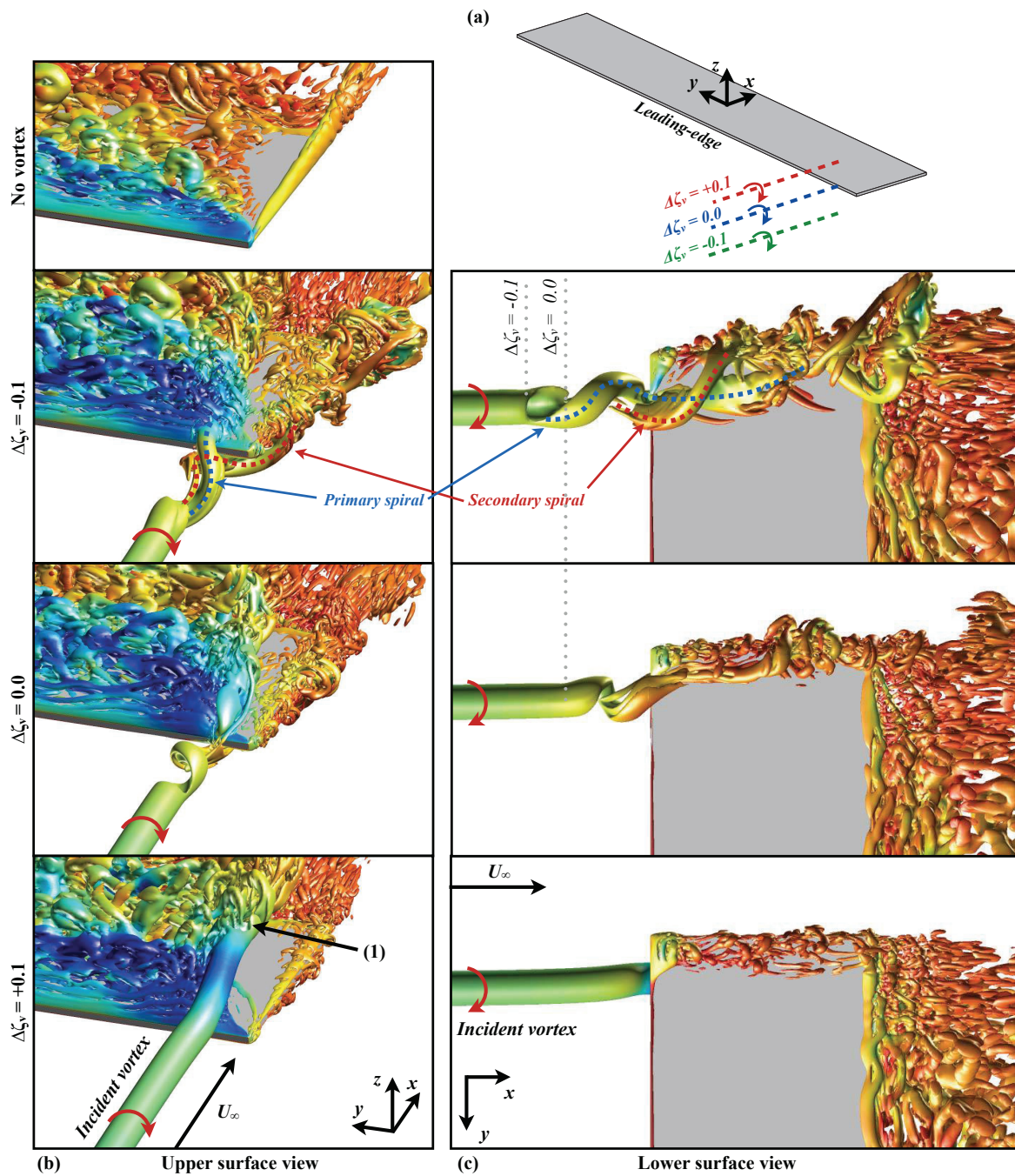


Figure 13: Iso-surfaces of instantaneous Q-criterion for no vortex and several vertical positions on rigid wings, $Q = 15$. Dotted line roughly locates the onset of instability

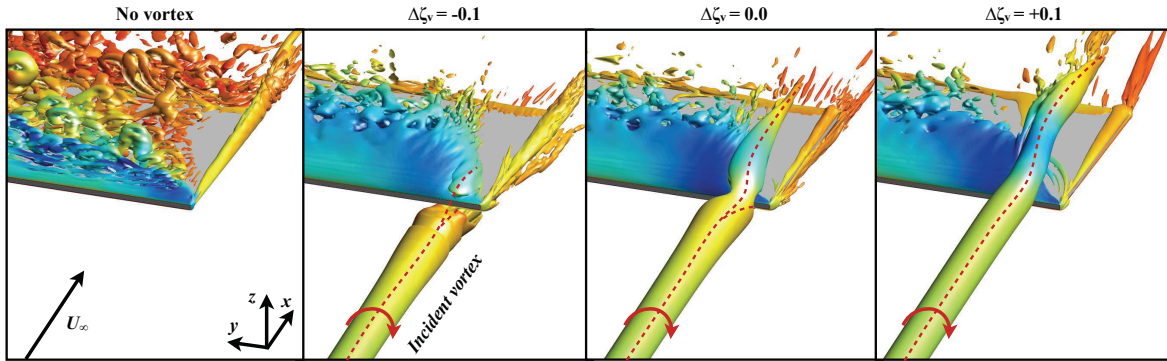


Figure 14: Iso-surfaces of time-mean Q-criterion for no vortex and several vertical positions on rigid wings, $Q = 5$

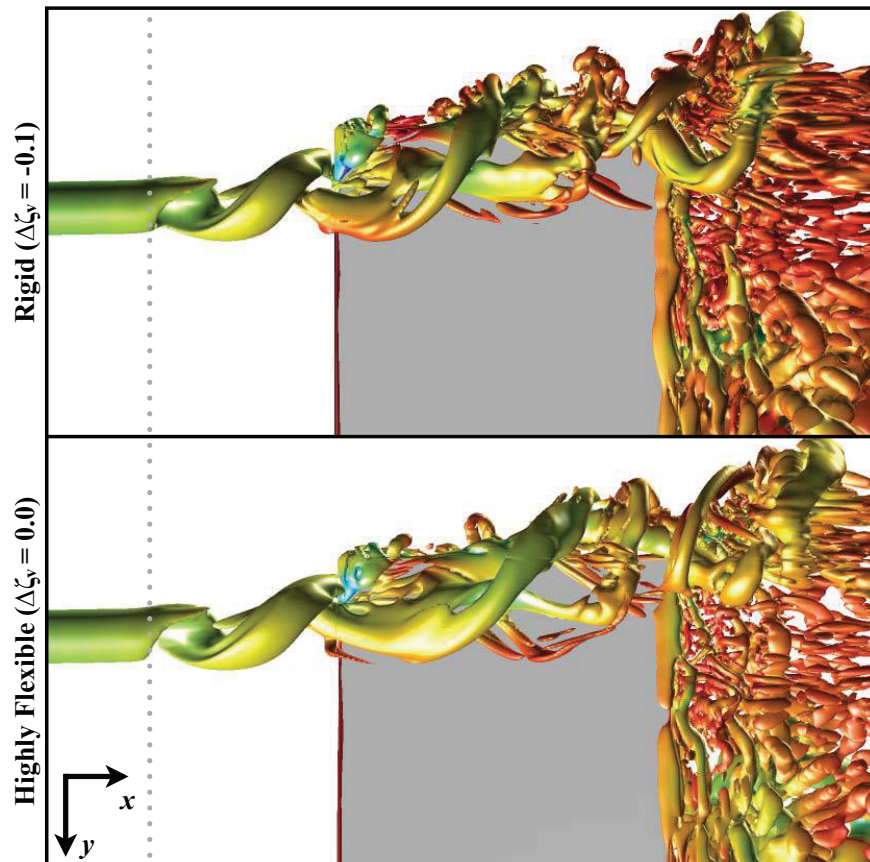


Figure 15: Lower surface view of an instantaneous Q-criterion iso-surface for the *rigid* $\Delta\zeta_v = -0.1$ and *highly flexible* $\Delta\zeta_v = 0.0$ cases. The dotted line roughly locates onset of helical instability

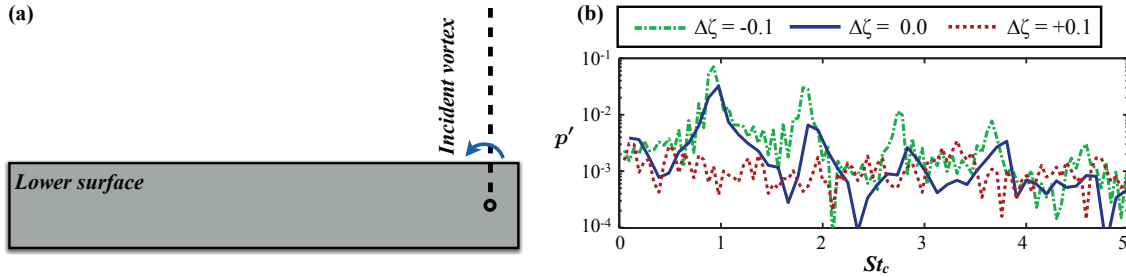


Figure 16: Statistical data (a) collected at the lower surface mid chord just off the wing surface and in-line with the incident vortex and (b) Frequency spectra of pressure fluctuations for several vertical offsets where the vertical axis is plotted on a log-scale

Contours of streamwise velocity at a spanwise plane intersecting the incident vortex core are shown in Fig. 17(a) and provide insight into the mechanisms which differentiate the vortex-surface interaction for each vertical position. For instance, $\Delta\zeta_v = 0.0$ exhibits a large streamwise velocity deficit as the vortex approaches the leading-edge. This diminished flow speed becomes significantly larger when the vortex is placed below the wing for $\Delta\zeta_v = -0.1$. However, at $\Delta\zeta_v = +0.1$ the axial velocity actually accelerates with the flow over the leading-edge. This variation of streamwise velocity locally modifies properties of the vortex just upstream of the wing and has implications for vortex stability.

For instance, Leibovich and Stewartson⁶⁴ derived a stability criterion for the q-vortex which predicts a lower bound for the swirl of $q \geq \sqrt{2}$ to prevent amplification of small-wave perturbations. Because q , defined in Eq. 16, is a function of the velocity deficit which is strongly affected by the vertical position as shown in Fig. 17(a), a proportional influence on the incident vortex stability can also be expected. The swirl and minimum axial velocity (u_{min}) for the incident vortex is plotted in the streamwise direction upstream of the wing in Fig. 18(a) and (b) respectively for each $\Delta\zeta_v$. For the case of direct impingement ($\Delta\zeta_v = 0.0$) or negative vertical offset ($\Delta\zeta_v = -0.1$) the streamwise velocity decreases rather quickly while q follows proportionally and drops well below the stability threshold of $q = \sqrt{2}$. The locally diminished swirl parameter for these two cases indicates a susceptibility to short-wavelength instabilities inline with the onset of helical disruptions observed to form in Fig. 13. The earlier drop of the swirl parameter for $\Delta\zeta_v = -0.1$ is consistent with the advanced onset of the spiraling flow compared to $\Delta\zeta_v = 0.0$. Unstable modes are incapable of propagating far upstream in either case because the swirl parameter of the undisturbed incident vortex falls well within the stable regime. When the vortex is placed above the wing, as in $\Delta\zeta_v = +0.1$, the axial velocity remains fairly constant approaching the leading-edge and maintains sufficient swirl for stability at all points in the streamwise direction. Similarly, Fig. 18(c) shows the maximum tangential velocity upstream of the wing is also influenced by vertical position, but to a much lesser extent.

Axial pressure gradients are known to have a significant influence on columnar vortices. For instance, Sarpkaya⁶⁵ first subjected a streamwise vortex to an axial pressure gradient in a tube and observed a significant impact on vortex breakdown. More recently, Visbal⁶⁶ clarified the dominant role of the axial pressure-gradient for breakdown over delta wings. It should be no surprise to find that pressure gradients play a significant role in the different flow behaviors that can occur with vertical positioning. Therefore, observation of the streamwise pressure gradient $\partial p / \partial x$ can further illuminate the shift in behavior that occurs with changes to vertical position. Figure 17(b) shows contours of $\partial p / \partial x$ on a streamwise plane interesting the vortex core. For $\Delta\zeta_v = 0.0$, the incident vortex is subjected to an adverse streamwise pressure gradient associated with stagnation of flow against the leading-edge. The influence of the vortex-surface interaction is felt upstream and manifests in the form of increasing pressure in the vortex core which would tend to decelerate the streamwise flow. A slower core flow can be expected to diminish swirl and therefore promote hydrodynamic instability as previously shown. For $\Delta\zeta_v = -0.1$, the pressure gradient induced by stagnation at the leading-edge is diminished compared to the $\Delta\zeta_v = 0.0$ case, but results in an adverse gradient along the lower surface contrary to favorable $\partial p / \partial x$ that is typical on the pressure-side. This consequence of the vortex-surface interaction elicits a more pronounced upstream influence resulting in a quicker swirl decay and allows instabilities to propagate further upstream. It would be no surprise to find that more severe conditions result in a stronger adverse-pressure gradient and evolve into spiral-breakdown of the trailing vortex; perhaps at a higher Reynolds number or angle of attack.

While the $\Delta\zeta_v = 0.0$ and -0.1 cases subject the incident vortex to adverse pressure gradients promoting instability, the $\Delta\zeta_v = +0.1$ position shows the streamwise vortex permeating into a favorable $\partial p/\partial x$ above the wing due to accelerating flow over the leading-edge. Axial flow in the vortex core is preserved maintaining swirl and facilitating stability of the incident vortex over the upper surface. The flow visualizations of McAlister and Tung⁶⁷ portray breakdown of a trailing vortex over a stalled two-dimensional airfoil which would suggest a positive $\Delta\zeta_v$ may not be sufficient to guarantee stability of the incident vortex. Rather, the influence of α is also likely to play a significant role. For instance, a stronger separation/stall-induced adverse pressure gradient on the suction-side could promote instability and breakdown on the upper-surface counteracting stabilizing mechanisms demonstrated for positive $\Delta\zeta_v$. In fact, this influence begins to appear in the present case. As the vortex approaches the trailing-edge it is subjected to a large adverse $\partial p/\partial x$ in the separated flow region. This results in significantly decelerated axial velocity, shown in Fig. 17(a), which would tend to destabilize the incident vortex and promote transition into smaller-scale structures as shown by label (1) in Fig. 13(b).

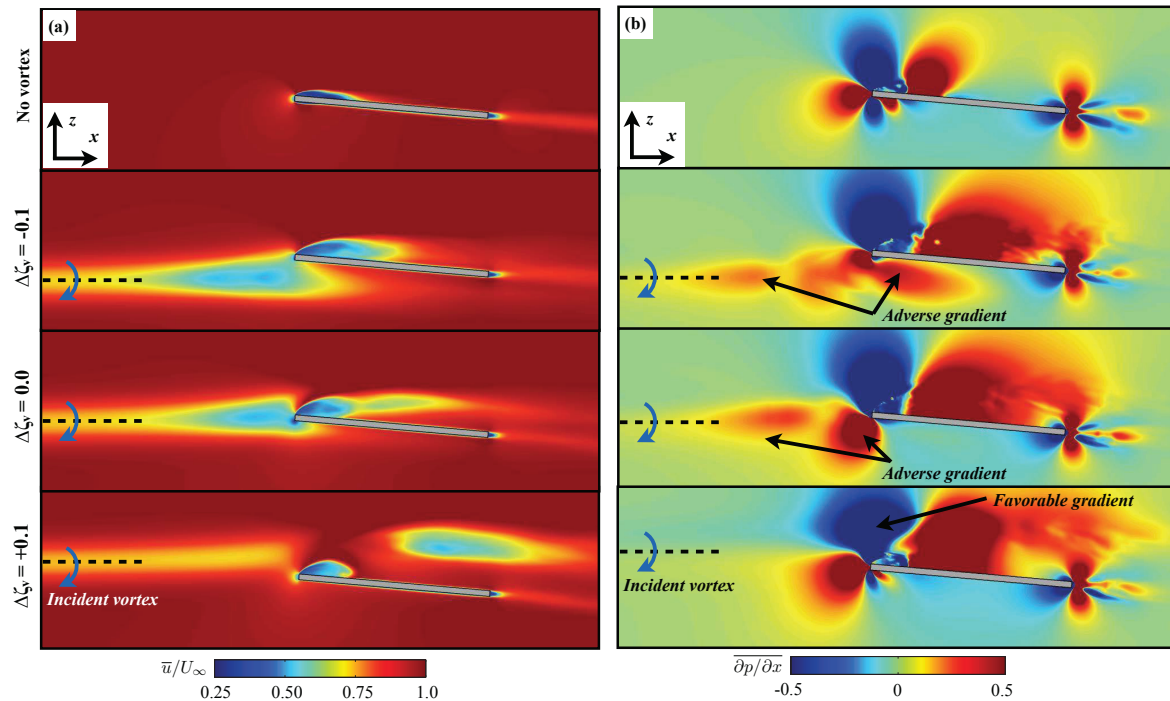


Figure 17: Time-mean contours of (a) streamwise velocity and (b) streamwise pressure gradient at $y/c = -2.75$ for a rigid wing subject to several $\Delta\zeta_v$

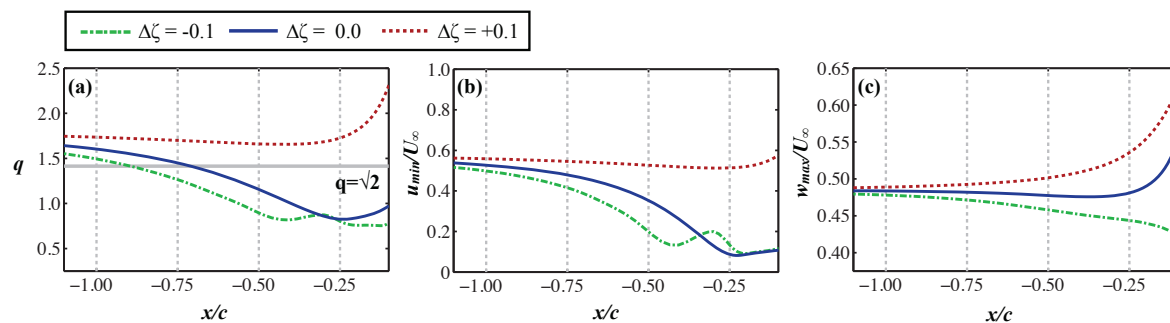


Figure 18: Time-mean (a) swirl parameter, (b) minimum streamwise velocity, (c) maximum vertical velocity versus the streamwise direction upstream of the leading-edge for a rigid wing subject to several $\Delta\zeta_v$

Time-averaged surface pressure coefficient and surface-restricted streamlines are shown in Fig. 19 for both the upper and lower surface for several $\Delta\zeta_v$ and an isolated wing. On the suction-side, the streamlines for each of the vertical positions reveal a significant increase in the separation bubble in that the line of attachment, traced by the dashed white line, has moved toward the trailing-edge compared to an isolated wing at the same angle of attack. Furthermore, a strong swirling flow pattern, denoted by a red arrow, is observed near the vortex encounter associated with locally enhanced suction. For a wing subject to a longitudinal vortex under similar conditions, Garmann and Visbal³⁴ showed this magnified swirl draws fluid inward from the outboard section and tends to alleviate the influence of downwash on the upper-surface. While this three-dimensional effect remains for all vertical positions in the current work it is likely to provide a significant impact on the interaction between vortex and wing for positive $\Delta\zeta_v$ and may be conducive to preserving stability. The particular role of this factor is not clear at this time and is a topic for further study.

A greater distinction between the cases can be made on the lower surface of the wing. For instance, the imprint of a dominant pressure-side component of the incident vortex for $\Delta\zeta_v = -0.10$ is more prominently displayed as a band of negative C_p near the wingtip. This effect diminishes as the vortex is moved upward and the lower-surface component diminishes. The influence of the incident vortex on the time-mean pressure-side limiting surface streamlines is also apparent between the three vertical positions displayed. For $\Delta\zeta_v = +0.1$, the lower surface streamlines maintain a dominantly streamwise orientation in the vicinity of the vortex encounter. Moving the vortex downward as in $\Delta\zeta_v = 0.0$ reveals streamlines which tend outboard due to the induced velocity of the lower-surface component of the vortex interacting with its mirror image in the surface. The negative vertical offset of $\Delta\zeta_v = -0.1$ enhances the spanwise flow near the wingtip. In this case, the juxtaposition of the stronger lower-surface component of the vortex results in a stronger interaction with the lower surface which appears to be conducive to the formation of the adverse $\partial p/\partial x$ beneath the lower surface for this case.

Finally, Fig. 20 portrays contours of mean-squared pressure fluctuations on the suction and pressure-surfaces of the wing for several $\Delta\zeta_v$. On the upper-surface, each of the vertical positions exhibits a wider band concentration of $\overline{p'p'}$ closer to the trailing-edge compared to the isolated wing. This behavior is again indicative of the increased separation associated with the higher local effective angle of attack induced by the incident vortex upwash and relatively similar for each case. On the pressure-side, the imprint of the unsteady streamwise vortex for the negative vertical offset ($\Delta\zeta = -0.1$) is revealed by a streamwise band of $\overline{p'p'}$ near the wingtip and traced by a dashed white line. This fluctuation in surface loading, absent in the other cases, portrays the unsteady influence of the unstable vortex on surface loading and underscores the importance of vortex positioning on buffeting response.

As a final note to this section, the current work demonstrates a tendency for the vortex surface interaction to elicit unsteady fluid dynamics and identifies trends that may lead to more severe conditions in streamwise vortex interactions. Once identified, these conditions might result in behaviors reminiscent of the unsteady loading and buffeting response of fins subject to a broken-down vortex emitted from delta wings presented by Mayori and Rockwell,⁶⁸ Wolfe *et al.*,⁶⁹ Kandil *et al.*,⁷⁰ Gordnier and Visbal,²⁸ and more recently, Gursul and Xie⁶³ or Lambert and Gursul^{71,72} to name a few. Aeroelastic effects are likely to complicate the interaction. For instance, as shown in the present work, relatively small deflections of the wing can produce very different behaviors by simply repositioning the incident vortex. A more dynamic response could produce fluctuations in the vertical positioning and angle of attack, both of which are projected to significantly influence behavior even in the static case. Furthermore, Gursul and Xie⁶³ showed vortex breakdown is sensitive to lower frequency oscillations of a fin. Therefore, aeroelastic analysis becomes an increasingly interesting area of discovery for the current problem. Detailed high-fidelity computational analysis of the unsteady viscous flow will be necessary to fully understand the complex physics associated with these interactions.

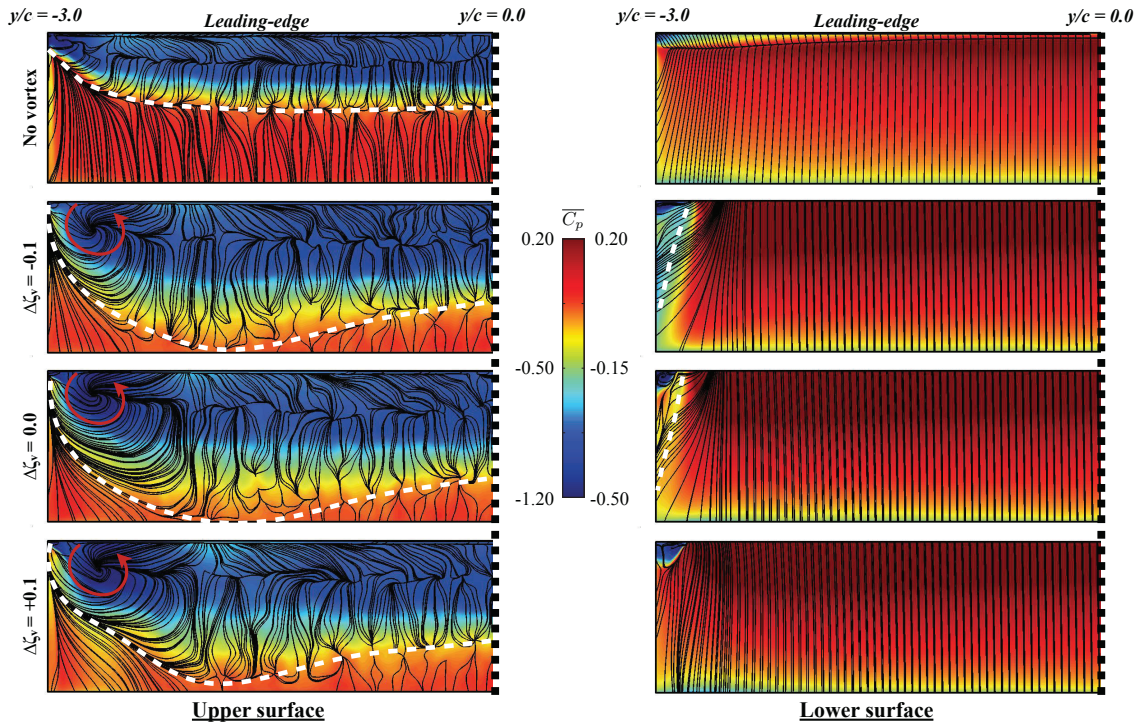


Figure 19: Contours of time-mean surface pressure and limiting surface streamlines on the vortex-encounter semi-span for a rigid wing subject to several $\Delta\zeta_v$

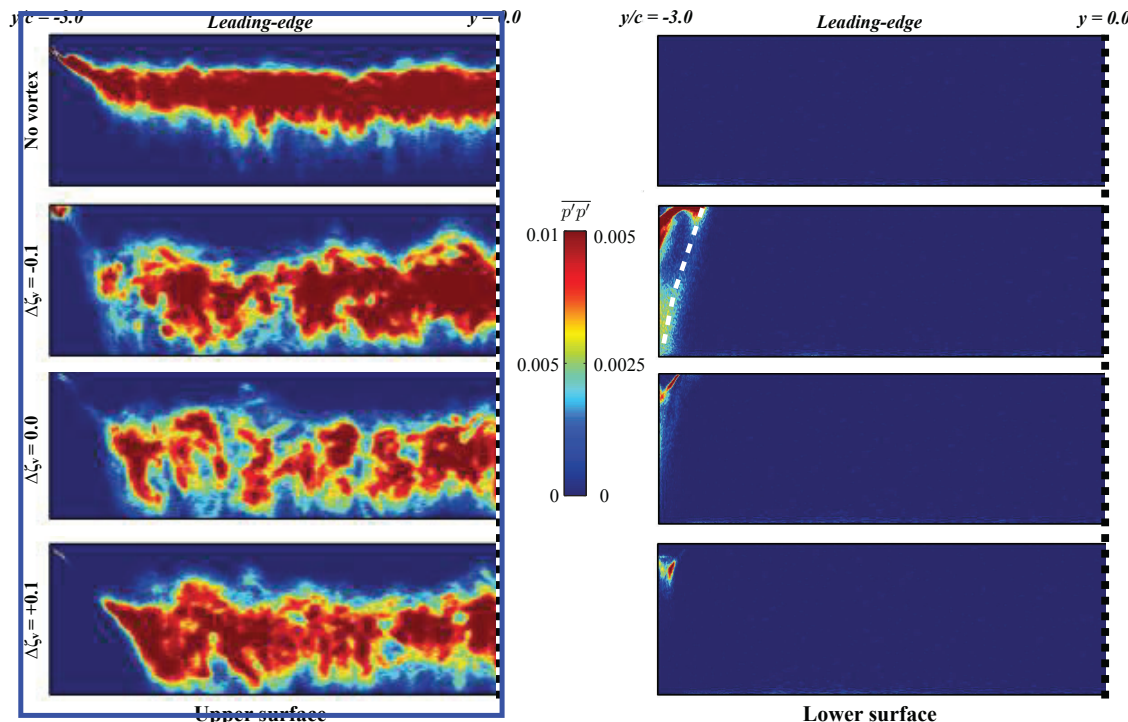


Figure 20: Contours of mean-squared surface pressure fluctuations on the vortex-encounter semi-span for a rigid wing subject to several $\Delta\zeta_v$

IV.C.1. Aerodynamic loads

Table 6 provides the time-mean aerodynamic loads compared to an isolated wing for each of the vertical positions computed while Fig. 21 provides a graphical representation for comparison purposes. Initial observations suggest that $\Delta\zeta_v = 0.0$, which has the largest L/D , is of the greatest aerodynamic advantage. However, observation of the four vertical offsets provided here suggest that aerodynamic benefits attenuate gradually compared to previous observations on the influence of lateral positioning, $\Delta\eta_v$, on aerodynamic forces.³⁴ Furthermore, this diminished sensitivity with $\Delta\zeta_v$ is consistent with the experimental observations of Blake and Gingras.³⁰ Therefore, the implications of vertical offset are more likely to be dictated by the ramifications of vortex stability and unsteady loading.

Figure 22(a) shows the sectional lift distribution across the span at several $\Delta\zeta_v$ positions. For a vortex aligned with the mid chord, $\Delta\zeta_v = 0.0$, a significant increase in lift is observed across the entire span compared with the isolated wing and a local peak in lift occurs just inboard of the vortex impingement which corresponds with the strong spanwise recirculation just inboard of the vortex encounter. This localized enhancement is reduced for $\Delta\zeta_v = -0.1$ due to diminished recirculation on the upper surface, similar to that observed for the flexible wings.

Fourier analysis of the lift C_L , rolling moment C_{M_x} , and quarter-chord pitching moment coefficients $C_{M_{y,(c/4)}}$ is provided in Fig. 22(b). Most notably, dominant frequencies in the rolling moment coefficient are observed for all cases at $St_c = 0.53$, slightly above the dominant frequency of deformations for the flexible wings. Interestingly, this sub-harmonic of the primary helix is pronounced for all three vertical positions. Furthermore, the $\Delta\zeta_v = 0.0$ case elicits oscillations in loading directly corresponding with the measured fluctuations in the vortex core. The repeated observation that dominant frequencies in both the rigid and flexible cases for loading and deformations are multiples of each other suggest these frequencies are closely related and that deformations of the flexible wings are driven by unsteady fluid dynamics rather than excitation of structural modes.

Table 6: Time-mean aerodynamic loads for several $\Delta\zeta_v$

	C_D		C_L		L/D		C_{M_x}	$C_{M_{x,rms}}$
	Value	% diff.	Value	% diff.	Value	% diff.	Value	Value
No vortex	0.077	-	0.433	-	5.648	-	0.002	9.8×10^{-3}
$\Delta\zeta_v = -0.10$	0.091	+17.5%	0.626	+44.6%	6.92	+23.0%	-0.128	13.9×10^{-3}
$\Delta\zeta_v = 0.00$	0.091	+17.8%	0.631	+45.7%	6.96	+23.7%	-0.136	12.9×10^{-3}
$\Delta\zeta_v = +0.05$	0.091	+18.1%	0.624	+44.1%	6.87	+22.1%	-0.136	10.9×10^{-3}
$\Delta\zeta_v = +0.10$	0.091	+18.6%	0.621	+43.4%	6.80	+21.0%	-0.127	11.6×10^{-3}

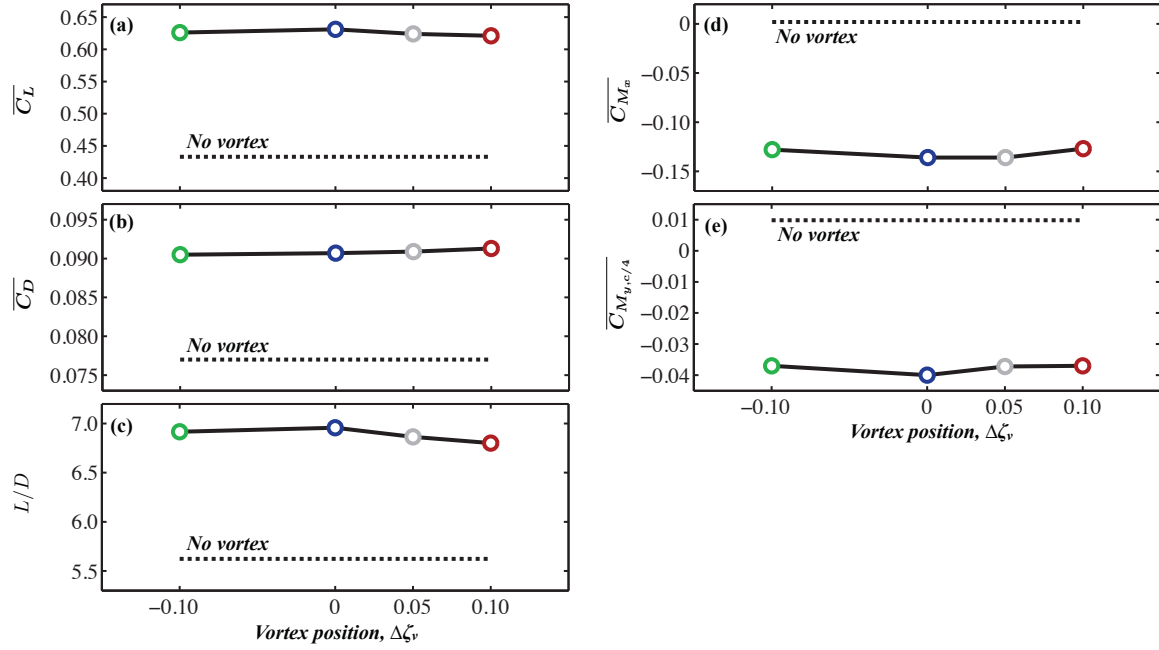


Figure 21: Time-mean (a) lift, (b) drag, (c) lift-to-drag ratio, (d) rolling moment and (e) pitching moment about the quarter-chord for several vertical positions

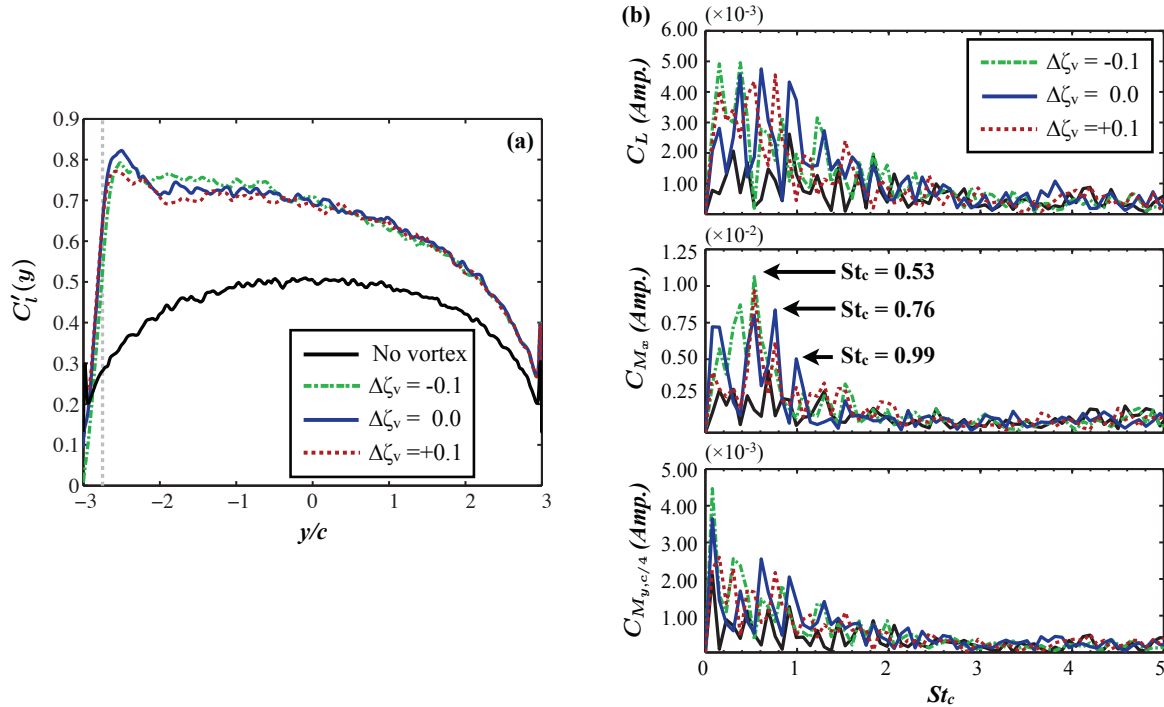


Figure 22: (a) Time-mean sectional lift coefficient per unit span and (b) Fourier analysis of aerodynamic loads for several incident vortex positions

V. Concluding Remarks

Aeroelastic computations using a high-fidelity implicit LES fluid solver coupled with geometrically nonlinear Reisner-Mindlin plate elements were conducted to evaluate the influence of a streamwise-oriented vortex impinging upon rigid and flexible wings. Each case consisted of an $AR = 6$ flat plate wing operating at a Reynolds number of $Re_c = 30,000$ and a $\alpha = 5^\circ$ angle of attack. The vortex was aligned with the wing mid chord and positioned inboard of the wingtip. Three levels of flexibility were considered for evaluation including *rigid*, *flexible*, and *highly flexible* wings.

In the case of the rigid wing, the incident vortex core was shown to develop helical instabilities upstream of the leading-edge which wind in a sense opposite the rotation of the vortex swirl. This spiraling structure alternates between the upper and lower surfaces producing vortical flows on both sides of the wing and appears as a bifurcation in the time-mean flow. Introducing flexibility to the wing structure resulted in several interesting behaviors. First, a dynamic response was elicited in both the bending and twisting deformations on the vortex-encounter side of the wing. Second, increasing flexibility tended to enhance the unsteady behavior of the streamwise vortex. This in turn would have implications on the unsteady loading and wing fatigue-life. In order to clarify the influence of static and dynamic-aeroelastic effects on the unsteady flow structure, the rigid wing was subjected to several vertical positions of the incident vortex. Moving the vortex beneath the wing is representative of a time-mean vertical deflection of the wingtip, but removes the influence of structural oscillations. Remarkable similarity in the flow structure and onset of helical instability between the *rigid* $\Delta\zeta_v = -0.1$ and *highly flexible* $\Delta\zeta_v = 0$ cases strongly suggest static deformation is the primary contributor to the increase in vortex instability rather than feedback effects from wing oscillations.

Further evaluation of vortex positioning on the rigid wing revealed that vertical offset of the incident vortex can produce very different behaviors in the unsteady flow. When the vortex was placed beneath the wing, $\Delta\zeta_v = -0.1$, the close proximity and orientation of the lower surface resulted in an adverse streamwise pressure gradient beneath the wing which tends to decelerate the axial velocity, diminish swirl, and promote helical instability of the incident vortex. Compared to direct impingement, $\Delta\zeta_v = 0.0$, the vortex-surface interaction produced a stronger velocity deficit which allowed hydrodynamic instabilities to develop further upstream. A stronger adverse pressure gradient under more severe conditions could evolve into breakdown of the streamwise vortex. Placing the vortex above the wing positioned the core in line with a favorable pressure gradient produced by acceleration of the free stream over the leading-edge. This increase in axial velocity preserved swirl, and prevented formation of the helical instability observed in all other cases. Downstream, the coherent vortex became susceptible to the adverse pressure gradient near the trailing-edge and began to degrade into smaller-scale structures. At a higher angle of attack, this effect could result in suction-side breakdown of the streamwise vortex.

Evaluation of the aerodynamic loading revealed that the case of no vertical offset in the incident vortex provided the most favorable lift-to-drag ratio. However, this benefit varied slowly with changes in vertical positioning compared with past observations of lateral positioning. In the context of formation flight, considerations of vertical offset may be dictated by its ramifications on vortex stability and unsteady loading rather than optimization of the time-mean forces.

Acknowledgments

This work was supported in part by AFOSR under a task monitored by Dr. D. Smith, and by a grant of HPC time from the DoD HPC Major Shared Resource Center at AFRL, WPAFB.

References

- ¹Lissaman, S. and Shollenberger, C. A., "Formation flight of birds," *Science*, Vol. 168, 1970, pp. 1003–1005.
- ²Wieselsberger, C., "Beitrag zur Erklärung des Winkelfluges Einer Zugvögel," *Z. Flugtechnik & Motorluftschiffahrt*, Vol. 5, 1914, pp. 225–229.
- ³Hummel, D., "Aerodynamic aspects of formation flight in birds," *J. Theor. Biol.*, Vol. 104, 1983, pp. 321–347.
- ⁴Hummel, D., "Formation flight as an energy-saving mechanism," *Israel J. Zool.*, Vol. 41, 1995, pp. 261–278.
- ⁵Hainsworth, F. R., "Precision and dynamics of positioning by Canada geese flying in formation," *J. Exp. Biol.*, Vol. 128, 1987, pp. 445–462.
- ⁶Cutts, C., "Energy savings in formation flight of pink-footed geese," *J. Exp. Biol.*, Vol. 189, No. 1, 1994, pp. 251–261.
- ⁷Weimerskirch, H., Martin, J., Clerquin, Y., Alexandre, P., and Jiraskova, S., "Energy saving in flight formation," *Nature*, Vol. 413, No. 6857, 2001, pp. 697–698.

⁸Cobleigh, B., "Capabilities and future applications of the NASA autonomous formation flight (AFF) aircraft," AIAA paper 2002-3443, AIAA, May 2002.

⁹Vachon, M., Ray, R., Walsh, K., and Ennix, K., "F/A-18 aircraft performance benefits measured during the autonomous formation flight project," AIAA paper 2002-4492, AIAA, Aug. 2002.

¹⁰Hansen, J. L. and Cobleigh, B. R., "Induced moment effects of formation flight using two F/A-18 aircraft," AIAA paper 2002-4489, AIAA, 2002.

¹¹Ray, R. J., Cobleigh, B., Vachon, M., and John, C. S., "Flight test techniques used to evaluate performance benefits during formation flight," AIAA paper 2002-4492, AIAA, Aug. 2002.

¹²Ianotta, B., "Vortex draws flight research forward," *AIAA Aerospace America*, Vol. 40, No. 3, March 2012, pp. 26–30.

¹³Wagner, G., Jacques, D., Blake, B., and Pacher, M., "Flight test results of close formation flight for fuel savings," AIAA paper 2002-4490, AIAA, Aug. 2002.

¹⁴Pahle, J., Berger, D., Venti, M., Duggan, C., Faber, J., and Cardinal, K., "An initial flight investigation of formation flight for drag reduction on the C-17 aircraft," AIAA paper 2012-4802, AIAA, Aug. 2012.

¹⁵Bizinos, N. and Redelinghuys, C., "Tentative study of passenger comfort during formation flight within atmospheric turbulence," *J. Aircraft*, Vol. 50, No. 3, 2013, pp. 886–900.

¹⁶Blake, W. and Multhopp, D., "Design and performance and modeling considerations for close formation flight," AIAA paper 98-4343, AIAA, Aug. 1998.

¹⁷Venkataraman, S., Dogan, A., and Blake, W., "Vortex effect modeling in aircraft formation flight," AIAA paper 2003-5385, AIAA, 2003.

¹⁸Binetti, P., Ariyur, K., Krstic, M., and Bernelli, F., "Formation flight optimization using extremum seeking feedback," *J. Guid. Control Dynam.*, Vol. 26, No. 1, 2003, pp. 132–142.

¹⁹Blake, W. B. and Gingras, D. R., "Comparison of predicted and measured formation flight," AIAA paper 2001-4136, AIAA, Aug. 2001.

²⁰Wagner, G., Jacques, D., Blake, B., and Pacher, M., "An analytical study of drag reduction in tight formation flight," AIAA paper 2001-4075, AIAA, Aug. 2001.

²¹Wang, Z. and Mook, D. T., "Numerical aerodynamic analysis of formation flight," AIAA paper 2003-0610, AIAA, Jan. 2003.

²²Iglesias, S. and Mason, W. H., "Optimum spanloads in formation flight," AIAA paper 2002-0258, AIAA, Jan. 2002.

²³Frazier, J. W. and Gopalarathnam, A., "Optimum downwash behind wings in formation flight," *J. Aircraft*, Vol. 40, No. 4, 2003, pp. 799–803.

²⁴Inasawa, A., Mori, F., and Asai, M., "Detailed observations of interactions of wingtip vortices in close-formation Flight," *J. Aircraft*, Vol. 49, No. 1, 2012, pp. 206–213.

²⁵Ning, S. A., Flanzer, T. C., and Kroo, I. M., "Aerodynamic performance of extended formation flight," *J. Aircraft*, Vol. 48, No. 3, 2011, pp. 855–865.

²⁶Kless, J. E., Aftosmis, M. J., Ning, S. A., and Nemec, M., "Inviscid analysis of extended-formation flight," *AIAA J.*, Vol. 51, No. 7, 2013, pp. 1703–1715.

²⁷Rockwell, D., "Vortex-body interactions," *Annu. Rev. Fluid Mech.*, Vol. 30, 1998, pp. 199–229.

²⁸Gordnier, R. and Visbal, M., "Numerical simulation of the impingement of a streamwise vortex on a plate," *Int. J. Comput. Fluid D.*, Vol. 12, 1999.

²⁹Crow, S. C., "Stability theory of a pair of trailing vortices," *AIAA J.*, Vol. 8, 1970, pp. 2172–2179.

³⁰Blake, W. B. and Gingras, D. R., "Comparison of predicted and measured formation flight," *J. Aircraft*, Vol. 41, No. 2, 2004, pp. 201–207.

³¹Magill, S. A., Schetz, J. A., and Mason, W. H., "Compound aircraft transport: a comparison of wingtop-docked and close-formation flight," AIAA paper 2003-607, AIAA, Jan. 2003.

³²Bangash, Z. A., Sanchez, R. P., and Ahmed, A., "Aerodynamics of formation flight," *J. Aircraft*, Vol. 43, No. 4, 2006, pp. 907–912.

³³Barnes, C. J., Visbal, M. R., and Gordnier, R. E., "Investigation of aeroelastic effects in streamwise-oriented vortex/wing interactions," AIAA paper 2014-1281, AIAA, Jan. 2014.

³⁴Garman, D. J. and Visbal, M. R., "Interaction of a streamwise-oriented vortex with a wing," AIAA paper 2014-1282, AIAA, Jan. 2014.

³⁵Vinokur, M., "Conservation equations of gasdynamics in curvilinear coordinate systems," *J. Comput. Phys.*, Vol. 14, 1974, pp. 105–125.

³⁶Steger, J. L., "Implicit finite-difference simulation of flow about arbitrary two-dimensional Geometries," *AIAA J.*, Vol. 16, No. 7, 1978, pp. 679–686.

³⁷Tannehill, J. C., Anderson, D. A., and Pletcher, R. H., *Computational Fluid Mechanics and Heat Transfer*, McGraw-Hill Book Company, 1997.

³⁸Visbal, M. R. and Rizzetta, D. P., "Large-eddy simulation on curvilinear grids using compact differencing and Filtering Schemes," *J. Fluid. Eng.*, Vol. 124, 2002, pp. 836–847.

³⁹Visbal, M. R., Morgan, P. E., and Rizzetta, D. P., "An implicit LES approach based on high-order compact differencing and Filtering Schemes," AIAA paper 2003-4098, AIAA, Jun. 2003.

⁴⁰Stolz, S. and Adams, N., "An approximate deconvolution procedure for large-eddy simulation," *Phys. Fluids*, Vol. 11, No. 7, 1999, pp. 1699–1701.

⁴¹Mathew, J., Lechner, R., Foysi, H., Sesterhenn, J., and Friedrich, R., "An explicit filtering method for large eddy simulation of compressible Flows," *Phys. Fluids*, Vol. 15, No. 8, 2003, pp. 2279–2289.

⁴²Visbal, M. R. and Gaitonde, D. V., "High-order-accurate methods for complex unsteady subsonic flows," *AIAA J.*, Vol. 37, No. 10, 1999, pp. 1231–1239.

⁴³Gaitonde, D. V. and Visbal, M. R., "High-order schemes for Navier-Stokes equations: algorithm and implementation into FDL3DI," Technical report AFRL-VI-WP-TR-1998-3060, Air Force Research Laboratory, Wright-Patterson AFB, 1998.

⁴⁴Lele, S., "Compact finite difference schemes with spectral-like resolution," *J. Comput. Phys.*, Vol. 103, 1992, pp. 16–42.

⁴⁵Gaitonde, D. and Visbal, M., "Further development of a Navier-Stokes solution procedure based on higher-order formulas," AIAA paper 1999-0557, AIAA, 1999.

⁴⁶Alpert, P., "Implicit filtering in conjunction with explicit filtering," *J. Comput. Phys.*, Vol. 44, 1981, pp. 212–219.

⁴⁷Garman, D. J., Visbal, M. R., and Orkwis, P. D., "Comparative study of implicit and subgrid-scale model large-eddy simulation techniques for low-reynolds number airfoil applications," *Int. J. Numer. Methods Fluids*, Vol. 71, No. 12, 2012, pp. 1546–1565.

⁴⁸Beam, R. and Warming, R., "An implicit factored scheme for the compressible Navier-Stokes equations," *AIAA J.*, Vol. 16, 1978, pp. 393–402.

⁴⁹Pulliam, T. and Chaussee, D., "A diagonal form of an implicit approximate-factorization algorithm," *J. Comput. Phys.*, Vol. 17, No. 10, 1981, pp. 347–363.

⁵⁰Rizzetta, D. P., Visbal, M. R., and Morgan, P. E., "A high-order compact finite-difference scheme for large-eddy simulation of active flow control (Invited)," AIAA paper 2008-526, AIAA, 2008.

⁵¹Attar, P. J., "Some results for approximate strain and rotation tensor formulations in geometrically non-linear Reissner-Mindlin plate theory," *Int. J. Nonlinear Mech.*, Vol. 43, 2008, pp. 81–99.

⁵²Szabó, B. and Babuška, I., *Finite Element Analysis*, John Wiley and Sons, New York, 1991.

⁵³Cook, R. D., Malkus, D. S., Plesha, M. E., and Witt, R. J., *Concepts and Applications of Finite Element Analysis*, John Wiley & Sons, 4th ed., 2002.

⁵⁴Attar, P. J. and Gordnier, R. E., "Aeroelastic modeling using a geometrically nonlinear p-version mixed Reissner-Mindlin plate element," AIAA paper 2007-2318, AIAA, Apr. 2007.

⁵⁵Melville, R., "Dynamic aeroelastic simulation of complex configurations using overset Grid Systems," AIAA paper 2000-2341, AIAA, Jun. 2000.

⁵⁶Gordnier, R. and Visbal, M., "Development of a three-dimensional viscous aeroelastic solver for nonlinear panel flutter," *J. Fluid Struc.*, Vol. 16, No. 4, 2002, pp. 497–527.

⁵⁷Batchelor, G., "Axial flow in trailing line vortices," *J. Fluid Mech.*, Vol. 20, No. 4, 1964, pp. 645–658.

⁵⁸Steger, J., Dougherty, F., and Benek, J., "A chimera grid scheme," *Advances in Grid Generation*, edited by K. Ghia and U. Ghia, Vol. 5, American Society of Mechanical Engineers, 1983, pp. 59–69.

⁵⁹Sherer, S. E. and Scott, J. N., "High-order compact finite-difference methods on general overset grids," *J. Comput. Phys.*, Vol. 210, 2005, pp. 459–496.

⁶⁰Visbal, M. and Gaitonde, D., "Very high-order spatially implicit schemes for computational acoustics on Curvilinear Meshes," *J. Comput. Acoust.*, Vol. 9, No. 4, 2001, pp. 1259–1286.

⁶¹Jeong, J. and Hussain, F., "On the identification of a vortex," *J. Fluid Mech.*, Vol. 285, 1995, pp. 69–94.

⁶²Leibovich, S., "The structure of vortex breakdown," *Annu. Rev. Fluid Mech.*, Vol. 10, 1978, pp. 221–246.

⁶³Gursul, I. and Xie, W., "Interaction of vortex breakdown with an oscillating fin," *AIAA J.*, Vol. 39, No. 3, Mar. 2001, pp. 438–446.

⁶⁴Leibovich, S. and Stewartson, K., "A sufficient condition for the instability of columnar vortices," *J. Fluid Mech.*, Vol. 126, January 1983, pp. 335–356.

⁶⁵Sarpkaya, T., "Effect of the adverse pressure gradient on vortex breakdown," *AIAA J.*, Vol. 12, No. 5, 1974, pp. 602–607.

⁶⁶Visbal, M. R., "Onset of vortex breakdown about a pitching delta wing," *AIAA J.*, Vol. 38, No. 8, 1994, pp. 1568–1575.

⁶⁷McAlister, K. W. and Tung, C., "Airfoil interaction with an impinging vortex," NASA Tech. Pap. 2273, NASA, 1984.

⁶⁸Mayori, A. and Rockwell, D., "Interaction of a streamwise vortex with a thin plate: a source of turbulent buffeting," *AIAA J.*, Vol. 32, No. 10, 1994, pp. 2022–2029.

⁶⁹Wolfe, S., Lin, J.-C., and Rockwell, D., "Buffeting at the leading-edge of a flat plate due to a streamwise vortex: flow structure and surface pressure loading," *J. Fluid. Struc.*, Vol. 9, 1995, pp. 359–370.

⁷⁰Kandil, O. A., Sheta, E. F., and Massey, S. J., "Buffet responses of a vertical tail in vortex breakdown flows," AIAA paper 95-3464, AIAA, 1995.

⁷¹Lambert, C. and Gursul, I., "Buffeting of a flexible fin over a delta wing," AIAA paper 2001-2426, AIAA, Jun. 2001.

⁷²Lambert, C. and Gursul, I., "Fin buffeting over various delta wings," AIAA paper 2003-3529, AIAA, Jun. 2003.

APPENDIX D

Streamwise-Oriented Vortex Interactions with a NACA0012 Wing

Daniel J. Garmann* and Miguel R. Visbal †

Air Force Research Laboratory, Wright-Patterson AFB, OH 45433

The unsteady interactions of a streamwise-oriented vortex impacting a NACA0012 wing are investigated using high-fidelity numerical simulation. The unsteady modes of interaction and taxonomy of a generic vortex/surface impingement are characterized for two spanwise positions of an incoming vortex, which is imposed analytically upstream of the aspect-ratio-six wing and freely convected in a free stream at a Reynolds number of $Re = 2.0 \times 10^5$. Tip-aligned and inboard-positioned incident vortices are examined and shown to produce rich dynamics through their impingement with the wing. This includes a self-similar flow structure inboard of impingement, whereby earlier separation, reattachment, and abrupt transition of the shear layer are encountered with closer proximity to the incoming vortex. Inboard positioning of the vortex exposes the wingtip to the vortex downwash, thereby reducing the effective angle of attack and resulting in a mostly attached flow outboard of impingement that effectively unloads the wingtip. The core dynamics of the impingement along the leading edge are driven by the development of a spiraling mode instability that alternately deflects the vortex over the suction and pressure sides of the wing. These findings, along with the outboard unloading of the wingtip are consistent with a previous study for flat plates and much lower Reynolds numbers, which may support future numerical studies of these generic vortex/surface interactions at low Reynolds number.

I. Introduction

Columnar vortices impacting a surface can be separated into three fundamental classes of interactions: (1) parallel, (2) normal, or (3) streamwise (perpendicular) vortex-body encounters with an excellent and extensive review of each of these interactions provided by Rockwell.¹ While the unsteady physics of the first two vortex representations have been well-documented, considerably less attention has been paid to streamwise-oriented vortex-body interactions; in particular, to the unsteady, three-dimensional nature of the vortex and how it relates to the induced loading on a finite wing as would be encountered in turbomachinery blade-row interactions or formation flight, for example. Even less understood are the implications of a wandering vortex impinging upon a wing that not only dynamically shifts from the upstream influence of the wing, but also from atmospheric turbulence, aircraft wandering, or crow-instability effects, to name a few.

Either a single vortex or systems of streamwise-oriented vortices are known to exhibit a rich dynamics. Long wavelength,² short wavelength (elliptical) and spiral breakdown³ constitute examples of potential outcomes that may affect the evolution of a streamwise-oriented vortex and its interaction with aerodynamic surfaces encountered in its path. Furthermore, axial vortices may also exhibit spiral sub-structures generated during their roll-up process.^{4,5} These instabilities and unsteady features can result in additional sources of buffeting while impinging upon a finite wing. To further compound the problem, either deliberate or unanticipated motions of the incident vortex can provide another degree of uncertainty in the predicted flow structure, even experimentally. Heyes *et al.*,⁶ for example, discuss the difficulties in extracting reliable measurements from wandering vortices and demonstrate how vortex wandering effects must be corrected to prevent false conclusions from being drawn about the vortex structure, i.e. breakdown. These difficult-to-predict unsteady phenomena engendered by the vortex/surface interaction will impact the unsteady loading

*Research Aerospace Engineer. AIAA Senior Member.

†Technical Area Leader. AIAA Fellow.

This material is declared a work of the U.S. Government and is not subject to copyright protection in the United States.

or buffeting experienced by the wing. Another unresolved critical aspect of the problem is the modification of the incident vortex and its instability modes generated by the process of impingement upon the wing. This feedback will most likely be limited to a region of upstream influence in front of the wing. Nonetheless coupling of vortex instabilities with the unsteady separation is in general not well understood and could give rise to a resonant behavior with significant impact on the vortex/surface interaction.

Streamwise-oriented vortex/wing interactions in the context of formation flight, which has long been understood to provide significant benefits in aerodynamic performance, have been analyzed in a series of papers by Hummel^{7,8} and Beukenberg and Hummel⁹ using classic aerodynamic theory, wherein citations to earlier seminal work can also be found. With proper positioning, trailing aircraft can capture the upwash from the tip vortex left in the wake of a lead aircraft. The result is a forward-tilted lift vector that provides increased lift and a reduction in induced drag and can lead to significant energy savings.¹⁰ Recently, Ning *et al.*¹¹ performed an investigation of several factors affecting the benefits and feasibility of extended formation flight for three aircraft in canonical echelon and V-type arrangements. These factors included wake roll-up, vortex core size, vortex decay and gust effects. Kless *et al.*¹² provided a computational inviscid flow analysis of several aspects of extended formation flight with consideration of optimal incident vortex location, roll trim effects and transonic flow effects. Vortex meandering induced from wind-tunnel unsteadiness, atmospheric turbulence, crow instability, or upstream feedback from the surface,¹³ can also pose a problem for reliable wake capturing in this context, wherein significant deviation of the impacting vortex core can lead to unintended separation or unsteady loading. Despite advances in the understanding, prediction and demonstration of the benefits of formation flight, significant challenges still require further investigation before this technology becomes a viable and safe operational capability.

The recent high-fidelity numerical studies of Barnes *et al.*¹⁴ and Garmann and Visbal¹⁵ have investigated the unsteady interactions of a streamwise-oriented vortex impinging upon a finite wing operating at low Reynolds numbers, $Re \sim \mathcal{O}(10^4)$. In the former, two aspect-ratio-six flat plate wings, arranged in tandem, were simulated at a Reynolds number of 30,000 as a generic problem of formation flight-like conditions. Several spanwise positions and incidence angles of the lead wing were varied for both rigid and flexible follower wings in an effort to engender the most significant aeroelastic response. The resulting flow structure with outboard-positioning yielded vortex dipole-like pairing between the incident and tip vortices, while more inboard locations presented a time-mean bifurcation of the incident vortex. It was also concluded from the unsteady loading that lead-wing wandering may be a more dominant driver of structural response. Wing compliance also led to substantial repositioning and stabilizing effect of the incident vortex.

In the latter investigation of Garmann and Visbal,¹⁵ the lead wing was neglected and, instead, an analytically-defined vortex was superimposed in the free stream and convected towards a finite wing. This was in an effort to gain greater control over the strength, size, position, and stability of the incident vortex as a canonical problem of streamwise-oriented vortex/surface interactions. The imposed vortex actually compares quite well to an enlarged trailing vortex from Barnes *et al.*,¹⁴ which was chosen to exacerbate the unsteady interaction. To that end, three distinct flow regimes were found: When the vortex was positioned outboard of, but in close proximity to, the wingtip, it paired with the tip vortex to form a dipole that propelled itself away from the plate due to its self-induced velocity and diffused slowly. When the incoming vortex was aligned with the wingtip, the incident and tip vortex feeding sheets interacted quite strongly and became entrained in the circulation of the opposite structure, which diminished the coherence of both vortices into the wake. Finally, when the incident vortex was positioned inboard of the wingtip, the vortex bifurcated in the time-mean sense with portions convecting above and below the wing. The increased effective angle of attack inboard of impingement enhanced the three-dimensional recirculation region created by the separated boundary layer off the leading edge which draws fluid from the incident vortex inboard and diminishes its impact on the outboard section of the wing. The slight but remaining downwash present outboard of impingement reduced the effective angle of attack in that region resulting in a small separation bubble on either side of the wing in the time-mean solution that effectively unloaded the tip outboard of impingement. All incident vortex positions provided substantial increases in the wing's lift-to-drag ratio; however, significant sustained rolling moments also resulted. As the vortex was brought inboard, the rolling moment diminished and eventually switched sign, indicating that small changes in vortex position can cause dramatic variations in the unsteady loading.

Vortex meandering and wandering effects on surface impingement were further studied in the more recent work of Garmann and Visbal.¹⁶ Here, the incident vortex was prescribed analytically upstream of the wing as before, but this time, it was defined with a sinusoidal variation in its spanwise position and its wandering

impact on the surface was examined. Two wandering amplitudes were considered, $a_y = 0.25c$ and $0.5c$, oscillating around a mean location measured $0.25c$ inboard of the wingtip at a normalized frequency of $f^* = fc/U_\infty = 0.2$. The imposed lateral motion of the vortex spatially evolved as it approached the wing by inclining relative to its initial horizontal trajectory and also diminished in amplitude. Just ahead of the wing, both wandering amplitudes were reduced by 36%, and the horizontal trajectory inclined by nearly 38° and 53° , respectively, for the initial wandering amplitudes of $0.5c$ and $0.25c$. This streamwise development of the incident vortex path has implications on the subsequent interaction with the wing, as the wing's streamwise position relative to the vortex self-induced motion dictates how the surface will be impacted. The vertical offset of the vortex core was also shown to drive an eventual pinch-off and alternating attachment to the upper and lower surfaces, which then evolved into a horseshoe-like structure before coalescing into a ring vortex and convecting into the wake. This is in contrast to the pinch-off experienced by a stationary vortex impacting a wing, which is driven by a spiraling instability in the vortex core induced by the upstream influence of the wing that reorients the vortex ahead of the leading edge. The wandering vortices examined exhibited no signs of the same spiraling undulation. This finding prevents conclusions about the flow structure engendered by a stationary vortex impingement from being generalized to the more dynamic wandering vortex interaction. Despite the differing pinch-off mechanisms, the unsteady loading experienced by the wing is shown to fall within the bounds of the time-mean loading of the stationary impinging vortices.

The purpose of the current work is to examine the unsteady interactions of a streamwise-oriented vortex impinging upon a NACA0012, finite wing. This is in an effort to build upon the two previous studies by the current authors on perpendicular vortex/body interactions that utilized a flat plate model at lower Reynolds number, $Re = 20,000$. In this study, however, the Reynolds number is an order of magnitude larger ($Re = 2.0 \times 10^5$) and a streamlined body, i.e. NACA0012 wing, is used. An analytically-defined vortex superimposed in a free stream is convected towards the finite wing to provide a canonical problem of perpendicular vortex/surface interactions. This allows fundamental understanding of the unsteady interaction in the absence of the many interrelated and complicated effects such as atmospheric turbulence, crow-instability, etc. that can lead to premature vortex distortion and breakdown that may be unassociated with the surface impingement.

II. Governing equations

The governing equations for the current work are the compressible, three-dimensional Navier-Stokes equations. After a general time-dependent transformation from Cartesian coordinates (x, y, z, t) to computational space (ξ, η, ζ, τ) , these equations can be written in strong conservation form¹⁷ as follows:

$$\frac{\partial}{\partial \tau} \left(\frac{\mathbf{U}}{J} \right) + \frac{\partial \mathbf{F}}{\partial \xi} + \frac{\partial \mathbf{G}}{\partial \eta} + \frac{\partial \mathbf{H}}{\partial \zeta} = \frac{1}{Re} \left[\frac{\partial \mathbf{F}_v}{\partial \xi} + \frac{\partial \mathbf{G}_v}{\partial \eta} + \frac{\partial \mathbf{H}_v}{\partial \zeta} \right] \quad (1)$$

where the solution vector is

$$\mathbf{U} = [\rho, \rho u, \rho v, \rho w, \rho e]^T \quad (2)$$

and the inviscid flux vectors are

$$\mathbf{F} = \frac{1}{J} \begin{bmatrix} \rho U \\ \rho u U + \xi_x p \\ \rho v U + \xi_y p \\ \rho w U + \xi_z p \\ (\rho e + p) U - \xi_t p \end{bmatrix}, \quad \mathbf{G} = \frac{1}{J} \begin{bmatrix} \rho V \\ \rho u V + \eta_x p \\ \rho v V + \eta_y p \\ \rho w V + \eta_z p \\ (\rho e + p) V - \eta_t p \end{bmatrix}, \quad \mathbf{H} = \frac{1}{J} \begin{bmatrix} \rho W \\ \rho u W + \zeta_x p \\ \rho v W + \zeta_y p \\ \rho w W + \zeta_z p \\ (\rho e + p) W - \zeta_t p \end{bmatrix} \quad (3)$$

In these expressions, $J = \partial(\xi, \eta, \zeta, \tau)/\partial(x, y, z, t)$ is the Jacobian of the transformation, and the metrics are $\xi_t = \partial \xi / \partial t$ and $\xi_x = \partial \xi / \partial x$, for example, with similar definitions for the other terms; u , v , and w are the Cartesian velocity components, ρ is the density, and p is the pressure. The contravariant velocities, U , V , and W , are

$$\begin{aligned} U &= \xi_t + \xi_x u + \xi_y v + \xi_z w \\ V &= \eta_t + \eta_x u + \eta_y v + \eta_z w \\ W &= \zeta_t + \zeta_x u + \zeta_y v + \zeta_z w \end{aligned} \quad (4)$$

and the specific internal energy, e , is

$$e = \frac{T}{\gamma(\gamma-1) M_\infty^2} + \frac{1}{2} (u^2 + v^2 + w^2) \quad (5)$$

where T is the temperature, γ is the ratio of specific heats, and M_∞ is the free stream Mach number. For the sake of brevity, the viscous fluxes, \mathbf{F}_v , \mathbf{G}_v , and \mathbf{H}_v , are not shown, but they are provided in Ref. 17, for instance.

The governing equations are also supplemented with the perfect gas equation, $p = \rho T / \gamma M_\infty^2$, and Sutherland's viscosity law. A constant Prandtl number ($Pr = 0.72$ for air) is assumed along with Stokes' hypothesis for the bulk viscosity coefficient ($\lambda = -2/3\mu$). All flow variables are normalized by their respective free stream counterparts, except for pressure, which is scaled by twice the dynamic pressure, $\rho_\infty U_\infty^2$. The reference length is taken as the wing chord, c .

This set of equations corresponds to the *unfiltered* Navier-Stokes equations and is used without change in laminar, transitional or fully turbulent regions of the flow for the ILES procedure. Unlike the standard LES approach, no additional subgrid-scale (SGS) model or heat flux terms are appended. Instead, a high-order, low-pass filter operator, which will be discussed later, is applied to the conserved variables during the solution of the standard Navier-Stokes equations. This highly-discriminating, Padé-type filter selectively damps only the high-frequency components of the solution, that are often times under-resolved by the mesh.¹⁸ The filtering regularization procedure provides an attractive alternative to the use of standard SGS models, and has been found to yield suitable results for several turbulent and transitional flows on LES level grids.¹⁹ A reinterpretation of this ILES approach in the context of an Approximate Deconvolution Model²⁰ has been provided by Mattheq *et al.*²¹ For low Reynolds numbers and/or high spatial resolutions, the ILES approach is effectively direct numerical simulation (DNS).

III. Numerical procedure

All simulations were performed with the extensively validated high-order, Navier-Stokes flow solver, *FDL3DI*.^{22,23} In this code, the governing equations are discretized through a finite-difference approach with all spatial derivatives obtained using high-order compact-differencing schemes.²⁴ The spatial derivative of any scalar quantity, ϕ , such as a metric, flux component, or flow variable, is obtained along a coordinate line in computational space by solving the following tridiagonal system:

$$\alpha \phi'_{i-1} + \phi'_i + \alpha \phi'_{i+1} = a \left(\frac{\phi_{i+1} - \phi_{i-1}}{2} \right) + b \left(\frac{\phi_{i+2} - \phi_{i-2}}{4} \right) \quad (6)$$

where proper choice of the coefficients, α , a , and b , provides up to sixth-order spatial accuracy. At boundary points, higher-order, one-sided formulae are utilized that retain the tridiagonal form of the scheme.^{22,23} For all the computations presented in this work, the interior coefficients are $\alpha = 1/3$, $a = 14/9$, and $b = 1/9$, which correspond to a sixth-order accurate, compact scheme. The boundary point and first off-boundary point use fourth- and fifth-order compact schemes, respectively.

The derivatives of the inviscid fluxes are obtained by forming the fluxes at the nodes and differentiating each component with the compact differencing scheme. Viscous terms are obtained by first computing the derivatives of the primitive variables and then constructing the components of the viscous fluxes at each node and differentiating by a second application of the same scheme.

In order to eliminate spurious components of the solution, a high-order, low-pass spatial filtering operator^{23,25} is applied to the conserved variables along each transformed coordinate direction one time after each time step or sub-iteration. If a typical component of the solution vector is denoted by ϕ , filtered values $\hat{\phi}$ at interior points in computational space satisfy,

$$\alpha_f \hat{\phi}_{i-1} + \hat{\phi}_i + \alpha_f \hat{\phi}_{i+1} = \sum_{n=0}^N a_n \left(\frac{\phi_{i-n} + \phi_{i+n}}{2} \right) \quad (7)$$

where proper choice of the coefficients, (a_0, a_1, \dots, a_N) , provides a $2N^{th}$ -order formula on a $2N + 1$ point stencil. The filtering technique is based on templates proposed by Lele²⁴ and Alpert;²⁶ The coefficients, along with representative filter transfer functions, can be found in the works of Gaitonde and Visbal.^{22,25}

The parameter, α_f , is left as a free variable in order to provide limited control of the cutoff frequency of the low-pass filter operator. Typical values are in the range: $0.3 \leq \alpha_f \leq 0.49$. For the near-boundary points, the filtering strategies described in Refs. 23 and 25 are used. For transitional and turbulent flows, the high-fidelity spatial algorithmic components provide an effective implicit LES (ILES) approach in lieu of traditional SGS models, as demonstrated in Refs. 18 and 27, and more recently by Garmann *et al.*¹⁹ All computations presented in this work utilized an eighth-order accurate interior filter with a coefficient of $\alpha_f = 0.40$ for targeted dissipation.

Time marching of the governing equations is achieved through the iterative, implicit approximately-factored integration method of Beam and Warming²⁸ and supplemented with the use of Newton-like sub-iterations to achieve second-order accuracy^{18,27} and reduce errors due to factorization, linearization, diagonalization, and explicit application of boundary conditions.²⁹ The block-tridiagonal form of the algorithm can be written in delta form as

$$\begin{aligned} & \left[\left(\frac{1}{J} \right)^{p+1} + \phi^i \Delta\tau \delta_\xi^{(2)} \left(\frac{\partial \mathbf{F}^p}{\partial \mathbf{U}} - \frac{1}{Re} \frac{\partial \mathbf{F}_v^p}{\partial \mathbf{U}} \right) \right] J^{p+1} \times \\ & \left[\left(\frac{1}{J} \right)^{p+1} + \phi^i \Delta\tau \delta_\eta^{(2)} \left(\frac{\partial \mathbf{G}^p}{\partial \mathbf{U}} - \frac{1}{Re} \frac{\partial \mathbf{G}_v^p}{\partial \mathbf{U}} \right) \right] J^{p+1} \times \\ & \left[\left(\frac{1}{J} \right)^{p+1} + \phi^i \Delta\tau \delta_\zeta^{(2)} \left(\frac{\partial \mathbf{H}^p}{\partial \mathbf{U}} - \frac{1}{Re} \frac{\partial \mathbf{H}_v^p}{\partial \mathbf{U}} \right) \right] \Delta \mathbf{U} \\ & = -\phi^i \Delta\tau \left[\left(\frac{1}{J} \right)^{p+1} \frac{(1+\phi)\mathbf{U}^p - (1+2\phi)\mathbf{U}^n + \phi\mathbf{U}^{n-1}}{\Delta\tau} + \mathbf{U}^p \left(\frac{1}{J} \right)_\tau^p + \right. \\ & \quad \left. \delta_\xi \left(\mathbf{F}^p - \frac{1}{Re} \mathbf{F}_v^p \right) + \delta_\eta \left(\mathbf{G}^p - \frac{1}{Re} \mathbf{G}_v^p \right) + \delta_\zeta \left(\mathbf{H}^p - \frac{1}{Re} \mathbf{H}_v^p \right) \right] \end{aligned} \quad (8)$$

where \mathbf{U}^p is the p^{th} approximation to \mathbf{U} at the $n+1$ time level and $\Delta \mathbf{U} = \mathbf{U}^{n+1} - \mathbf{U}^p$. For the first iteration $\mathbf{U}^p = \mathbf{U}^n$, and as $p \rightarrow \infty$, $\mathbf{U}^p \rightarrow \mathbf{U}^{n+1}$. The block-tridiagonal form of Eq. (8) is further simplified through the diagonalization of Pulliam and Chaussee,³⁰ and fourth-order, nonlinear dissipation terms^{31,32} are also appended to the implicit operator to augment stability, although these are not shown in Eq. (8) for clarity. Second-order finite differencing is used in the implicit operator, while high-order compact differencing is employed in the residual. Iteration drives the left-hand-side to zero, so only the high-order spatial error of the residual remains.

IV. Details of the computations

A. Geometry and vortex model

An analytically defined vortex is superimposed on a free stream and convected toward a wing as shown in Fig. 1. The NACA0012 wing has an aspect ratio of six ($AR = b/c = 6$) and is oriented at an angle of attack of $\alpha = 4^\circ$ relative to the free stream. The incident vortex is selected as a Batchelor or q-vortex vortex,³³ which provides a simple model with known stability properties. The vortex is superimposed into the incoming flow upstream of the wing and is described analytically as

$$u_r(r) = 0 \quad (9)$$

$$u_\theta(r) = \frac{\Gamma_0}{2\pi r} \left(1 - e^{-(r/r_0)^2} \right) \quad (10)$$

$$u_x(r) = 1 - \Delta u e^{-(r/r_0)^2} \quad (11)$$

where u_r , u_θ , and u_x correspond to the radial, circumferential, and axial velocities, respectively, Γ_0 is the vortex circulation, r_0 is a measure of the vortex radius, and Δu is the axial velocity deficit in the vortex core. Rather than circulation, the swirl parameter, q , is used to specify the strength of the vortex. This parameter is defined as

$$q = \frac{\Gamma_0}{2\pi r_0 \Delta u} \approx 1.567 \frac{V_0}{\Delta u} \quad (12)$$

where V_0 is the maximum circumferential velocity. This shows that q is a measure of the relative tangential and axial velocity intensities.³⁴ The circumferential velocity recast in terms of q becomes

$$u_\theta(r) = \frac{q \Delta u}{r/r_0} \left(1 - e^{-(r/r_0)^2}\right) \quad (13)$$

The radius, r , in the above equations is defined as

$$r = \sqrt{(y - y_c)^2 + (z - z_c)^2} \quad (14)$$

where (y_c, z_c) is the vortex center in a $x = \text{constant}$ inflow plane. The spanwise position, y_c , is

$$y_c = y_{\text{tip}} - \Delta y \quad (15)$$

where Δy is the distance measured inboard from the wingtip, y_{tip} as indicated in Fig. 1. Likewise, the vertical position, z_c , is

$$z_c = z_{\text{LE}} - \Delta z \quad (16)$$

where Δz is the distance measured below the wing's leading edge, z_{LE} . Preliminary computations, which are not presented here, showed that the vortex deflects upward as it approaches the wing and could convect completely over the wing when positioned at or above the leading edge in the vertical direction due to the accelerating flow over the lifting body. To prevent this and facilitate a more dramatic interaction of a head-on collision for this study, the incident vortex is, instead, positioned under the leading edge such that its axis intersects with the mid-chord of the wing ($\Delta z = 0.035$) in the vertical direction.

A stability criterion for the q -vortex was established by Leibovich and Stewartson³⁵ to prevent amplification of small-wave perturbations at any r . This restriction is given as

$$\sigma^2(r) = \frac{2u_\theta(r u'_\theta - u_\theta)(u_\theta^2/r^2 - u'_\theta^2 - u_x'^2)}{(r u'_\theta - u_\theta)^2 + (r u'_x)^2} < 0 \quad (17)$$

Substitution of Eqs. (11) and (13) into the stability criterion leads to a lower bound prediction on the swirl parameter of $q \geq \sqrt{2}$ to maintain stability of the vortex.

For the cases presented here, the swirl parameter is selected as $q = 2.0$ to prevent the vortex from breaking down prior to its interaction with the wing. To achieve a maximum circumferential velocity of $V_0 = 0.5 U_\infty$, the axial velocity deficit is chosen as $\Delta u = 0.4 U_\infty$. The vortex core radius is set as $r_0 = 0.1c$, and the Reynolds number based on wing chord and free stream velocity is selected as $Re = 2.0 \times 10^5$. Each of these parameters has been selected based on the previous work by the current authors¹⁵ and vortex profiles documented within the literature by the Euler computations of Kless *et al.*¹² and the experiments of Inasawa *et al.*³⁶ in which a lead wing was actually tested and the wake was analyzed. The estimated values for the maximum circumferential velocity and its radial location are listed in Table 1 along with details of the lead wing geometry and orientation. The maximum velocity radial location, $r_{u_{\max}}$, is related to the core radius of the Q-vortex by $r_{u_{\max}} \approx 1.121 r_0$, leading to the choice of $r_0/c = 0.1$ for the current study, which falls in between the values appearing in the reported literature.

Reference	Solution method	Lead wing	V_0/U_∞	$r_{u_{\max}}/c$
Kless <i>et al.</i> ¹²	Euler computations	NACA0012, AR=8, $\alpha \approx 4^\circ$	0.10	≈ 0.20
Inasawa <i>et al.</i> ³⁶	Experiments	NACA23012, AR=5, $\alpha = 8^\circ$	0.5	≈ 0.05

Table 1: Vortex profiles from the literature

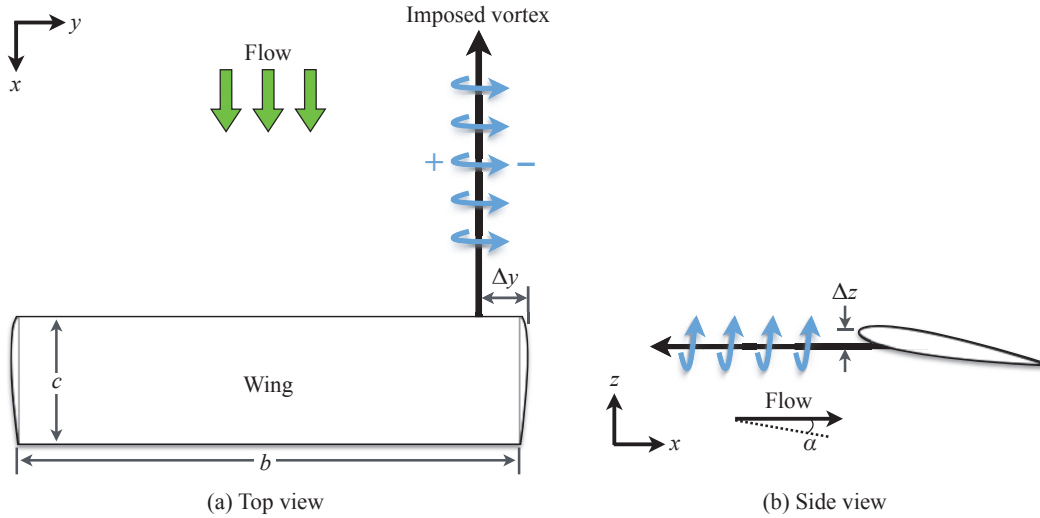


Figure 1: Streamwise-oriented vortex/wing configuration; (a) Top view, (b) Side view

B. Computational mesh and boundary conditions

A nested mesh system that utilizes Chimera overset³⁷ with high-order interpolation³⁸ has been created to efficiently discretize the domain around the wing. An extruded O-grid topology is utilized around the airfoil profile with 642 elements prescribed circumferentially and 1224 elements distributed along the span with a spacing of $\Delta y = 0.005c$ across the majority of the wing that decreases to a refined spacing of $0.002c$ near the wingtips. A C-grid topology is used to discretize the rounded wingtips that are wrapped by 100 elements, which can be seen in Fig. 2 along with the near-field O-grid and far field background mesh. The two surface mesh topologies are hyperbolically extruded normal from the surface with an initial spacing of $\Delta n = 0.5c \times 10^{-4}$ and increased stretching until reaching a distance of $1.0c$ from the wing. A stretched Cartesian background mesh then extends from the near field meshes to the far field boundaries, which are all located $100c$ from the surface except for the upstream boundary, which is positioned $10c$ ahead of the wing, resulting in a nested mesh system consisting of approximately 336 million cells.

The analytically-defined vortex is imposed on the upstream boundary and is allowed to convect freely into the domain. All other far field boundaries are prescribed as outflow conditions, which in conjunction with the increased grid-stretching and high-order filtering, provides a buffer-like treatment that prevents reflections from corrupting the interior of the domain. The wing surface is set as a no-slip, adiabatic wall enforced by a fourth-order-accurate, zero-normal pressure gradient.

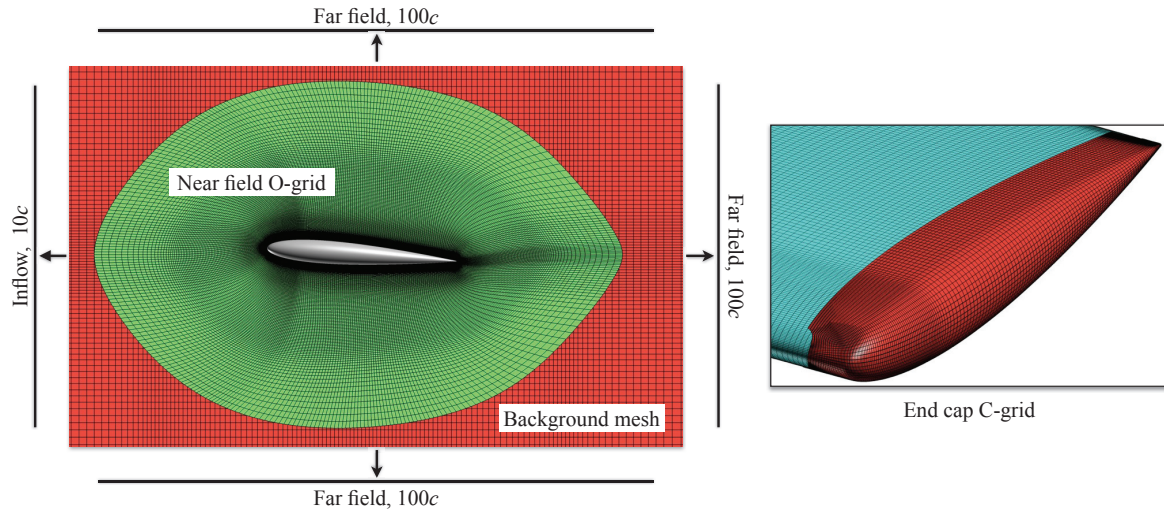


Figure 2: The O-grid airfoil profile mesh, surface mesh, and wing end cap. Every other gridline is shown for clarity

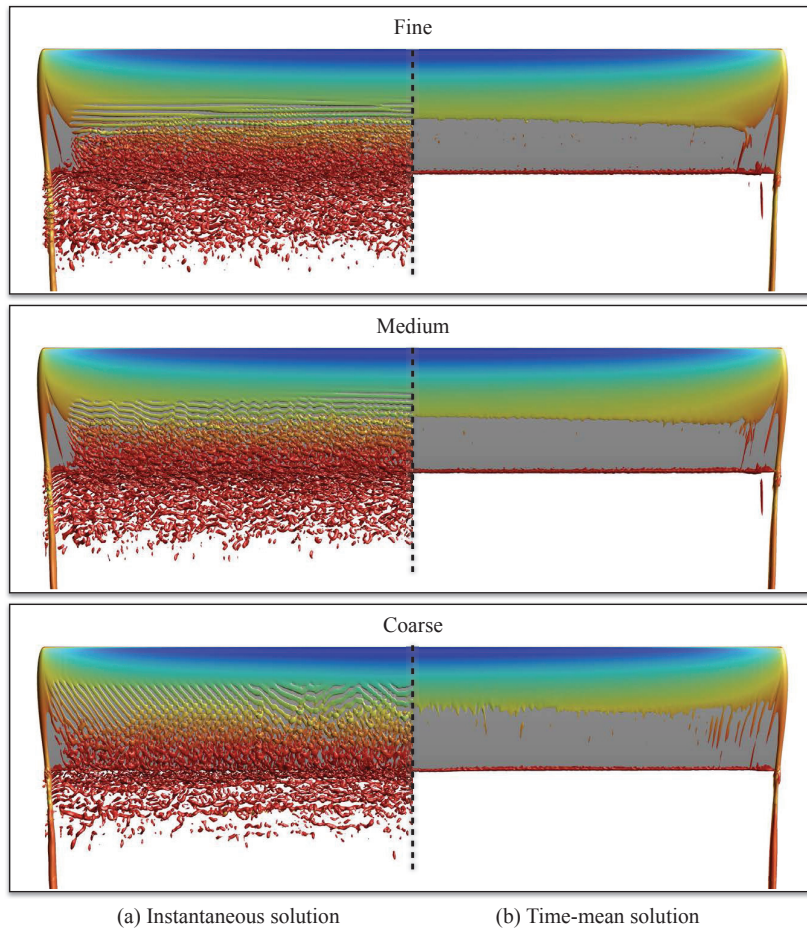
C. Effects of spatial resolution on the baseline configuration

The sensitivity of the computed solutions to spatial resolution is demonstrated on a clean configuration of a stationary wing without an incident vortex, oriented at an angle of $\alpha = 4^\circ$ and operating at a Reynolds number of $Re = 2.0 \times 10^5$. The grid system that was described above is referred to as the fine resolution and is coarsened in the streamwise and normal directions in order to provide two meshes of geometric similarity for comparison. The spanwise discretization is left unaltered as this direction is the most limiting at such a large aspect ratio, and further reductions in resolution may disallow transition of the flow. The medium resolution is formed by coarsening the fine mesh by 75% in both the streamwise and normal directions, while the coarse resolution corresponds to directional coarsening of 50%. Details of the total cell counts for each grid system are listed in Table 2 along with the maximum surface spacings in the normal, streamwise, and spanwise directions.

All simulations are initialized with free-stream quantities and allowed to evolve for 20 convective times with a time step of $\Delta\tau = 5.0 \times 10^{-5}$ to establish the flow around the wing and wash out spurious transients associated with the startup. Time-mean and statistical information is then gathered over an additional 10 convective times and is presented below.

Figure 3 depicts the instantaneous and time-mean flow over the suction side of the wing. Due to the flow symmetry about mid-span, only half of the two flow realizations are shown on either side of the wing. The instantaneous flow structure is characterized by a separated shear layer that rolls-up into discrete spanwise vortices around midchord. These small structures become susceptible to spanwise Kelvin-Helmholtz instabilities that grow after reattachment of the flow and quickly transition into the wake. The fine and medium resolutions show this unsteady progression quite similarly; however, the coarse mesh lacks necessary resolution to allow the flow to separate across the entire span, leading to more streamwise-oriented structures that transition differently. The time-mean flow masks the transitional and turbulent structures as they are uncorrelated in time and instead, shows a laminar separation bubble as a thin structure along the surface for each resolution. The laminar tip vortex is also well-defined and discernible in both flow realizations.

Mesh	Total cell count	Maximum surface spacings ($\times 10^3$)		
		Normal	Streamwise	Spanwise
Fine	336,105,248	0.052	5.093	5.000
Medium	182,037,936	0.069	6.784	5.000
Coarse	82,509,186	0.103	10.186	5.000

Table 2: Details of the computational domains**Figure 3:** Effect of spatial resolution on the (a) instantaneous and (b) time-mean solutions shown through iso-surfaces of Q-criterion ($Q = 25$) colored by pressure

A quantitative measure of the spatial resolution quality is provided by wall-normalized spacings from the time-mean solution measured at a location past reattachment, $x/c = 0.8$, along the wing's mid-span. These values in the normal, streamwise, and spanwise directions are listed in Table 3. Each mesh provides adequate resolution for LES based on the recommendations of Georgiadis *et al.*;³⁹ however, the coarsest resolution is quite marginal in the streamwise and normal directions, which likely results in the odd transitional behavior seen in Fig. 3. Additionally, the time-averaged lift, drag and pitching moment coefficients are listed in Table 4. These quantities show a good collapse with increased resolution indicating that the relevant scales associated with the integrated quantities have been adequately captured.

Finally, the time-mean skin friction profile at the mid-span and the sectional lift distribution across the wing are shown in Figs. 4(a) and (b), respectively. The mid-span skin friction shows no separation

with the coarse resolution and a very slow transition process. The medium and fine resolutions, however, exhibit separation around $x/c = 0.4$ and reattachment just before $x/c = 0.6$, which is accompanied by an abrupt transition. These profiles also show a good collapse with grid refinement with the medium mesh promoting only a minor upstream shift of transition from the fine mesh solution due to the added numerical dissipation that causes the flow to reattach slightly sooner. The sectional lift distribution across the wing in (b) tells a similar story with the coarse resolution showing an odd behavior away from mid-span where the odd streamwise-oriented sub-structures were seen, and the medium and fine resolutions are almost indistinguishable.

The very small sensitivity of spatial resolution on the flow between the medium and fine resolutions provides necessary confidence in the *fine* mesh to be used in the remainder of this study.

Table 3: Mesh spacings in wall units on the surface measured along the wing's mid-span at $x/c = 0.8$

Mesh	Normal	Streamwise	Spanwise
Fine	0.345	36.3	35.7
Medium	0.480	50.6	35.9
Coarse	0.695	73.1	37.3

Table 4: Effect of spatial resolution on the time-mean loading

Mesh	C_L	C_D	C_M
Fine	0.367	0.0183	-0.0104
Medium	0.364	0.0183	-0.0097
Coarse	0.350	0.0179	-0.0061

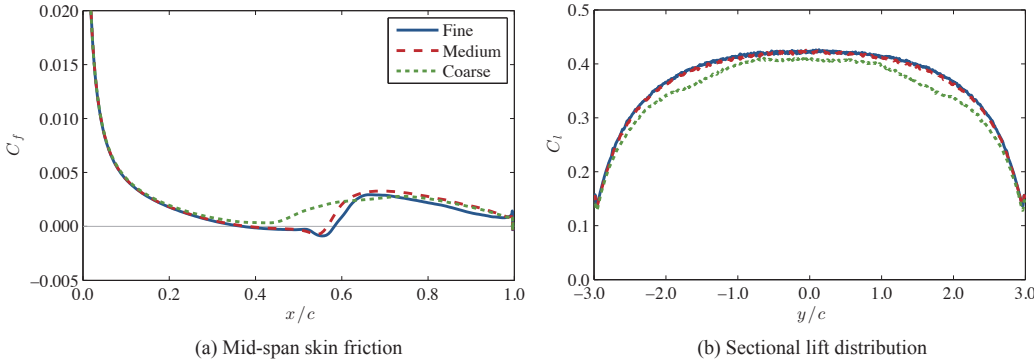


Figure 4: Effect of spatial resolution on the time-mean profiles of (a) mid-span skin friction coefficient and (b) sectional lift coefficient along the span

V. Results

In this section, the unsteady and time-mean flow structure are examined for a tip-aligned and an inboard-positioned incident vortex. All simulations utilize a nondimensional time step of $\Delta\tau = 5.0 \times 10^{-5}$, and the flow fields are initialized with free stream conditions, except at the inflow plane, where the incident vortex is prescribed at the appropriate spanwise position. The vortex required 10 convective times to reach the wing, and an additional 70 convective times to achieve a well-established interaction. Time-mean and statistical information is then gathered over another 10 convective times.

A. Description of the unsteady flow structure

The instantaneous flow structure is depicted in Figs. 5 and 6 for the tip-aligned and inboard interactions, respectively. Iso-surfaces of Q-criterion colored by pressure are presented over the suction and pressure sides of the wing along with additional insets of the encounter for clarity. On the far side of the wing, away from the interaction, both flows show a very similar structure over the suction side of the wing that closely resembles the baseline flow with no vortex that was shown in Fig. 3. In this region, a well-defined tip vortex exists along with a separated shear layer around mid-chord that rolls up and sheds as discrete vortices that transition and breakdown into the wake. Moving inboard, towards the interaction, however, a departure from the baseline configuration is quickly observed. For both vortex positions, the increasing upwash with closer proximity to the incoming vortex promotes an earlier separation and transition of the shear layer that reaches the leading edge just inboard of impingement. With tip-aligned positioning (Fig. 5), the incoming structure reorients just ahead of the leading edge and is permitted completely to the suction side of the wing, leaving the wing's underside mostly undisturbed. Persistent interaction with the tip vortex and transitional substructures off the surface leads to attenuation of the incident vortex into the wake as instabilities quickly arise within its feeding sheet.

Inboard positioning of the incident vortex (Fig. 6) exposes an outboard section of the wing to the incoming structure's downwash that reduces the effective angle of attack in that region, resulting in a mostly attached flow over the limited spanwise extent and virtually suppresses the tip vortex formation. At the impingement location, separation is noticeable on either side of the wing from the unsteady interaction of the incident vortex along the wing's leading edge, which is shown in more detail in Fig. 7. Here, several instances are depicted through iso-surfaces of total pressure, which are used to highlight the core dynamics a little more clearly while masking many of the small scale, transitional features. At instant (i), the incoming structure is completely deflected over the suction side of the wing leading to very little underside disruptions. However, a moment later (ii), the induced spiral of the vortex core upstream of the wing reorients the structure ahead of the leading edge allowing portions of its outer shear layer to spill onto the wing's pressure side, forcing the core to pinch off at the leading edge. In instant (iii), the incident vortex has deflected to the underside of the wing before its evolving spiral yields an alternate pinch-off and upper side deflection a moment later that returns the flow to the state observed in (i).

A measure of the spiraling frequency is provided in Fig. 8 through the turbulent kinetic energy spectra extracted from within the vortex core just upstream of the wing, $x/c = -0.1$. For the inboard position ($\Delta y = 1.0$), a dominant frequency is observed at a Strouhal number of $St = 1.1$, which corresponds to the frequency of the upper/lower surface deflection and pinch-off of the incident vortex. Several lower power harmonics are also seen in the spectra resulting from slight phase differences in the signal. The same frequency is also observed in the core of the tip-aligned vortex, but at much lower power. As it turns out, the tip-aligned vortex exhibits a similar spiraling mode as it nears the wing, however, to a much lesser extent that never permits the structure to the underside of the wing. Persistent interaction of the incident structure with the tip vortex does lead to a more pronounced spiraling instability as it passes over the wing and into the wake. It is interesting to note that the core dynamics of the spiraling mode closely relates to those observed for streamwise-oriented vortex interactions over a flat plate operating at a Reynolds number of $Re = 20,000$.¹⁵ Despite the differences in geometry and Reynolds number between this study and that of Ref. 15, the same frequency and unsteady mode of interaction results, indicating that it is, indeed, a character of the chosen vortex size and strength.

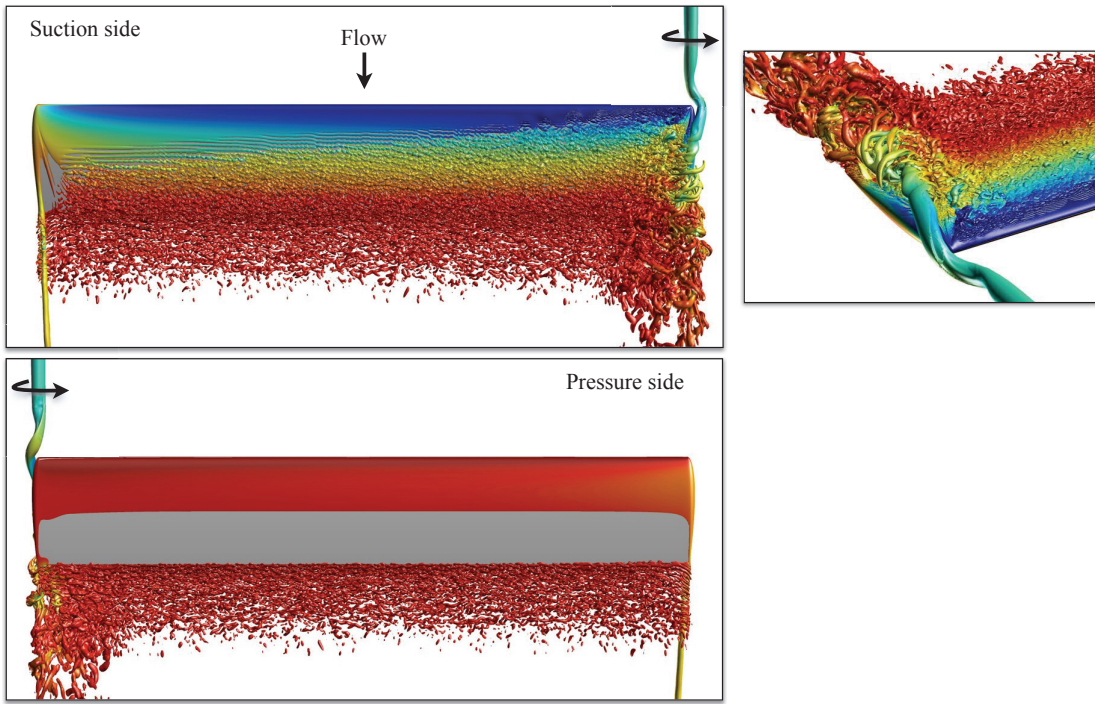


Figure 5: Instantaneous flow structure of a tip-aligned impingement

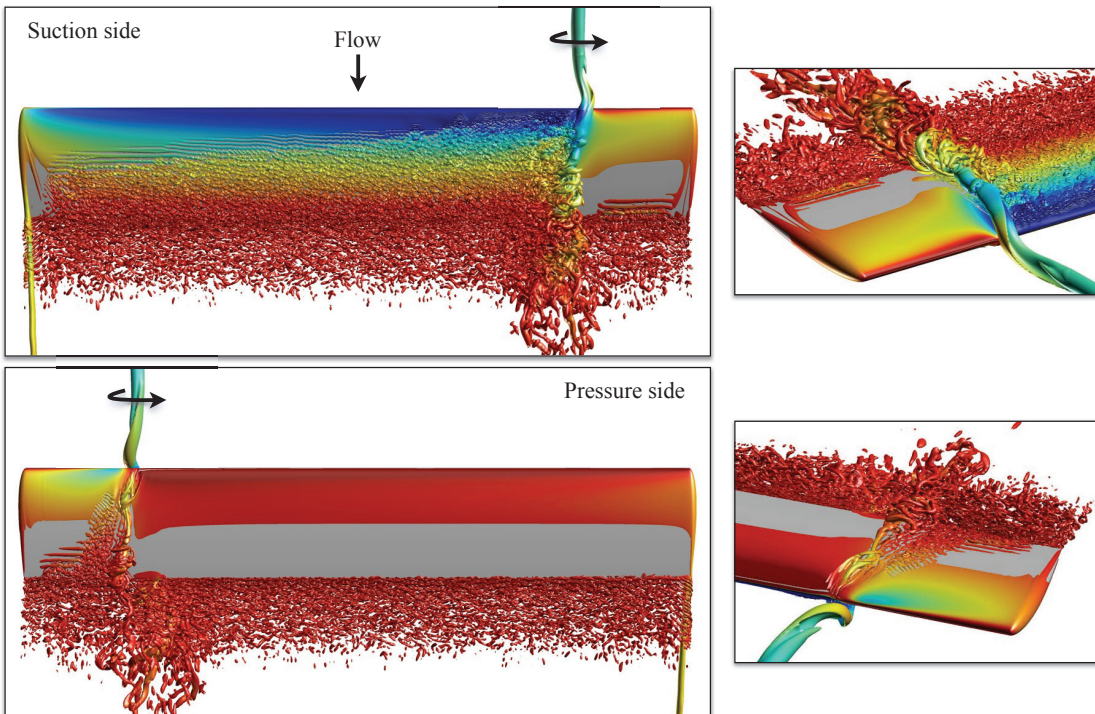


Figure 6: Instantaneous flow structure of an inboard positioned impingement

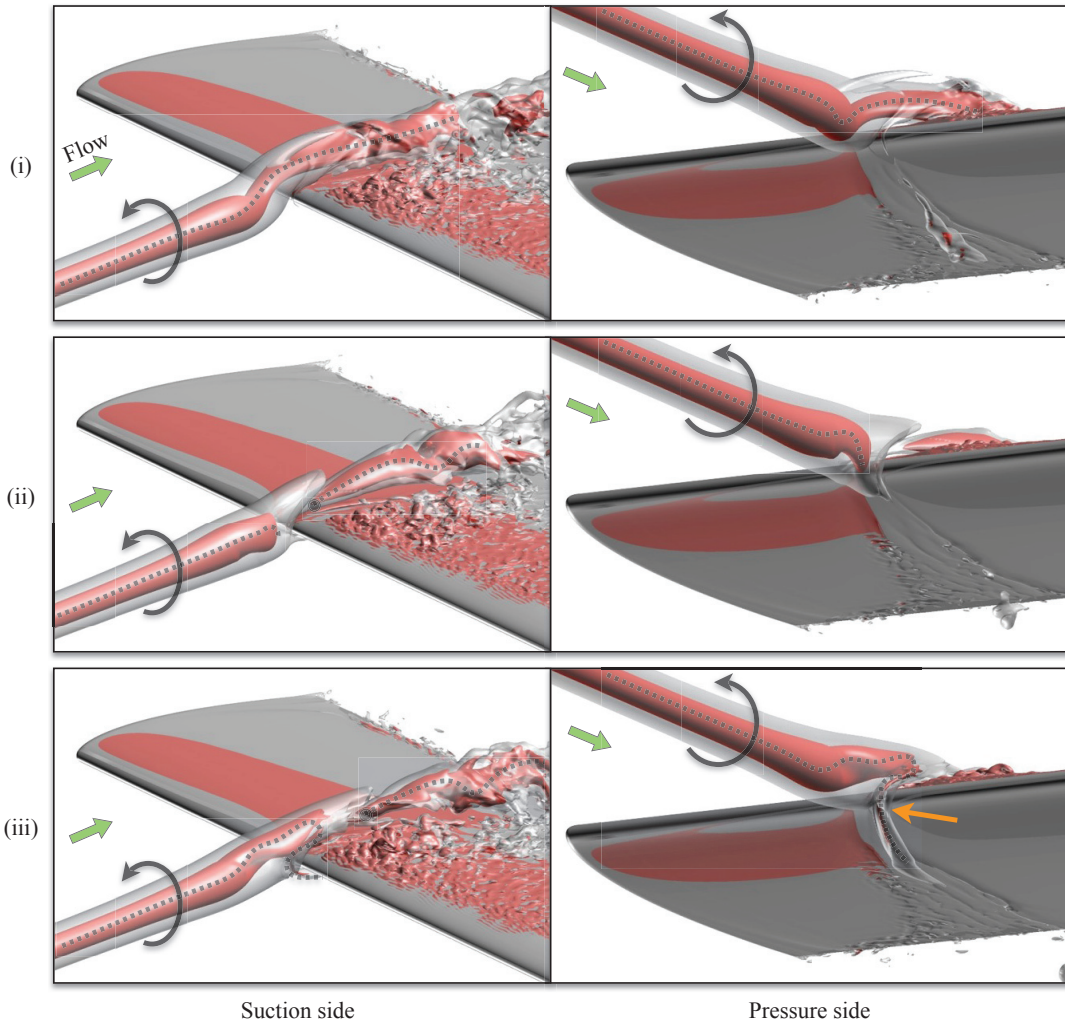


Figure 7: Dual iso-surfaces of instantaneous total pressure showing the spiraling impingement of the incident vortex characterized by (i) suction side deflection, (ii) leading edge pinch-off, and (iii) pressure side deflection. Flow direction and incident vortex orientation are shown by arrows for each view.

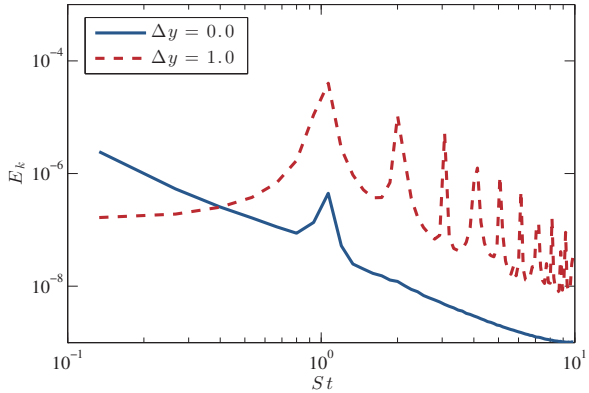


Figure 8: Turbulent kinetic energy spectra in the vortex core upstream of the wing ($x/c = -0.1$)

B. Description of the time-mean flow structure

The time-mean flow structure resulting from the tip-aligned and inboard-positioned incident vortex is displayed in Fig. 9 through iso-surfaces of Q-criterion ($\bar{Q} = 10$). The baseline wing with no incoming structure is also shown for comparison. As with the unsteady analysis presented in the previous section, the tip-aligned vortex is observed completely deflected to the suction side of the wing with no residual impact noticeable on the underside. For the inboard vortex, however, the unsteady spiraling impingement along the leading edge presents as a vortex bifurcation in the time-mean solution with portions of the vortex seen on either side of the wing, which are denoted as IV1 and IV2 in Fig. 9(c). The increased effective angle of attack inboard of impingement that led to an earlier separation and transition in the unsteady solution, also promotes an earlier attachment of the laminar separation bubble near the impingement in the time-mean flow.

A closer look at the impingement for both cases is presented in Fig. 10, where an almost self-similar solution is exhibited inboard of impingement regardless of vortex position. This is characterized by a minor induced separation just inboard of the incident vortex likely as a result of the extreme angles of attack, followed by a well-behaved line of attachment that extends farther downstream with decreasing and moderate angles of attack away from impingement. These points are emphasized again with the surface-restricted streamlines and surface pressure distributions in Fig. 11 for each configuration. The incident vortex encounter promotes an earlier separation and attachment of the boundary layer off the leading edge due to the increased effective angle of attack inboard of impingement, resulting in a shorter separation bubble in the time-mean solution, which is also accompanied by increased suction. Outboard of impingement for $\Delta y = 1.0$, the attached flow promotes similarly sized regions of suction due on either side of the wing, which has implications on the loading. These effects can be seen in the sectional lift coefficient plotted in Fig. 13(a). Outboard of impingement for $\Delta y = 1.0$, the attached flow with canceling regions of suction on either side of the wing effectively unloads the wingtip, yielding no benefits to lift production. In general, however, significant lift augmentation is observed across the majority of the wing when compared to the baseline wing, with a peak sectional lift observed $1.0c$ inboard of impingement for both cases. Skin friction profiles at the position of peak sectional lift are shown in Fig. 13(b), where, again, the self-similarity of the two vortex positions is seen. Returning to the sectional lift, this peak lift corresponds to an effective angle of attack around $\alpha_{\text{eff}} \approx 11.5^\circ$, which is very near the stall angle of the NACA0012 airfoil. The minor separation or stall experienced just inboard of impingement but outboard of the peak lift position can account for some of the lift reduction, however, another effect is also to blame. As the laminar separation bubble continues its collapse and moves upstream as it approaches the incident vortex, its shrinking, but enhanced region of suction also moves forward, and eventually along the curved leading edge. This forward tilts the normal force vector and brings it out of alignment with the lift, but also leads to a slight reduction in drag.

Next, the incoming vortex is dissected and shown through contours of time-mean streamwise vorticity in Fig. 12 as it interacts with the wing. The view is directed from a downstream location towards the inflow boundary, and the incoming vortex is identified by negatively-signed (blue) vorticity in each image. The slices start $0.5c$ upstream of the wing and end $1.5c$ into the wake. With tip alignment (b), the incident

vortex remains largely coherent and intact through its interaction with the wing. The tip vortex is apparent across the chord of the wing, but is mostly encompassed by the incident vortex until the wake, where the incoming structure is propelled upward slightly, allowing the tip vortex to entrain the same-signed vorticity from the boundary layer off the wing's underside. Progressing further into the wake, the tip vortex quickly loses its coherence from the persistent interaction of the pair. Inboard positioning of the incident vortex is shown in (c). The time-mean structure undergoes a bifurcation as it impacts the wing's leading edge with portions convecting over either side of the wing that persist as independent and coherent structures into the wake, labeled as IV1 and IV2. Along the wing's chord, both structures interact and pair with their corresponding images in the wing surface which leads to a slight inboard shifting of the upper surface vortex and outboard progression for the underside vortex. Past the trailing edge, the wall-induced vorticity formed between the incident vortices and the wing surface on either side coalesces into a shear layer vortex (SLV) that is reminiscent of the tip vortex seen in the baseline and tip-aligned cases.

Finally, the mean aerodynamic loading is listed in Table 5. Both vortex positions achieve significant lift enhancement and drag reduction over the baseline wing, however, the loss of lift from the unloaded tip for inboard positioning is evident. The pitching moment is also less pitch-down with the addition of the incoming vortex from the increased suction ahead of the aerodynamic center. A significant rolling moment, C_X , is encountered with the tip-aligned vortex from the variable loading that increases near the wingtip. The inboard-aligned vortex also shows a rolling moment but of opposite sign as the unloaded tip outboard of impingement balances the enhanced loading inboard.

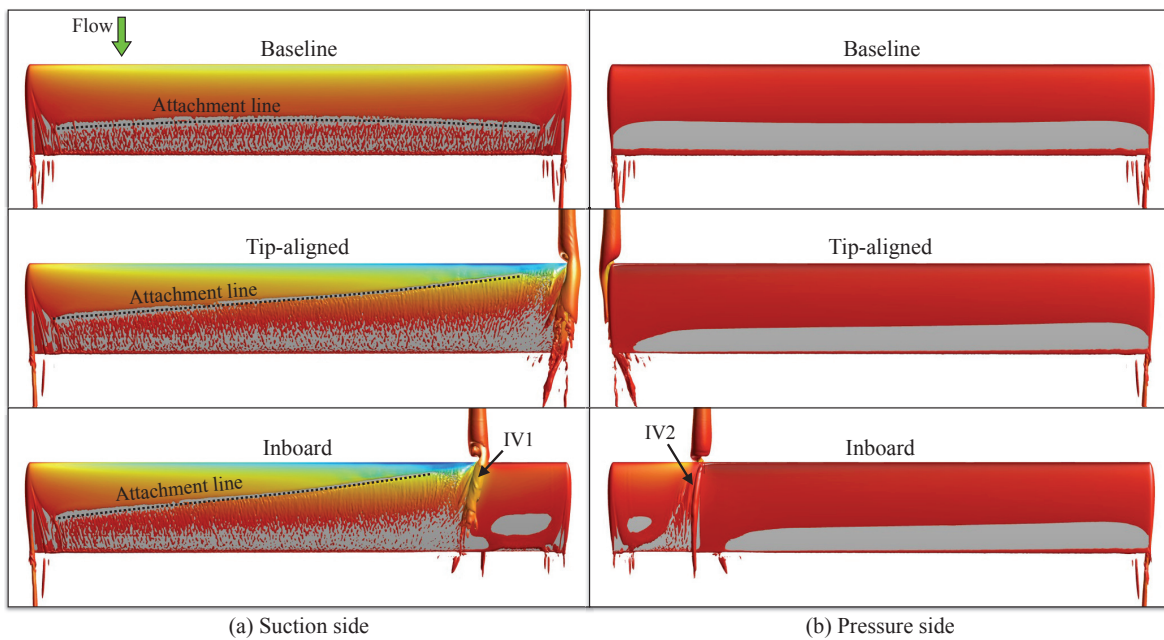


Figure 9: Time-mean flow structure (iso-surfaces of Q-criterion, $Q = 10$) of the baseline configuration along with the tip-aligned and inboard positioned incident vortices.

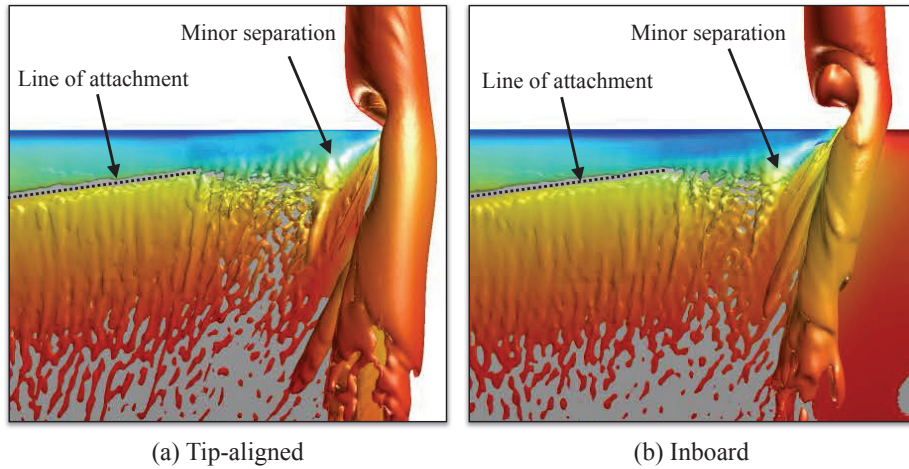


Figure 10: Self-similarity of the time-mean flow structure inboard of impingement

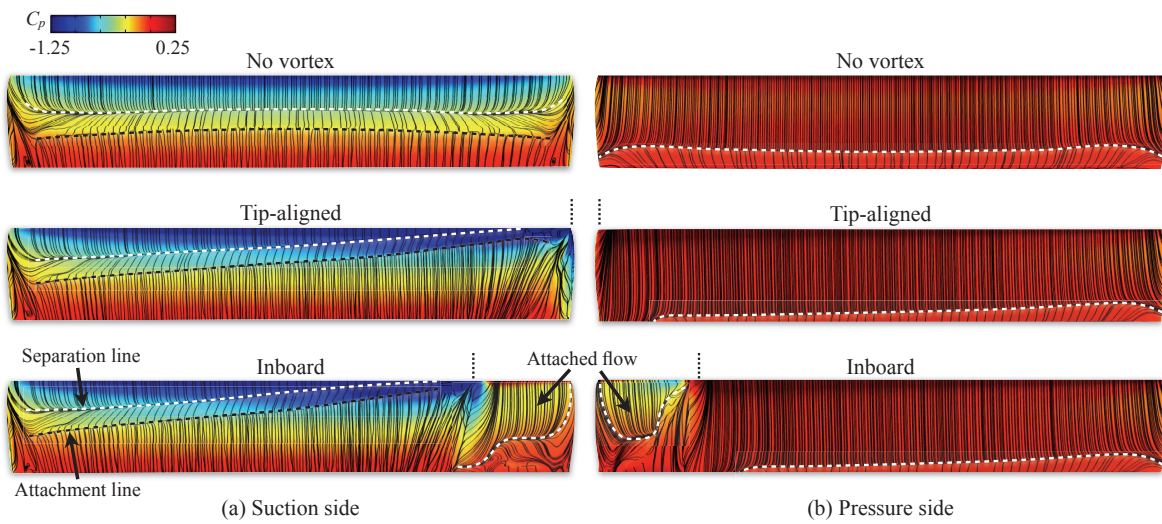


Figure 11: Surface streamlines and pressure distributions on the suction and pressure sides of the wing

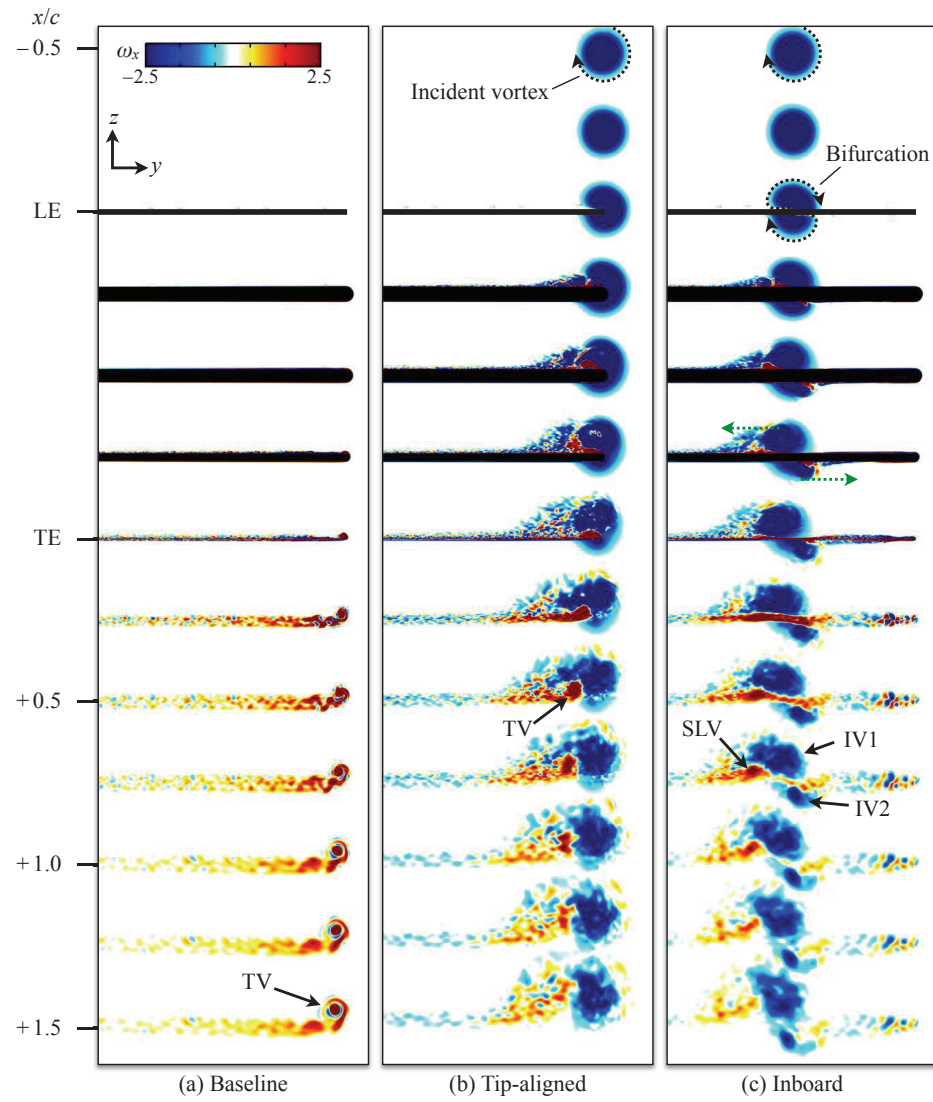


Figure 12: Time-mean streamwise vorticity contours dissecting the incident vortex near the wingtip: (a) No vortex, (b) Tip-aligned, (c) Inboard. TV: tip vortex, SLV: shear layer vortex, IV: incident vortex

Mesh	C_L	C_D	C_M	C_X
Baseline	0.367	0.0183	-0.0104	0.006
Tip-aligned	0.532	0.0025	-0.0035	0.176
Inboard	0.447	0.0013	-0.0043	-0.086

Table 5: Effect of vortex position on the time-mean loading

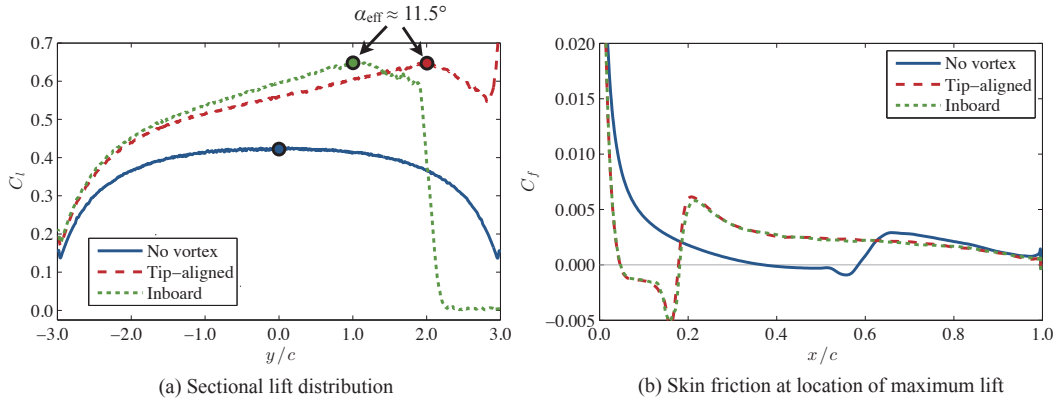


Figure 13: Skin friction profiles at position of maximum sectional lift and corresponding lift distribution

VI. Conclusions

In this work, the unsteady modes of interaction and taxonomy of a streamwise-oriented vortex impacting a NACA0012 wing were investigated using high-fidelity numerical simulation. The incident vortex was prescribed analytically upstream of an aspect-ratio-six wing that was operating at a Reynolds number of $Re = 2.0 \times 10^5$. Tip-aligned and inboard-positioned incident vortices were examined and shown to produce rich dynamics through their impingement with the wing. This included a self-similar flow structure inboard of impingement, whereby earlier separation, reattachment, and abrupt transition of the shear layer were encountered with closer proximity to the incoming vortex. Inboard positioning of the vortex exposed the wingtip to the incident vortex downwash that reduced the effective angle, resulting in a mostly attached flow outboard of impingement and effectively unloaded the wingtip. The observed core dynamics of the impingement included the development of a spiraling mode instability that alternately deflected the vortex over the suction and pressure sides of the wing. These findings, along with the outboard unloading of the wingtip, are consistent with a previous study for flat plates and much lower Reynolds numbers, which can be of significance for directing future LES investigations with much lower computational expense.

Acknowledgements

This work is supported in part by AFOSR under a task monitored by Dr. D. Smith and also by a grant of HPC time from the DoD HPC Shared Resource Centers at AFRL and ERDC.

References

- ¹Rockwell, D., "Vortex-body interactions," *Annual Review of Fluid Mechanics*, Vol. 30, 1998, pp. 199–229.
- ²Crow, S. C., "Stability Theory of a Pair of Training Vortices," *AIAA Journal*, Vol. 8, 1970, pp. 2172–2179.
- ³Gordnier, R. E. and Visbal, M. R., "Numerical Simulation of the Impingement of Streamwise Vortex on a Plate," *International Journal for Computational Fluid Dynamics*, Vol. 12, No. 1, 1999, pp. 49–66.
- ⁴Visbal, M. and Gordnier, R., "On the Structure of the Shear Layer Emanating from a Swept Leading Edge at Angle of Attack," AIAA Paper 2003-4016, AIAA, 2003.
- ⁵Richez, A., Le Pape, A., Costes, M., and Gavéraiaux, R., "Zonal Detached-Eddy Simulation (ZDES) of the three-dimensional stalled flow around a finite span wing," AIAA Paper 2012-3281, AIAA, 2012.
- ⁶Heyes, A. L., Jones, R. F., and Smith, D. A. R., "Wandering of wing-tip vortices," *12th International Symposium on Application of Laser Techniques to Fluid Mechanics*, Lisbon, Portugal, July 2004.
- ⁷Hummel, D., "Aerodynamic Aspects of Formation Flight in Birds," *Journal of Theoretical Biology*, Vol. 104, No. 3, 1983, pp. 321–347.
- ⁸Hummel, D., "Formation Flight as an Energy-Saving Mechanism," *Israel Journal of Zoology*, Vol. 41, No. 3, 1995, pp. 261–278.
- ⁹Beukenberg, M. and Hummel, D., "Aerodynamics, Performance and Control of Airplanes in Formation Flight," *Proceedings of the 17th Congress of the International Council of the Aeronautical Sciences*, Vol. 2, September 1990, pp. 1777–1794.
- ¹⁰Lissaman, P. B. S. and Shollenberger, C. A., "Formation Flight of Birds," *Science*, Vol. 168, No. 3934, May 1970, pp. 1003–1005.
- ¹¹Ning, S. A., Flanzer, T. C., and Kroo, I. M., "Aerodynamic Performance of Extended Formation Flight," AIAA Paper 2010-1240, AIAA, 2010.
- ¹²Kless, J., Aftosmis, M. J., Ning, S. A., and Nemec, M., "Inviscid Analysis of Extended-Formation Flight," *AIAA Journal*, Vol. 51, No. 7, July 2013.
- ¹³Jacquin, L., Fabre, D., and Geffroy, P., "The properties of a transport aircraft wake in the extended near field: an experimental study," AIAA Paper 2001-1038, AIAA, 2001.
- ¹⁴Barnes, C. J., Visbal, M. R., and Gordnier, R. E., "Investigation of aeroelastic effects in streamwise-oriented vortex/wing interactions," AIAA Paper 2014-1281, AIAA, 2014.
- ¹⁵Garmann, D. and Visbal, M., "Interaction of a streamwise-oriented vortex with a wing," AIAA Paper 2014-1282, AIAA, 2014.
- ¹⁶Garmann, D. J. and Visbal, M. R., "Unsteady interactions of a wandering streamwise-oriented vortex with a wing," AIAA Paper 2014-2105, AIAA, 2014.
- ¹⁷Tannehill, J., Anderson, D., and Pletcher, R., "Computational Fluid Mechanics and Heat Transfer," *Series in computational and physical processes in mechanics and thermal sciences*, Taylor & Francis, 2nd ed., 1997.
- ¹⁸Visbal, M. and Rizzetta, D., "Large-Eddy Simulation on Curvilinear Grids Using Compact Differencing and Filtering Schemes," *Journal of Fluids Engineering*, Vol. 124, 2002, pp. 836–847.
- ¹⁹Garmann, D., Visbal, M., and Orkwis, P., "Comparative study of implicit and subgrid-scale model large-eddy simulation techniques for low-Reynolds number airfoil applications," *International Journal for Numerical Methods in Fluids*, Vol. 71, No. 12, 2013, pp. 1546–1565.
- ²⁰Stolz, S. and Adams, N., "An Approximate Deconvolution Procedure for Large-Eddy Simulation," *Physics of Fluids*, Vol. 11, No. 7, 1999, pp. 1699–1701.
- ²¹Matthew, J., Lechner, R., Foysi, H., Sesterhenn, J., and Friedrich, R., "An Explicit Filtering Method for LES of Compressible Flows," *Physics of Fluids*, Vol. 15, No. 8, 2003, pp. 2279–2289.
- ²²Gaitonde, D. and Visbal, M., "High-Order Schemes for Navier-Stokes Equations: Algorithm and Implementation into FDL3DI," Technical Report AFRL-VA-WP-TR-1998-3060, Air Force Research Laboratory, Wright-Patterson AFB, 1998.
- ²³Visbal, M. and Gaitonde, D., "High-Order Accurate Methods for Complex Unsteady Subsonic Flows," *AIAA Journal*, Vol. 37, No. 10, 1999, pp. 1231–1239.
- ²⁴Lele, S., "Compact Finite Difference Schemes with Spectral-like Resolution," *Journal of Computational Physics*, Vol. 103, No. 1, 1992, pp. 16–42.
- ²⁵Gaitonde, D. and Visbal, M., "Further Development of a Navier-Stokes Solution Procedure Based on Higher-Order Formulas," AIAA Paper 99-0557, AIAA, 1999.
- ²⁶Alpert, P., "Implicit Filtering in Conjunction with Explicit Filtering," *Journal of Computational Physics*, Vol. 44, No. 1, 1981, pp. 212–219.
- ²⁷Visbal, M., Morgan, P., and Rizzetta, D., "An Implicit LES Approach Based on High-Order Compact Differencing and Filtering Schemes," AIAA Paper 2003-4098, AIAA, June 2003.
- ²⁸Beam, R. and Warming, R., "An Implicit Factored Scheme for the Compressible Navier-Stokes Equations," *AIAA Journal*, Vol. 16, No. 4, 1978, pp. 393–402.
- ²⁹Rizzetta, D., Visbal, M., and Morgan, P., "A High-Order Compact Finite-Difference Scheme for Large-Eddy Simulation of Active Flow Control (Invited)," AIAA Paper 2008-526, AIAA, 2008.
- ³⁰Pulliam, T. and Chaussee, D., "A Diagonal Form of an Implicit Approximate-Factorization Algorithm," *Journal of Computational Physics*, Vol. 17, No. 10, 1981, pp. 347–363.
- ³¹Jameson, A., Schmidt, W., and Turkel, E., "Numerical Solutions of the Euler Equations by Finite Volume Methods Using Runge-Kutta Time Stepping Schemes," AIAA Paper 1981-1259, AIAA, 1981.
- ³²Pulliam, T., "Artificial Dissipation Models for the Euler Equations," *AIAA Journal*, Vol. 24, No. 12, Dec. 1986, pp. 1931–1940.
- ³³Batchelor, G., "Axial Flow in trailing line vortices," *Journal of Fluid Mechanics*, Vol. 20, No. 4, 1964, pp. 645–658.

³⁴Jacquin, L. and Pantano, C., "On the persistence of trailing vortices," *Journal of Fluid Mechanics*, Vol. 471, November 2002, pp. 159–168.

³⁵Leibovich, S. and Stewartson, K., "A sufficient condition for the instability of columnar vortices," *Journal of Fluid Mechanics*, Vol. 126, January 1983, pp. 335–356.

³⁶Inasawa, A., Mori, F., and Asai, M., "Detailed Observations of Interactions of Wingtip Vortices in Close-Formation Flight," *Journal of Aircraft*, Vol. 49, No. 1, January–February 2012.

³⁷Steger, J., Dougherty, F., and Benek, J., "A Chimera Grid Scheme," *Advances in Grid Generation*, edited by K. Ghia and U. Ghia, Vol. 5, American Society of Mechanical Engineers, 1983, pp. 59–69.

³⁸Sherer, S. and Scott, J., "High-Order Compact Finite-Difference Methods on General Overset Grids," *Journal of Computational Physics*, Vol. 210, No. 2, 2005, pp. 459–496.

³⁹Georgiadis, N., Rizzetta, D., and Fureby, C., "Large-Eddy Simulation: Current Capabilities, Recommended Practices, and Future Research," *AIAA Journal*, Vol. 48, No. 8, 2010.

APPENDIX E

Analysis of the Onset of Dynamic Stall Using High-Fidelity Large-Eddy Simulations

Miguel R. Visbal *

*Aerospace Systems Directorate
Air Force Research Laboratory
Wright-Patterson AFB, OH 45433*

The onset of unsteady separation and dynamic stall vortex formation over a constant-rate pitching airfoil is analyzed by means of high-fidelity large-eddy simulations. The flow fields are computed employing a previously developed and extensively validated high-fidelity implicit large-eddy simulation (ILES) approach. This methodology is based on a 6th-order compact-differencing scheme augmented by an 8th-order lowpass spatial filter which provides an effective alternative to standard sub-grid-stress regularization. The primary case studied consists of a SD7003 airfoil section at a freestream Mach number $M_\infty = 0.1$ and chord Reynolds numbers $Re_c = 0.5 \times 10^6$. The wing is pitched about its quarter chord axis at a nominal constant rate $\Omega_o^+ = 0.05$ from a small initial incidence to a high angle of attack beyond the onset of dynamic stall. The unsteady boundary layer behavior which precedes the dynamic stall vortex (DSV) formation is described in detail. It is found that the process is characterized by the presence of a laminar separation bubble (LSB) which contracts with increasing angle of attack as leading edge suction builds up. Beyond a critical incidence, the LSB breaks down and rapid suction collapse ensues. Abrupt turbulent separation follows allowing the turbulent boundary-layer vorticity to coalesce into a coherent DSV ahead of $x/c = 0.1$. The remaining turbulent boundary layer vorticity rolls up into a shear-layer vortex which imparts a much weaker signature on the surface pressure. Maximum surface pressure fluctuations are observed near the leading edge just prior to LSB bursting resulting in significant noise radiation. The overall process remained qualitatively unaltered for a reduced Reynolds number ($Re_c = 0.2 \times 10^6$) but exhibited an earlier breakdown of the larger LSB and a less abrupt leading-edge suction collapse. For a thicker NACA 0012 airfoil, a small delay in the LSB bursting is observed relative to the SD7003 section. In addition, the process is less abrupt and the DSV inception point is displaced slightly downstream.

Nomenclature

c	= airfoil chord
C_L, C_D, C_M	= lift, drag and quarter-chord moment coefficients
C_N	= normal force coefficient
C_p	= pressure coefficient
DSV	= dynamic stall vortex
E	= total specific energy
$\hat{F}, \hat{G}, \hat{H},$	= inviscid vector fluxes
$\hat{F}_v, \hat{G}_v, \hat{H}_v$	= viscous vector fluxes
J	= Jacobian of the coordinate transformation
LSB	= laminar separation bubble
M	= Mach number
p	= static pressure
\vec{Q}	= vector of dependent variables
Re_c	= Reynolds number based on chord, $\rho_\infty U_\infty c / \mu_\infty$
s	= span width for spanwise-periodic computations
SLV	= shear-layer vortex
t	= time

*Principal Research Aerospace Engineer, Computational Sciences Center. AIAA Fellow

This material is declared a work of the U.S. Government and is not subject to copyright protection in the United States.

u, v, w	= Cartesian velocity components
u_{nw}	= near-wall streamwise velocity
$\hat{U}, \hat{V}, \hat{W}$	= contravariant velocity components
x, y, z	= Cartesian coordinates
α	= angle of attack
γ	= specific heat ratio, 1.4 for air
Δt	= time step size
μ	= molecular viscosity coefficient
ξ, η, ζ	= body-fitted computational coordinates
ρ	= fluid density
$\omega_x, \omega_y, \omega_z$	= vorticity components
Ω	= pitch rate, rad/sec
Ω^+	= non-dimensional pitch rate, $= \Omega c/U_\infty$
$\langle \rangle$	= denotes spanwise-averaged quantities
$\langle \rangle_f$	= denotes spanwise-averaged lowpass-filtered quantities

I. INTRODUCTION

Maneuvering wings subjected to large excursions in effective angle of attack exhibit the phenomenon referred to in general as dynamic stall. Dynamic stall is characterized by a transient delay in separation (relative to the static situation) followed by the abrupt onset of unsteady separation which culminates in the formation of a large-scale dynamic stall vortex (DSV). The angular lag in separation in conjunction with the DSV-induced suction promote a transiently elevated aerodynamic lift. However, as the DSV is shed and propagates along the wing it induces sudden and difficult to predict variations in aerodynamic forces and pitching moment which severely impact controllability, vibrations, structural integrity and noise generation. Dynamic stall is found in a broad range of engineering applications including retreating blades of helicopter rotors in forward flight, maneuvering aircraft and wind turbines. It is also important in severe wing-gust encounters where large excursions in effective angle of attack may be generated over a wing in nominal steady flight. For the extensive body of literature on the subject, the reader is referred to several comprehensive reviews addressing various aspects of this complex phenomenon. These include the works of McCroskey,¹ Carr,² Ericsson and Reding,³ Visbal,⁴ Ekaterinaris and Platzer⁵ and Carr and Chandrasekhara.⁶

Previous experimental investigations have provided a great deal of information on the overall flow events which occur during dynamic stall and on the accompanying transient aerodynamic loads. A broad range of experimental techniques have been applied to this challenging problem, including flow visualizations,^{7,8} force measurements,^{9,10} surface pressure and hot-film measurements,¹¹⁻¹⁴ as well as planar whole field velocity and density surveys employing PIV^{15,16} and interferometric techniques.¹⁷ Numerous computational studies have also appeared in the literature attempting to reproduce and describe important details of this complex phenomenon. These include a number of 2-D laminar studies¹⁸⁻²⁰ at chord-based Reynolds numbers of order $Re_c = 10^4$. For higher Reynolds numbers, Reynolds-averaged (RANS) computations employing a hierarchy of turbulence models have been presented.^{5,21} Collectively, it is found⁵ that Reynolds-averaged approaches may exhibit significant deficiencies, which in some instances can be partially corrected through the incorporation of empirical transitional models.

Over a broad range of flow conditions and kinematics, the gross characteristics of deep dynamic stall are by now well established. For instance, the presence of a coherent DSV which forms near the leading edge and then convects along the airfoil inducing large overshoots in the aerodynamic loads is universally observed for a wide range of Reynolds numbers ($10^4 \leq Re_c \leq 10^6$). However, the detailed underlying viscous mechanisms which precede the emergence of the DSV are not yet fully understood. This task is hindered not only by the inherently complex unsteady boundary-layer behavior but also by the presence of several interrelated flow effects, including compressibility, transition, type and rate of motion and leading-edge geometry. Although suitably-calibrated RANS methodologies will continue to be employed for design purposes, they cannot be expected to be truly predictive given the complex flow physics at play near the leading edge. In particular, they are of limited value for probing the detailed viscous mechanisms, for exploring active flow sensing and control strategies and for characterizing noise generation. Limitations apply also to experimental efforts which rely mainly on flow visualizations or on low spatio-temporal resolution techniques.

Recent progress in high-order numerical methods and large-eddy simulation (LES) techniques coupled to vastly improved computational power makes it now possible to address the onset of dynamic stall using a first-principles

approach, at least under certain set of flow conditions and for simplified geometries. The investigations of Refs. 22–24 addressed for the first time the direct numerical simulation of the transitional dynamic stall vortex evolution over plunging and pitching airfoils. This work, motivated by micro-air-vehicle applications, considered fairly high rates of motion and low Reynolds numbers $Re_c \leq 0.6 \times 10^5$. It was demonstrated that even when the incipient separation and dynamic stall vortex formation were initially laminar, the subsequent abrupt onset of transition played a critical role in the vortex dynamics beginning at modest Reynolds numbers ($Re_c \approx 10^4$).

In the present investigation, we address the process of unsteady separation and DSV formation for higher Reynolds numbers ($Re_c = 0.2 \times 10^6, 0.5 \times 10^6$) and for more practical rates of motion. In order to separate significant effects of compressibility, a low freestream Mach number ($M_\infty = 0.1$) is employed. A previously studied^{22,24,25} SD7003 as well as a standard NACA 0012 airfoil sections are used. The airfoil is pitched about its quarter-chord axis at a nominal constant rate $\Omega^+ = \Omega c/U_\infty = 0.05$ starting from a prescribed low incidence ($\alpha_o = 4^\circ$) to a high angle of attack beyond the onset of dynamic stall. This motion is selected instead of the typical harmonic pitching case in order to make the simulations more computationally feasible. This is achieved by performing a single transient pitch-up maneuver rather than multiple cycles. In addition, the initial incidence helps to maintain a laminar boundary layer along the airfoil pressure surface. It is expected that the onset of stall for this constant-rate pitching motion will be of general applicability to a broader class of motions. Indeed, experiments by Lorber and Carta¹² demonstrated many similarities between constant-rate and sinusoidally pitching airfoils. They also showed that the process is not significantly altered if the starting incidence α_o is well below the static stall angle.

The flow fields are computed employing a high-order implicit large-eddy simulation (ILES) approach. This methodology, previously introduced in Refs. 26 and 27, is based on high-order compact schemes for the spatial derivatives augmented with a Pade-type lowpass filter to ensure stability. The high-order scheme is essential for accurately capturing the transition process near the leading edge, whereas the discriminating lowpass filter operator provides regularization in turbulent flow regions in lieu of a standard sub-grid-scale (SGS) model. The governing equations and high-fidelity computational approach are presented in Sections I and II, respectively.

The main objective of this investigation is to provide a detailed description (Section IV) of the unsteady boundary layer behavior which precedes the formation of the dynamic stall vortex. For completeness, the history of the aerodynamic loads is also given. In addition, a limited exploration of the effects of Reynolds number and airfoil geometry is performed.

II. GOVERNING EQUATIONS

The governing equations are the unfiltered full compressible Navier-Stokes equations cast in strong conservative form after introducing a general time-dependent curvilinear coordinate transformation $(x, y, z, t) \rightarrow (\xi, \eta, \zeta, \tau)$ ^{28,29} from physical to computational space. In terms of non-dimensional variables, these equations can be written in vector notation as:

$$\frac{\partial}{\partial \tau} \left(\frac{\vec{Q}}{J} \right) + \frac{\partial \hat{F}}{\partial \xi} + \frac{\partial \hat{G}}{\partial \eta} + \frac{\partial \hat{H}}{\partial \zeta} = \frac{1}{Re} \left[\frac{\partial \hat{F}_v}{\partial \xi} + \frac{\partial \hat{G}_v}{\partial \eta} + \frac{\partial \hat{H}_v}{\partial \zeta} \right] \quad (1)$$

where $\vec{Q} = \{\rho, \rho u, \rho v, \rho w, \rho E\}$ denotes the solution vector, $J = \partial(\xi, \eta, \zeta, \tau) / \partial(x, y, z, t)$ is the transformation Jacobian, and \hat{F} , \hat{G} and \hat{H} are the inviscid fluxes given by:

$$\hat{F} = \begin{bmatrix} \rho \hat{U} \\ \rho u \hat{U} + \hat{\xi}_x p \\ \rho v \hat{U} + \hat{\xi}_y p \\ \rho w \hat{U} + \hat{\xi}_z p \\ (\rho E + p) \hat{U} - \hat{\xi}_t p \end{bmatrix} \quad (2)$$

$$\hat{G} = \begin{bmatrix} \rho \hat{V} \\ \rho u \hat{V} + \hat{\eta}_x p \\ \rho v \hat{V} + \hat{\eta}_y p \\ \rho w \hat{V} + \hat{\eta}_z p \\ (\rho E + p) \hat{V} - \hat{\eta}_t p \end{bmatrix} \quad (3)$$

$$\hat{H} = \begin{bmatrix} \rho \hat{W} \\ \rho u \hat{W} + \hat{\zeta}_x p \\ \rho v \hat{W} + \hat{\zeta}_y p \\ \rho w \hat{W} + \hat{\zeta}_z p \\ (\rho E + p) \hat{W} - \hat{\zeta}_t p \end{bmatrix} \quad (4)$$

where

$$\hat{U} = \hat{\xi}_t + \hat{\xi}_x u + \hat{\xi}_y v + \hat{\xi}_z w \quad (5)$$

$$\hat{V} = \hat{\eta}_t + \hat{\eta}_x u + \hat{\eta}_y v + \hat{\eta}_z w \quad (6)$$

$$\hat{W} = \hat{\zeta}_t + \hat{\zeta}_x u + \hat{\zeta}_y v + \hat{\zeta}_z w \quad (7)$$

$$E = \frac{T}{\gamma(\gamma-1)M_\infty^2} + \frac{1}{2}(u^2 + v^2 + w^2). \quad (8)$$

Here, $\hat{\xi}_x = J^{-1}\partial\xi/\partial x$ with similar definitions for the other metric quantities. The viscous fluxes, \hat{F}_v , \hat{G}_v and \hat{H}_v can be found, for instance, in Ref. 30. In the expressions above, u, v, w are the Cartesian velocity components, ρ the density, p the pressure, and T the temperature. The perfect gas relationship $p = \rho T / \gamma M_\infty^2$ is also assumed. All flow variables have been normalized by their respective reference freestream values except for pressure which has been non-dimensionalized by $\rho_\infty U_\infty^2$.

It should be noted that the above governing equations correspond to the original *unfiltered* Navier-Stokes equations, and are used without change in laminar, transitional or fully turbulent regions of the flow. Unlike the standard LES approach, no additional sub-grid stress (SGS) and heat flux terms are appended. Instead, a high-order lowpass filter operator (to be described later) is applied to the conserved dependent variables during the solution of the standard Navier-Stokes equations. This highly-discriminating filter selectively damps only the evolving poorly resolved high-frequency content of the solution.^{26,27} This filtering regularization procedure provides an attractive alternative to the use of standard sub-grid-scale (SGS) models, and has been found to yield suitable results for several turbulent flows on LES level grids. A re-interpretation of this implicit LES (ILES) approach in the context of an Approximate Deconvolution Model³¹ has been provided by Mathew *et al.*³²

III. NUMERICAL PROCEDURE

All simulations are performed with the extensively validated high-order Navier-Stokes solver *FDL3DI*.^{33,34} In this code, a finite-difference approach is employed to discretize the governing equations, and all spatial derivatives are obtained with high-order compact-differencing schemes.³⁵ For any scalar quantity, ϕ , such as a metric, flux component or flow variable, the spatial derivative ϕ' is obtained along a coordinate line in the transformed plane by solving the tridiagonal system:

$$\alpha \phi'_{i-1} + \phi'_i + \alpha \phi'_{i+1} = \beta \frac{\phi_{i+2} - \phi_{i-2}}{4} + \gamma \frac{\phi_{i+1} - \phi_{i-1}}{2} \quad (9)$$

where α , γ and β determine the spatial properties of the algorithm. For the airfoil computations reported in this paper, a sixth-order scheme is used corresponding to $\alpha = \frac{1}{3}$, $\gamma = \frac{14}{9}$ and $\beta = \frac{1}{9}$. At boundary points, higher-order one-sided formulas are utilized which retain the tridiagonal form of the scheme.^{33,34} Typically, Neumann boundary conditions are implemented with third-order one-sided expressions.

The derivatives of the inviscid fluxes are obtained by forming the fluxes at the nodes and differentiating each component with the above formula. Viscous terms are obtained by first computing the derivatives of the primitive variables. The components of the viscous flux are then constructed at each node and differentiated by a second application of the same scheme.

For the case of a pitching airfoil, the grid is moved in a rigid fashion using the prescribed airfoil motion. To ensure that the Geometric Conservation Law (GCL) is satisfied, the time metric terms are evaluated employing the procedures described in detail in Ref. 36.

In order to eliminate spurious components, a high-order lowpass spatial filtering technique^{33,37} is incorporated. If a typical component of the solution vector is denoted by ϕ , filtered values $\hat{\phi}$ at interior points in transformed space satisfy,

$$\alpha_f \hat{\phi}_{i-1} + \hat{\phi}_i + \alpha_f \hat{\phi}_{i+1} = \sum_{n=0}^N \frac{a_n}{2} (\phi_{i+n} + \phi_{i-n}) \quad (10)$$

Equation (10) is based on templates proposed in Refs. 35 and 38 and with proper choice of coefficients, provides a $2N$ th-order formula on a $2N + 1$ point stencil. The $N + 1$ coefficients, a_0, a_1, \dots, a_N , are derived in terms of α_f using Taylor- and Fourier-series analysis. These coefficients, along with representative filter transfer functions, can be found in Refs. 34 and 39. The filter is applied to the conserved variables along each transformed coordinate direction once after each time step or sub-iteration. For the near-boundary points, the filtering strategies described in Refs. 33 and 39 are used. In the present simulations, an 8^{th} -order filter with $\alpha_f = 0.4$ is applied in the interior. For transitional and turbulent flows, the previous high-fidelity spatial algorithmic components provide an effective implicit LES approach in lieu of traditional SGS models, as demonstrated in Refs. 26 and 27. Finally, time-marching is accomplished by incorporating an iterative, implicit approximately-factored procedure.^{26,27}

IV. RESULTS

A. Preliminary Considerations

Unless otherwise stated, computations are performed for the SD7003 wing section, shown in Fig. 1. This airfoil has a maximum thickness of 8.5%, maximum camber of 1.45% (at $x/c = 0.35$) and a leading-edge radius $r_o/c = 0.0055$. This profile has been used in several recent experimental and computational investigations.^{22,24,25,40} In particular, in Ref. 24, the dynamic stall process during periodic heaving and at a much lower Reynolds number ($Re_c = 6 \times 10^4$) was investigated using the present high-fidelity approach.

A spanwise section of the coarsest grid used is displayed in Fig. 1c with only every other line in the streamwise and normal directions plotted for clarity. The original sharp trailing edge was rounded with a very small circular arc in order to facilitate the use on an O-mesh topology. Grid points were concentrated near the airfoil in order to capture the dynamic stall formation and initial convection. Sectional 2-D grids were used to construct the three-dimensional mesh which extended a distance $s/c = 0.1$ in the spanwise direction and had a uniform Δz spacing.

Boundary conditions are prescribed as follows (see Fig. 1). Along the airfoil surface, a no-slip adiabatic condition is employed in conjunction with a zero normal pressure gradient. The surface velocity components (u_s, v_s, w_s) are determined from the imposed pitching motion. Along the far field boundary, located more than 100 chords away from the airfoil, freestream conditions are specified. It should be noted that prior to reaching this boundary, the grid is stretched rapidly. This stretching in conjunction with the lowpass spatial filter provides a buffer-type treatment found previously⁴¹ to be quite effective in reducing spurious reflections. Spatially-periodic conditions were enforced in both the azimuthal and spanwise (homogeneous) directions using five-plane overlaps.

The wing is pitched about its quarter-chord axis at a nominal constant rate $\Omega_o^+ = \Omega c/U_\infty = 0.05$ from an initial incidence $\alpha_o = 4^\circ$ to a large angle of attack beyond the onset of dynamic stall. The small initial incidence is specified in order to effectively maintain a laminar boundary layer along the airfoil pressure side which in turn allows for improved streamwise spatial resolution on the suction surface. As noted in Ref. 12, the dynamic stall process is not significantly altered provided α_o is well below the static stall angle. Furthermore, preliminary comparison (not shown) of computed solutions for $\alpha_o = 4^\circ$ and 8° indicated no differences in the unsteady separation behavior and dynamic stall vortex formation.

In order to avoid discontinuities in the angular acceleration, the angle of attack is prescribed employing a modified version of the ramping function of Eldredge et al.⁴² Pitching simulations are started from a previously computed static solution at α_o . A very small computational non-dimensional time step $\Delta t U_\infty/c = 0.00002$ is prescribed in order to provide sufficient temporal resolution of fine-scale features. This value of Δt corresponds approximately to 17450 time steps per degree of angular rotation.

B. Effect of Grid Resolution

In order to assess effects of spatial resolution, three different grid systems were employed. Some details of these grids, denoted as Grid 1 to Grid 3 are summarized in Table 1. Grid refinement in the streamwise direction was concentrated on the airfoil upper surface in order to more effectively capture unsteady boundary-layer separation and dynamic stall vortex formation.

The effect of grid resolution on the computed initial stationary airfoil solution at $\alpha_o = 4^\circ$ and $Re_c = 0.5 \times 10^6$ is shown in Fig. 2 in terms of the time-averaged surface pressure and skin-friction distributions. There are significant changes going from Grid 1 to Grid 2, however, results on Grid 2 and Grid 3 appear to be in fairly close agreement. The spatial resolution in wall units for two values of Reynolds number is provided in Table 2 at the streamwise station $x/c = 0.8$ downstream of transition where a fully turbulent boundary layer is present. Based on the resolution in wall

Table 1. Computational mesh parameters

Grid	dimensions	size x 10 ⁻⁶	N_U	$\Delta s_{min}/c$	$\Delta s_{max}/c$	$\Delta n/c$	$\Delta z/c$
Grid 1	649 × 395 × 51	13.1	323	0.001	0.005	5.0 × 10 ⁻⁵	0.002
Grid 2	968 × 410 × 101	40.1	645	0.0005	0.0025	2.5 × 10 ⁻⁵	0.001
Grid 3	1353 × 410 × 133	73.8	973	0.00025	0.0015	2.5 × 10 ⁻⁵	0.00078

N_U : number of points on airfoil upper surface
 $\Delta s_{min}/c$: minimum streamwise spacing near airfoil leading edge
 $\Delta s_{max}/c$: maximum streamwise spacing along airfoil upper surface
 $\Delta n/c$: nominal normal spacing on airfoil surface
 $\Delta z/c$: spanwise spacing

units and standard LES practices,⁴³ both Grids 2 and 3 should be appropriate for $Re_c = 0.2 \times 10^6$. For the higher value of Reynolds number, only Grid 3 with approximately 74 million points will be employed.

Grid	$Re_c = 0.2 \times 10^6$			$Re_c = 0.5 \times 10^6$		
	Δx^+	Δy^+	Δz^+	Δx^+	Δy^+	Δz^+
Grid 1	-	-	-	92.8	0.93	36.8
Grid 2	24.5	0.25	9.8	51.6	0.52	20.5
Grid 3	15.1	0.25	7.8	32.2	0.52	16.6

Table 2. Resolution in wall units for initial stationary airfoil solution at $x/c = 0.8$

The effect of spatial resolution on the computed dynamic stall process for $Re_c = 0.2 \times 10^6$ is shown in Fig. 3. Very good agreement is observed between solutions obtained using Grids 2 and 3 in terms of a number of quantities. These include the aerodynamic loads C_N , C_D , C_M (Figs. 3a,b), the history of the surface pressure near the airfoil leading edge (Fig. 3c), as well as the flow structure (Fig. 3d) and corresponding surface pressure distribution at a selected instant following the DSV formation. The present comparison demonstrates that the dynamic stall process to be described in detail later has been captured with sufficient spatial resolution. All results that follow correspond only to the finest grid (Grid 3).

C. Dynamic Stall Process for Pitching SD7003 Airfoil

In this section, a detailed description of the dynamic stall process is provided for the pitching SD7003 airfoil with the following flow and kinematic parameters: $M_\infty = 0.1$, $Re_c = 0.5 \times 10^6$, $\Omega^+ = 0.05$ and $\alpha_o = 4^\circ$.

The computed flowfield was saved every 2000 time steps during the pitching motion which corresponds to time and angular intervals of $\Delta t U/c = 0.04$ and $\Delta \alpha = 0.115^\circ$, respectively. The pressure as well as the streamwise velocity (at a normal distance $s_n/c \approx 5.0 \times 10^{-5}$ above the wall) were also monitored at seventeen stations along the airfoil upper surface ($x/c = 0.0025, 0.005, 0.01, 0.025, 0.05, 0.1, 0.15, 0.2, 0.3, 0.4, 0.5, 0.6, 0.7, 0.8, 0.9, 0.95, 0.99$). At these stations, both the instantaneous surface pressure and velocity at mid-span, as well as the spanwise-averaged values were recorded. Sample pressure histories at $x/c = 0.005$ and 0.05 are shown in Fig. 4a which displays both the instantaneous (C_p) and spanwise-averaged ($\langle C_p \rangle$) values. It is apparent that averaging in the spanwise direction diminishes significantly the high-frequency oscillations present in the instantaneous C_p signal. For further clarity, the span-averaged pressure is also lowpass filtered and denoted as $\langle C_p \rangle_f$ in the figure. As a measure of the unsteadiness, the span-averaged *rms* pressure fluctuations can be defined relative to this filtered datum, i.e., $C_{p_{rms}} = [\langle C_p \rangle - \langle C_p \rangle_f]^2]^{1/2}$. The history of the near-wall span-averaged and filtered velocity at $x/c = 0.05$ is shown in Fig. 4b. Several features can be noted for future reference, including: the smooth laminar character prior to the passage of the upstream-propagating transition, a turbulent boundary layer, abrupt turbulent separation and DSV formation. In dynamic stall experiments (e.g. Ref. 12), the measured surface quantities are phased-averaged employing a sufficiently large number of realizations and *rms* fluctuations can be determined based on such averaging. In the present transient computations, that technique is not feasible and therefore, the spanwise-averaged and lowpass filtered variables are introduced as an alternate (although not necessarily equivalent) approach.

The overall unsteady flowfield evolution about the pitching airfoil is provided in Figs. 5-7 in terms of an iso-surface of the instantaneous Q-criterion⁴⁴ ($Q = 5000$) colored by streamwise velocity for clarity, as well as contours of instantaneous vorticity magnitude and pressure on the mid-plane. In Fig. 5a,b, one can observe the region of transition (denoted as '1') which propagates upstream as the angle of attack increases. This transition zone is characterized by spanwise-coherent structures which eventually breakdown into fine-scale features leading to a fully turbulent boundary layer further downstream. By $\alpha = 12.9^\circ$ (Fig. 5c), transition has moved very close to the airfoil leading edge, and a turbulent boundary layer exists over the major portion of the wing, with the exception of a very short laminar separation bubble (LSB) to be described in more detail later. The last three frames in Fig. 5 display the emergence and initial propagation of the DSV. Just prior to its emergence, there appear to be spanwise coherent large-scale structures in the front portion of the airfoil (denoted as '2' in Fig. 5d). However, shortly afterwards only the DSV and a "shear-layer" vortical structure (denoted as '3' and '4' respectively in Fig. 5e) are dominant. By $\alpha = 22.6^\circ$ (Fig. 5f), the DSV is the most prominent feature. At this stage, it is interesting to note the strong coherent longitudinal streaks (denoted as '5') which are generated by the strong interaction of the DSV with the boundary layer underneath.

Contours of vorticity magnitude (Figs. 6a,b) show a significant thickening of the turbulent boundary layer although the flow is still effectively attached and body-conforming around the wing section. By $\alpha = 20.8^\circ$ (Fig. 6c), the emergence of the DSV is apparent. At subsequent instants (Figs. 6d-f), the DSV is observed to grow in size and its center moves away from the surface as it propagates along the airfoil chord. At this stage, the DSV is still connected to the shear layer emanating from the airfoil leading edge. There is significant induced entrainment of outer inviscid fluid between the vortex and the airfoil surface forming a strong reversed viscous layer along the wall which also experiences secondary separation (denoted as '1' in Fig. 6f). As the DSV forms, the vorticity on the remaining portion of the upper surface turbulent boundary layer reorganizes itself into a coherent shear-layer vortex (SLV, denoted as '2') which is eventually shed past the trailing edge. Prior to the DSV formation, the corresponding instantaneous pressure field around the airfoil (Fig. 7) exhibits a strong build-up of suction in the leading edge region. Subsequent to the DSV emergence, the pressure is dominated by the strong concentric region of low pressure induced by the vortex with minimum values of C_p found in the vortex center.

The overall evolution of the pressure on the airfoil upper surface is discussed next. Figure 8 displays the spatio-temporal distribution of the spanwise-averaged pressure on the airfoil upper surface. Spatial $\langle C_p \rangle$ -distributions at select angles of attack are also shown. Several noteworthy features can be extracted from the 3D pressure plot. The first feature or ridge (denoted as '1') corresponds to the forward propagation of the transition region. Initially, this transition region remains fairly stationary but after $\alpha \approx 7^\circ$ ($tU/c \approx 1.2$) it proceeds at a more rapid pace towards the leading edge. The $\langle C_p \rangle$ -distribution plot at $\alpha = 8^\circ$ includes also the available computed static case. It is apparent, that the pitching motion induces an angular delay in both the build-up of leading edge suction (circulation delay), as well as in the upstream propagation of transition. A lag in the forward movement of transition with increasing pitch rate is also noted in the experiments of Ref. 12.

As transition moves closer to the leading edge (see $\langle C_p \rangle$ distribution at $\alpha = 10.6^\circ$), a distinct pressure plateau followed by a rapid pressure recovery are observed associated with the LSB and its transition to turbulence. The next pronounced feature (denoted as '2' in Fig. 8) is the high level of suction achieved near the leading edge which is followed by a rapid collapse. This process is also clearly displayed by the corresponding span-averaged $\langle C_p \rangle$ distributions at $\alpha = 19.8^\circ$ and 20.3° where a precipitous drop in $\langle -C_{p_{min}} \rangle$ from 14.4 to 9.6 is observed over $\Delta\alpha = 0.5^\circ$. The high suction level achieved near the leading edge due to the delay in separation induced by the pitching motion is accompanied as expected by an increased Mach number. Prior to the collapse of suction, the Mach number reaches a maximum value of approximately 0.41 which is four times M_∞ . It is therefore apparent that compressibility effects^{21,45} will emerge at relatively modest freestream Mach numbers ($M_\infty \geq 0.25$). Following the leading-edge suction collapse and the formation of the DSV, a well-defined peak (denoted as '3') is seen in the spatio-temporal surface pressure and in corresponding $\langle C_p \rangle$ distributions at $\alpha = 20.8^\circ, 21.5^\circ$ and 24.3° . A less pronounced feature (denoted as '4') corresponds to the formation and propagation of the shear-layer vortex (SLV) described earlier in reference to Fig. 6. Its signature is also visible in the pressure distribution plot at $\alpha = 21.5^\circ$.

The temporal histories of the lowpass-filtered spanwise-averaged pressure introduced earlier ($\langle C_p \rangle_f$) at several sampling stations are provided in Fig. 9. The pressure at $x/c = 0.005$ decreases smoothly during the airfoil pitch-up and reaches a minimum at $\alpha \approx 19.5^\circ$ after which point it rapidly increases corresponding to the loss of suction noted earlier. The pressure at the next downstream stations in Fig. 9a decrease smoothly but at a lower rate. They also exhibit a small bump (denoted as '1') associated with the passage of transition. For instance, at $x/c = 0.05$ this secondary feature is observed at $\alpha \approx 10.5^\circ$ which coincides with the transition location clearly seen in the instantaneous surface pressure and near-wall velocity fluctuations shown in Fig. 4. A distinct low-pressure peak induced by the DSV is seen in Fig. 9 for $x/c \geq 0.1$ implying formation of the DSV just ahead of this station. It is

interesting to note that the vortex-induced pressure drop is first preceded by a small increase (denoted as '2') associated with the entrainment of fluid toward the airfoil surface. The minimum vortex-induced suction magnitude decreases downstream as the center of the vortex moves away from the airfoil surface (Fig. 7). Finally from the location of the surface pressure minimum, an averaged vortex propagation speed along the airfoil chord can be determined and found to be approximately $U_v/U_\infty = 0.24$. It should be noted that the present surface pressure histories display many similarities with the experimental data of Lorber and Carta¹² for a constant-rate pitching SSC-A09 airfoil at $M_\infty = 0.2$ and a much higher Reynolds number ($Re_c = 2 \times 10^6$). The process appears to be even more abrupt in the higher-Reynolds-number experiments.

Unsteady Boundary-Layer Behavior

Next, the behavior of the unsteady viscous flow is examined in more detail with emphasis on the events preceding the DSV formation. Contours of vorticity magnitude, pressure and the reversed-flow region near the leading edge are shown in Figs. 10 - 13. In addition, selected surface pressure and skin-friction distributions are presented in Fig. 14. The reversed flow at early stages of the motion ($\alpha = 8.3^\circ$, Figs. 12 and 13) displays discrete reversed-flow pockets associated with the 2D instability modes in the relatively long separated laminar shear layer. By $\alpha = 10.6^\circ$ (Fig. 12b), a short LSB with reattachment at $x/c \approx 0.056$ is already established and continues to contract in streamwise extent with increasing incidence (Figs. 12c, 13b). The surface pressure distributions in Fig. 14a display a well-defined plateau and rapid recovery associated with the LSB. This plateau region contracts as leading-edge suction continues to build. The corresponding skin-friction distributions (Fig. 14b) indicate that the end of the LSB or reattachment moves from $x/c \approx 0.026$ to $x/c \approx 0.013$ between 12.9° and 18.6° . Downstream of the LSB, an attached turbulent boundary layer is present as seen by the recovery in C_f and the absence of reversed flow near the airfoil surface (Fig. 13b). The history of the filtered near-wall velocity at $x/c = 0.05$ is shown in Fig. 16a. One can clearly observe that after the forward passage at this station of laminar separation and transition, a turbulent boundary layer is present prior to the DSV formation. The existence of a LSB on stationary airfoils is well known, as discussed, for instance, in Tani⁴⁶ and references therein. Under quasi-static conditions, the LSB is also observed to contract in streamwise extent with increasing incidence.

In a time-averaged sense the LSB bubble prior to static stall is sometimes interpreted as a region of fairly quiescent slow-recirculating flow. This characterization is however misleading in an unsteady sense. The highest *rms* pressure and near-wall velocity fluctuations actually occur near the leading edge in the LSB prior to suction collapse and DSV formation. Significant pressure oscillations at $x/c = 0.005$ can be seen in Fig. 4a. Also, the *rms* fluctuations in the near-wall velocity at $x/c = 0.01$ are provided in Fig. 16b. The peak in the velocity fluctuations takes place at $\alpha \approx 18^\circ$ shortly before the collapse of leading-edge suction. Examination of the instantaneous vorticity and pressure contours near the leading edge (see, for instance, Figs. 10c, 11c) reveals that in an instantaneous sense, the LSB contains a separated shear layer which rolls up into discrete and initially spanwise-coherent sub-structures which propagate (prior to stall) close to the surface hence generating significant pressure and velocity oscillations. These high surface pressure fluctuations are in turn responsible for significant sound radiation from the leading edge. This is depicted in Fig. 17 which shows the dilatation in the near-field of the airfoil at $\alpha = 18.6^\circ$ prior to suction collapse. Although not examined in detail here, this observed leading-edge acoustic radiation subsides following the DSV formation. It is worth noting that in the experiments of Ref. 12, the largest *rms* surface pressure fluctuations were also measured near the leading edge and increased sharply just prior to the DSV formation. The increase in leading-edge surface fluctuations may therefore be considered as a precursor of the imminent dynamic stall process for active flow control applications.

As the airfoil angle of attack continues to increase beyond a critical incidence (in this case near $\alpha = 20^\circ$), the by now extremely contracted LSB bubble can no longer persist due to the increasing pressure gradient and the short distance over which transition to turbulence must be established. This abrupt onset of separation found also in static stall is referred to as bubble breakdown or bubble bursting.⁴⁶ As shown in Figs. 12 and 13, there is a rapid increase in the region of reversed flow near the leading edge as the angle of attack increases from $\alpha = 19.8^\circ$ to $\alpha = 20.3^\circ$. The pressure distribution at $\alpha = 20.3^\circ$ in Fig. 14a clearly displays the rapid collapse in suction as the flow turns less sharply around the leading edge due to the increased displacement effect caused by separation. The corresponding skin-friction coefficient (Fig. 14b) indicates that the reversed-flow region has abruptly extended to $x/c \approx 0.09$. Comparing the C_f -distributions just prior and after suction collapse (curves '3' and '4' in the figure) shows the abrupt onset of separation in the previously fully attached turbulent boundary layer. This is also clearly seen in the near-wall velocity history at $x/c = 0.05$ displayed in Fig. 16a. The existence of reversed-flow allows the separated turbulent boundary layer vorticity to coalesce into the DSV. This process is shown in Fig. 15 which provides contours of spanwise-averaged z -component of vorticity in the leading-edge region for the first 10% of the airfoil chord. In frames (a) and (b) of the

figure, the propagation of the thin reversed-flow region can be inferred from the positive (blue) contours of $\langle \omega_z \rangle$ near the surface. The first emergence of a sufficiently coherent DSV is observed near $x/c \approx 0.07$ which correlates with its distinct signature on the surface pressure distribution.

As the DSV organizes into a well-defined coherent structure, it induces a strong reversed-flow current underneath. This is apparent from the corresponding skin-friction distribution (Fig. 14b), as well as the contours of velocity in Fig. 13f. The magnitude of the reversed flow velocity exceeds twice the freestream value. Due to the DSV influence, the shear layer emanating from the leading edge is displaced away from the airfoil (Fig. 10e) leading to a significant drop in the pressure and near-wall velocity fluctuations noted earlier (Fig. 16b). The separated shear layer exhibits discrete spanwise sub-structures (Kelvin-Helmholtz instabilities), vortex pairing and eventual spanwise breakdown (Figs. 10e, 11e). The existence of these shear-layer sub-structures is also noted in the experiments of Ref. 16 for an oscillating NACA 0012 airfoil at $M_\infty = 0.1$ and $Re_c = 1 \times 10^6$.

The initiation of the DSV formation preceded by LSB breakdown found in the present computations seems to be consistent with experimental findings of Chandrasekhara et al.¹⁷ Their non-intrusive interferometric measurements for a constant-rate pitching NACA 0012 airfoil at $M_\infty = 0.3$, $Re_c = 54 \times 10^6$ and $\Omega^+ = 0.035$ show clear evidence of the presence of a LSB which bursts prior to dynamic stall onset.

While the process of DSV formation is dominated by events near the leading-edge (LSB breakdown and abrupt turbulent separation), further downstream along the airfoil upper surface the turbulent boundary layer also experiences separation as the angle of attack increases. This process is illustrated by considering the region of reversed flow over the entire airfoil upper surface, shown in Fig. 18 using contours of negative spanwise-averaged streamwise velocity. Several skin-friction distributions in the turbulent boundary layer are also provided in Fig. 19. There is clearly a region on turbulent separation which first appears near the trailing edge. The history of the near-wall velocity at $x/c = 0.8$ shown in Fig. 16a exhibits a mild turbulent separation which takes place well before the arrival at this station of the shear-layer and dynamic stall vortices. Turbulent boundary-layer separation propagates forward along the airfoil. This process of separation is also fairly rapid and the front of this turbulent separated region moves from $x/c \approx 0.75$ to $x/c \approx 0.2$ as α increases from 18.6° to 19.8° . The precise separation location becomes harder to pinpoint from the span-averaged C_f -distributions since these begin to exhibit increasing spatial oscillations. At the approximate time of suction collapse ($\alpha \geq 19.8^\circ$) initiated by LSB bursting, the reversed flow in the turbulent boundary layer has also spread over a significant portion of the airfoil ($x/c > 0.2$, in Fig. 19). It is therefore apparent that these two viscous processes are at play simultaneously. Nonetheless, the stronger reversed flow takes place very close to the airfoil leading edge ($x/c < 0.1$) where the DSV emerges, as seen in Figs. 13 and 18.

The precise evolution of the reversed-flow region in pitching airfoils can be quite complex^{11,45} and depends on multiple factors including airfoil geometry, kinematics, Reynolds number and Mach number. The existence of abrupt turbulent separation near the leading edge for an oscillating NACA 0012 airfoil at high Reynolds number ($Re_c = 2.0 \times 10^6$) is noted in Ref. 11. The complex process of unsteady separation found in the present computations for a moderate Reynolds number has significant implications for numerical prediction of the phenomena, as well as for its experimental characterization. Clearly the structure of the LSB must be properly reproduced in truly predictive simulations. First, at low incidence, the LSB evolution determines the location of transition and its forward propagation. Even in experiments¹² at much higher Reynolds number ($Re_c = 2.0 \times 10^6$), a contracting LSB can be inferred from surface measurements. Secondly, prediction of the sudden LSB bursting and leading-edge suction collapse is critical to the initiation of dynamic stall. Given the very abrupt onset of this process, a general quantitative predictive capability based on Reynolds-averaged turbulence modeling approaches (RANS), even those incorporating empirical transition models, may be difficult to achieve. The contraction of the LSB also imposes severe constraints with increasing Re_c on the resolution requirements in particular for low-order numerical methodologies. Stringent spatial and temporal resolution requirements also impact experimental measurements given the small scale of the LSB and its abrupt breakdown. Furthermore, comparison of computations and experiments is likely to be hindered (at least below certain value of Reynolds number) by the sensitivity of transition to wind tunnel disturbances not reproducible in the computations.

Aerodynamic Loads

The history of the aerodynamic loads is provided in Fig. 20a-c. After acceleration effects have subsided, the normal force and drag coefficients display a smooth linear variation. The pitching moment coefficient is approximately constant and its value is reduced by rotation-induced chordwise camber effects.^{10,21,47} The C_L -slope, plotted in Fig. 20d, is fairly constant (in an averaged sense) and below the corresponding value based on steady thin-airfoil theory. This slope depression is caused by a delay in the establishment of circulation around the airfoil for a given angle of attack relative to the static situation (i.e., a Wagner-type effect).^{10,21} The slopes of the drag and normal force coefficients

exhibit a sharp increase just before $\alpha = 20^\circ$ as the leading edge suction collapses and the DSV emerges. Shortly afterwards, moment stall is also apparent. Maximum lift is attained for $\alpha \approx 27^\circ$ at which point the DSV has already passed the mid-chord station (see Fig. 9b).

D. Effect of Reynolds Number

In order to assess Reynolds number effects, the same pitching SD7003 case was computed for $Re_c = 0.2 \times 10^6$. Only highlights of this case are shown in Figs. 21-23, and more detailed results can be found in Ref. 48. The overall process of dynamic stall onset is found to be qualitatively similar at both Reynolds numbers in terms of the previously described flow features and sequence of events. These include the build-up of suction near the leading edge, suction collapse due to LSB breakdown and abrupt turbulent boundary-layer separation at the DSV inception point. Despite these similarities, important quantitative differences are observed. These primary differences can be listed as follows:

- (i) considerably lower leading-edge pressure is achieved at higher Re_c (see Figs. 8 and 21). Minimum C_p reaches -6.0 and -14.4 for $Re_c = 0.2 \times 10^6$ and 0.5×10^6 , respectively. In the carpet plot of Fig. 21, a clear signature of the shear-layer vortex is not present. This may be related to the fact that significantly less turbulent boundary-layer separation is observed⁴⁸ in the aft-portion of the airfoil at the lower Re_c .
- (ii) LSB bursting and accompanying collapse of leading-edge suction take place approximately 4.5° earlier for the lower Re_c corresponding to roughly 1.5 convective times (see Figs. 9a and 22a).
- (iii) a larger LSB is evident at the lower Reynolds number (see Figs. 14b and 23). The LSB contracts to a minimum chordwise extent $x/c \approx 0.05$ at $Re_c = 0.2 \times 10^6$ versus 0.013 at $Re_c = 0.5 \times 10^6$.
- (iv) the initial location of the DSV formation moves from $x/c \approx 0.07$ to $x/c \approx 0.13$ with decreasing Re_c .
- (v) although the overshoots in the aerodynamic loads are comparable (Fig. 20a-c), the rapid rise in C_N and C_D as well as moment stall are shifted to a smaller angle of attack for reduced Re_c . In addition, the sharp increase in normal force and drag coefficient slopes during DSV formation is not as pronounced as that found at the higher Reynolds number.

E. Effect of Airfoil Geometry

In order to investigate the effects of airfoil geometry on the previously described dynamic stall process, computations were also performed for a pitching NACA 0012 profile employing the same flow and kinematic conditions ($M_\infty = 0.1$, $Re_c = 0.5 \times 10^6$, $\Omega^+ = 0.05$). A comparison of the two airfoil profiles is shown in Fig. 1d. Relative to the SD7003 section, the NACA 0012 airfoil is symmetric, much thicker (12% vs 8.5% thickness) and has a much larger leading edge radius ($r_o/c = 0.0158$ vs 0.0055). Details of the unsteady flow structure and corresponding boundary-layer behavior for the NACA airfoil are provided in Ref. 48 where an additional Reynolds number is also considered. In this paper, only key results are presented in Figs. 24-26 to permit comparison between the two airfoil geometries. Comparison of the dynamic stall process for the two airfoils reveals the main following conclusions:

- (i) a similar qualitative spatio-temporal evolution of the surface pressure is observed (see Figs. 8 and 24) including the signature of the shear-layer vortex noted earlier.
- (ii) For the sharper SD7003 airfoil, higher levels of leading-edge suction and a more abrupt suction collapse are observed. The leading-edge pressure over the NACA airfoil reaches a minimum value $C_{p_{min}} \approx -10.5$ compared to $C_{p_{min}} \approx -14.4$ for the SD7003 wing.
- (iii) A LSB bubble is also observed near the leading edge which bursts prior to the formation of the DSV (Fig. 26). In its most contracted state, the LSB reattachment extends to $x/c \approx 0.029$ versus $x/c \approx 0.013$ for the SD7003 airfoil.
- (iv) There is a small delay ($\Delta\alpha \approx 1.2^\circ$, $\Delta t U_\infty/c \approx 0.42$) in the onset of suction collapse and DSV formation for the NACA section.
- (v) The aerodynamic loads (Fig. 20a-c) display similar trends and maximum overshoots with some quantitative distinctions. At early stages during the pitch-up motion, the C_N is lower and C_M is higher for the NACA 0012 due to the camber of the SD7003 airfoil not present in the symmetric section. The rapid rise in C_N and C_D occurs later due to the delay in LSB collapse. The lift slope prior to stall (Fig. 20d) exhibits the same depression (relative to the theoretical steady thin airfoil value) which is followed by a rapid increase during DSV formation.

V. CONCLUSIONS

The onset of unsteady separation and dynamic stall vortex formation over a transiently pitching airfoil was studied numerically employing high-fidelity large-eddy simulations at a Reynolds number higher than previously considered. The computational implicit LES methodology is based on a 6th-order accurate compact scheme coupled to an 8th-order Pade-type lowpass filter which have been implemented within an extensively validated massively-parallel overset-grid

solver (FDL3DI). The previous algorithmic components seamlessly enable the direct simulation of boundary-layer transition near the airfoil leading edge and provide regularization in the turbulent region. The primary case considered consists of a SD7003 airfoil section at a freestream Mach number 0.1 and chord Reynolds number 0.5×10^6 . The airfoil is pitched about its quarter-chord axis at a nominally constant rate $\Omega^+ = 0.05$ from a small initial incidence to a high angle of attack beyond the onset of dynamic stall. The unsteady flow is studied in detail with emphasis on characterizing the unsteady boundary layer behavior which precedes the formation of the dynamic stall vortex.

As the wing is pitched, the transition location propagates forward along the airfoil upper surface and forms a laminar separation bubble which contracts significantly with increasing incidence reaching a minimum chordwise extent $x/c \approx 0.013$. Downstream of the LSB, a turbulent boundary layer is observed whose thickness increases with angle of attack while the flow remains effectively attached and body-conforming. The accompanying expansion around the leading edge promotes very low surface pressures and a local Mach number four times higher than the freestream value. During these early stages, the normal force increases linearly albeit with a reduced slope relative to steady inviscid theory reflecting the lag in circulation build-up around the airfoil. The pitching moment is also shifted to a lower value due to rotation-induced camber effects.

Beyond a critical incidence, the contracted LSB breaks down and a sudden collapse of leading-edge suction ensues. A very abrupt separation of the turbulent boundary layer at the DSV inception point is also observed. The rapid appearance of reversed flow allows the turbulent boundary-layer vorticity to coalesce into a nascent dynamic stall vortex. Based on the surface pressure signature, the DSV is detected initially at $x/c \approx 0.07$. As the DSV increases in strength, it induces very high values of reversed flow velocity underneath, with magnitudes greater than twice U_∞ . This reversed flow subsequently detaches due to the high vortex-induced pressure gradient forming a secondary separation region. The shear layer emanating from the leading-edge is also displaced away from the wing due to the growing DSV. This feeding sheet is characterized by discrete Kelvin-Helmholtz type sub-structures which exhibit pairing and subsequent breakdown due to spanwise instabilities. Maximum surface pressure fluctuations are observed near the leading edge resulting in significant acoustic radiation. These fluctuations, associated with the LSB, decrease in magnitude as the shear layer moves away from the wall.

In order to investigate the effect of Reynolds number, the previous SD7003 pitching maneuver was computed for $Re_c = 0.2 \times 10^6$. In addition, to explore airfoil geometry effects, a NACA 0012 airfoil section was also considered. In all cases, the initiation of dynamic stall was found to be associated with bursting of the laminar separation bubble followed by leading-edge suction collapse and by the roll up of the separated turbulent boundary layer. There were quantitative differences including a larger LSB, earlier collapse and a downstream displacement of the vortex inception location with reduced Reynolds number. The sharper SD7003 airfoil also exhibited higher suction and a more abrupt collapse in relation to the thicker NACA 0012 section.

The aforementioned unsteady boundary layer behavior appears to be in agreement with available experimental observations, even some obtained at higher Reynolds number. It is clear that at least for the conditions considered, the LSB plays a critical role both in establishing the propagation of transition along the pitching airfoil, as well as in the collapse of suction and subsequent DSV emergence. The importance of the LSB has significant implications for the quantitative prediction of the phenomenon. It remains to be seen if Reynolds-averaged approaches can be calibrated to reproduce the abrupt nature of LSB bursting and suction collapse. Furthermore, the extreme contraction of the LSB imposes severe requirements on spatial resolution for low-order numerical schemes. Comparison with experiment can also be potentially hindered by the sensitivity of transition to extraneous wind tunnel disturbances. On the positive side, this sensitivity could be exploited for delay of the onset of dynamic stall employing active flow control. Future work will examine higher Reynolds number, the interrelated effects of compressibility and transition, as well as strategies for flow control.

ACKNOWLEDGMENTS

This work was supported in part by AFOSR under a task monitored by Dr. D. Smith, and by a grant of HPC time from the DoD HPC Shared Resource Center at AFRL.

References

- ¹W. J. McCroskey. Unsteady Airfoils. *Annual Rev. Fluid Mech.*, 14:285–311, 1982.
- ²L. Carr. Progress in Analysis and Prediction of Dynamic Stall. *Journal of Aircraft*, 25(1):6–17, 1988.
- ³Ericsson. L. E. and Reding. Fluid Dynamics of Unsteady Separated Flow. Part II. Lifting Surfaces. *Progress in Aerospace Sciences*, 24:249–356, 1987.

⁴M. R. Visbal. On Some Physical Aspects of Airfoil Dynamic Stall. *Proceedings of the International Symposium on Non-Unsteady Fluid Dynamics*, (Edited by J. Miller and D. Telionis, Vol. 92, ASME), 1990.

⁵J. Ekaterinaris and M. Platzer. Computational Prediction of Airfoil Dynamic Stall. *Progress in Aerospace Sciences*, 33:759–846, 1997.

⁶L. W. Carr and M. S. Chandrasekhara. Compressibility Effects on Dynamic Stall. *Progress in Aerospace Sciences*, 32:523–573, 1996.

⁷P. Freymuth. Vortices. *Handbook of Flow Visualization, Ch IV-3, Ed. by Yang, W., Hemisphere Publishing*, 1989.

⁸K. W. McAlister and L. W. Carr. Water Tunnel Visualizations of Dynamic Stall. *J. of Fluids Engineering*, 101, 1979.

⁹J. H. Strickland and G. M. Graham. Force Coefficients for a NACA-0015 Airfoil Undergoing Constant Pitch Rate Motions. *AIAA Journal*, 25(4):622–624, 1987.

¹⁰E. J. Jumper, S. J. Shreck, and R. L. Dimmick. Lift-Curve Characteristics of an Airfoil Pitching at Constant Rate. *J. of Aircraft*, 24(10):680–687, Sep.-Oct. 1987.

¹¹L. W. Carr, K. W. McAlister, and W. J. McCroskey. Analysis of the development of dynamic stall based on oscillating airfoil experiments. *NASA TN D-8382*, 1977.

¹²P. F. Lorber and F. O. Carta. Airfoil dynamic stall at constant pitch rate and high reynolds number. *Journal of Aircraft*, 25(6):548–556, 1988.

¹³R. N. Conger and B. R. Ramaprian. Presure Measurements on a Pitching Airfoil in a Water Channel. *AIAA Journal*, 32(1):108–115, 1994.

¹⁴T. Lee and P. Gerontakos. Investigation of Flow Over an Oscillating Airfoil. *J. Fluid Mech.*, 512:313–341, 2004.

¹⁵K. Mulleners and M. Raffel. The Onset of Dynamic Stall Revisited. *Experiments in Fluids*, 52:779–793, 2012.

¹⁶B. J. Pruski and R. D. W. Bowersox. Leading-Edge Flow Structure of a Dynamically Pitching NACA 0012 Airfoil. *AIAA Journal*, 51(5):1042–1053, 2013.

¹⁷M. S. Chandrasekhara, L. W. Carr, and M. C. Wilder. Interferometric investigations of compressible dynamic stall over a transiently pitching airfoil. *AIAA Paper 93-0211*, January 1993.

¹⁸U. B. Mehta. Dynamic Stall of an Oscillating Airfoil. *Paper No. 23, AGARD CP-227*, 1977.

¹⁹M. R. Visbal and J. S. Shang. Investigation of the Flow Structure Around a Rapidly Pitching Airfoil. *AIAA Journal*, 27(8):1044–1051, 1989.

²⁰P. G. Choudhuri, D. D. Knight, and M. R. Visbal. Two-Dimensional Unsteady Leading-Edge Separation on a Pitching Airfoil. *AIAA Journal*, 32(4):673–681, 1994.

²¹M. R. Visbal. Dynamic Stall of a Constant-Rate Pitching Airfoil. *Journal of Aircraft*, 27(5):400–407, 1990.

²²M. R. Visbal. High-Fidelity Simulation of Transitional Flows past a Plunging Airfoil. *AIAA Journal*, 47(11):2685–2697, 2009.

²³D. J. Garmann and M. R. Visbal. Numerical Investigation of Transitional Flow Over a Rapidly Pitching Plate. *Physics of Fluids*, 23, 2011.

²⁴M. R. Visbal. Numerical Investigation of Deep Dynamic Stall of a Plunging Airfoil. *AIAA Journal*, 49(10):2152–2170, 2011.

²⁵Y. S. Baik, J. M. Rausch, L. P. Bernal, and M. V. Ol. Experimental Investigation of Pitching and Plunging Airfoils at Reynolds Number Between 1×10^4 and 6×10^4 . *AIAA Paper 2009-4030*, June 2009.

²⁶M. R. Visbal and D. P. Rizzetta. Large-Eddy Simulation on Curvilinear Grids Using Compact Differencing and Filtering Schemes. *Journal of Fluids Engineering*, 124:836–847, 2002.

²⁷M. R. Visbal, P. E. Morgan, and D. P. Rizzetta. An Implicit LES Approach Based on High-Order Compact Differencing and Filtering Schemes. *AIAA Paper 2003-4098*, June 2003.

²⁸M. Vinokur. Conservation Equations of Gasdynamics in Curvilinear Coordinate Systems. *Journal of Computational Physics*, 14:105–125, 1974.

²⁹J. L. Steger. Implicit Finite-Difference Simulation of Flow about Arbitrary Two-Dimensional Geometries. *AIAA Journal*, 16(7):679–686, 1978.

³⁰D. A. Anderson, J. C. Tannehill, and R. H. Pletcher. *Computational Fluid Mechanics and Heat Transfer*. McGraw-Hill Book Company, 1984.

³¹S. Stolz and N. Adams. An Approximate Deconvolution Procedure for Large-Eddy Simulation. *Physics of Fluids*, 11(7):1699–1701, 1999.

³²J. Mathew, R. Lechner, H. Foysi, J. Sesterhenn, and R. Friedrich. An explicit filtering method for LES of compressible flows. *Phys. Fluids*, 15(8):2279–2289, 2003.

³³M. R. Visbal and D. V. Gaitonde. High-Order Accurate Methods for Complex Unsteady Subsonic Flows. *AIAA Journal*, 37(10):1231–1239, 1999.

³⁴D. V. Gaitonde and M. R. Visbal. High-Order Schemes for Navier-Stokes Equations: Algorithm and Implementation into FDL3DI. Technical Report AFRL-VA-WP-TR-1998-3060, Air Force Research Laboratory, Wright-Patterson AFB, 1998.

³⁵S. K. Lele. Compact Finite Difference Schemes with Spectral-like Resolution. *Journal of Computational Physics*, 103:16–42, 1992.

³⁶M. R. Visbal and D. V. Gaitonde. On the Use of High-Order Finite-Difference Schemes on Curvilinear and Deforming Meshes. *Journal of Computational Physics*, 181:155–185, 2002.

³⁷D. V. Gaitonde, J. S. Shang, and J. L. Young. Practical Aspects of Higher-Order Numerical Schemes for Wave Propagation Phenomena. *Int. Jnl. for Num. Methods in Eng.*, 45:1849–1869, 1999.

³⁸P. Alpert. Implicit Filtering in Conjunction with Explicit Filtering. *J. Comp. Phys.*, 44:212–219, 1981.

³⁹D. V. Gaitonde and M. R. Visbal. Further Development of a Navier-Stokes Solution Procedure Based on Higher-Order Formulas. *AIAA Paper 99-0557*, January 1999.

⁴⁰C-K Kang, Y. S. Baik, L. P. Bernal, M. V. Ol, and W. Shyy. Fluid Dynamics of Pitching and Plunging Airfoils for Reynolds Number Between 1×10^4 and 6×10^4 . *AIAA Paper 2009-536*, January 2009.

⁴¹M. Visbal and D. Gaitonde. Very High-Order Spatially Implicit Schemes for Computational Acoustics on Curvilinear Meshes. *J. Comp. Acoustics*, 9(4):1259–1286, 2001.

⁴²J. Eldredge, C. Wang, and M. Ol. A computational study of a canonical pitch-up, pitch-down maneuver. *AIAA Paper 2009-3687*, June 2009.

⁴³N. J. Georgiadis, D. P. Rizetta, and C. Fureby. Large-Eddy Simulation: Current Capabilities, Recommended Practices and Future Research. *AIAA Journal*, 48(8):1772–1784, 2010.

⁴⁴J. Jeong and F. Hussain. On the identification of a vortex. *J. Fluid Mech.*, 285:69–94, 1995.

⁴⁵W. J. McCroskey, K. W. McAlister, L. W. Carr, S. L. Pucci, O. Lambert, and R. F. Indergrand. Dynamic Stall on Advanced Airfoil Sections. *Journal of the American Helicopter Society*, 26(7):40–50, 1981.

⁴⁶I. Tani. Low-speed flows involving bubble separations. *Progress in Aeronautical Science*, 5:70–103, 1964.

⁴⁷M.R. Visbal and R.E. Gordnier. Pitch Rate and Pitch-Axis Location Effects on Vortex Breakdown Onset. *J. of Aircraft*, 32(5):929–935, Sep.-Oct. 1995.

⁴⁸M.R. Visbal. High-Fidelity Simulations of Dynamic Stall on Constant-Rate Pitching Airfoils. Technical Report in preparation, Air Force Research Laboratory, Wright-Patterson AFB, 2014.

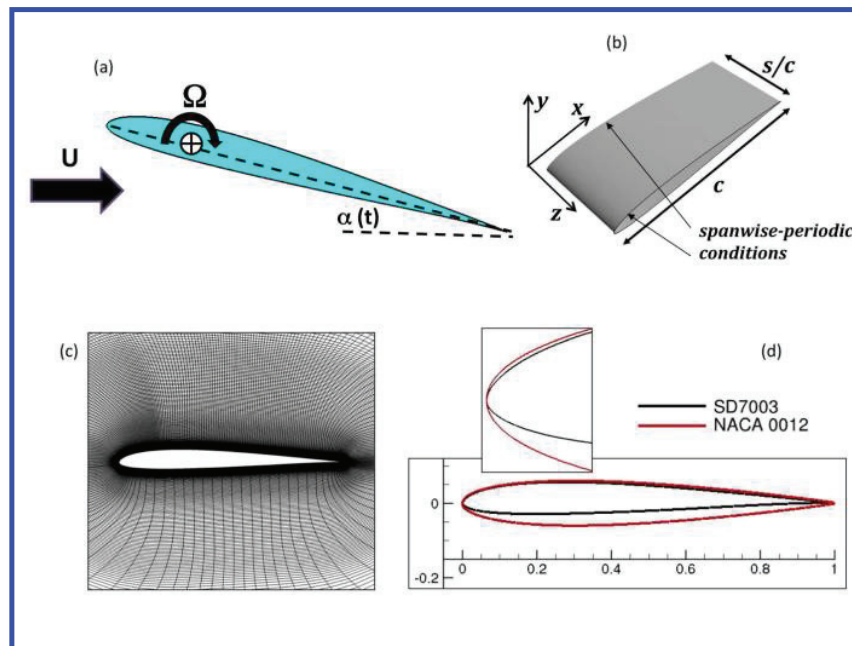


Figure 1. Pitching airfoil configuration and sectional mesh

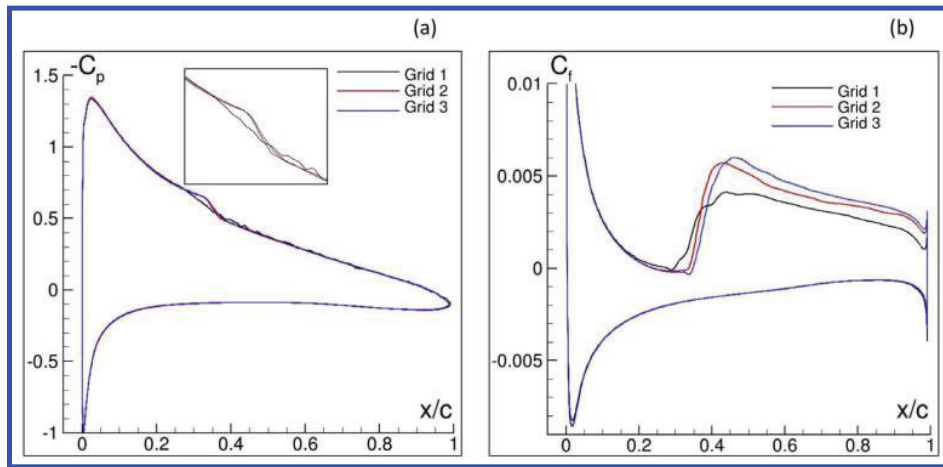


Figure 2. Effect of spatial resolution on computed stationary SD7003 solution at $\alpha = 4^\circ$ and $Re_c = 0.5 \times 10^6$: (a) mean surface pressure and (b) skin-friction distribution

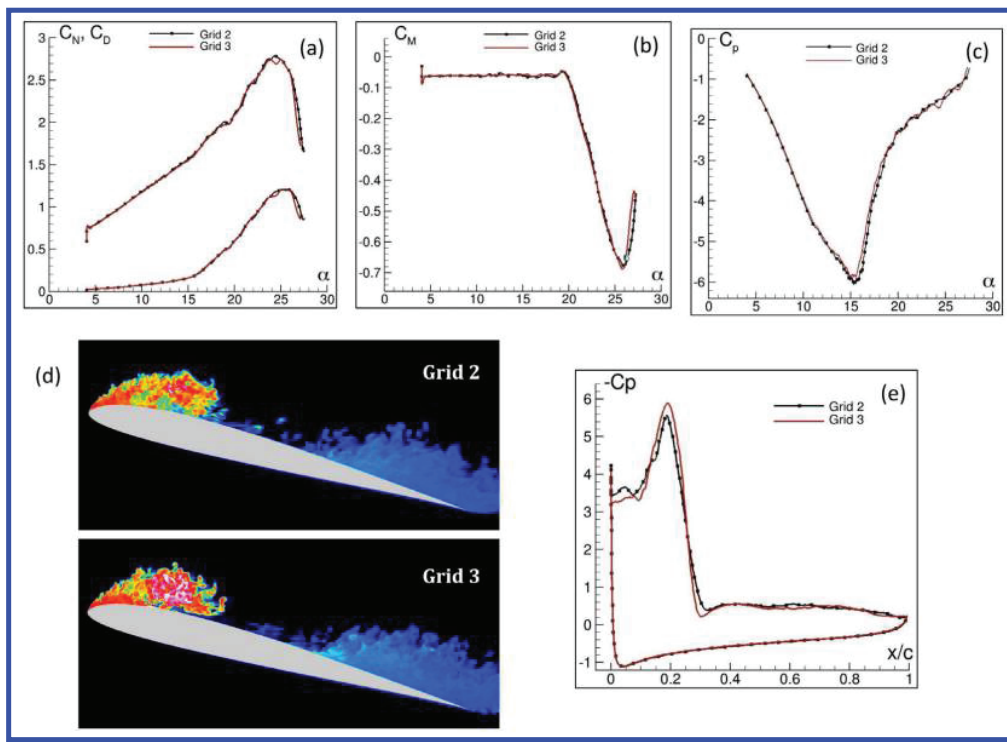


Figure 3. Effect of spatial resolution on pitching SD7003 airfoil solution at $Re_c = 0.2 \times 10^6$: (a,b) aerodynamic coefficients, (c) history of surface pressure at $x/c = 0.005$, (d) instantaneous flow structure at $\alpha = 18.2^\circ$ depicted using entropy contours and (e) corresponding spanwise-averaged surface pressure distribution

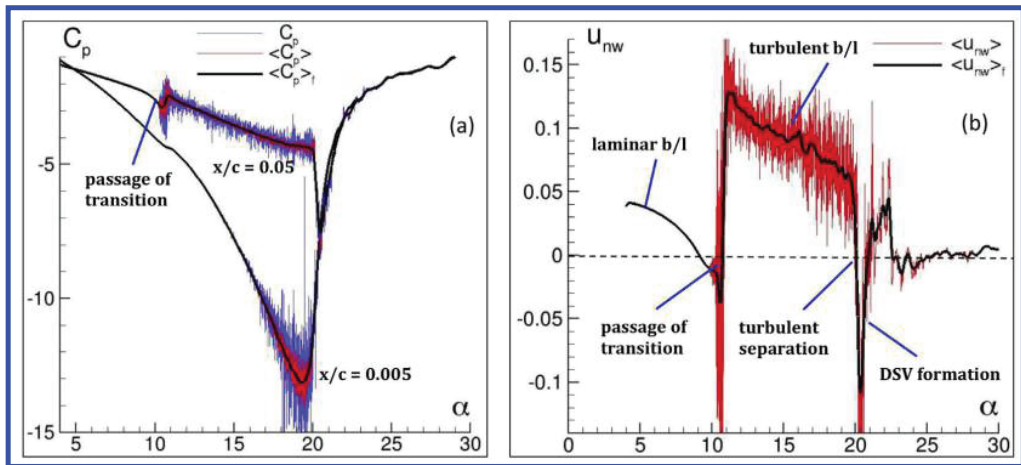


Figure 4. Sample time histories of (a) surface pressure at $x/c = 0.005$ and 0.05 and (b) near-wall streamwise velocity at $x/c = 0.05$

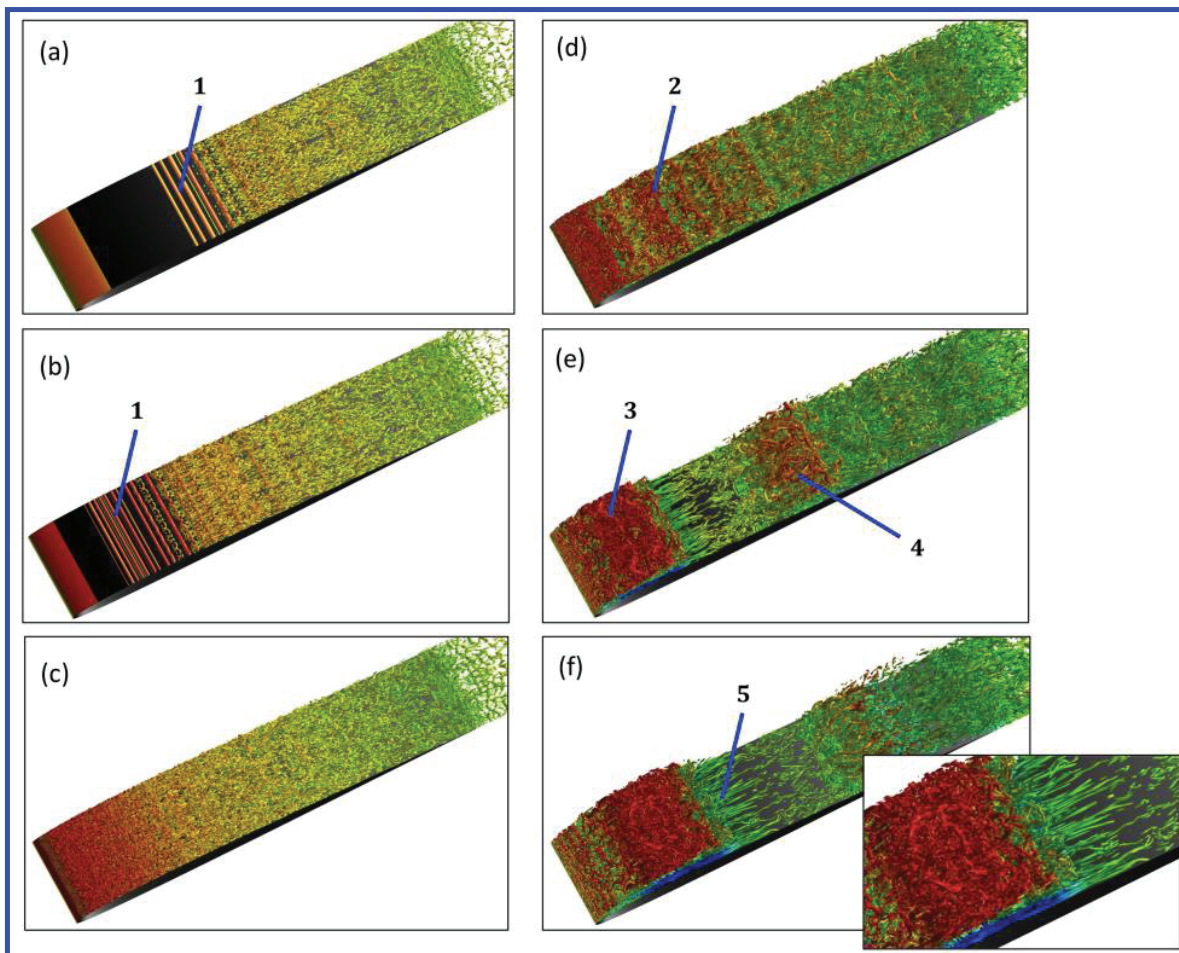


Figure 5. Iso-surface of instantaneous Q-criterion at selected instants during pitch-up motion: (a) 4.8°, (b) 8.3°, (c) 12.9°, (d) 20.3°, (e) 21.6° and (f) 22.6°

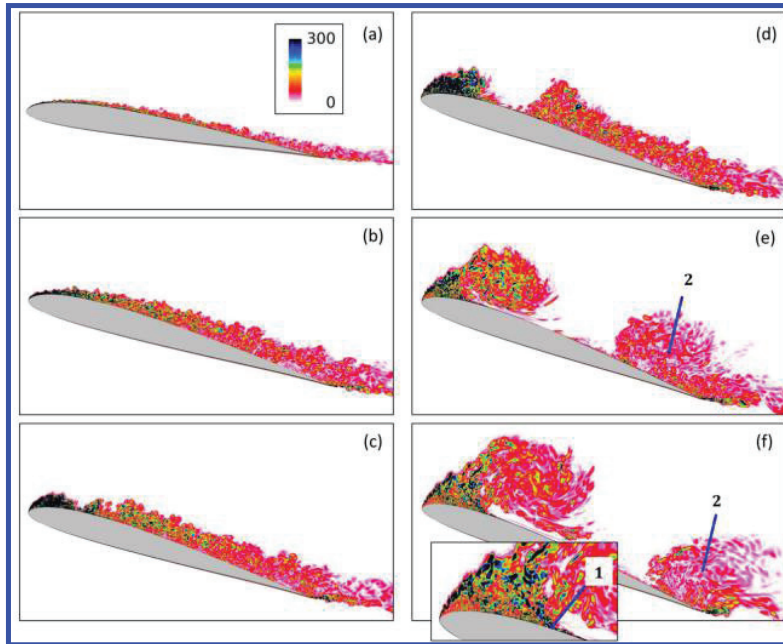


Figure 6. Contours of instantaneous vorticity magnitude on mid-plane at selected instants during pitch-up motion: (a) 12.9° , (b) 19.8° , (c) 20.8° , (d) 21.5° , (e) 23.2° and (f) 24.3°

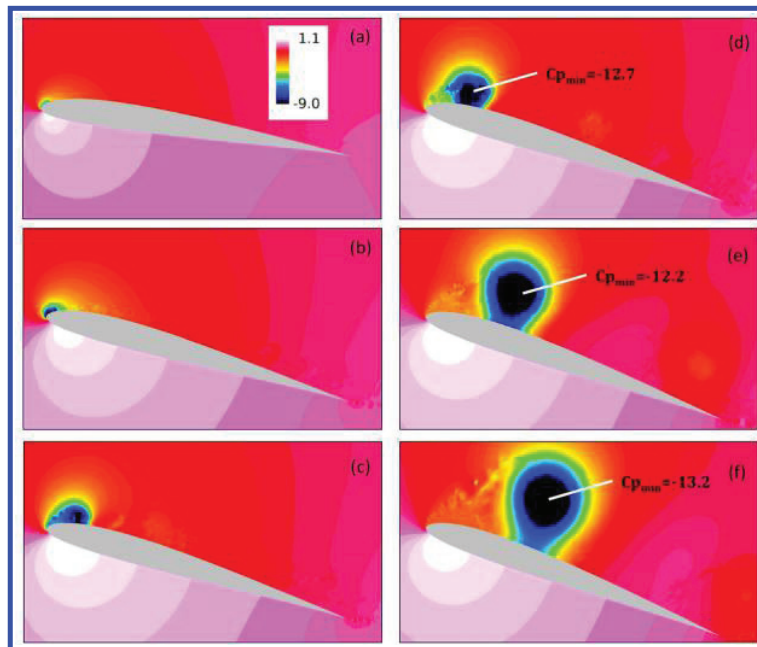


Figure 7. Contours of instantaneous pressure on mid-plane at selected instants during pitch-up motion: (a) 12.9° , (b) 19.8° , (c) 20.8° , (d) 21.5° , (e) 23.2° and (f) 24.3°

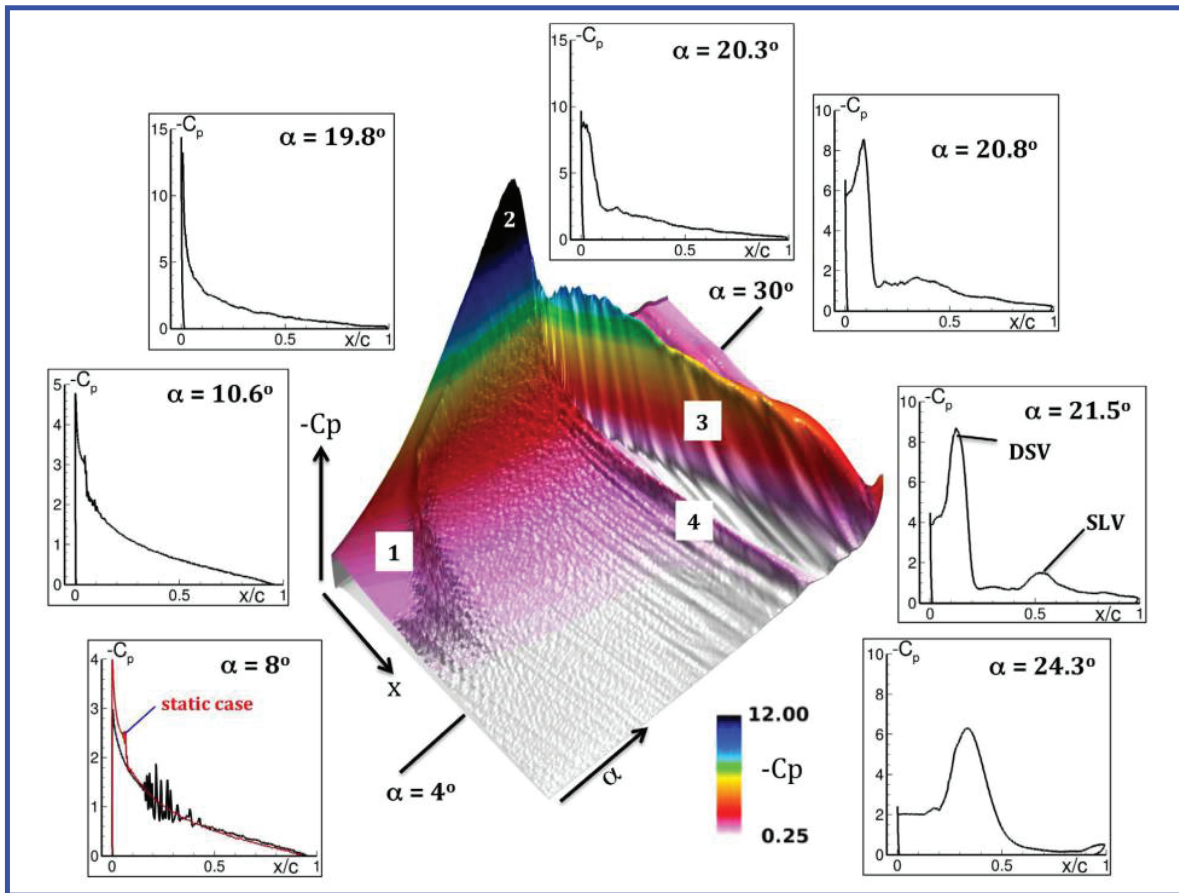


Figure 8. Spatio-temporal distribution of spanwise-averaged surface pressure on pitching airfoil and selected C_p -distributions

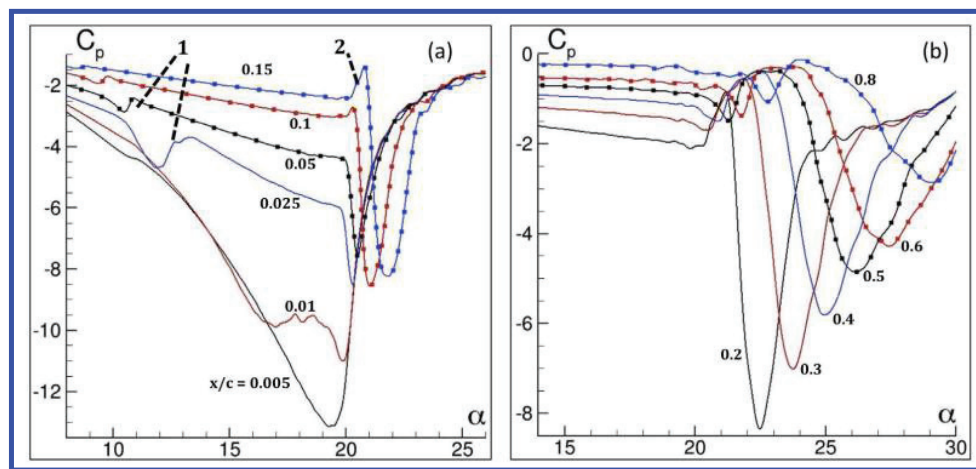


Figure 9. Histories of lowpass filtered spanwise-averaged pressure at selected stations on airfoil upper surface

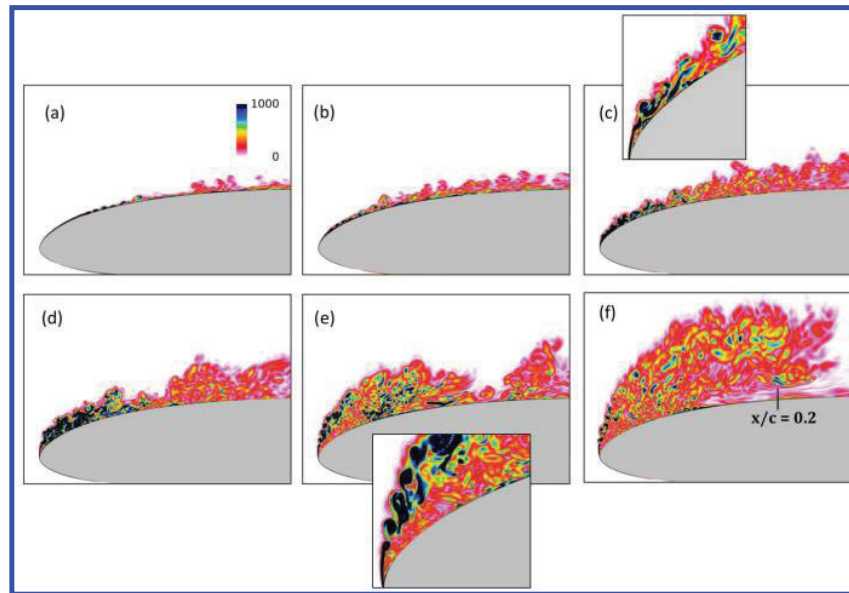


Figure 10. Contours of instantaneous vorticity magnitude near leading edge at selected instants during pitch-up motion: (a) 10.6° , (b) 15.2° , (c) 19.8° , (d) 20.3° , (e) 20.8° and (f) 21.6°

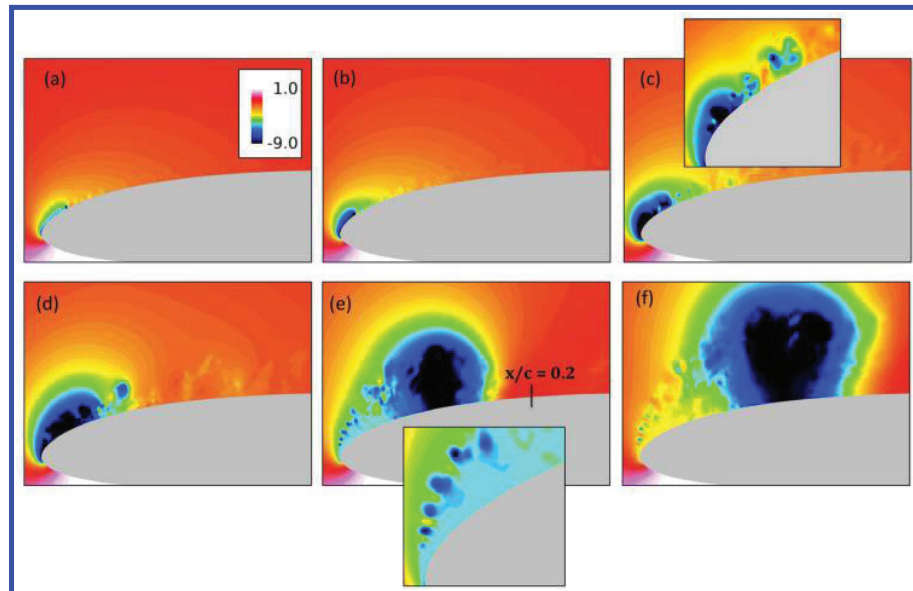


Figure 11. Contours of instantaneous pressure near leading edge at selected instants during pitch-up motion: (a) 12.9° , (b) 15.2° , (c) 19.8° , (d) 20.3° , (e) 20.8° and (f) 21.6°

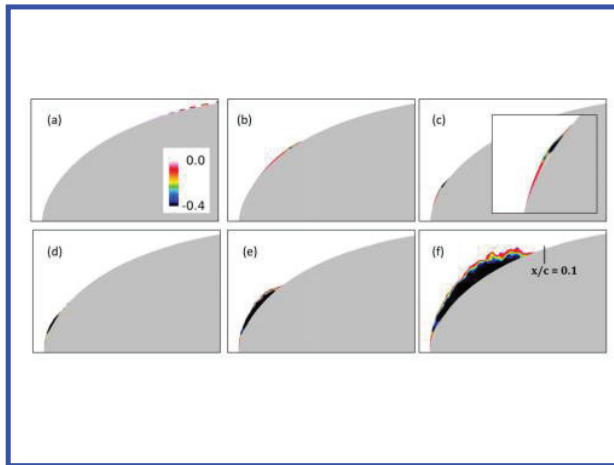


Figure 12. Spanwise-averaged reversed-flow region near leading edge in airfoil frame of reference at selected instants during pitch-up motion: (a) 8.3° , (b) 10.6° , (c) 15.2° , (d) 19.8° , (e) 20.1° and (f) 20.3° . Vertical scale has been enlarged by a factor of two for clarity

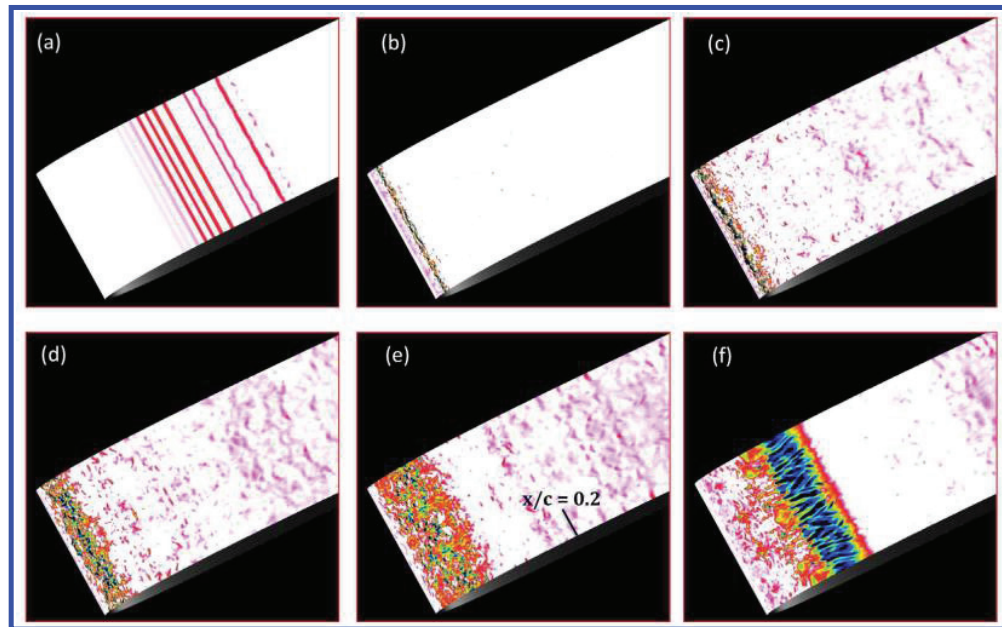


Figure 13. Contours of instantaneous reversed flow region on grid plane above airfoil surface ($s_n/c \approx 1.25 \times 10^{-4}$) at selected instants during pitch-up motion: (a) 8.3° , (b) 15.2° , (c) 19.8° , (d) 20.1° , (e) 20.3° and (f) 20.8°

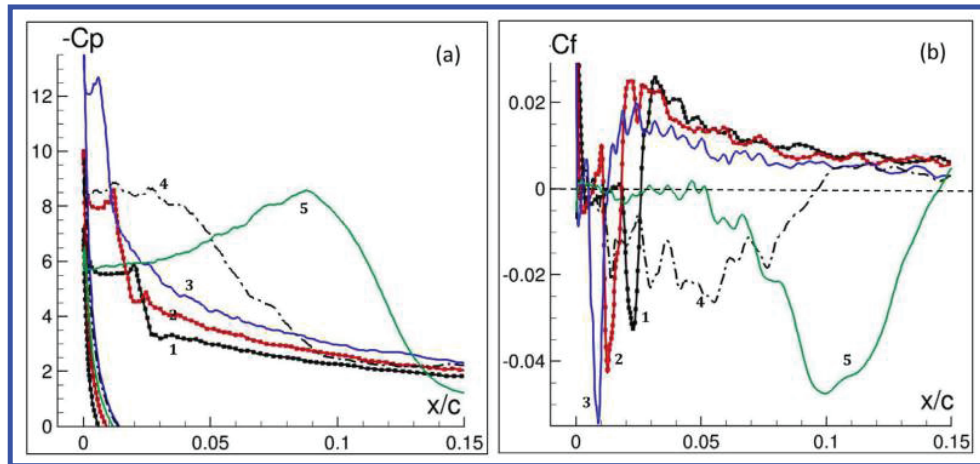


Figure 14. Spanwise-averaged (a) surface pressure and (b) skin-friction distributions at selected instants during leading-edge suction collapse and DSV formation ($\alpha = 12.9^\circ, 15.2^\circ, 18.6^\circ, 20.3^\circ, 20.8^\circ$)

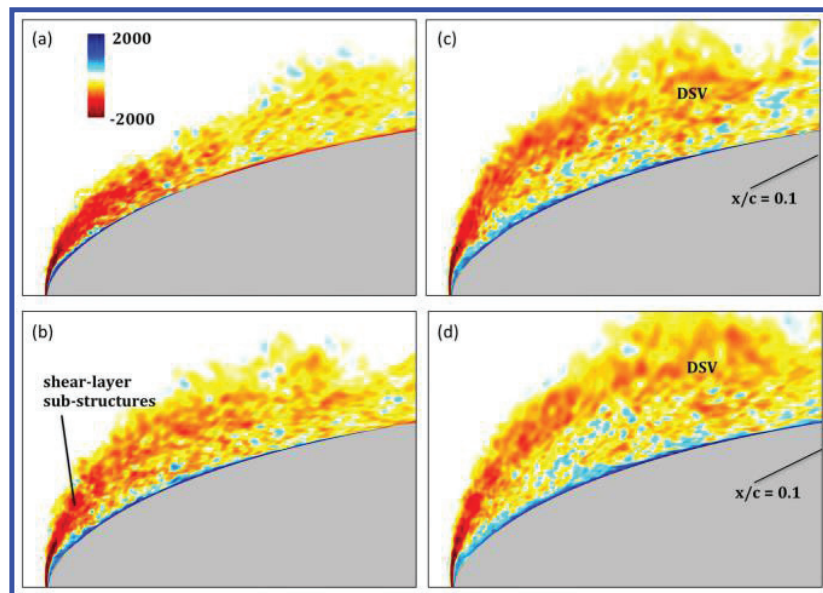


Figure 15. Contours of spanwise-averaged z -vorticity component at selected instants during the DSV formation: (a) $\alpha = 20.07^\circ$, (b) 20.30° , (c) 20.42° and (d) 20.53°

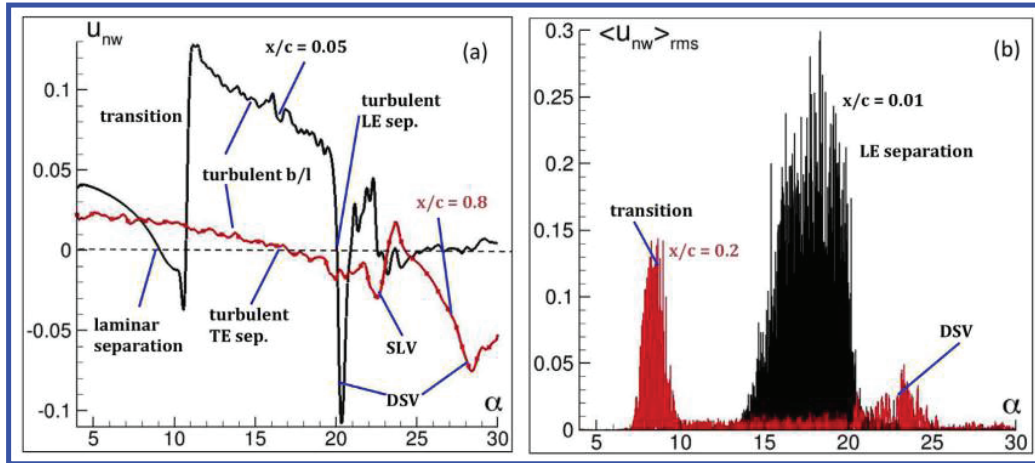


Figure 16. Histories of (a) lowpass filtered spanwise-averaged near-wall velocity and (b) fluctuations at selected streamwise stations on airfoil upper surface

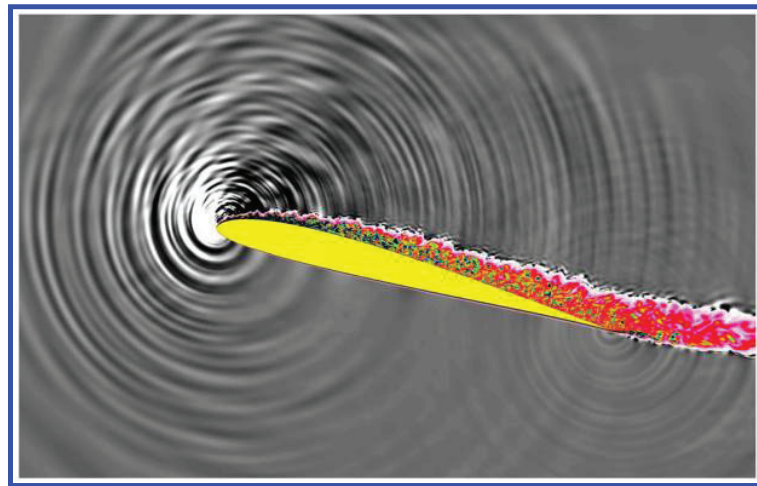


Figure 17. Sound radiation from airfoil leading edge at $\alpha = 18.6^\circ$ prior to the onset of suction collapse and DSV formation. Shown are contours of dilatation superimposed on vorticity magnitude

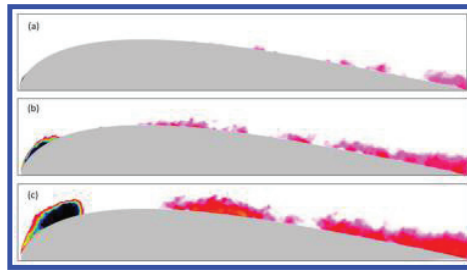


Figure 18. Spanwise-averaged reversed-flow region in airfoil frame of reference at selected instants during DSV emergence: (a) 19.8° , (b) 20.3° and (c) 20.8° . Vertical scale enlarged by a factor of two for clarity

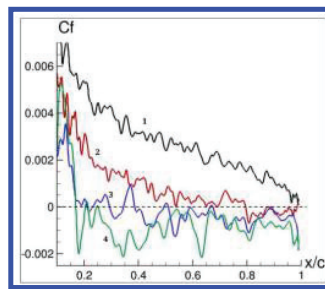


Figure 19. Spanwise-averaged skin-friction distributions in turbulent boundary layer at selected instants during pitch-up motion: $\alpha = 15.2^\circ, 18.6^\circ, 19.8^\circ$ and 20.3°

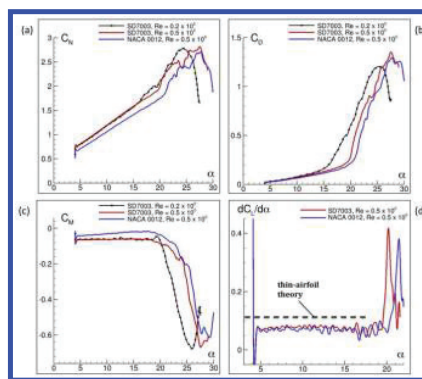


Figure 20. Aerodynamic load histories for all pitching cases: (a) normal, (b) drag and (c) pitching moment coefficients; (d) lift slope

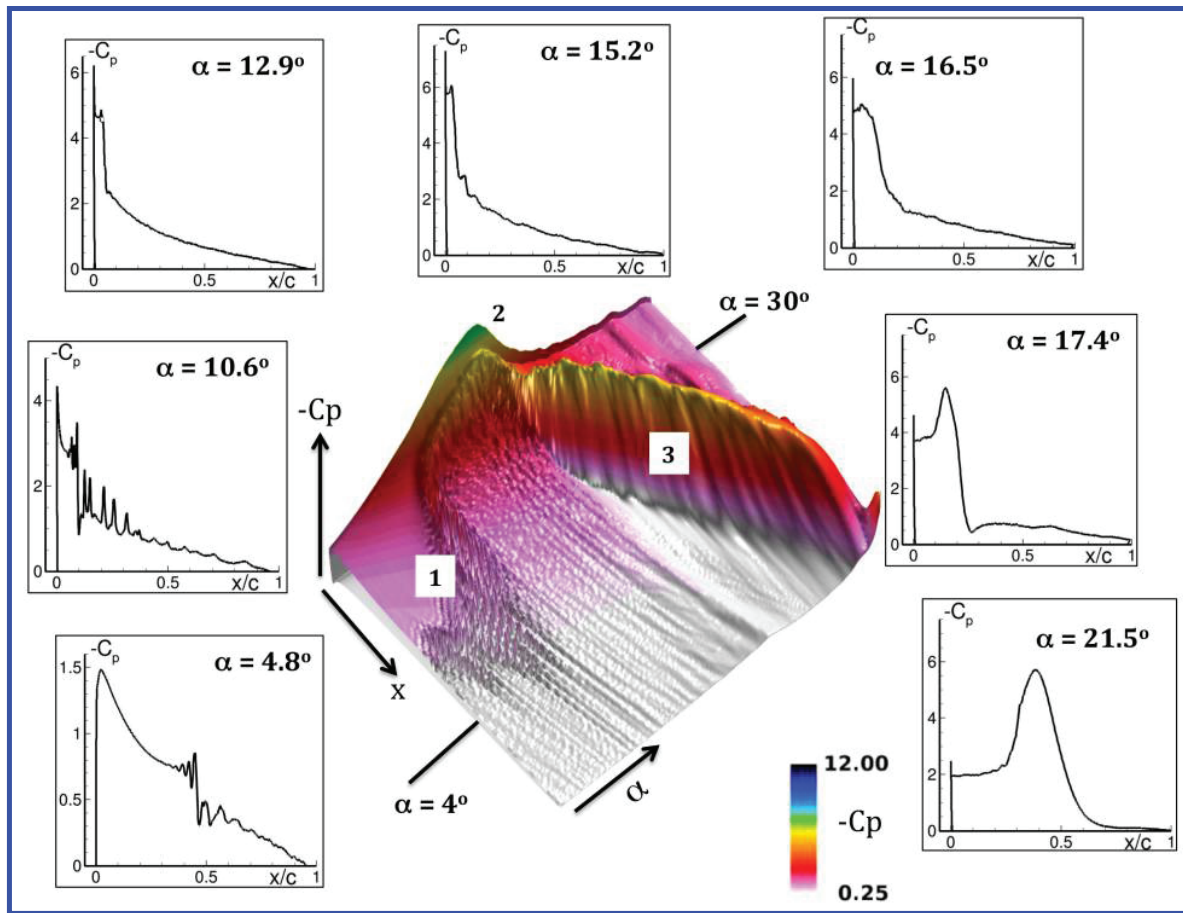


Figure 21. Spatio-temporal distribution of spanwise-averaged surface pressure on pitching airfoil and selected C_p -distributions, (SD7003 airfoil, $Re_c = 0.2 \times 10^6$)

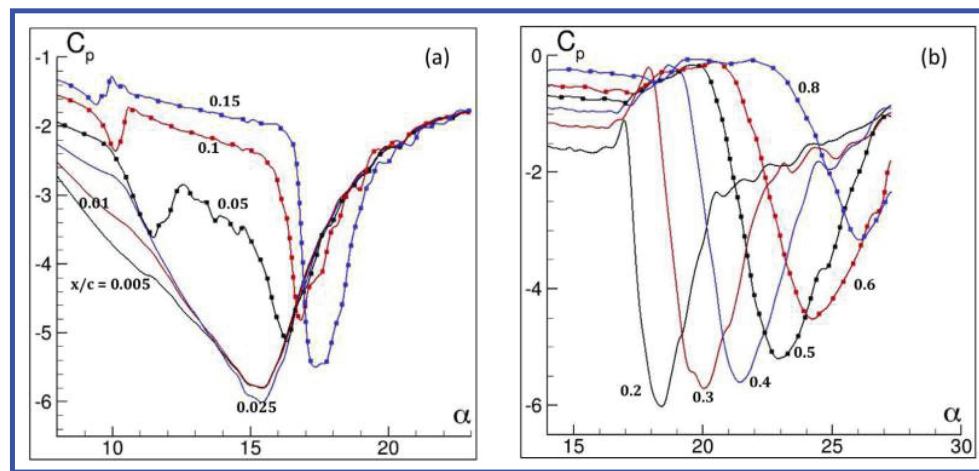


Figure 22. Histories of lowpass-filtered spanwise-averaged pressure at selected stations on airfoil upper surface, (SD7003 airfoil, $Re_c = 0.2 \times 10^6$)

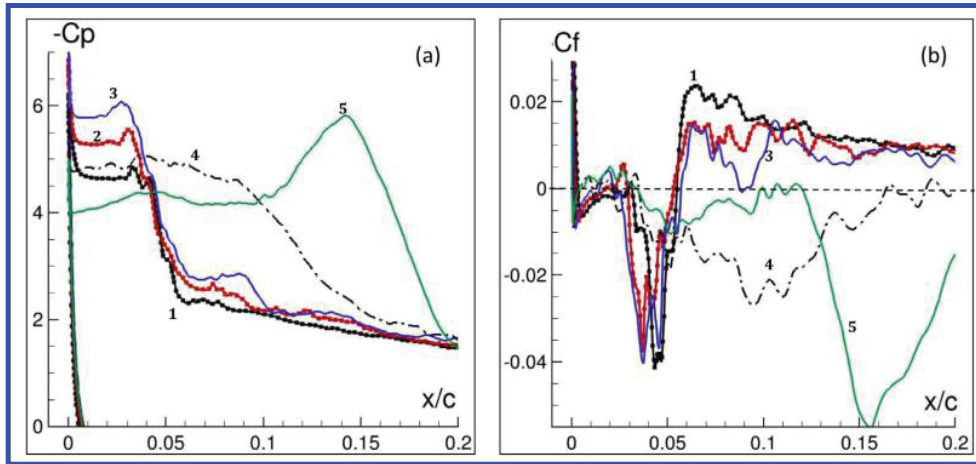


Figure 23. Spanwise-averaged (a) surface pressure and (b) skin-friction distributions at selected instants during leading-edge suction collapse and DSV formation ($\alpha = 12.9^\circ, 14.0^\circ, 15.2^\circ, 16.5^\circ, 17.1^\circ$; SD7003 airfoil, $Re_c = 0.2 \times 10^6$)

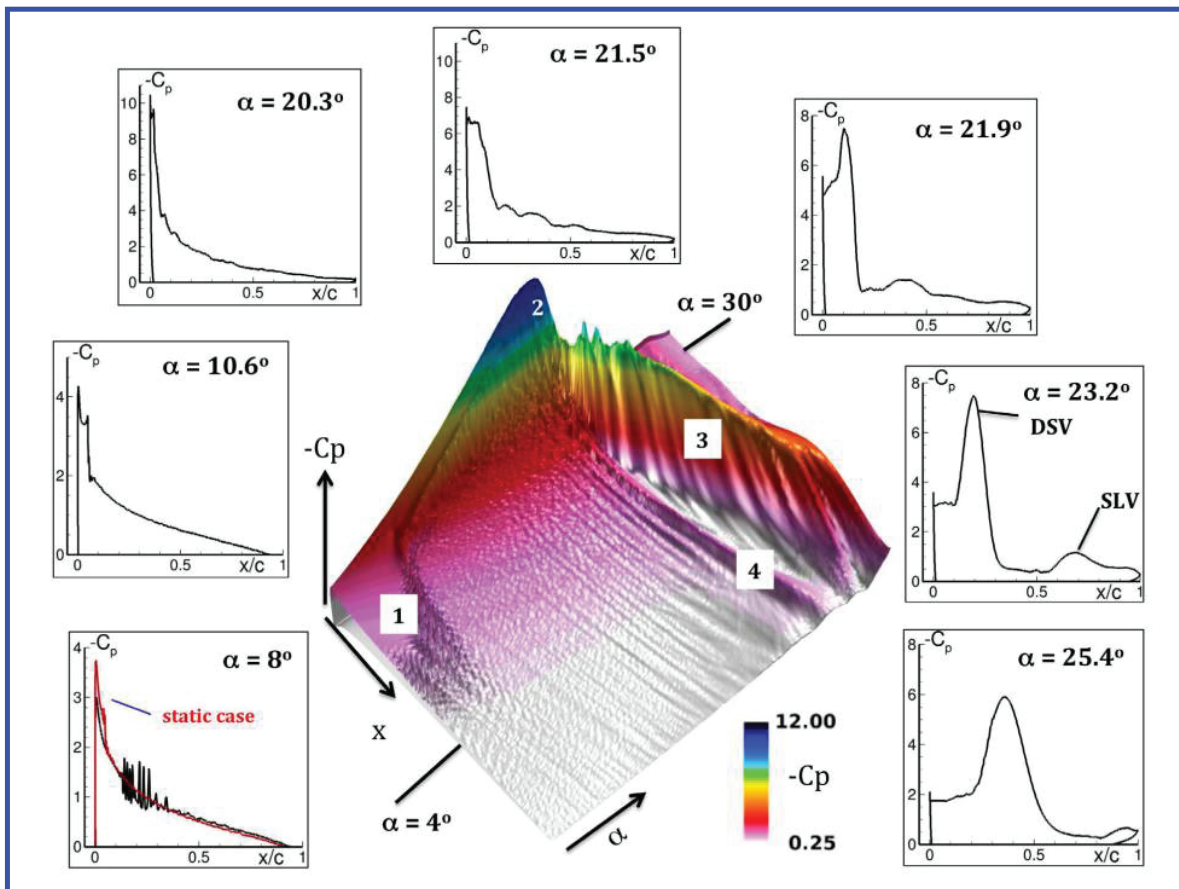


Figure 24. Spatio-temporal distribution of spanwise-averaged surface pressure on pitching airfoil and selected C_p -distributions, (NACA 0012 airfoil, $Re_c = 0.5 \times 10^6$)

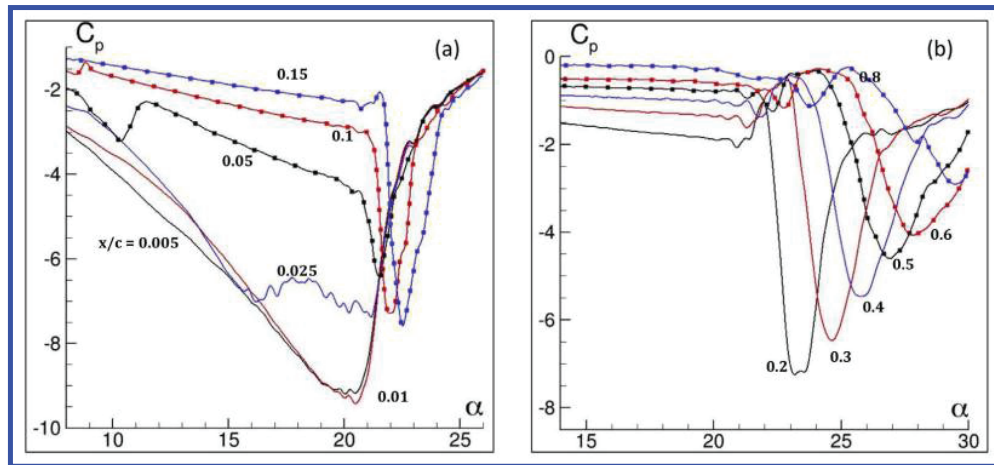


Figure 25. Histories of lowpass-filtered spanwise-averaged pressure at selected streamwise stations on airfoil upper surface, (NACA 0012 airfoil, $Re_c = 0.5 \times 10^6$)

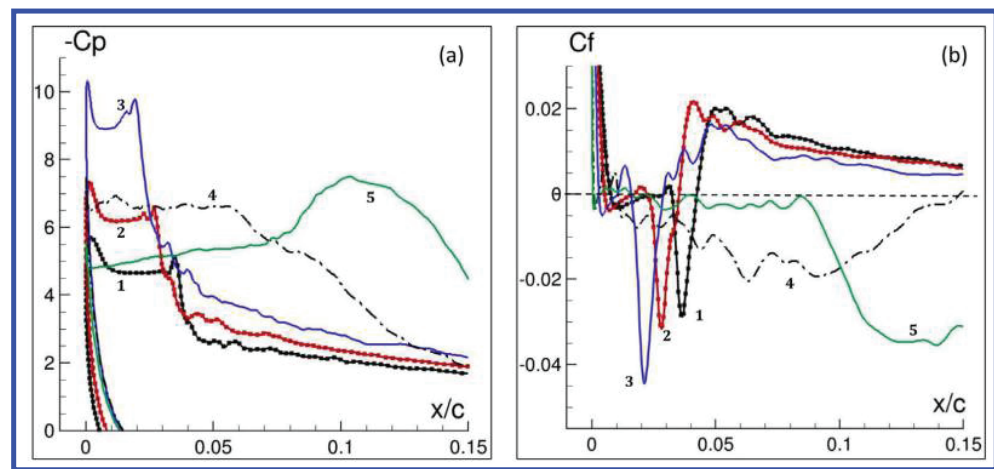


Figure 26. Spanwise-averaged (a) surface pressure and (b) skin-friction distributions at selected instants during leading-edge suction collapse and DSV formation ($\alpha = 12.9^\circ, 15.2^\circ, 19.2^\circ, 21.5^\circ, 21.9^\circ$; NACA 0012 airfoil, $Re_c = 0.5 \times 10^6$)

APPENDIX F

Control of Dynamic Stall on a Pitching Airfoil Using High-Frequency Actuation

Miguel R. Visbal *

*Aerospace Systems Directorate
Air Force Research Laboratory
Wright-Patterson AFB, OH 45433*

A flow control strategy for the delay of unsteady separation and dynamic stall on a pitching NACA 0012 airfoil is explored by means of high-fidelity large-eddy simulations. The flow fields are computed employing a high-fidelity large-eddy simulation (LES) approach. The flow parameters are freestream Mach number $M_\infty = 0.1$ and chord Reynolds numbers $Re_c = 5 \times 10^5$. Both constant-rate and oscillatory pitching motions are considered. For the baseline cases, dynamic stall is initiated with the bursting of a contracted laminar separation bubble (LSB) present in the leading-edge region. This observation motivated a flow control approach employing high-frequency pulsed actuation imparted through a zero-net mass flow blowing/suction slot located on the airfoil lower surface just downstream of the leading edge. For the constant-rate pitching case, both pulsed and harmonic spanwise-nonuniform forcing are considered with a maximum non-dimensional frequency $St_f = fc/U = 50.0$ which corresponds to a sub-harmonic of the dominant natural LSB fluctuations for a baseline static case used for reference purposes. A significant delay in the onset of dynamic stall is demonstrated with pulsed forcing at high frequencies ($St_f = 25.0, 50.0$), however, control effectiveness diminishes with decreasing frequency. At $St_f = 12.5$, pulsed actuation is shown to be superior to harmonic forcing suggesting that the higher harmonic content present in the pulsed mode is still capable of energizing the LSB. For the oscillatory pitching motion, pulsed high-frequency flow control with $St_f = 50.0$ is considered for two cases exhibiting light and deep dynamic stall respectively. For light dynamic stall, flow actuation is capable of maintaining an effectively attached flow during the entire pitching cycle thereby inhibiting the formation of large-scale leading-edge and shear-layer vortical structures. For deep dynamic stall, control is found to also be very effective in eliminating leading-edge separation and the formation of a dynamic stall vortex. Nonetheless, trailing-edge separation eventually occurs at high incidence. For both cases, actuation provided a significant reduction in the cycle-averaged drag and in the force and moment fluctuations. In addition, the negative (unstable) net-cycle pitch damping found in the baseline cases was eliminated.

Nomenclature

c	= airfoil chord
C_L, C_D, C_M	= lift, drag and quarter-chord moment coefficients
C_p	= pressure coefficient
DSV	= dynamic stall vortex
E	= total specific energy
$\hat{F}, \hat{G}, \hat{H},$	= inviscid vector fluxes
$\hat{F}_v, \hat{G}_v, \hat{H}_v$	= viscous vector fluxes
J	= Jacobian of the coordinate transformation
k	= reduced frequency, $\pi fc/U_\infty$
LSB	= laminar separation bubble
M	= Mach number
p	= static pressure
\vec{Q}	= vector of dependent variables
Re_c	= Reynolds number based on chord, $\rho_\infty U_\infty c / \mu_\infty$

*Principal Research Aerospace Engineer, Computational Sciences Center. AIAA Fellow

This material is declared a work of the U.S. Government and is not subject to copyright protection in the United States.

s	= span width for spanwise-periodic computations
SLV	= shear-layer vortex
St	= non-dimensional frequency, fc/U_∞
t	= time
u, v, w	= Cartesian velocity components
$\hat{U}, \hat{V}, \hat{W}$	= contravariant velocity components
$u'u', v'v', u'v'$	= Reynolds stresses
x, y, z	= Cartesian coordinates
α	= angle of attack
γ	= specific heat ratio, 1.4 for air
Δt	= time step size
μ	= molecular viscosity coefficient
ξ, η, ζ	= body-fitted computational coordinates
ζ_d	= net-cycle pitch damping
ρ	= fluid density
$\omega_x, \omega_y, \omega_z$	= vorticity components
Ω	= pitch rate, rad/sec
Ω^+	= non-dimensional pitch rate, $= \Omega c/U_\infty$

I. INTRODUCTION

Wings subjected to large excursions in angle of attack exhibit the phenomenon of dynamic stall characterized by a transient delay in separation (relative to the static situation), the abrupt onset of unsteady separation and the formation of a large-scale dynamic stall vortex (DSV). The angular lag in separation in conjunction with the DSV-induced suction promote a transiently elevated aerodynamic lift. However, as the DSV propagates along the wing it induces undesirable variations in aerodynamic forces and pitching moment which severely impact controllability, vibrations, structural integrity and noise generation. Dynamic stall is found in a broad range of engineering applications including retreating blades of helicopter rotors in forward flight, maneuvering aircraft and wind turbines. It is also important in severe wing-gust encounters where large excursions in effective angle of attack may be generated over a wing in otherwise nominal steady flight. For the extensive body of literature on the subject, the reader is referred to several comprehensive reviews addressing various aspects of this complex phenomenon. These include the works of McCroskey,¹ Carr,² Ericsson and Reding,³ Visbal,⁴ Ekaterinaris and Platzer⁵ and Carr and Chandrasekhara.⁶

The gross characteristics of deep dynamic stall are by now well established. For instance, the presence of a coherent DSV which forms near the leading edge and then convects along the airfoil inducing large overshoots in the aerodynamic loads is universally observed for a wide range of Reynolds numbers ($10^4 \leq Re_c \leq 10^6$). Nonetheless, the detailed underlying viscous mechanisms which precede the emergence of the DSV are less understood. This task is challenging given the complex unsteady boundary-layer behavior under the influence of several interrelated flow effects, including compressibility, transition, type and rate of motion and leading-edge geometry.

Experimental investigations have provided a great deal of information on the dynamic stall flow events and the accompanying transient aerodynamic loads. A broad range of experimental techniques have been applied to this challenging problem, including flow visualizations,^{7,8} force measurements,^{9,10} surface pressure and hot-film measurements,¹¹⁻¹⁴ as well as planar whole field velocity and density surveys employing PIV^{15,16} and interferometric techniques.¹⁷ A number of experimental studies have also explored the control of dynamic stall employing both passive and active techniques including a leading-edge slat,¹⁸ a dynamically deforming airfoil nose,¹⁹ 3D protuberances,²⁰ periodic jet forcing,²¹ steady blowing,²² pulsed jets²³ and plasma-based actuators.^{24,25}

Numerous dynamic stall computational investigations have been conducted. These include a number of 2-D laminar studies²⁶⁻²⁸ at chord-based Reynolds numbers of order $Re_c = 10^4$. For higher Reynolds numbers, Reynolds-averaged (RANS) computations employing a hierarchy of turbulence models have been presented.^{5,29} Collectively, it is found⁵ that Reynolds-averaged approaches may exhibit significant deficiencies, which in some instances can be partially corrected through the incorporation of empirical transitional models. The investigations of Refs. 30-32 addressed for the first time the direct numerical simulation of the transitional dynamic stall vortex evolution over plunging and pitching airfoils. This work, motivated by micro-air-vehicle applications, considered fairly high rates of motion and low Reynolds numbers $Re_c \leq 6 \times 10^4$. It was demonstrated that even when the incipient separation and dynamic stall vortex formation were initially laminar, the subsequent abrupt onset of transition played a critical role in the vortex dynamics beginning at modest Reynolds numbers ($Re_c \approx 10^4$).

In Ref. 33, the process of dynamic stall was studied by means of large-eddy simulations for a constant-rate pitching airfoil at higher Reynolds numbers ($Re_c = 2 \times 10^5, 5 \times 10^5$) and more practical rates of motion ($\Omega^+ = \Omega c/U_\infty = 0.05$). The airfoil was pitched about its quarter-chord axis starting from a prescribed low incidence to a high angle of attack beyond the onset of dynamic stall. This transient motion was selected instead of the typical harmonic pitching case in order to make the simulations more computationally feasible by eliminating the need to compute multiple cycles. In addition, the initial non-zero incidence promotes a laminar boundary layer along the airfoil pressure surface thereby requiring less spatial resolution. The onset of stall for this constant-rate pitching motion is still of general applicability to a broader class of motions. Indeed, experiments by Lorber and Carta¹² demonstrated many similarities between constant-rate and sinusoidally pitching airfoils. They also showed that the process is not significantly altered if the starting incidence is well below the static stall angle.

In Ref. 33 it was found that the unsteady boundary layer process is characterized by the presence of a laminar separation bubble (LSB) which contracts with increasing angle of attack as leading edge suction builds up. Beyond a critical incidence, the LSB breaks down and rapid suction collapse ensues. Abrupt turbulent separation follows allowing the turbulent boundary-layer vorticity to coalesce into a coherent DSV. The initiation of the DSV formation preceded by LSB breakdown found in the computations³³ is consistent with experimental findings of Chandrasekhara et al.¹⁷

The critical role of the LSB on the initiation of the DSV provides the impetus to investigate strategies for dynamic stall delay based on manipulation of the LSB. In Ref. 34, high-frequency active flow control of the LSB was explored for a NACA 0012 airfoil under stationary and constant-pitch-rate motion at two values of Reynolds number ($Re_c = 2 \times 10^5, 5 \times 10^5$). Flow control was implemented by means of a zero-net mass blowing/suction slot located on the airfoil lower surface just downstream of the leading edge, as depicted in Fig. 1d. This allowed for the introduction of disturbances in the boundary layer as early as possible and without direct brute-force modification of the suction surface boundary layer. Both 2D and spanwise-nonuniform pulsed forcing were considered at a very high non-dimensional frequency $St_f = fU/c = 50.0$ corresponding to a sub-harmonic of the dominant LSB frequency for a baseline static case used for reference purposes. Significant benefits in delaying the onset of unsteady separation and DSV formation were demonstrated.

In the present study, we investigate further the effect of actuation frequency on control efficacy, as well as the application of the approach to the case of an oscillating pitching maneuver. The flow fields are computed employing a high-order implicit large-eddy simulation (ILES) approach. This methodology, previously introduced in Refs. 35 and 36, is based on high-order compact schemes for the spatial derivatives augmented with a Pade-type lowpass filter to ensure stability. The high-order scheme is essential for accurately capturing the transition process near the leading edge, whereas the discriminating lowpass filter operator provides regularization in turbulent flow regions in lieu of a standard sub-grid-scale (SGS) model. The governing equations and high-fidelity computational approach are presented in Sections II and III, respectively. The effects of forcing for both a constant-rate and an oscillatory pitching NACA 0012 airfoil are considered in Sections IV-C and IV-D respectively.

II. GOVERNING EQUATIONS

The governing equations are the unfiltered full compressible Navier-Stokes equations cast in strong conservative form after introducing a general time-dependent curvilinear coordinate transformation $(x, y, z, t) \rightarrow (\xi, \eta, \zeta, \tau)$ ^{37,38} from physical to computational space. In terms of non-dimensional variables, these equations can be written in vector notation as:

$$\frac{\partial}{\partial \tau} \left(\frac{\vec{Q}}{J} \right) + \frac{\partial \hat{F}}{\partial \xi} + \frac{\partial \hat{G}}{\partial \eta} + \frac{\partial \hat{H}}{\partial \zeta} = \frac{1}{Re} \left[\frac{\partial \hat{F}_v}{\partial \xi} + \frac{\partial \hat{G}_v}{\partial \eta} + \frac{\partial \hat{H}_v}{\partial \zeta} \right] \quad (1)$$

where $\vec{Q} = \{\rho, \rho u, \rho v, \rho w, \rho E\}$ denotes the solution vector, $J = \partial(\xi, \eta, \zeta, \tau) / \partial(x, y, z, t)$ is the transformation Jacobian, and \hat{F} , \hat{G} and \hat{H} are the inviscid fluxes given by:

$$\hat{F} = \begin{bmatrix} \rho \hat{U} \\ \rho u \hat{U} + \hat{\xi}_x p \\ \rho v \hat{U} + \hat{\xi}_y p \\ \rho w \hat{U} + \hat{\xi}_z p \\ (\rho E + p) \hat{U} - \hat{\xi}_t p \end{bmatrix} \quad (2)$$

$$\hat{G} = \begin{bmatrix} \rho \hat{V} \\ \rho u \hat{V} + \hat{\eta}_x p \\ \rho v \hat{V} + \hat{\eta}_y p \\ \rho w \hat{V} + \hat{\eta}_z p \\ (\rho E + p) \hat{V} - \hat{\eta}_t p \end{bmatrix} \quad (3)$$

$$\hat{H} = \begin{bmatrix} \rho \hat{W} \\ \rho u \hat{W} + \hat{\zeta}_x p \\ \rho v \hat{W} + \hat{\zeta}_y p \\ \rho w \hat{W} + \hat{\zeta}_z p \\ (\rho E + p) \hat{W} - \hat{\zeta}_t p \end{bmatrix} \quad (4)$$

where

$$\hat{U} = \hat{\xi}_t + \hat{\xi}_x u + \hat{\xi}_y v + \hat{\xi}_z w \quad (5)$$

$$\hat{V} = \hat{\eta}_t + \hat{\eta}_x u + \hat{\eta}_y v + \hat{\eta}_z w \quad (6)$$

$$\hat{W} = \hat{\zeta}_t + \hat{\zeta}_x u + \hat{\zeta}_y v + \hat{\zeta}_z w \quad (7)$$

$$E = \frac{T}{\gamma(\gamma-1)M_\infty^2} + \frac{1}{2}(u^2 + v^2 + w^2). \quad (8)$$

Here, $\hat{\xi}_x = J^{-1} \partial \xi / \partial x$ with similar definitions for the other metric quantities. The viscous fluxes, \hat{F}_v , \hat{G}_v and \hat{H}_v can be found, for instance, in Ref. 39. In the expressions above, u, v, w are the Cartesian velocity components, ρ the density, p the pressure, and T the temperature. The perfect gas relationship $p = \rho T / \gamma M_\infty^2$ is also assumed. All flow variables have been normalized by their respective reference freestream values except for pressure which has been non-dimensionalized by $\rho_\infty U_\infty^2$.

It should be noted that the above governing equations correspond to the original *unfiltered* Navier-Stokes equations, and are used without change in laminar, transitional or fully turbulent regions of the flow. Unlike the standard LES approach, no additional sub-grid stress (SGS) and heat flux terms are appended. Instead, a high-order lowpass filter operator (to be described later) is applied to the conserved dependent variables during the solution of the standard Navier-Stokes equations. This highly-discriminating filter selectively damps only the evolving poorly resolved high-frequency content of the solution.^{35,36} This filtering regularization procedure provides an attractive alternative to the use of standard sub-grid-scale (SGS) models, and has been validated for several canonical turbulent flows. A re-interpretation of this implicit LES (ILES) approach in the context of an Approximate Deconvolution Model⁴⁰ has been provided by Mathew *et al.*⁴¹

III. NUMERICAL PROCEDURE

All simulations are performed with the extensively validated high-order Navier-Stokes solver *FDL3DI*.^{42,43} In this code, a finite-difference approach is employed to discretize the governing equations, and all spatial derivatives are obtained with high-order compact-differencing schemes.⁴⁴ For any scalar quantity, ϕ , such as a metric, flux component or flow variable, the spatial derivative ϕ' is obtained along a coordinate line in the transformed plane by solving the tridiagonal system:

$$\alpha \phi'_{i-1} + \phi'_i + \alpha \phi'_{i+1} = \beta \frac{\phi_{i+2} - \phi_{i-2}}{4} + \gamma \frac{\phi_{i+1} - \phi_{i-1}}{2} \quad (9)$$

where α , γ and β determine the spatial properties of the algorithm. For the airfoil computations reported in this paper, a sixth-order scheme is used corresponding to $\alpha = \frac{1}{3}$, $\gamma = \frac{14}{9}$ and $\beta = \frac{1}{9}$. At boundary points, higher-order one-sided formulas are utilized which retain the tridiagonal form of the scheme.^{42,43} Typically, Neumann boundary conditions are implemented with third-order one-sided expressions.

The derivatives of the inviscid fluxes are obtained by forming the fluxes at the nodes and differentiating each component with the above formula. Viscous terms are obtained by first computing the derivatives of the primitive variables. The components of the viscous flux are then constructed at each node and differentiated by a second application of the same scheme.

For the case of a pitching airfoil, the grid is moved in a rigid fashion using the prescribed airfoil motion. To ensure that the Geometric Conservation Law (GCL) is satisfied, the time metric terms are evaluated employing the procedures described in detail in Ref. 45.

In order to eliminate spurious components, a high-order lowpass spatial filtering technique^{42,46} is incorporated. If a typical component of the solution vector is denoted by ϕ , filtered values $\hat{\phi}$ at interior points in transformed space satisfy,

$$\alpha_f \hat{\phi}_{i-1} + \hat{\phi}_i + \alpha_f \hat{\phi}_{i+1} = \Sigma_{n=0}^N \frac{a_n}{2} (\phi_{i+n} + \phi_{i-n}) \quad (10)$$

Equation (10) is based on templates proposed in Refs. 44 and 47 and with proper choice of coefficients, provides a $2N$ th-order formula on a $2N + 1$ point stencil. The $N + 1$ coefficients, a_0, a_1, \dots, a_N , are derived in terms of α_f using Taylor- and Fourier-series analysis. These coefficients, along with representative filter transfer functions, can be found in Refs. 43 and 48. The filter is applied to the conserved variables along each transformed coordinate direction once after each time step or sub-iteration. For the near-boundary points, the filtering strategies described in Refs. 42 and 48 are used. In the present simulations, an 8th-order filter with $\alpha_f = 0.4$ is applied in the interior. For transitional and turbulent flows, the previous high-fidelity spatial algorithmic components provide an effective implicit LES approach in lieu of traditional SGS models, as demonstrated in Refs. 35 and 36. Finally, time-marching is accomplished by incorporating an iterative, implicit approximately-factored procedure.^{35,36}

IV. RESULTS

A. Preliminary Considerations

Computations are performed for the NACA 0012 wing configuration, shown in Fig. 1. In order to limit compressibility effects, a low freestream Mach number $M_\infty = 0.1$ is specified. The Reynolds number based on airfoil chord is $Re_c = 5 \times 10^5$.

A spanwise section of the baseline grid used is displayed in Fig. 1c where only every other line in the normal and every fourth line in the streamwise directions are plotted for clarity. The original sharp trailing edge was rounded with a very small circular arc ($r/c \approx 0.0013$) in order to facilitate the use of an O-mesh topology. Grid points were concentrated near the airfoil in order to capture the dynamic stall formation and its initial convection. Sectional 2-D grids were used to construct the three-dimensional mesh which extended a distance $s/c = 0.1$ in the spanwise direction and had a uniform Δz spacing. The grid contained $1341 \times 410 \times 133$ points in the streamwise, normal and spanwise directions respectively. Additional details of the mesh, as well as a grid sensitivity study is provided in Ref. 34.

Boundary conditions are prescribed as follows (see Fig. 1). Along the airfoil surface, a no-slip adiabatic condition is employed in conjunction with a zero normal pressure gradient. The surface velocity components (u_s, v_s, w_s) are determined from the imposed pitching motion to be described below. Along the far field boundary, located more than 100 chords away from the airfoil, freestream conditions are specified. It should be noted that prior to reaching this boundary, the grid is stretched rapidly. This stretching in conjunction with the lowpass spatial filter provides a buffer-type treatment found previously⁴⁹ to be quite effective in reducing spurious reflections. Spatially-periodic conditions were enforced in both the azimuthal and spanwise (homogeneous) directions using five-plane overlaps.

For all computations a very small non-dimensional time step $\Delta t U_\infty / c = 0.00002$ is prescribed in order to provide sufficient temporal resolution of fine-scale features. For the constant-rate pitching cases, this value of Δt corresponds approximately to 17,450 time steps per degree of angular rotation.

B. Flow Control Approach

As demonstrated in previous computations,³³ the LSB plays a critical role in the initiation of the dynamic stall process. This provides the impetus to explore means of delaying dynamic stall onset by energizing the LSB. In Ref. 34, the effectiveness of high-frequency actuation on delaying the onset of unsteady separation was demonstrated for a constant-rate pitching airfoil. In the present paper, we investigate the effect of actuation frequency on control efficacy, as well as the application of the approach to the case of an oscillating pitching maneuver.

High-frequency active flow control is implemented by means of a blowing/suction slot located on the airfoil lower surface downstream of the leading edge, as depicted in Fig. 1d. This allows for the introduction of disturbances in the boundary layer as early as possible and without direct brute-force modification of the suction surface boundary layer. It should also be noted than in dynamic stall applications the stagnation point on the airfoil lower surface moves away from the leading edge at high angles of attack facilitating this control configuration. Although a blowing/suction slot is used to expedite computational exploration, other more practical high-frequency control approaches such as plasma-based actuators would be preferable for actual implementation.

Control is introduced by a zero-net-mass blowing/suction slot, where the velocity normal to the airfoil surface is specified as follows:

$$v_n/U_\infty = A_o F(x) F(z) F(t), \quad (11)$$

$$F(x) = \sin[2\pi \left(\frac{s - s_1}{s_2 - s_1} \right)], \quad (12)$$

$$F(z) = \sin(2\pi n z / S) \quad (13)$$

In the above, s_1 and s_2 represent the edges of the slot, $A_o = V_{max}/U_\infty$ is the actuation amplitude, n the spanwise wavenumber for 3D forcing and S the span width. In all cases to be considered here, a slot size $(s_2 - s_1)/c \approx 0.01$, amplitude $A_o = 0.1$ and wavenumber $n = 2$ were specified. Results for spanwise-uniform forcing ($n = 0$) can be found in Ref. 34. For reference purposes, assuming a uniform amplitude A_o over the entire slot would result in a blowing coefficient $C_\mu = 2 \frac{(s_2 - s_1)}{c} \frac{V_{max}^2}{U_\infty^2} \approx 2.0 \times 10^{-4}$ which represents a very small actuation input.

In this investigation, a harmonic time function $F(t) = \sin(2\pi f t)$ as well as pulsed actuation are considered. For the latter, the forcing amplitude is modulated according to the duty cycle shown in Fig. 2a where T_p denotes the fundamental period and T_d the portion of the cycle over which the actuator is switched on. The duty cycle is typically expressed as the percentage $T_d/T_p \times 100\%$. In all cases described below, a 50 % duty cycle is employed. As shown in the spectrum of Fig. 2b, this waveform introduces multiple harmonics in addition to the imposed primary frequency $St_f = c/T_p U_\infty$.

Since the approach for control of dynamic stall is based on the manipulation of the LSB, a stationary airfoil case at $\alpha = 8^\circ$ which exhibits a contracted LSB (Fig. 3a) is used for reference. The corresponding frequency spectrum of the surface pressure fluctuations at $x/c = 0.05$ is shown in Fig. 3b. The spectrum displays a broad peak centered about $St \approx 120$ which is associated with the rollup of the separated shear layer. It is of interest to correlate this frequency with that corresponding to the inviscid instability of a shear layer.⁵⁰⁻⁵² For a hyperbolic tangent profile, the most amplified non-dimensional frequency is given by $\omega = \frac{1}{4} \delta_\omega \frac{2\pi f}{\bar{u}} \approx 0.21$ where $\delta_\omega = \Delta u / \frac{\partial u}{\partial y}_{max}$ is the vorticity thickness and $\Delta u = u_2 - u_1$ and $\bar{u} = \frac{1}{2}(u_1 + u_2)$ are the shear layer velocity difference and averaged velocity respectively. Based on the computed time-averaged solution at $x/c = 0.05$, the non-dimensional frequency predicted by inviscid theory is $St = f c / U_\infty \approx 110$ which falls within the broad peak exhibited by the spectrum of Fig. 3b. In this study, the fairly high frequency associated with the LSB will be targeted.

The maximum forcing frequency employed in the dynamic stall simulations described below is limited to $St_f = 50.0$. This value is a sub-harmonic of the observed shear layer fluctuations found for the reference static case (Fig. 3b). Nonetheless, it is still much higher than those typically employed for control of large-scale separation in static stall. Furthermore, as noted earlier, the duty cycle introduces higher harmonics which fall within the range of the natural LSB dominant fluctuations. As it is demonstrated below, the highest frequency considered here is already fairly effective in delaying dynamic stall. Higher values of St_f would demand finer computational temporal resolution and in addition are less achievable in practical flow control devices. It is interesting to note that when scaled in terms of the time-averaged LSB length (L_s) and the local freestream velocity (U_s) for the reference static case, this maximum non-dimensional forcing frequency ($St_f = 50.0$) corresponds to $F^+ = f L_s / U_s \approx 1.4$ which is still of order one as suggested for periodic separation control.⁵³ Finally, flow control was started while the airfoil was stationary at its initial incidence $\alpha_o = 4^\circ$, approximately one convective time prior to the onset of the pitching motion, and remained on throughout the entire maneuver.

C. Control of Dynamic Stall for a Constant-Rate Pitching Airfoil

Control of the onset of dynamic stall for a constant-rate pitching wing is considered in order to investigate the effect of actuation frequency and mode of forcing (harmonic versus pulsed) using a simpler pitching maneuver. The airfoil is pitched about its quarter-chord axis at a nominal constant rate $\Omega^+ = \Omega c / U_\infty = 0.05$ from an initial incidence $\alpha_o = 4^\circ$ to a large angle of attack beyond the onset of dynamic stall. The small initial incidence is specified in order to effectively maintain a laminar boundary layer along the airfoil pressure side which in turn allows for improved streamwise spatial resolution on the suction surface. As noted in Ref. 12, the dynamic stall process is not significantly altered provided α_o is well below the static stall angle. Furthermore, a comparison (not shown) of computed solutions for $\alpha_o = 4^\circ$ and 8° indicated no differences in the unsteady separation behavior and dynamic stall vortex formation. In order to avoid discontinuities in the angular acceleration, the angle of attack is prescribed employing a modified version of the ramping function of Eldredge et al.⁵⁴ Pitching simulations are started from a corresponding static solution at α_o .

The effect of actuation frequency on the onset of unsteady separation is shown in Figs. 4-6 in terms of the evolution of the instantaneous vorticity field and the region of reversed-flow in the airfoil frame of reference. Four different

actuation frequencies are considered, namely $St_f = 50.0, 25.0, 12.5$ and 6.25 . Significant delay of leading-edge separation and dynamic stall vortex (DSV) formation is clearly apparent for $St_f = 50.0$ and 25.0 up to the highest angle of attack shown in the figures ($\alpha = 26.6^\circ$). In fact, for these cases, the flow remains attached around the airfoil leading edge and no DSV is present. Instead, a trailing-edge separation grows in extent and propagates upstream. For $St_f = 12.5$, leading-edge separation and DSV formation is apparent at $\alpha = 26.6^\circ$ and even earlier ($\alpha = 24.3^\circ$) for the lowest frequency of actuation, $St_f = 6.25$. While in all actuated cases a delay in the onset of leading-edge separation is observed, it is clear that control effectiveness diminishes with decreasing frequency.

A more quantitative measure of the delay of unsteady separation with forcing is shown in Figs. 7a,b in terms of the lowpass-filtered spanwise-averaged surface pressure^{33,34} histories at $x/c = 0.0025$ and 0.15 . At the first station, the collapse of leading edge suction induced by the onset of separation is progressively delayed with increasing actuation frequency. The corresponding minimum pressure or suction level achieved is plotted in Fig. 7c. At $x/c = 0.15$ (Fig. 7b), the drastic pressure peak induced by the formation of the dynamic stall vortex in the baseline case is considerably reduced with flow control. The rapid rise in drag coefficient typically seen in dynamic stall (Fig. 7d) is observed to be displaced to higher incidences as actuation frequency increases. The behavior of the drag coefficient and leading-edge suction levels indicate that although the benefits of flow control continue to increase with St_f , this effect seems to saturate beyond a given frequency of pulsed actuation ($St_f = 25.0$).

A comparison of pulsed and harmonic actuation for $St_f = 12.5$ is provided in Figs. 8 and 9. At this intermediate value of forcing frequency, it is apparent that pulsed actuation is significantly superior in terms of control effectiveness. This is believed to be due to the higher harmonic content present in the pulsed mode to which the LSB is receptive. At this value of St_f , harmonic forcing has a very limited effect on the delay of DSV formation. It is anticipated that harmonic actuation at a much higher actuation frequency would regain control effectiveness. This statement is based on preliminary simulations (not shown) for the reference static case ($\alpha = 8^\circ$) which demonstrated a significant reduction of the LSB for harmonic forcing with $St_f = 100.0$.

D. Control of Dynamic Stall for an Oscillating Airfoil

In the previous section, the present high-frequency flow control approach was found to be very effective in delaying the onset of unsteady separation and DSV vortex formation for a ramp-type pitching maneuver. In several applications (e.g., maneuvering, gust encounters or rotorcraft), control must be sustained in situations involving both an increase followed by a decrease in angle of attack. It is therefore of interest to assess the effectiveness of the control approach for an oscillating airfoil.

To this end, the airfoil is pitched about its quarter-chord axis according to the following expressions for the angle of attack and pitch rate:

$$\alpha = \alpha_o + \alpha_1(1 - \cos(2kt)) \quad (14)$$

$$\dot{\alpha} = 2k\alpha_1 \sin(2kt) \quad (15)$$

where α_o and α_1 are the minimum incidence and angular amplitude respectively, and $k = \pi fc/U_\infty$ denotes the reduced frequency. Although the above equations represent a periodic motion, only one cycle of the maneuver was computed to demonstrate the effect of actuation. Two different cases corresponding to light and deep dynamic stall situations are investigated and the motion parameters are given in Table 1.

Table 1. Oscillating Airfoil Parameters

Case	k	α_o	α_1	α_{max}	$\dot{\alpha}_{max}$
light stall	0.2	4°	7°	18°	0.049
deep stall	0.2	4°	9°	22°	0.063

1. Flow Control for Light Dynamic Stall Case

The flow field evolution for the light dynamic stall baseline case is displayed in Figs. 10-12. Since the flow is effectively attached during the upstroke portion of the cycle, only select angles during the downstroke are shown in the figures. At the maximum angle of attack ($\alpha = 18^\circ$), the upper surface viscous region has thickened (Figs. 10,11) but the flow still remains effectively body conforming with only a small trailing-edge separation region (Fig. 12). By $\alpha = 15.5^\circ$,

the separation region has propagated upstream and grown significantly in the normal direction. The vorticity contours near the leading edge (Fig. 11) display the formation of coherent structures which convect downstream but do not coalesce into a large-scale DSV.

The near-wall velocity history at $x/c = 0.0025$ in Fig. 13b indicates that the flow is incipiently separated near the leading edge. The velocity signal displays significant fluctuations with an approximate non-dimensional dominant frequency $fc/U_\infty \approx 5.5$. Examination of a sequence of images also revealed intense flapping of the separated laminar shear layer emanating from the leading edge. The distributions of spanwise-averaged surface pressure in Fig. 14a indicate the collapse of leading edge suction by $\alpha = 15.5^\circ$ associated with the increased viscous displacement.

As the downstroke motion continues, large-scale vortical structures are formed over the airfoil in the separated region (Fig. 10) which induce the undulations seen in the surface pressure distribution at $\alpha = 14.7^\circ$ (Fig. 14a). Figure 15 shows the imprint of the separated flow on the upper surface pressure at $x/c = 0.8$ both as function of time and angle of attack. A low-pressure peak is induced by the separated region in the rear portion of the airfoil which has detrimental effects on the pitching moment coefficient to be discussed later. With further decrease in angle of attack, the separated flow vortical structure is shed past the trailing edge and the boundary layer reattaches progressively from the leading edge onwards.

The histories of the aerodynamic loads as function of angle of attack are shown in Fig. 16. The force and moment coefficients are well behaved during the upstroke since the flow is effectively attached. Following separation as the airfoil pitches downward, these coefficients exhibit significant hysteresis. There is a rapid increase in C_D and a significant drop in C_M . The maximum departures in the drag and moment coefficients, as well as the cycle-averaged $\langle C_N \rangle$ and $\langle C_D \rangle$ are given in Table 2. Of interest is the computed net-cycle pitch damping defined as $\zeta_d = -\frac{1}{\alpha_1} \int C_m d\alpha$. For this case, the computed net damping is negative $\zeta_d = -0.034$ implying that the airfoil extracts energy from the flow stream which can lead to self-sustained oscillations or single-degree-of-freedom stall flutter.¹

Table 2. Oscillating Airfoil Loads

Case	$C_{D_{max}}$	$C_{M_{min}}$	$\langle C_N \rangle$	$\langle C_D \rangle$	ζ_d
light stall baseline	0.236	-0.183	0.946	0.080	-0.034
light stall control	0.106	-0.033	1.033	0.036	+0.008
deep stall baseline	0.840	-0.878	1.190	0.257	-0.404
deep stall control	0.253	-0.228	1.080	0.086	+0.017

The application of high-frequency pulsed flow control, as described in Section IV-B, with $St_f = 50.0$ is considered next. The evolution of the unsteady flow field during the downstroke is shown and compared to the baseline case in Figs. 10-12. In contrast with the baseline case, the flow control approach is capable of maintaining an effectively attached flow during the entire pitching cycle. Comparison of the near-wall velocity histories at $x/c = 0.0025$ (Fig. 13b) indicates that the boundary layer remains fully attached at this station. The surface pressure distributions for the control case (Fig. 14b) display the characteristics of an attached flow. Flow control has also eliminated the large excursion in surface pressure observed for the baseline case in the rear portion of the airfoil (Fig. 15).

The effect of flow control on the aerodynamic loads is provided in Fig. 16 as well as in Table 2. Flow control reduces the maximum C_D and the minimum C_M by a factor of 2.2 and 5.5 respectively. The cycle-averaged drag is also more than halved with actuation. Finally, the net-cycle pitch damping becomes positive ($\zeta_d = +0.008$) with the application of flow control.

The present results clearly demonstrate that for the case of light dynamic stall, the proposed low-amplitude high-frequency pulsed actuation effectively suppresses boundary-layer separation and improves the behavior of the aerodynamic loads including the elimination of the undesirable negative net pitch damping which could lead to stall flutter.

2. Flow Control for Deep Dynamic Stall Case

Next, the effect of the same pulsed high-frequency actuation (with $St_f = 50.0$) is considered for a more severe deep dynamic stall condition. The corresponding pitching motion parameters are given in Table 1.

The evolution of the vorticity field for the baseline case is shown in Figs. 17 and 18. The sequence of events observed are those typically found in deep dynamic stall and include: the formation of a leading-edge DSV during the upstroke, its growth and propagation over the airfoil, the formation of a trailing edge edge vortex (TEV) and the

subsequent shedding of both vortices. During the downstroke, the flow reattaches to the surface and the location of transition also propagates downstream.

The actuated case shown in Figs. 17 and 18 demonstrates that the present flow control approach entirely eliminates leading-edge separation and the subsequent formation of the DSV. However, even with flow control, separation occurs in the rear portion of the airfoil and grows in extent during the downstroke. Eventually, as incidence continues to decrease, this separated vortical structure is shed and the boundary layer progressively reattaches.

Comparison of the surface pressure for the baseline and control cases at stations $x/c = 0.0025$ and 0.1 is shown in Fig. 19 both as function of time and angle of attack. At the first station, flow control results in a much lower minimum pressure and there is no abrupt collapse of suction. At $x/c = 0.1$, flow control has eliminated the pronounced peak associated with the DSV formation. At both streamwise locations, actuation diminishes significantly the hysteresis in surface pressure observed for the baseline case (Figs. 19b,d).

The histories of the near-wall velocity at station $x/c = 0.1$ are shown in Fig. 20a. For the baseline situation, the signal displays laminar separation, the upstream propagation of transition, turbulent separation and DSV formation during the upstroke. Turbulent reattachment and downstream propagation of transition are observed during the downstroke. The hysteresis in the transition location during the upstroke and downstroke portions of the cycle is also apparent in Fig. 20b where the near-wall velocity is displayed for the baseline case as a function of angle of attack. The near-wall velocity trace near the leading-edge for the actuated case (Fig. 20a) does not exhibit either laminar or turbulent separation and the strong DSV-induced peak is completely absent.

The effect of flow control on the aerodynamic loads is shown in Fig. 21 and Table 2. Forcing eliminates the rapid increase in lift induced during the DSV formation. The maximum departures in drag and pitching moment coefficients are reduced significantly. For instance, maximum C_D and minimum C_M are decreased by a factor of 3.3 and 3.8 respectively. The cycle-averaged drag is also reduced by a factor of 3.0. Finally, the computed net-cycle pitch damping changes from a negative (unstable) value in the baseline case ($\zeta_d = -0.404$) to a positive (stable) value ($\zeta_d = +0.017$) with flow control.

V. CONCLUSIONS

A flow control strategy for the delay of unsteady separation and dynamic stall on a pitching NACA 0012 airfoil is explored by means of high-fidelity large-eddy simulations. The flow fields are computed employing a high-fidelity large-eddy simulation (LES) approach based on 6th-order compact schemes and 8th-order low-pass spatial filters which provide an effective alternative to standard sub-grid-stress model closures. The flow parameters are freestream Mach number $M_\infty = 0.1$ and chord Reynolds numbers $Re_c = 5 \times 10^5$. Both constant-rate and oscillatory pitching motions are considered.

For the baseline cases, dynamic stall is initiated with the bursting of a contracted laminar separation bubble (LSB) present in the leading-edge region. This observation motivated a flow control approach employing high-frequency pulsed actuation imparted through a zero-net mass flow blowing/suction slot located on the airfoil lower surface just downstream of the leading edge.

For the constant-rate pitching case ($\Omega^+ = 0.05$), both pulsed and harmonic spanwise-nonuniform forcing is considered with a maximum non-dimensional frequency $St_f = fc/U = 50.0$ which corresponds to a sub-harmonic of the dominant natural LSB fluctuations for a baseline static case ($\alpha = 8^\circ$, $Re_c = 5 \times 10^5$) used for reference purposes. A significant delay in the onset of dynamic stall is demonstrated for the pulsed forcing at high frequencies ($St_f = 25.0, 50.0$), however, control effectiveness diminishes with decreasing frequency. At $St_f = 12.5$, pulsed actuation is found to be superior to harmonic forcing suggesting that the higher harmonic content present in the pulsed mode is still capable of energizing the LSB.

For the oscillatory pitching motion ($k = 0.2$) pulsed high-frequency flow control with $St_f = 50.0$ is considered for two cases exhibiting light ($\alpha_{max} = 18^\circ$) and deep ($\alpha_{max} = 22^\circ$) dynamic stall respectively. For light dynamic stall, flow actuation is capable of maintaining an effectively attached flow during the entire pitching cycle and inhibits the formation of large-scale leading-edge and shear-layer vortical structures. For deep dynamic stall, control is also found to be very effective in eliminating leading-edge separation and the subsequent DSV. Nonetheless, trailing-edge separation eventually occurs at high incidence during the downstroke. For both cases, actuation provided a significant reduction in the cycle-averaged drag, and in the force and moment fluctuations. In addition, the negative (unstable) net-cycle pitch damping found in the baseline cases was eliminated.

The flow control benefits demonstrated so far in this study should serve as motivation for additional computational and experiments investigations employing plasma-based devices or other means of high-frequency actuation.

ACKNOWLEDGMENTS

This work was supported in part by AFOSR under a task monitored by Dr. D. Smith, and by a grant of HPC time from the DoD HPC Shared Resource Centers at AFRL and ERDC.

References

- ¹W. J. McCroskey. Unsteady Airfoils. *Annual Rev. Fluid Mech.*, 14:285–311, 1982.
- ²L. Carr. Progress in Analysis and Prediction of Dynamic Stall. *Journal of Aircraft*, 25(1):6–17, 1988.
- ³Ericsson, L. E. and Reding. Fluid Dynamics of Unsteady Separated Flow. Part II. Lifting Surfaces. *Progress in Aerospace Sciences*, 24:249–356, 1987.
- ⁴M. R. Visbal. On Some Physical Aspects of Airfoil Dynamic Stall. *Proceedings of the International Symposium on Non-Unsteady Fluid Dynamics*, (Edited by J. Miller and D. Telionis, Vol. 92, ASME), 1990.
- ⁵J. Ekaterinaris and M. Platzer. Computational Prediction of Airfoil Dynamic Stall. *Progress in Aerospace Sciences*, 33:759–846, 1997.
- ⁶L. W. Carr and M. S. Chandrasekhara. Compressibility Effects on Dynamic Stall. *Progress in Aerospace Sciences*, 32:523–573, 1996.
- ⁷P. Freymuth. Vortices. *Handbook of Flow Visualization, Ch IV-3, Ed. by Yang, W.*, Hemisphere Publishing, 1989.
- ⁸K. W. McAlister and L. W. Carr. Water Tunnel Visualizations of Dynamic Stall. *J. of Fluids Engineering*, 101, 1979.
- ⁹J. H. Strickland and G. M. Graham. Force Coefficients for a NACA-0015 Airfoil Undergoing Constant Pitch Rate Motions. *AIAA Journal*, 25(4):622–624, 1987.
- ¹⁰E. J. Jumper, S. J. Shreck, and R. L. Dimmick. Lift-Curve Characteristics of an Airfoil Pitching at Constant Rate. *J. of Aircraft*, 24(10):680–687, Sep.–Oct. 1987.
- ¹¹L. W. Carr, K. W. McAlister, and W.J. McCroskey. Analysis of the development of dynamic stall based on oscillating airfoil experiments. *NASA TN D-8382*, 1977.
- ¹²P.F. Lorber and F.O. Carta. Airfoil dynamic stall at constant pitch rate and high reynolds number. *Journal of Aircraft*, 25(6):548–556, 1988.
- ¹³R. N. Conger and B. R. Ramaprian. Presure Measurements on a Pitching Airfoil in a Water Channel. *AIAA Journal*, 32(1):108–115, 1994.
- ¹⁴T. Lee and P. Gerontakos. Investigation of Flow Over an Oscillating Airfoil. *J. Fluid Mech.*, 512:313–341, 2004.
- ¹⁵K. Mulleners and M. Raffel. The Onset of Dynamic Stall Revisited. *Experiments in Fluids*, 52:779–793, 2012.
- ¹⁶B. J. Pruski and R. D. W. Bowersox. Leading-Edge Flow Structure of a Dynamically Pitching NACA 0012 Airfoil. *AIAA Journal*, 51(5):1042–1053, 2013.
- ¹⁷M. S. Chandrasekhara, L. W. Carr, and M. C. Wilder. Interferometric investigations of compressible dynamic stall over a transiently pitching airfoil. *AIAA Paper 93-0211*, January 1993.
- ¹⁸L. Carr and K. McAlister. The Effect of a Leading-Edge Slat on the Dynamic Stall of an Oscillating Airfoil. *AIAA Paper 1983-2533*, June 1983.
- ¹⁹M. Chandrasekhara, M. Wilder, and L. Carr. Unsteady Stall Control Using Dynamically Deforming Airfoils. *AIAA Journal*, 36(10):1792–1800, 1998.
- ²⁰B. Heine, K. Mulleners, G. Joubert, and M. Raffel. Dynamic Stall Control by Passive Disturbance Generators. *AIAA Paper 2011-3371*, June 2011.
- ²¹D. Greenblatt and I. Wygnanski. Dynamic Stall Control by Periodic Excitation, Part 1: NACA 0015 Parametric Study. *Journal of Aircraft*, 38(3):430–438, 2001.
- ²²H. Muller-Vahl, C. Strangfeld, C Nayeri, C. Paschereit, and D. Greenblatt. Thick Airfoil Deep Dynamic Stall and its Control. *AIAA Paper 2013-0854*, January 2013.
- ²³G. Woo and A. Glezer. Transient Control of Separating Flow over a Dynamically-Pitching Airfoil. *AIAA Paper 2010-0861*, January 2010.
- ²⁴M. Post and T. Corke. Separation Control Using Plasma Actuators- Dynamic Stall Control of an Oscillating Airfoil. *AIAA Paper 2004-2517*, June 2004.
- ²⁵A. Lombardi, P. Bowles, and T. Corke. Closed-Loop Dynamic Stall Control Using a Plasma Actuator. *AIAA Paper 2012-0918*, January 2012.
- ²⁶U. B. Mehta. Dynamic Stall of an Oscillating Airfoil. *Paper No. 23, AGARD CP-227*, 1977.
- ²⁷M.R. Visbal and J.S. Shang. Investigation of the Flow Structure Around a Rapidly Pitching Airfoil. *AIAA Journal*, 27(8):1044–1051, 1989.
- ²⁸P.G. Choudhuri, D.D. Knight, and M.R. Visbal. Two-Dimensional Unsteady Leading-Edge Separation on a Pitching Airfoil. *AIAA Journal*, 32(4):673–681, 1994.
- ²⁹M.R. Visbal. Dynamic Stall of a Constant-Rate Pitching Airfoil. *Journal of Aircraft*, 27(5):400–407, 1990.
- ³⁰M.R. Visbal. High-Fidelity Simulation of Transitional Flows past a Plunging Airfoil. *AIAA Journal*, 47(11):2685–2697, 2009.
- ³¹D. J. Garmann and M. R. Visbal. Numerical Investigation of Transitional Flow Over a Rapidly Pitching Plate. *Physics of Fluids*, 23, 2011.
- ³²M.R. Visbal. Numerical Investigation of Deep Dynamic Stall of a Plunging Airfoil. *AIAA Journal*, 49(10):2152–2170, 2011.
- ³³M.R. Visbal. Analysis of the Onset of Dynamic Stall Using High-Fidelity Large-Eddy Simulations. *AIAA Paper 2014-0591*, January 2014.
- ³⁴M.R. Visbal. Numerical Exploration of Flow Control for Delay of Dynamic Stall on a Pitching Airfoil. *AIAA Paper 2014-2044*, June 2014.
- ³⁵M.R. Visbal and D.P. Rizzetta. Large-Eddy Simulation on Curvilinear Grids Using Compact Differencing and Filtering Schemes. *Journal of Fluids Engineering*, 124:836–847, 2002.
- ³⁶M.R. Visbal, P.E. Morgan, and D.P. Rizzetta. An Implicit LES Approach Based on High-Order Compact Differencing and Filtering Schemes. *AIAA Paper 2003-4098*, June 2003.
- ³⁷M. Vinokur. Conservation Equations of Gasdynamics in Curvilinear Coordinate Systems. *Journal of Computational Physics*, 14:105–125, 1974.
- ³⁸J.L. Steger. Implicit Finite-Difference Simulation of Flow about Arbitrary Two-Dimensional Geometries. *AIAA Journal*, 16(7):679–686, 1978.

³⁹D.A. Anderson, J.C. Tannehill, and R.H. Pletcher. *Computational Fluid Mechanics and Heat Transfer*. McGraw-Hill Book Company, 1984.

⁴⁰S. Stolz and N. Adams. An Approximate Deconvolution Procedure for Large-Eddy Simulation. *Physics of Fluids*, 11(7):1699–1701, 1999.

⁴¹J. Mathew, R. Lechner, H. Foysi, J. Sesterhenn, and R. Friedrich. An explicit filtering method for LES of compressible flows. *Phys. Fluids*, 15(8):2279–2289, 2003.

⁴²M.R. Visbal and D.V. Gaitonde. High-Order Accurate Methods for Complex Unsteady Subsonic Flows. *AIAA Journal*, 37(10):1231–1239, 1999.

⁴³D.V. Gaitonde and M.R. Visbal. High-Order Schemes for Navier-Stokes Equations: Algorithm and Implementation into FDL3DI. Technical Report AFRL-VA-WP-TR-1998-3060, Air Force Research Laboratory, Wright-Patterson AFB, 1998.

⁴⁴S.K. Lele. Compact Finite Difference Schemes with Spectral-like Resolution. *Journal of Computational Physics*, 103:16–42, 1992.

⁴⁵M.R. Visbal and D.V. Gaitonde. On the Use of High-Order Finite-Difference Schemes on Curvilinear and Deforming Meshes. *Journal of Computational Physics*, 181:155–185, 2002.

⁴⁶D.V. Gaitonde, J.S. Shang, and J.L. Young. Practical Aspects of Higher-Order Numerical Schemes for Wave Propagation Phenomena. *Int. Jnl. for Num. Methods in Eng.*, 45:1849–1869, 1999.

⁴⁷P. Alpert. Implicit Filtering in Conjunction with Explicit Filtering. *J. Comp. Phys.*, 44:212–219, 1981.

⁴⁸D.V. Gaitonde and M.R. Visbal. Further Development of a Navier-Stokes Solution Procedure Based on Higher-Order Formulas. *AIAA Paper 99-0557*, January 1999.

⁴⁹M. Visbal and D. Gaitonde. Very High-Order Spatially Implicit Schemes for Computational Acoustics on Curvilinear Meshes. *J. Comp. Acoustics*, 9(4):1259–1286, 2001.

⁵⁰A. Michalke. On the inviscid instability of the hyperbolic-tangent velocity profile. *J. Fluid Mech.*, 19:543–556, 1964.

⁵¹L. Pauley, P. Moin, and W. Reynolds. The Structure of Two-Dimensional Separation. *J. Fluid Mech.*, 220:397–411, 1990.

⁵²R.E. Gordnier and M.R. Visbal. Unsteady Vortex Structure over a Delta Wing. *J. of Aircraft*, 31(1), Jan.-Feb. 1994.

⁵³D. Greenblatt and I. Wygnanski. The Control of Separation by Periodic Excitation. *Progress in Aerospace Sciences*, 36:487–545, 2000.

⁵⁴J. Eldredge, C. Wang, and M. Ol. A computational study of a canonical pitch-up, pitch-down maneuver. *AIAA Paper 2009-3687*, June 2009.

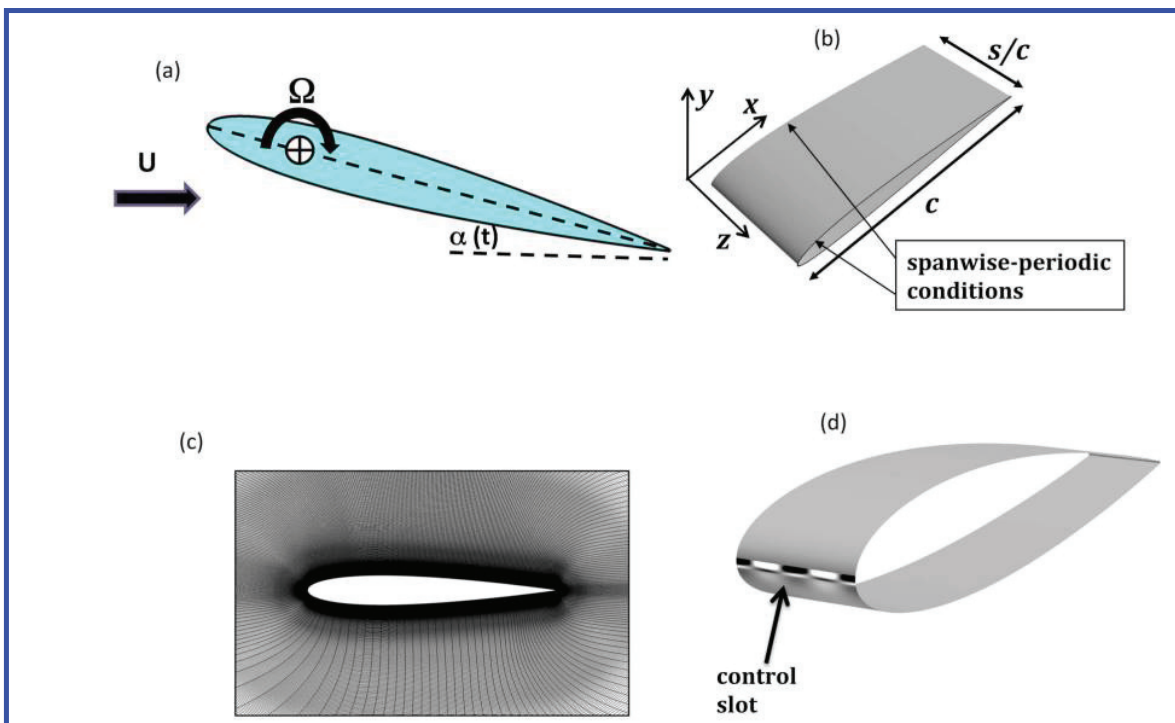


Figure 1. Airfoil configuration (a,b), computational mesh (c) and flow control slot (d)

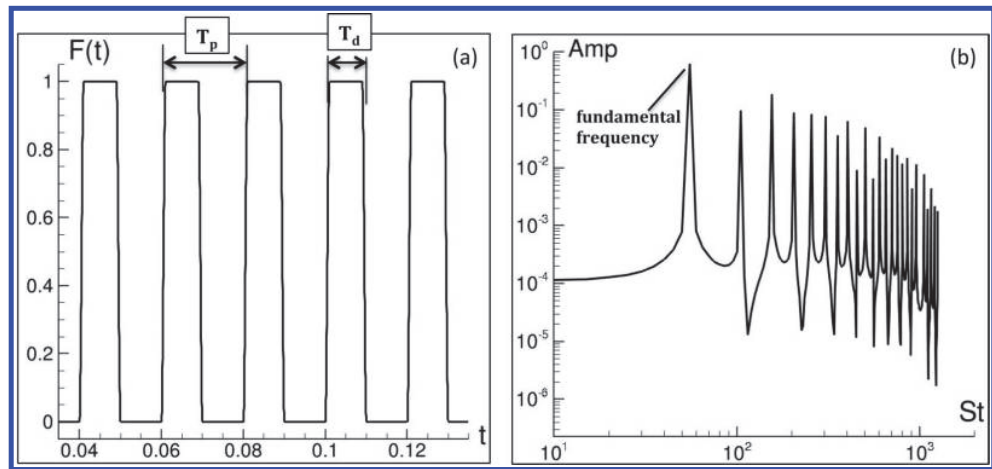


Figure 2. (a) Pulsed actuation amplitude modulation function employing a duty cycle and (b) corresponding spectrum

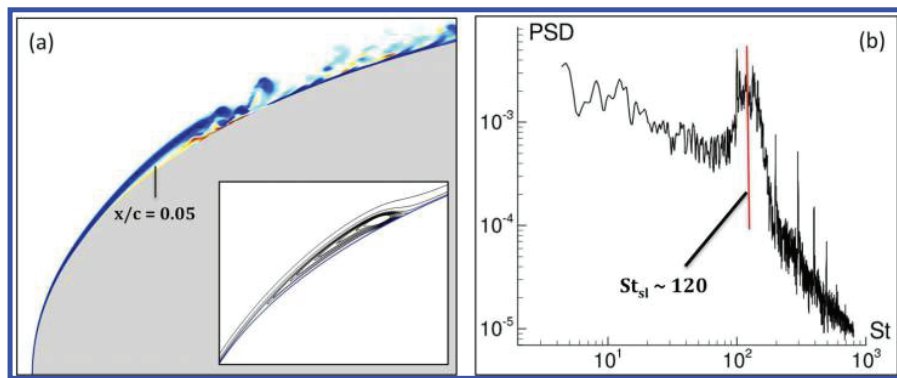


Figure 3. Reference stationary airfoil solution for $\alpha = 8^\circ$ and $Re_c = 5 \times 10^5$. (a) Contours of instantaneous spanwise vorticity near leading edge and time-averaged LSB (inset), (b) frequency spectrum of surface pressure fluctuations in LSB at $x/c = 0.05$

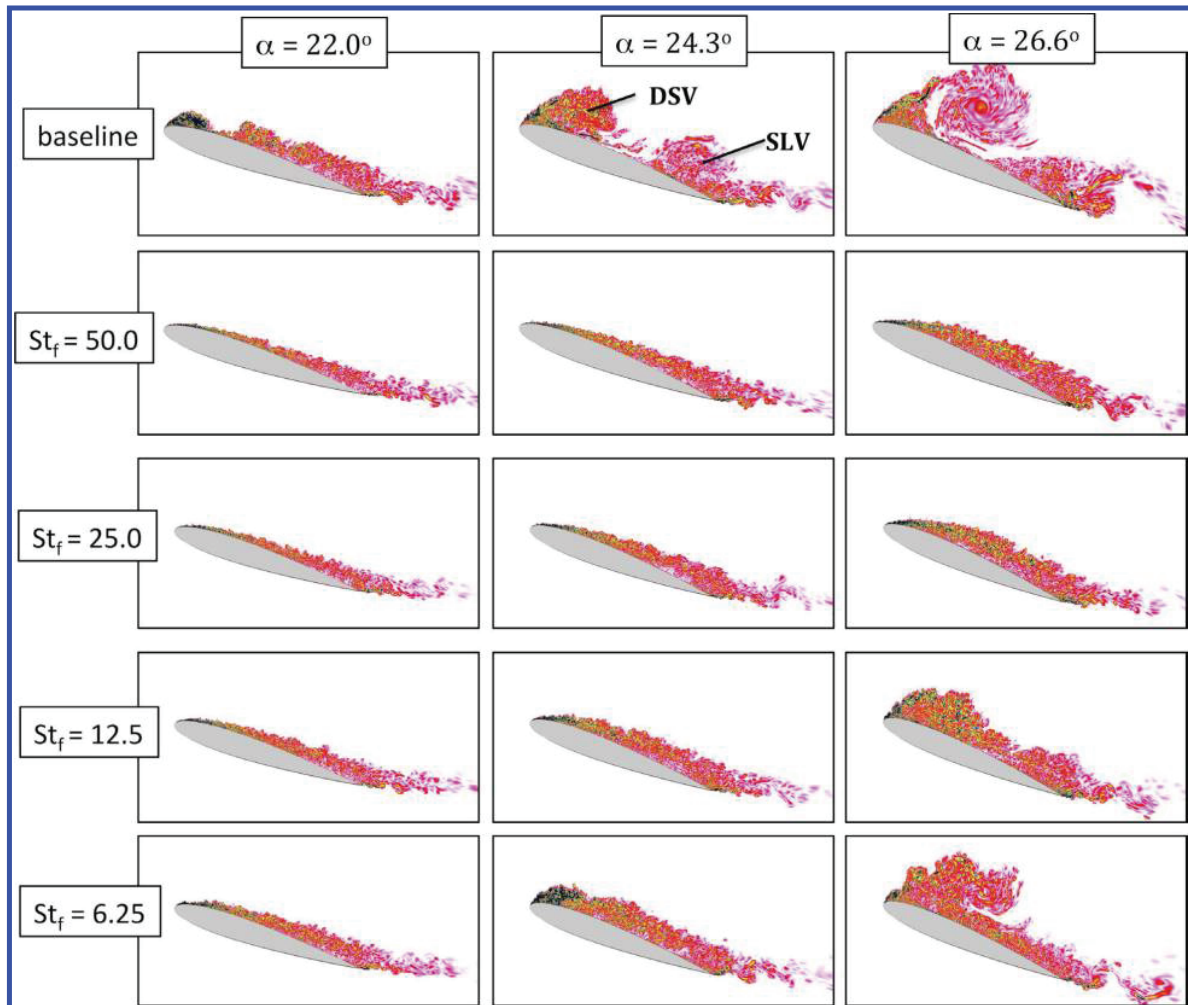


Figure 4. Effect of primary pulsed actuation frequency on evolution of unsteady flow field over constant-rate pitching airfoil shown using contours of instantaneous vorticity magnitude on midplane

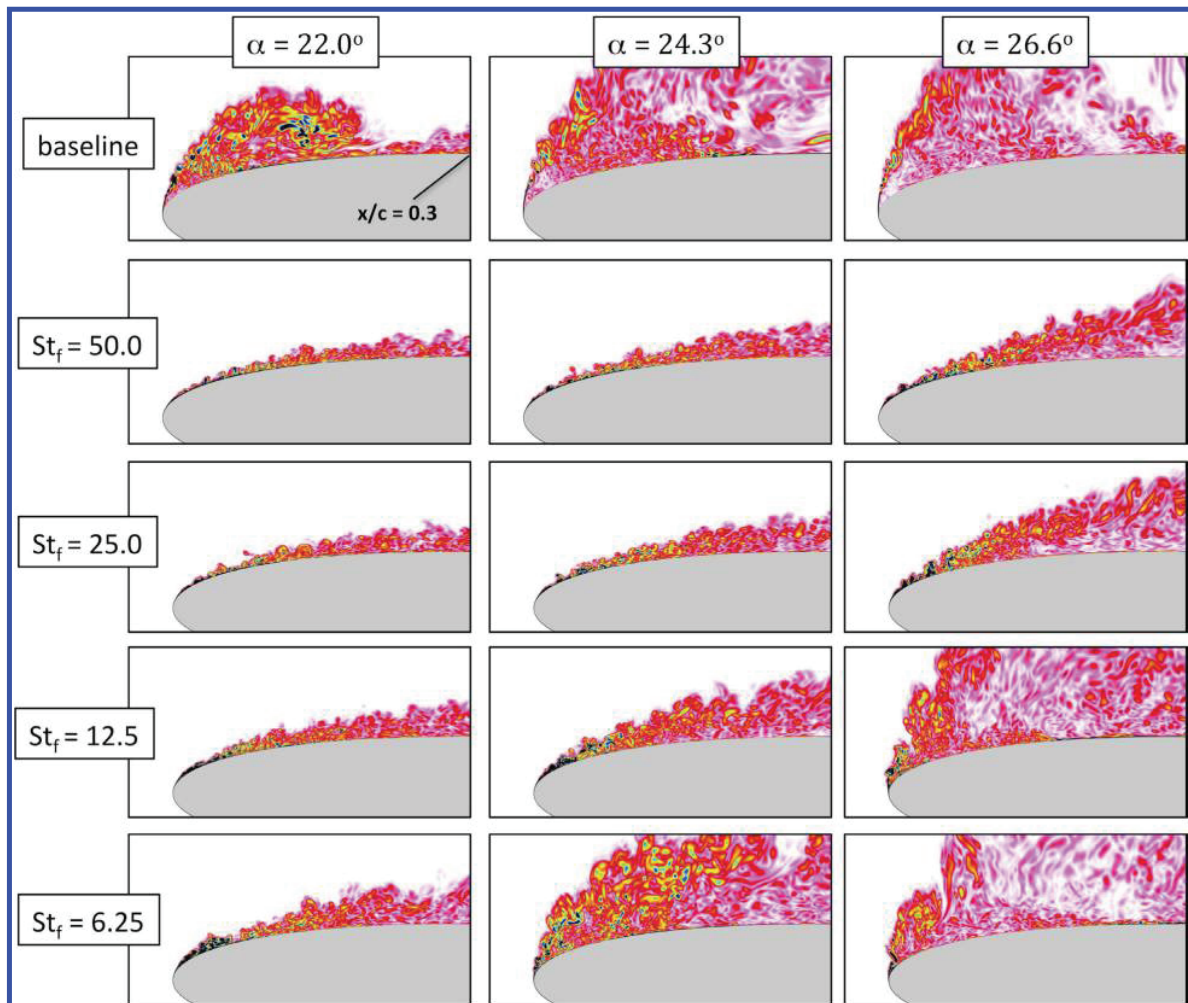


Figure 5. Effect of primary pulsed actuation frequency on evolution of unsteady flow field near leading edge of constant-rate pitching airfoil shown using contours of instantaneous vorticity magnitude on midplane in airfoil frame of reference

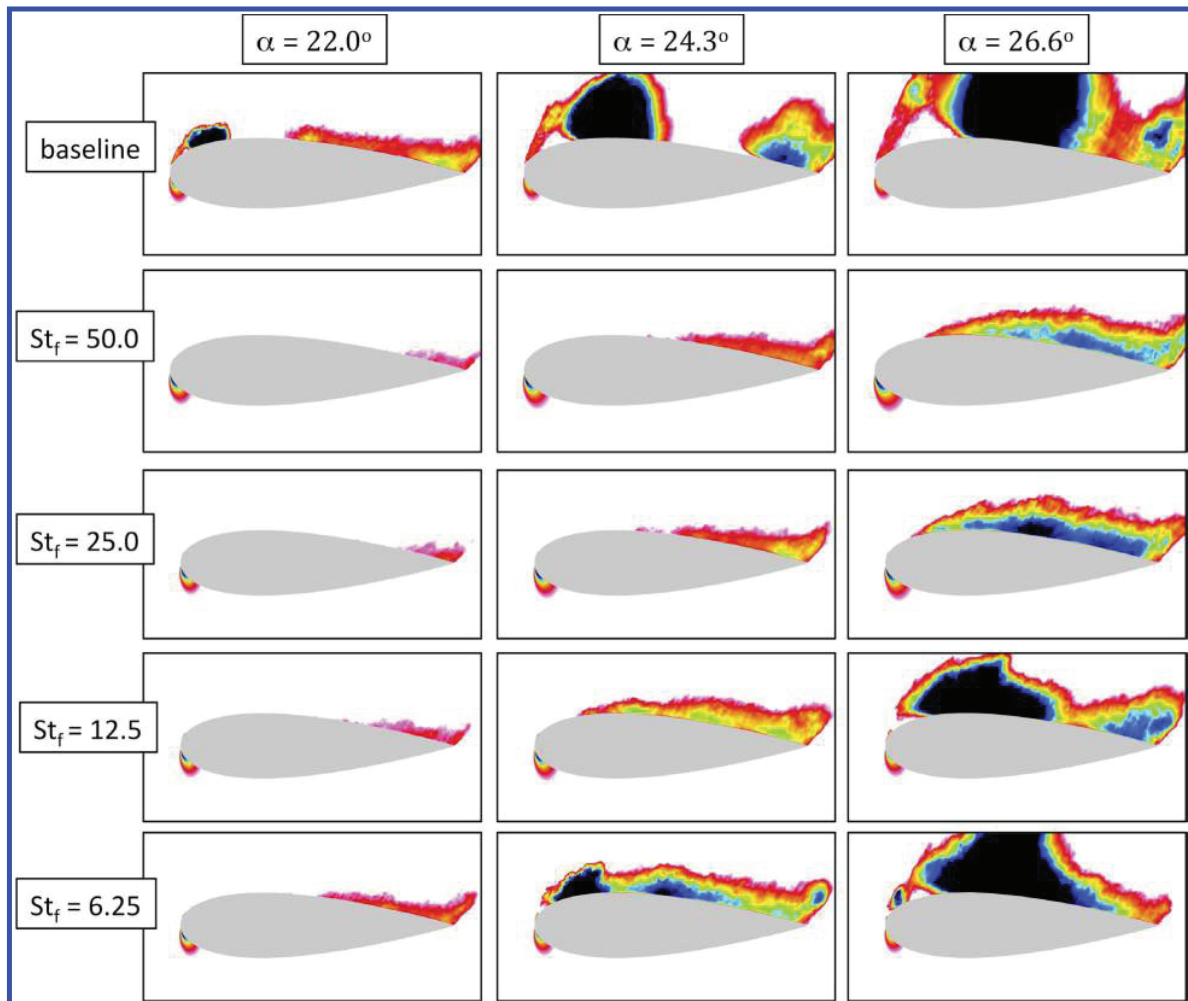


Figure 6. Effect of primary pulsed actuation frequency on evolution of reversed flow region over constant-rate pitching airfoil shown using contours of spanwise-averaged velocity in airfoil frame of reference. Vertical scale enlarged for clarity.

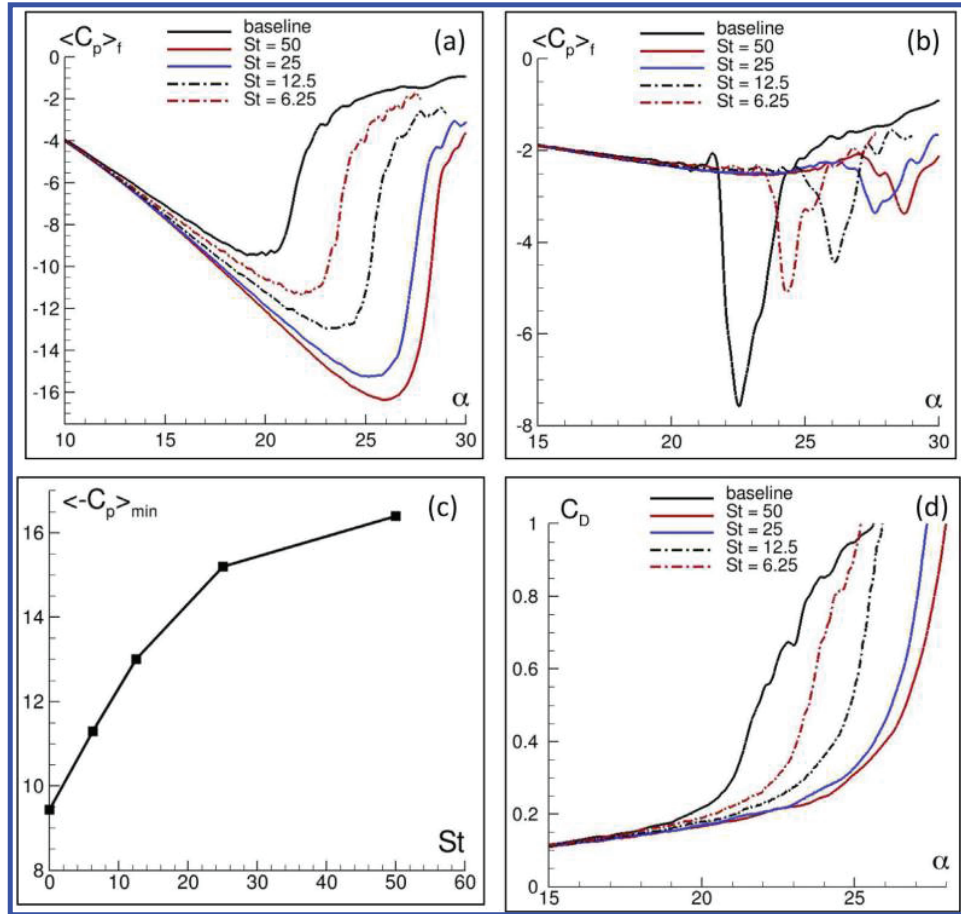


Figure 7. Effect of primary pulsed actuation frequency for constant-rate pitching airfoil. History of lowpass-filtered spanwise-averaged surface pressure at (a) $x/c = 0.0025$ and (b) $x/c = 0.15$; (c) minimum suction level at $x/c = 0.0025$ and (d) drag coefficient

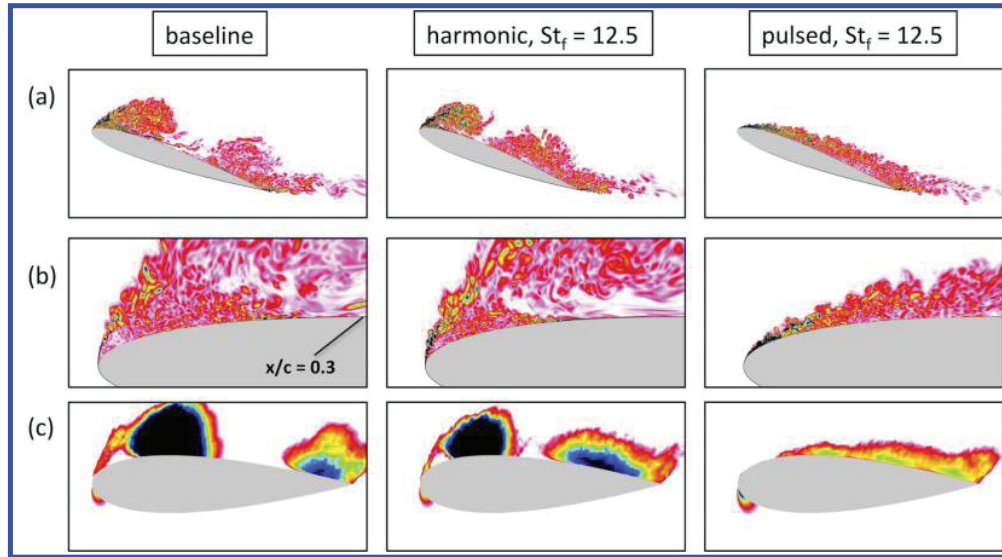


Figure 8. Comparison of pulsed and harmonic forcing for constant-rate pitching airfoil at $\alpha = 24.3^\circ$. Upper and middle rows show contours of instantaneous vorticity magnitude on midplane. Bottom row displays the spanwise-averaged reversed-flow region in the airfoil frame of reference (enlarged vertical scale)

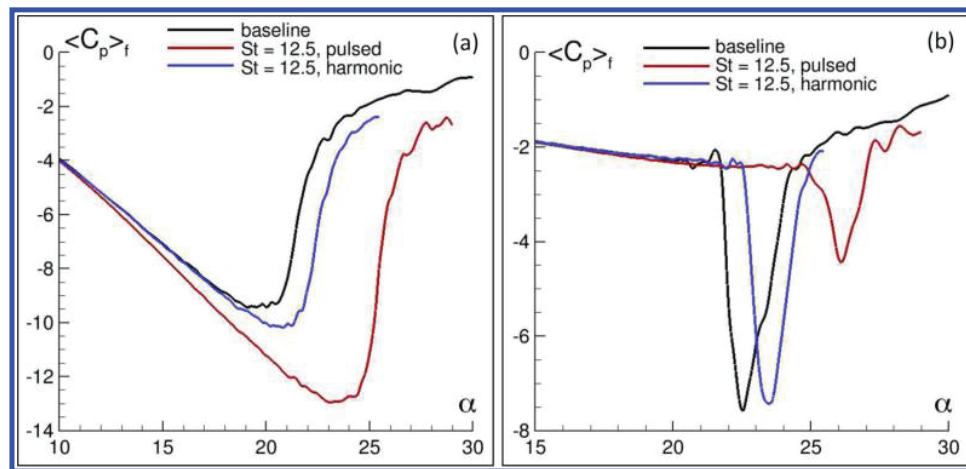


Figure 9. Comparison of pulsed and harmonic forcing for constant-rate pitching airfoil. Shown are the histories of lowpass-filtered spanwise-averaged surface pressures at (a) $x/c = 0.0025$ and (b) $x/c = 0.15$

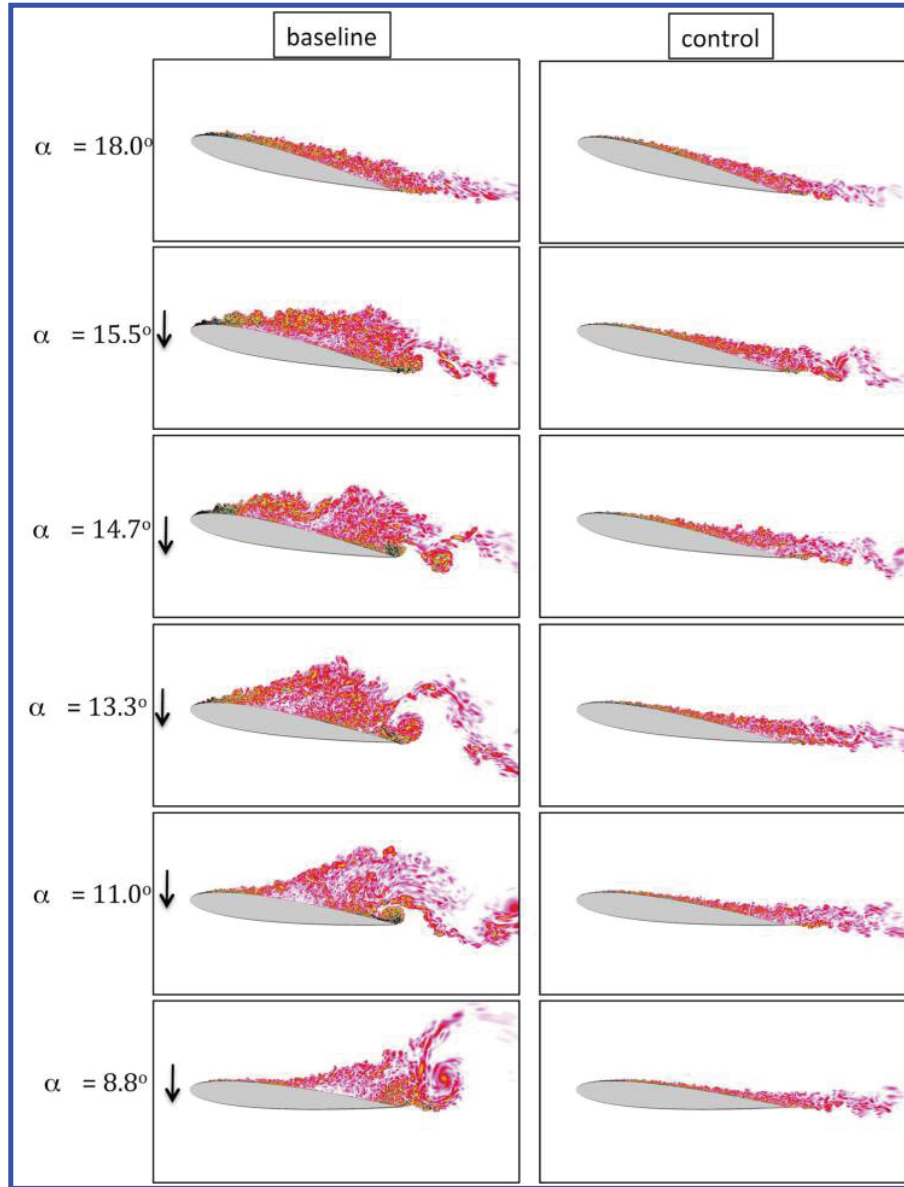


Figure 10. Contours of instantaneous vorticity magnitude on mid-plane at select angles of attack for light dynamic stall case with (right) and without (left) flow control

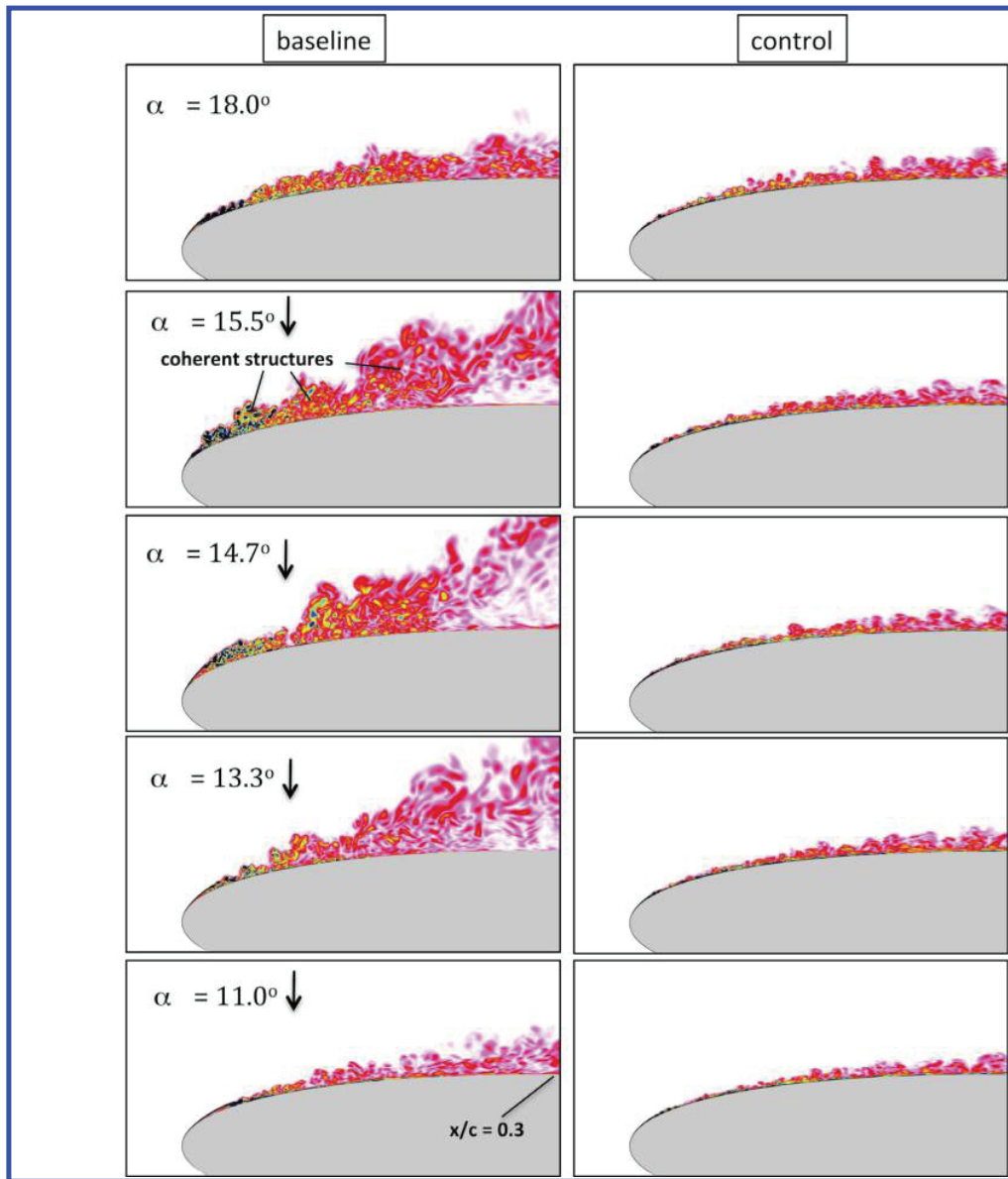


Figure 11. Contours of instantaneous vorticity magnitude on mid-plane near leading edge at select angles of attack for light dynamic stall case with (right) and without (left) flow control

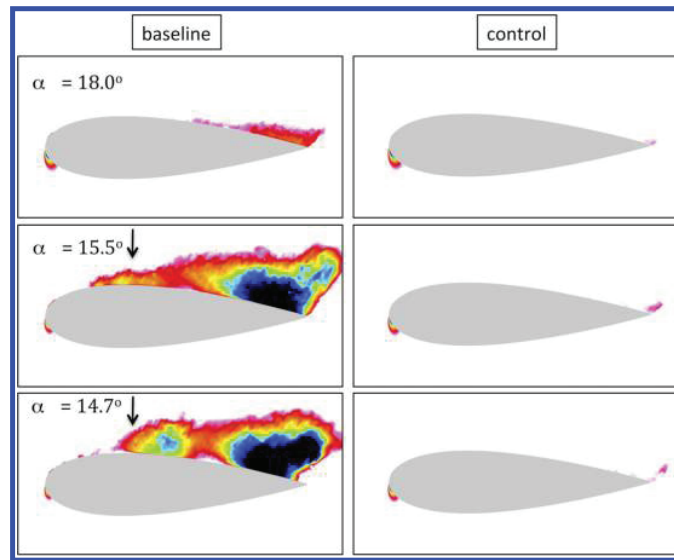


Figure 12. Contours of spanwise-averaged velocity showing reversed-flow region at select angles of attack for light dynamic stall case with (right) and without (left) flow control (enlarged vertical scale)

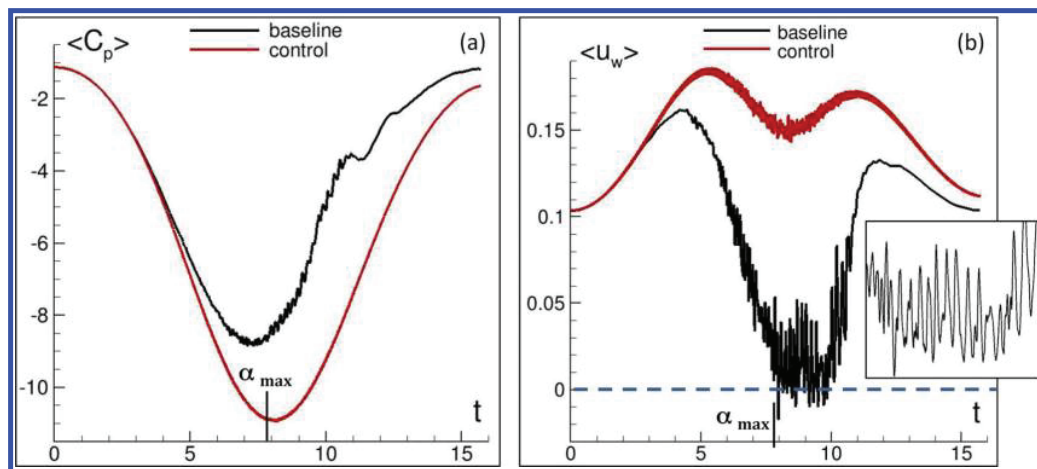


Figure 13. Effect of flow control on (a) surface pressure and (b) near-wall velocity at station $x/c = 0.0025$ for light dynamic stall case

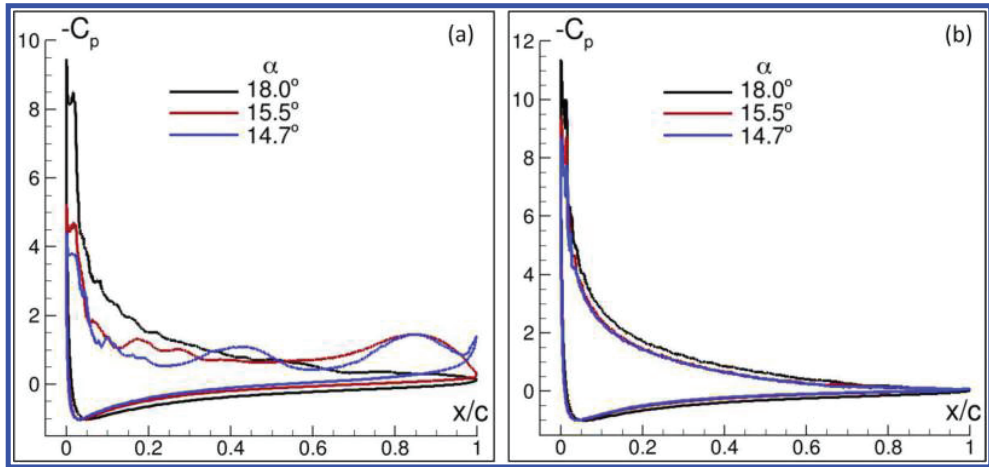


Figure 14. Spanwise-averaged surface pressure distributions at select angles of attack for light dynamic stall case, (a) baseline and (b) with flow control

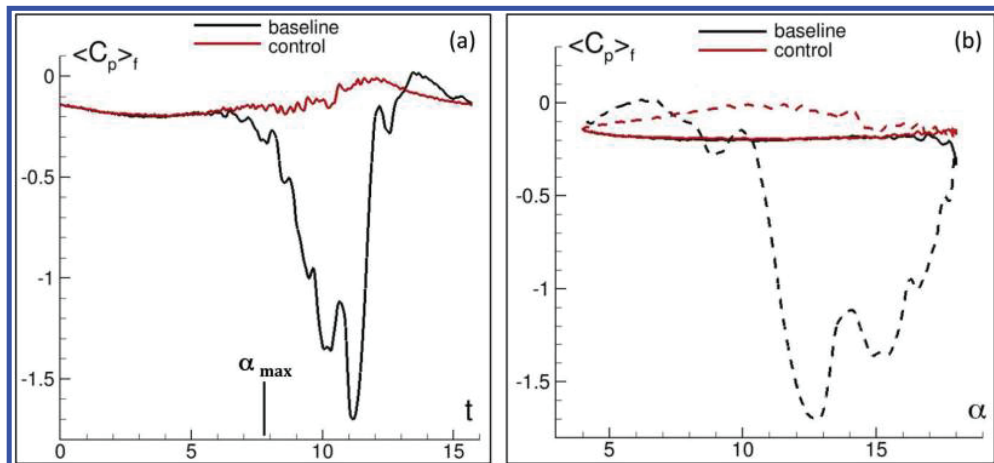


Figure 15. Effect of flow control on surface pressure at station $x/c = 0.8$ for light dynamic stall case, (in (b) dashed lines denote the downstroke portion of the cycle)

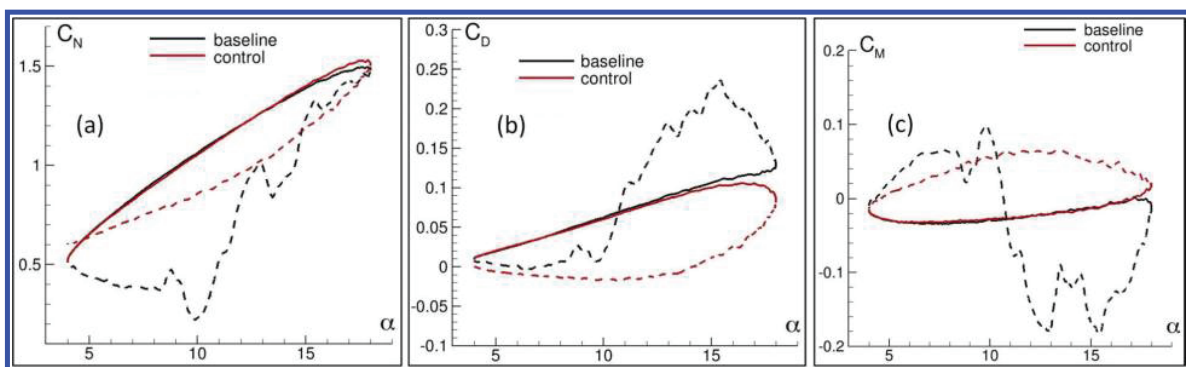


Figure 16. Effect of flow control on aerodynamic loads for light dynamic stall case, (dashed lines denote the downstroke portion of the cycle)

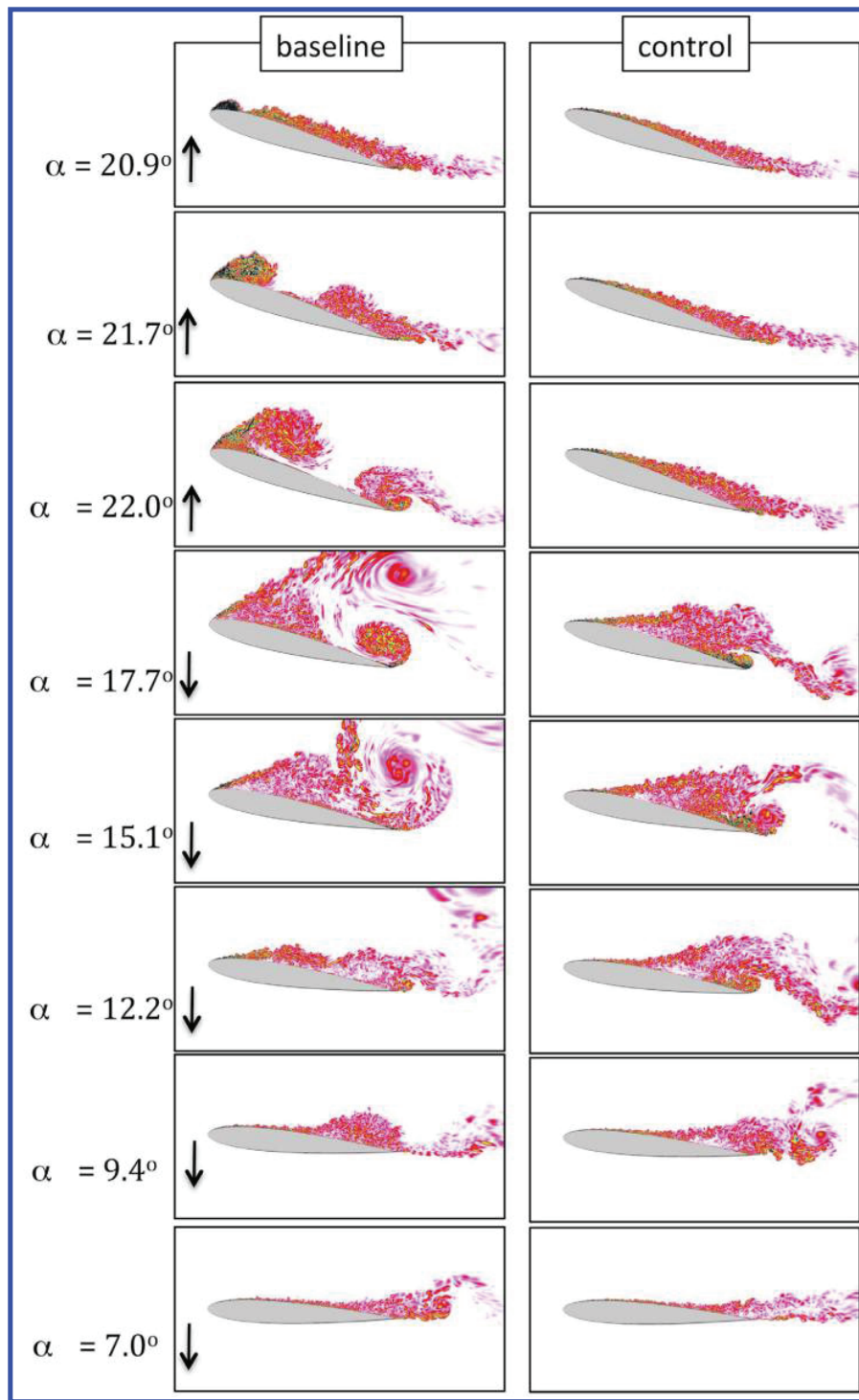


Figure 17. Contours of instantaneous vorticity magnitude on mid-plane at select angles of attack for deep dynamic stall case with (right) and without (left) flow control

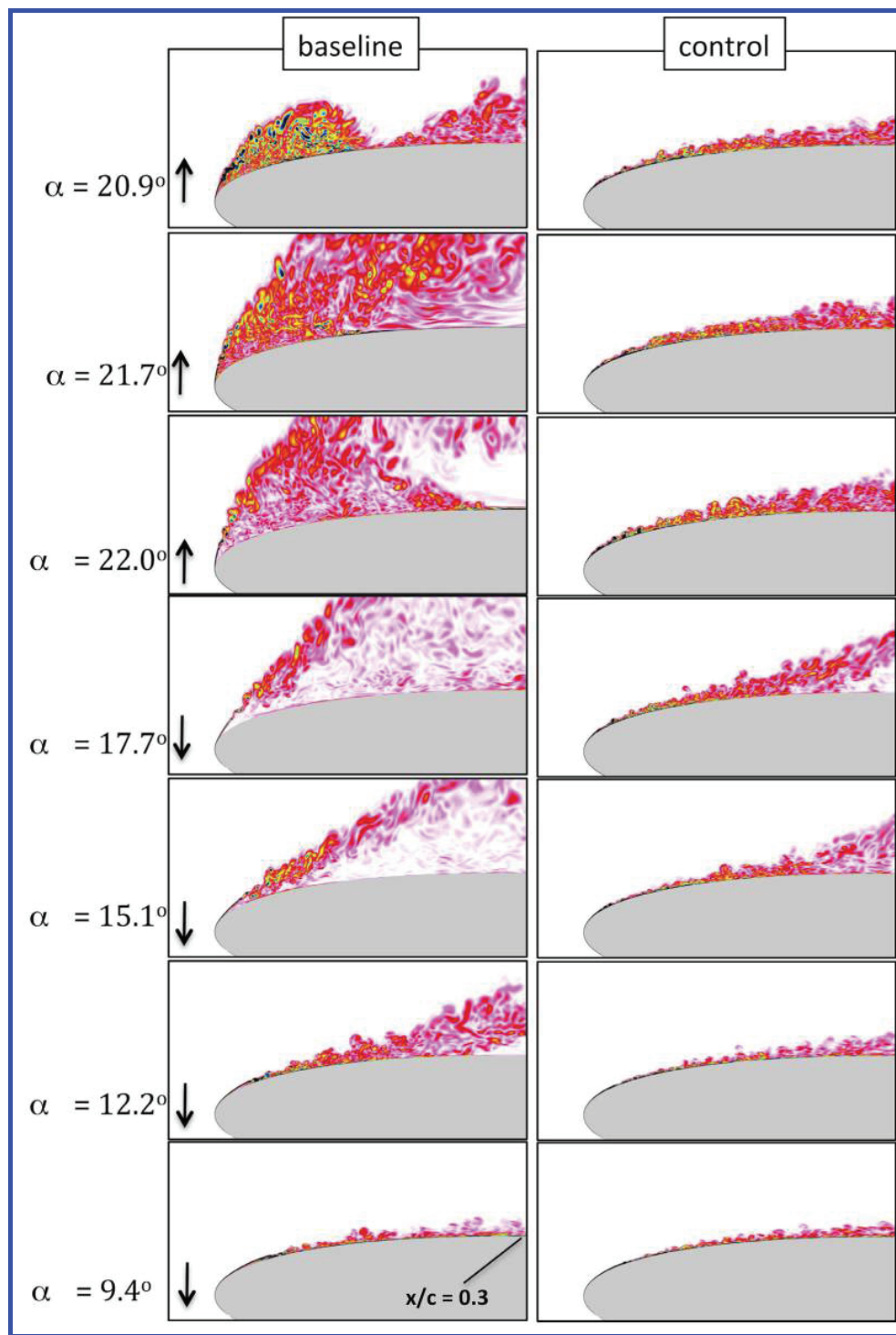


Figure 18. Contours of instantaneous vorticity magnitude on mid-plane near leading edge at select angles of attack for deep dynamic stall case with (right) and without (left) flow control

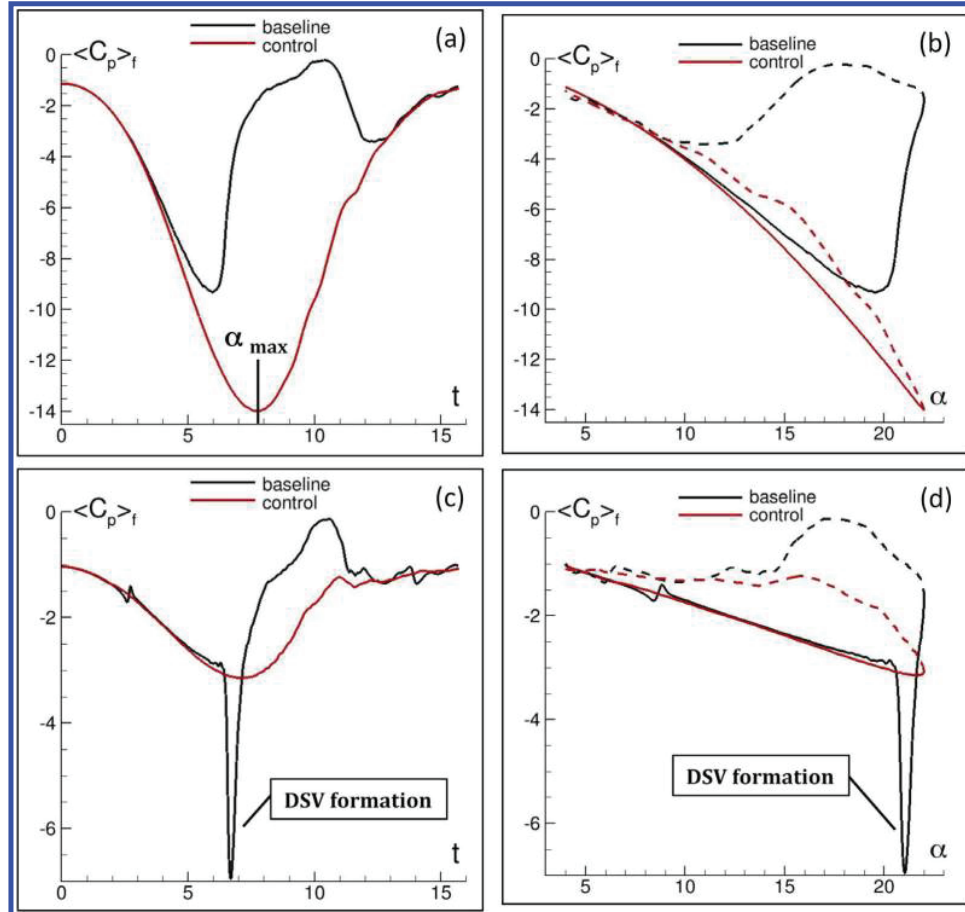


Figure 19. Comparison of baseline and actuated solutions for deep dynamic stall case: (a) and (b) display the lowpass-filtered spanwise-averaged surface pressure at $x/c = 0.0025$ as a function of time and angle of attack, respectively. (c) and (d) same for station $x/c = 0.1$, (in (b) and (d) dashed lines denote the downstroke portion of the cycle)

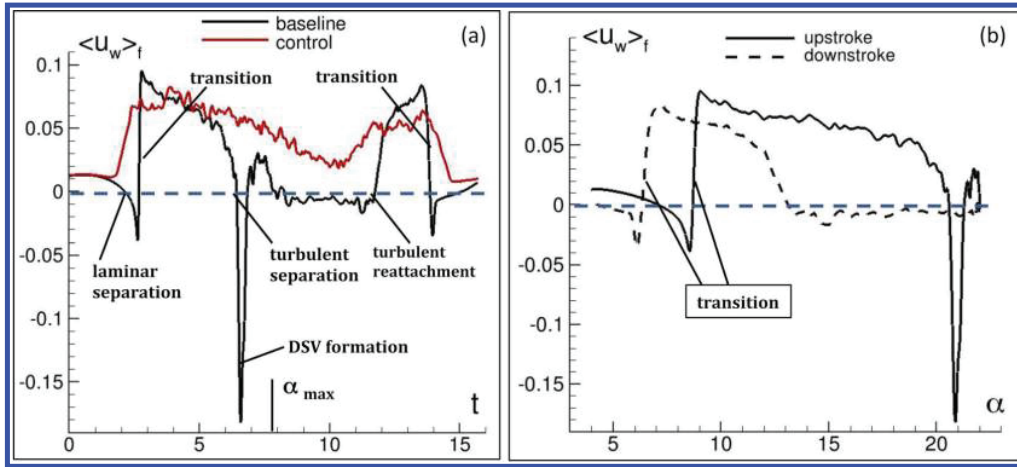


Figure 20. (a) Effect of flow control on lowpass-filtered spanwise-averaged near-wall velocity at station $x/c = 0.1$ for deep dynamic stall case. (b) Near-wall velocity at $x/c = 0.1$ for baseline case shown as a function of angle of attack displaying hysteresis in transition location between upstroke (solid line) and downstroke (dashed line) portions of the motion

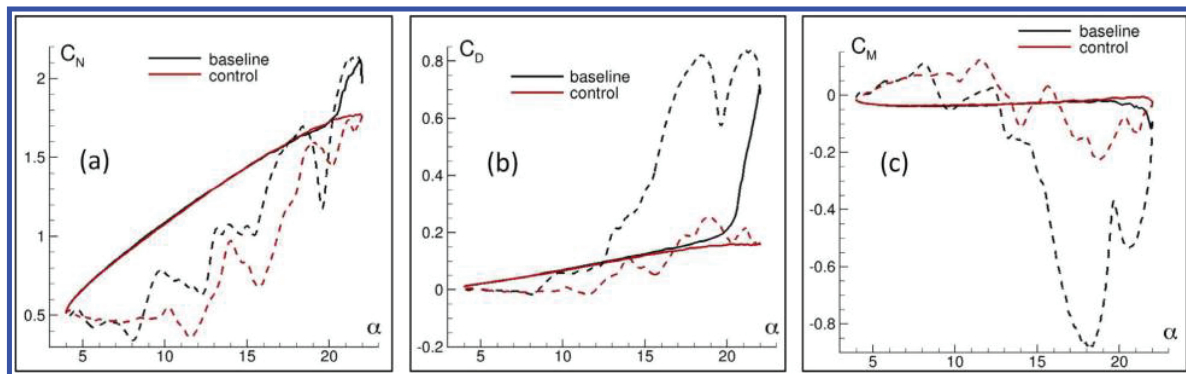


Figure 21. Effect of flow control on aerodynamic loads for deep dynamic stall case, (dashed lines denote the downstroke portion of the cycle)

APPENDIX G

Plasma-Based Flow Control for Delay of Excrescence-Generated Transition

Donald P. Rizzetta* and Miguel R. Visbal†

Air Force Research Laboratory, Wright-Patterson Air Force Base, Ohio 45433-7512, USA

Numerical simulations are carried out to explore flow control that delays transition generated by excrescence on a plate-like geometry in subsonic flow. Both forward-facing and rearward-facing steps of small roughness height are considered in the simulations. These are representative of joints and other surface imperfections on wing sections that disrupt laminar flow, thereby increasing skin friction and drag. Dielectric barrier discharge (DBD) plasma-based flow control is employed to delay transition and increase the extent of the laminar flow region. Solutions are obtained to the Navier-Stokes equations, that were augmented by source terms used to characterize the body force imparted by a plasma actuator on the fluid. A simple phenomenological model provided these forces resulting from the electric field generated by the plasma. The numerical method is based upon a high-fidelity numerical scheme and an implicit time-marching approach, on overset mesh systems used to describe the steps. Very small-amplitude numerical forcing is applied to generate perturbations, which are amplified by the geometric disturbances and result in transition, similar to the physical situation. Both continuous and pulsed operation of actuators is investigated. Features of the flowfields are described, and comparisons are provided between the baseline and control cases. It is found that use of plasma actuators can maintain laminar flow for the entire length of the computational domain, resulting in a reduction of the integrated drag by up to 70%.

Nomenclature

C_d	= time-mean integrated drag coefficient
C_f	= time-mean skin friction coefficient
C_p	= time-mean surface pressure coefficient
D_c	= plasma scale parameter
e_c	= electron charge, 1.6×10^{-19} coulomb
\mathbf{E}	= nondimensional electric field vector
E	= total specific energy
E_r	= reference electric field magnitude
E_x, E_y, E_z	= nondimensional components of the field vector
E_ω	= turbulent kinetic energy frequency spectral amplitude
$\mathbf{F}, \mathbf{G}, \mathbf{H},$	= inviscid vector fluxes
$\mathbf{F}_v, \mathbf{G}_v, \mathbf{H}_v$	= viscous vector fluxes
h	= dimensional plate thickness, 2.0in (0.0508m)
\mathcal{J}	= Jacobian of the coordinate transformation
k	= dimensional excrescence step height, 0.04in (0.001m)
K	= turbulent kinetic energy, $0.5(\bar{u'}u' + \bar{v'}v' + \bar{w'}w')$
K_i	= integrated turbulent kinetic energy, $\int_{y_s}^{\delta} K dy$
M	= Mach number
p	= nondimensional static pressure
Pr	= Prandtl number, 0.73 for air

*Senior Research Aerospace Engineer, Aerodynamic Technology Branch, AFRL/RQVA, Associate Fellow AIAA.

†Technical Area Leader, Aerodynamic Technology Branch, AFRL/RQVA, Fellow AIAA.

This material is declared a work of the U.S. Government and is not subject to copyright protection in the United States.

q_c	= nondimensional charge density
\mathbf{Q}	= vector of dependent variables
\mathbf{Q}_i	= components of the heat flux vector
Re	= reference Reynolds number, $\rho_\infty u_\infty h / \mu_\infty$
Re_k	= roughness-based Reynolds number, $Re u_k h / h$
\mathbf{S}	= source vector
t	= nondimensional time
T	= nondimensional static temperature
u, v, w	= nondimensional Cartesian velocity components in the x, y, z directions
u_1, u_2, u_3	= u, v, w
u_k	= nondimensional streamwise velocity of undisturbed flow evaluated at $x = x_k, y = k/h$
U, V, W	= contravariant velocity components
x, y, z	= nondimensional Cartesian coordinates in the streamwise, vertical, and spanwise directions
x_1, x_2, x_3	= x, y, z
x_a	= nondimensional streamwise actuator location
x_d	= nondimensional downstream location of resolved region
x_f	= nondimensional streamwise forcing location
x_k	= nondimensional streamwise step location
z_s	= nondimensional spanwise extent
γ	= specific heat ratio, 1.4 for air
δ	= nondimensional boundary-layer thickness defined by $u = 0.99$
δ^*	= nondimensional boundary-layer displacement thickness
δ_{ij}	= Kronecker delta function
$\delta_{\xi 2}, \delta_{\eta 2}, \delta_{\zeta 2}$	= 2nd-order and 6th-order finite-difference operators in ξ, η, ζ
$\delta_{\xi 6}, \delta_{\eta 6}, \delta_{\zeta 6}$	
$\Delta \mathbf{Q}$	= $\mathbf{Q}^{p+1} - \mathbf{Q}^p$
Δt	= time step size
$\Delta x, \Delta y, \Delta z$	= computational mesh spacing
ξ, η, ζ	= nondimensional body-fitted computational coordinates
$\xi_t, \xi_x, \xi_y, \xi_z$	= metric coefficients of the coordinate transformation
$\eta_t, \eta_x, \eta_y, \eta_z$	
$\zeta_t, \zeta_x, \zeta_y, \zeta_z$	
θ	= nondimensional boundary-layer momentum thickness
μ	= nondimensional molecular viscosity coefficient
ρ	= nondimensional fluid density
τ_{ij}	= components of the viscous stress tensor
ω	= nondimensional frequency
ω_a	= nondimensional actuator pulsing frequency
ω_f	= nondimensional forcing frequency

Subscripts

s	= evaluated at the surface
∞	= dimensional reference value

Superscripts

n	= time level
p	= subiteration level
$^{\wedge}$	= filtered value
$'$	= fluctuating component
$\overline{}$	= time-mean quantity
$+$	= law-of-the-wall variable

I. Introduction

One of the principal considerations in the design and construction of aircraft is that of configuration drag. This is especially true for unmanned air systems (UAS) and high altitude long endurance (HALE) vehicles, which are primarily used for intelligence, surveillance, and reconnaissance missions requiring extensive loiter times at altitude. An approach for reducing drag in such applications is the use of wings devised to maintain laminar flow. By applying a judicious design process, wings may be constructed so that the boundary layer can have a transition location which is significantly downstream of that in a conventional situation. This results in a smaller fraction of the vehicle wetted surface being exposed to turbulent flow and in a reduction in drag, leading directly to lower fuel consumption, greater energy efficiency, longer range, larger payloads, or increased flight times.

The exploitation of laminar flow on air vehicles requires stringent manufacturing tolerances in the production of aerodynamic surfaces. Specifically, the heights of steps, the width of gaps, and the undulations of surfaces must be minimized in order to preclude premature transition to a turbulent state. And, even if such excrescences are eliminated during fabrication, aerodynamic surfaces can suffer damage and/or fatigue leading to a decrease in the extent of laminar flow regions. It is the purpose of the present investigation to explore use of plasma-based flow control for delaying transition generated by the aforementioned geometric disturbances.

Studies on effects of surface imperfections upon aerodynamic performance have been carried out for many years. As early as 1939, Hood¹ investigated waves on the surface of a NACA 23012 airfoil. It was reported that sinusoidal undulations of the leading-edge region could result in premature transition, thereby increasing skin friction drag. Subsequently, Fage² conducted experiments on flat plates and airfoil models with geometric shapes that were similar to those of Hood. He determined that the size of the surface perturbations required to generate transition, was essentially independent of pressure gradient. This presumption is now generally considered to be incorrect. In contrast to a smooth surface variation, effects of isolated surface excrescences were examined by Gregory et al.³ Flight test were conducted, and criteria for permissible "pimple" heights were reported.

Smith and Clutter⁴ investigated flows over wire trips, and quantified critical roughness Reynolds numbers capable of producing transition. They also concluded that the transition process appeared to be insensitive to pressure gradient. Braslow⁵ compiled an early summary on the transition of boundary-layers due to surface roughness effects. It was found that roughness formed by integrated forward-facing or rearward-facing steps had a critical roughness-based Reynolds number of approximately 200. Flight experiments conducted by Drake et al.⁶ explored effects of integral steps and gaps on boundary-layer transition for a wing with a favorable pressure gradient.

The advent of long-endurance air vehicles has more recently spawned a current series of experimental studies devoted to the investigation of excrescence effects on transition.⁷⁻¹⁵ Early work of these studies was focussed on zero pressure gradient flows,^{7,9} but the long term goal was an examination of excrescence generated transition in conditions typical of laminar flow wings.¹⁰⁻¹⁵ It was generally determined that laminar flow continued to exist for excrescence heights that were larger than previously thought possible. Plasma-based flow control offers the possibility of maintaining laminar flow for even large heights, and while operating in adverse pressure gradient regimes.

Recent computations of Rizzetta and Visbal¹⁶ have demonstrated that it is possible to numerically simulate transition occurring in flows over steps of small heights at moderate roughness-based Reynolds numbers. Direct numerical simulations were carried out using a high-fidelity numerical scheme, and small-amplitude numerical forcing was applied in order to create perturbations that were amplified by the geometric disturbances. The approach was similar to that of the physical situation, which is receptive to freestream non-uniformities or other perturbations which eventually evolve into fully turbulent states. Predicted locations of transition were found to agree well with the experimental measurements of Drake and Bender.¹⁰ This previous effort now makes it possible to numerically examine the use of plasma-based actuation as a means of delaying transition generated in the flowfield downstream of excrescence-size steps.

A number of experimental works have evidenced the potential of plasma actuation for delaying transition and extending regions of laminar flow.¹⁷⁻²² For flat-plate flows, Grundmann and Tropea^{17,18} and Duchmann et al.²⁰ have shown that both continuous and pulsed plasma actuators could delay transition in the presence of zero and adverse pressure gradients. In experiments of Seraudie et al.¹⁹ and Kurz et al.,²¹ a plasma actuator was embedded near the leading edge of an unswept wing with a low-speed airfoil section. Hot wire anemometry and stability analyses confirmed that transition was delayed when the actuator was operated.

Flight experiments were carried out by Duchmann et al.,²² employing a plasma actuator on the pressure side of a laminar flow wing section test article. Microphone and hot wire measurements quantified a measurable, but modest amount of transition delay (3% chord).

For the present study, simulations were conducted for flow past a flat plate configuration with forward-facing and rearward-facing steps at a roughness-based Reynolds number of 1013. This situation corresponds to the previous simulations of Rizzetta and Visbal,¹⁶ and to several experiments.^{7,9,10} Plasma-based actuators were imposed downstream of the steps, and the effect upon transition was determined. Computations were facilitated by employing a simple phenomenological model to represent body forces resulting from the electric field generated by the plasma, and imparted to the flow. Both continuous and pulsed operation of actuators was considered in the investigation. In sections that follow, the governing equations are defined, the numerical method, DNS/LES approach, and plasma model are described, and details of the computations are outlined. Results of the simulations are summarized, and features of the flowfields are described. Flows with and without flow control are compared in order to assess benefits of plasma actuation. Comparisons are quantified in terms of skin friction distributions, and growth and spectral content of the turbulent kinetic energy.

II. Governing Equations

The governing fluid equations are taken as the unsteady three-dimensional compressible unfiltered Navier-Stokes equations. After introducing a generalized time-dependent curvilinear coordinate transformation to a body-fitted system, the equations are cast in the following nondimensional conservative form

$$\begin{aligned} \frac{\partial}{\partial t} \left(\frac{1}{\mathcal{J}} \mathbf{Q} \right) + \frac{\partial}{\partial \xi} \left(\mathbf{F} - \frac{1}{Re} \mathbf{F}_v \right) + \frac{\partial}{\partial \eta} \left(\mathbf{G} - \frac{1}{Re} \mathbf{G}_v \right) + \\ \frac{\partial}{\partial \zeta} \left(\mathbf{H} - \frac{1}{Re} \mathbf{H}_v \right) = D_c q_c \mathbf{S}. \end{aligned} \quad (1)$$

Here t is the time, ξ, η, ζ the computational coordinates, \mathbf{Q} the vector of dependent variables, $\mathbf{F}, \mathbf{G}, \mathbf{H}$ the inviscid flux vectors, $\mathbf{F}_v, \mathbf{G}_v, \mathbf{H}_v$ the viscous flux vectors, and \mathbf{S} the source vector representing the effect of plasma-induced body forces. The vector of dependent variables is given as

$$\mathbf{Q} = \begin{bmatrix} \rho & \rho u & \rho v & \rho w & \rho E \end{bmatrix}^T \quad (2)$$

the vector fluxes by

$$\begin{aligned} \mathbf{F} = \frac{1}{\mathcal{J}} \begin{bmatrix} \rho U \\ \rho u U + \xi_x p \\ \rho v U + \xi_y p \\ \rho w U + \xi_z p \\ \rho E U + \xi_{x_i} u_i p \end{bmatrix}, \quad \mathbf{G} = \frac{1}{\mathcal{J}} \begin{bmatrix} \rho V \\ \rho u V + \eta_x p \\ \rho v V + \eta_y p \\ \rho w V + \eta_z p \\ \rho E V + \eta_{x_i} u_i p \end{bmatrix}, \\ \mathbf{H} = \frac{1}{\mathcal{J}} \begin{bmatrix} \rho W \\ \rho u W + \zeta_x p \\ \rho v W + \zeta_y p \\ \rho w W + \zeta_z p \\ \rho E W + \zeta_{x_i} u_i p \end{bmatrix} \quad (3) \\ \mathbf{F}_v = \frac{1}{\mathcal{J}} \begin{bmatrix} 0 \\ \xi_{x_i} \tau_{i1} \\ \xi_{x_i} \tau_{i2} \\ \xi_{x_i} \tau_{i3} \\ \xi_{x_i} (u_j \tau_{ij} - \mathcal{Q}_i) \end{bmatrix}, \quad \mathbf{G}_v = \frac{1}{\mathcal{J}} \begin{bmatrix} 0 \\ \eta_{x_i} \tau_{i1} \\ \eta_{x_i} \tau_{i2} \\ \eta_{x_i} \tau_{i3} \\ \eta_{x_i} (u_j \tau_{ij} - \mathcal{Q}_i) \end{bmatrix}, \end{aligned}$$

$$\mathbf{H}_v = \frac{1}{\mathcal{J}} \begin{bmatrix} 0 \\ \zeta_{x_i} \tau_{i1} \\ \zeta_{x_i} \tau_{i2} \\ \zeta_{x_i} \tau_{i3} \\ \zeta_{x_i} (u_j \tau_{ij} - \mathcal{Q}_i) \end{bmatrix} \quad (4)$$

with the source term

$$\mathbf{S} = \frac{1}{\mathcal{J}} \begin{bmatrix} 0 \\ E_x \\ E_y \\ E_z \\ uE_x + vE_y + wE_z \end{bmatrix} \quad (5)$$

and

$$D_c = \frac{\rho_c e_c E_r h}{\rho_\infty u_\infty^2} \quad (6)$$

where

$$U = \xi_t + \xi_{x_i} u_i, \quad V = \eta_t + \eta_{x_i} u_i, \quad W = \zeta_t + \zeta_{x_i} u_i \quad (7)$$

$$E = \frac{T}{\gamma(\gamma-1)M_\infty^2} + \frac{1}{2} (u^2 + v^2 + w^2). \quad (8)$$

In the preceding expressions, u, v, w are the Cartesian velocity components, ρ the density, p the pressure, and T the temperature. All length scales have been nondimensionalized by the plate thickness h , and dependent variables have been normalized by reference values except for p which has been nondimensionalized by $\rho_\infty u_\infty^2$. Components of the heat flux vector and stress tensor are expressed as

$$\mathcal{Q}_i = - \left[\frac{1}{(\gamma-1)M_\infty^2} \right] \left(\frac{\mu}{Pr} \right) \frac{\partial \xi_j}{\partial x_i} \frac{\partial T}{\partial \xi_j} \quad (9)$$

$$\tau_{ij} = \mu \left(\frac{\partial \xi_k}{\partial x_j} \frac{\partial u_i}{\partial \xi_k} + \frac{\partial \xi_k}{\partial x_i} \frac{\partial u_j}{\partial \xi_k} - \frac{2}{3} \delta_{ij} \frac{\partial \xi_l}{\partial x_k} \frac{\partial u_k}{\partial \xi_l} \right). \quad (10)$$

The Sutherland law for the molecular viscosity coefficient μ and the perfect gas relationship

$$p = \frac{\rho T}{\gamma M_\infty^2} \quad (11)$$

were also employed, and Stokes' hypothesis for the bulk viscosity coefficient has been invoked.

III. Empirical Plasma Model

Many quantitative aspects of the fundamental processes governing plasma/fluid interactions remain unknown or computationally prohibitive, particularly for transitional and turbulent flows. These circumstances have given rise to the development of a wide spectrum of models with varying degrees of sophistication, that may be employed for more practical simulations. Among the simplified methods focused specifically on discharge/fluid coupling is that of Roth et al.,^{23,24} who associated transfer of momentum from ions to neutral particles based upon the gradient of electric pressure. A more refined approach, suitable for coupling with fluid response was an empirical model proposed by Shyy et al.,²⁵ using separate estimates for the charge distribution and electric field. Known plasma physics parameters were linked to experimental data. This representation has been successfully employed for a number of previous simulations of plasma-controlled flows,²⁶⁻³⁴ and its basic formulation was also adopted in the present investigation.

A schematic representation of a typical single asymmetric DBD plasma actuator is depicted in Fig. 1. The actuator consists of two electrodes that are separated by a dielectric insulator, and mounted on a body surface. An oscillating voltage, in the 1-15 kHz frequency range, is applied across the electrodes, developing an electric field about the actuator. When the imposed voltage is sufficiently high, the dielectric produces a barrier discharge, that weakly ionizes the surrounding gas. Momentum acquired by the resulting charged particles from the electric field, is transferred to the primary neutral molecules by a combination

of electrodynamic body forces and poorly understood complex collisional interactions. Because the bulk fluid cannot respond rapidly to the high frequency alternating voltage, the dominant effect of actuation is to impose a time-mean electric field on the external flow. In the numerical simulation of control applications, the entire process may be modeled as a body force vector acting on the net fluid adjacent to the actuator, which produces a flow velocity.

The model for the geometric extent of the plasma field generated by such an actuator is indicated in Fig. 2. The triangular region defined by the line segments OA, OB, and AB constitutes the plasma boundary. Outside of this region the electric field is not considered strong enough to ionize the air.²⁵ The electric field has its maximum value at point O, and varies linear within OAB. The peak value of the electric field can be estimated from the applied voltage and the spacing between the electrodes. Along the segment AB, the electric field diminishes to its threshold value, which was taken as 30 kV/cm.²⁵ The electric body force is equal to $q_c \mathbf{E}$ and provides coupling from the plasma to the fluid, resulting in the source vector \mathbf{S} appearing in Eq. (1). Some uncertainty exists regarding the direction of the force vector, which was related to the ratio OA/OB in the original work of Shyy et al.²⁵ Within the region OAB, the charge density q_c is taken to be constant. The plasma scale parameter D_c arises from nondimensionalization of the governing equations, and represents the ratio of the electrical force of the plasma to the inertial force of the fluid. For the purposes of the present computations, it is assumed that the direction of the plasma force is tangential to the actuator surface. Due to empiricism of the formulation, there is ambiguity regarding the value of the scale parameter D_c , which can be increased or decreased to produce more or less force.

DBD actuators are inherently unsteady devices. As mentioned previously, within the context of the empirical model, the body force imposed on the fluid is assumed to be steady owing to the high frequency of the applied voltage. In addition to a continuous mode of actuation, these devices may also be operated in a pulsed manner as described by Corke and Post,³⁵ thereby reducing total power consumption. The pulsed mode of operation also introduces an additional frequency content to the flow, which may render it more receptive to control, and offers the potential of improved effectiveness. It should be noted that the body force ($q_c \mathbf{E}$) seen in Fig. 2 may be directed in a specific direction by proper orientation of the triangle OAB. In the present applications, this force is acting in the streamwise direction.

IV. Numerical Method

Time-accurate solutions to Eq. (1) were obtained numerically by the implicit approximately-factored finite-difference algorithm of Beam and Warming³⁶ employing Newton-like subiterations,³⁷ which has evolved as an efficient tool for generating solutions to a wide variety of complex fluid flow problems, and may be written as follows

$$\begin{aligned} & \left[\frac{1}{\mathcal{J}} + \left(\frac{2\Delta t}{3} \right) \delta_{\xi 2} \left(\frac{\partial \mathbf{F}^p}{\partial \mathbf{Q}} - \frac{1}{Re} \frac{\partial \mathbf{F}_v^p}{\partial \mathbf{Q}} \right) \right] \mathcal{J} \times \left[\frac{1}{\mathcal{J}} + \left(\frac{2\Delta t}{3} \right) \delta_{\eta 2} \left(\frac{\partial \mathbf{G}^p}{\partial \mathbf{Q}} - \frac{1}{Re} \frac{\partial \mathbf{G}_v^p}{\partial \mathbf{Q}} \right) \right] \mathcal{J} \times \\ & \left[\frac{1}{\mathcal{J}} + \left(\frac{2\Delta t}{3} \right) \delta_{\zeta 2} \left(\frac{\partial \mathbf{H}^p}{\partial \mathbf{Q}} - \frac{1}{Re} \frac{\partial \mathbf{H}_v^p}{\partial \mathbf{Q}} \right) \right] \Delta \mathbf{Q} = - \left(\frac{2\Delta t}{3} \right) \left[\left(\frac{1}{2\Delta t} \right) \left(\frac{3\mathbf{Q}^p - 4\mathbf{Q}^n + \mathbf{Q}^{n-1}}{\mathcal{J}} \right) \right. \\ & \left. + \delta_{\xi 6} \left(\mathbf{F}^p - \frac{1}{Re} \mathbf{F}_v^p \right) + \delta_{\eta 6} \left(\mathbf{G}^p - \frac{1}{Re} \mathbf{G}_v^p \right) + \delta_{\zeta 6} \left(\mathbf{H}^p - \frac{1}{Re} \mathbf{H}_v^p \right) - D_c q_c \mathbf{S}^p \right]. \end{aligned} \quad (12)$$

In this expression, which is employed to advance the solution in time, \mathbf{Q}^{p+1} is the $p+1$ approximation to \mathbf{Q} at the $n+1$ time level \mathbf{Q}^{n+1} , and $\Delta \mathbf{Q} = \mathbf{Q}^{p+1} - \mathbf{Q}^p$. For $p = 1$, $\mathbf{Q}^p = \mathbf{Q}^n$. Second-order-accurate backward-implicit time differencing was used to obtain temporal derivatives.

The implicit segment of the algorithm (left-hand side of Eq. 12) incorporates second-order-accurate centered differencing for all spatial derivatives, and utilizes nonlinear artificial dissipation³⁸ to augment stability. For simplicity, the dissipation terms are not shown in Eq. (12). Efficiency is enhanced by solving this implicit portion of the factorized equations in diagonalized form.³⁹ Temporal accuracy, which can be degraded by use of the diagonal form, is maintained by utilizing subiterations within a time step. This technique has been commonly invoked in order to reduce errors due to factorization, linearization, diagonalization, and explicit application of boundary conditions. It is useful for achieving temporal accuracy on overset zonal mesh systems, and for a domain decomposition implementation on parallel computing platforms. Any deterioration of the solution caused by use of artificial dissipation and by lower-order spatial resolution of

implicit operators is also reduced by the procedure. Three subiterations per time step have been applied in the current simulations to preserve second-order temporal accuracy.

The compact difference scheme employed on the right-hand side of Eq. 12 is based upon the pentadiagonal system of Lele,⁴⁰ and is capable of attaining spectral-like resolution. This is achieved through the use of a centered implicit difference operator with a compact stencil, thereby reducing the associated discretization error. For the present computations, a sixth-order tridiagonal subset of Lele's system is utilized, which is illustrated here in one spatial dimension as

$$\alpha_d \left(\frac{\partial \mathbf{F}}{\partial \xi} \right)_{i-1} + \left(\frac{\partial \mathbf{F}}{\partial \xi} \right)_i + \alpha_d \left(\frac{\partial \mathbf{F}}{\partial \xi} \right)_{i+1} = a \left(\frac{\mathbf{F}_{i+1} - \mathbf{F}_{i-1}}{2} \right) + b \left(\frac{\mathbf{F}_{i+2} - \mathbf{F}_{i-2}}{4} \right) \quad (13)$$

with $\alpha_d = 1/3$, $a = 14/9$, and $b = 1/9$. The scheme has been adapted by Visbal and Gaitonde⁴¹ as an implicit iterative time-marching technique, applicable for unsteady vortical flows, and has been used to obtain the spatial derivative of any scalar, flow variable, metric coefficient, or flux component. It is used in conjunction with a low-pass Pade-type non-dispersive spatial filter developed by Gaitonde et al.,⁴² which has been shown to be superior to the use of explicitly added artificial dissipation for maintaining both stability and accuracy on stretched curvilinear meshes.⁴¹ The filter is applied to the solution vector sequentially in each of the three computational directions following each subiteration, and is implemented in one dimension as

$$\alpha_f \hat{\mathbf{Q}}_{i-1} + \hat{\mathbf{Q}}_i + \alpha_f \hat{\mathbf{Q}}_{i+1} = \sum_{n=0}^4 \frac{a_n}{2} (\mathbf{Q}_{i+n} + \mathbf{Q}_{i-n}) \quad (14)$$

where $\hat{\mathbf{Q}}$ designates the filtered value of \mathbf{Q} . It is noted that the filtering operation is a post processing technique, applied to the evolving solution in order to regularize features that are captured but poorly resolved. Equation 14 represents a one-parameter family of eighth-order filters, where numerical values for the a_n 's may be found in Ref. 43. The filter coefficient α_f is a free adjustable parameter which may be selected for specific applications, where $|\alpha_f| < 0.5$. The value of α_f determines sharpness of the filter cutoff and has been set to 0.40 for the present simulations.

The aforementioned features of the numerical algorithm are embodied in a parallel version of the time-accurate three-dimensional computer code FDL3DI,⁴³ which has proven to be reliable for steady and unsteady fluid flow problems, including vortex breakdown,^{44,45} transitional wall jets,⁴⁶ synthetic jet actuators,⁴⁷ roughness elements,⁴⁸ plasma flows,^{26-33,49} and direct numerical and large-eddy simulations of subsonic^{50,51} and supersonic flowfields.^{52,53} In addition, the previous computations of transitional flow past excrescence-size steps¹⁶ was found to compare well with experimental measurements, and are closely related to the present work.

V. DNS/LES Approach

As will subsequently be shown, the step flowfields up to transition are fully resolved, and therefore correspond to direct numerical simulations. Downstream of transition however, the flow is fully turbulent, and the computations revert to large-eddy simulations. The previously described numerical technique is capable of treating both of these situations. In the LES approach, physical dissipation at length scales smaller than those in the inertial range is not resolved, thereby allowing for less spatial resolution and a savings in computational resources. For nondissipative numerical schemes, without use of subgrid-scale (SGS) models, this leads to an accumulation of energy at high mesh wave numbers, and ultimately to numerical instability. Traditionally, explicitly added SGS models are then employed as a means to dissipate this energy. In the present methodology, the effect of the smallest fluid structures is accounted for by a high-fidelity implicit large-eddy simulation (HFILES) technique, which has been successfully utilized for a number of turbulent and transitional computations. The present HFILES approach was first introduced by Visbal et al.^{54,55} as a formal alternative to conventional methodologies, and is predicated upon the high-order compact differencing and low-pass spatial filtering schemes, without the inclusion of additional SGS modeling. This technique is similar to monotonically integrated large-eddy simulation (MILES)⁵⁶ and other implicit LES methods⁵⁷ in that it relies upon the numerical solving procedure to provide the dissipation that is typically supplied by conventional SGS models. Unlike those schemes however, here dissipation is contributed by the aforementioned high-order Pade-type low-pass filter only at high spatial wavenumbers where the solution is poorly resolved. This provides a mechanism for the turbulence energy to

be dissipated at scales that cannot be accurately represented on a given mesh system, in a fashion similar to subgrid modeling. For purely laminar flows, filtering may be required to maintain numerical stability and preclude a transfer of energy to high-frequency spatial modes due to spurious numerical events. The HFILES methodology thereby permits a seamless transition from large-eddy simulation to direct numerical simulation as the resolution is increased. In the HFILES approach, the unfiltered governing equations may be employed, and the computational expense of evaluating subgrid models, which can be substantial, is avoided. This procedure also enables the unified simulation of flowfields where laminar, transitional, and turbulent regions simultaneously coexist. For the present situation, the range of fluid scales in the transition region is limited and thus may be fully resolved by the HFILES formulation. Here, the solution can be considered a direct numerical simulation, which may not be true if lower-order numerical methods are employed.

It should also be noted that the HFILES technique may be interpreted as an approximate deconvolution SGS model,⁵⁸ which is based upon a truncated series expansion of the inverse filter operator for the unfiltered flowfield equations. Mathew et al.⁵⁹ have shown that filtering provides a mathematically consistent approximation of unresolved terms arising from any type of nonlinearity. Filtering regularizes the solution, and generates virtual subgrid model terms that are equivalent to those of approximate deconvolution.

VI. Details of the Computations

A. Computational Configuration

The configuration to be considered in the computations corresponds to that of experimental arrangements detailed in Refs. 7, 9–15, and illustrated schematically in Fig. 3, where the spanwise direction has been stretched by a factor of 10.0 for clarity. The model geometry consists of a 2.0in (0.0508m) thick flat plate with a rounded leading edge. The thickness h was employed as a reference quantity to nondimensionalize all spatial lengths. For the purpose of these simulations, a Cartesian coordinate system was established with its origin located at the inboard leading edge of the plate. The shape of the leading edge was prescribed by a superellipse^{7,9,10} having the following functional form:

$$\left| \frac{(x_s - a)}{a} \right|^m + \left| \frac{y_s}{b} \right|^m = 1 \quad (15)$$

where a and b are the semi-diameters and $m = 2.2$. The aspect ratio of the ellipse was 6:1 such that $a/b = 6$, and $b = h/2$. In experiments, forward-facing and rearward-facing steps of 0.04in (0.001m) in height ($k/h = 0.02$), were located 18.85in (0.48m) downstream of the plate leading edge ($x_k = 9.42$). Simulations resolved the region for $x < x_d$ with $x_d = 42.0$. The spanwise extent of the computational domain was taken equal to the plate thickness ($z_s = 1.0$). This width was found to be adequate to capture relevant physical properties in the fully turbulent region downstream of the step.¹⁶

B. Computational Meshes

The overset computational mesh systems employed for the simulations are displayed in Fig. 4. Because the plate configuration is symmetric about $y = 0$ and the angle of attack is 0 deg, only the upper half of the geometry is represented in the computations. Shown in frame a) of the figure is the overall flowfield representation, where only a fraction of the total grid lines appear. The planar C-grid construct was generated such that the outer boundaries were stretched to a distance of 100 plate thicknesses from the leading edge. The planar grid structure was then distributed uniformly in the z direction, due to spanwise homogeneity of the configuration. The nondimensional grid spacing in the wall-normal direction at the surface was 0.0002. Downstream of the steps, a uniform distribution of $\Delta x = 0.025$ was employed. Seen in frame b) of Fig. 4 is the overset grid region for the forward-facing step, while that of the rearward-facing step appears in frame c). Because mesh points in the respective grids upstream and downstream of the step location (x_k) coincide in the overlap region, no interpolation between grids is required.

Besides the mesh system described above, additional grids were developed for the rearward-facing step in order to assess the effects of spatial resolution on computed results. For all systems, the same regions of clustering and mesh spacing ratios were maintained. This was achieved by fitting a cubic spline to each coordinate, and then redistributing the grid points. In each coordinate direction, approximately 75% of the number of grid points in the fine grid system were utilized for the medium mesh, and 50% for the coarse

Table 1. Computational mesh sizes

configuration	grid	upstream grid	downstream grid	total points
forward-facing step	fine	(559 × 438 × 205)	(1460 × 338 × 205)	151,356,010
rearward-facing step	fine	(563 × 338 × 205)	(1456 × 438 × 205)	169,744,510
rearward-facing step	medium	(424 × 254 × 155)	(1092 × 329 × 155)	72,379,420
rearward-facing step	coarse	(284 × 169 × 105)	(728 × 219 × 105)	21,779,940

mesh. Unless specifically stated otherwise, all results to be subsequently described will have been obtained on the finest computational grids. The number of points for each mesh is given in Table 1.

C. Boundary Conditions

On all solid surfaces, the no slip condition was enforced, along with an adiabatic wall and vanishing normal pressure gradient, that were implemented with third-order spatial accuracy. At the farfield boundaries (upstream, downstream, and upper), freestream conditions were specified for dependent variables. Grid stretching in farfield regions transferred information to high spatial wave numbers, and it was then dissipated by the low-pass numerical filter.⁶⁰ This technique prevents any spurious reflections, particularly in the outflow area of the computational domain. Periodic conditions were specified at the spanwise boundaries, where a five-grid plane overlap of the mesh systems was employed, and symmetry was applied along $y = 0$ upstream of the plate leading edge.

D. Flow Conditions

The freestream Mach number M_∞ was set to 0.1, and the Reynolds number based upon freestream conditions and the plate thickness was specified as $Re = 90,000$. These conditions are identical to those previously used by Rizzetta and Visbal,¹⁶ for which the roughness-based Reynolds number is 1013, where $Re_k = Re u_k k/h$. Here, u_k is the value of the streamwise velocity u evaluated at $x = x_k$ and $y = k/h$, in the undisturbed flow without a step. The value $Re_k = 1013$ is in the range of experimental measurements,¹⁰ which were shown to produce transition.

E. Numerical Forcing Methodology

Numerical forcing was implemented as an imposed vertical velocity at the surface, and has the following specified form

$$v_s = \mathcal{A}F_f(x)G_f(t) \quad (16)$$

where

$$F_f(x) = \sin \theta (1 - \cos \theta), \quad \theta = 2\pi \left(\frac{x - x_s}{x_e - x_s} \right) \quad (17)$$

$$G_f(t) = \sin(2\pi\omega_f t) \quad (18)$$

The locations x_s and x_e correspond to the beginning and end of the forcing region. The length $x_e - x_s$ was selected as a wave length within the unstable region based upon the stability diagram for the upstream flat-plate boundary layer,⁶¹ and was taken as 0.12 (this length is equal to 6 times the step height). Equation (16) represents a blowing/suction slot, which adds no mass to the flow. It results in the generation of vorticity waves that may be amplified by the geometric disturbances. This form is identical to that utilized by others for both subsonic⁶² and supersonic^{63,64} transition applications. The forcing slot was centered at $x_f = 5.0$ upstream of the steps (see Fig. 3). The non-dimensional frequency ω_f is taken as 0.5, whose choice was dictated by the stability diagram.⁶¹ This frequency was within the unstable range based upon displacement thickness generated by the step. The amplitude \mathcal{A} was set to 0.0001, and was sufficient to generate sustainable transition. This small amplitude is 0.01% of the freestream velocity, and is probably lower than common freestream turbulence levels.

F. Plasma Actuator Configuration

The plasma actuator was situated behind the steps, centered at $x_a = 10.3216$. This location was just downstream of the reattachment point in the time-mean flowfield for the baseline rearward-facing step. The actuator spanned the entire width of the plate/step configurations (see Fig. 3). The nondimensional height of the plasma force (OA in Fig. 2) is taken as 0.03, which was 1.5 times that of the steps. This height was such that it was generally less than one half of the boundary-layer thickness. The length of the plasma force region was 0.15, thus OB/OA in Fig. 2 was 5.0, which is similar to several previous simulations.^{29,33,65-67} The streamwise extent of the actuator is then defined as the region $10.2466 \leq x \leq 10.3966$.

Some preliminary simulations were carried out in order to establish a value of the plasma scale parameter D_c for which control was effective. With $D_c = 50.0$, it was found that transition could be substantially delayed. Because this was also true for $D_c = 20.0$, the value was lowered to $D_c = 10.0$. All control simulations were then conducted with $D_c = 10.0$. This value is much lower than that utilized for a maneuvering wing application⁶⁷ ($D_c = 1000.0$), and is of the same order as that employed for a fully turbulent separated boundary-layer flow⁴⁹ ($D_c = 4.5$). In the later case, the streamwise extent of the actuator was much longer than the present situation, because it was specified to correspond to the experimental arrangement.

As previously indicated, plasma actuators may be operated in either a continuous or pulsed mode. To apply pulsed actuation, a 50% duty cycle was applied at the nondimensional frequency $\omega_a = 4.0$. In the pulsed cases, the forcing amplitude was modulated by the duty cycle represented in Fig. 5. Here, t_d is the portion of the fundamental period t_p over which the device is active. The ratio $t_d/t_p \times 100$ expressed as a percentage, is commonly referred to as the duty cycle. The amplitude function A is applied as a factor to the source vector \mathbf{S} in Eq. (1). The 50% duty cycle results in power utilization which is one half that for continuous operation. The pulsing frequency $\omega_a = 4.0$ was taken to be sufficiently high, such that it was outside of the unstable range. It was thought that pulsing at lower frequencies might accelerate transition, rather than delaying it.

VII. Numerical Results

Simulations were carried out with a nondimensional time increment of $\Delta t = 0.000125$. This value was dictated by stability restrictions related to the overset mesh systems. The time increment provided 16,000 steps per cycle of the forcing frequency ω_f , and 2000 steps per cycle of the actuator pulsing frequency ω_a . After initializing forcing, the baseline cases without control were allowed to evolve to an equilibrium state that was fully turbulent downstream of the steps. Time-mean and statistical information was then collected for over 600,000 time steps. Flowfields for the control cases were initialized with baseline solutions. The control devices were activated, and solutions were allowed to develop to equilibrium flows. As will be shown subsequently, all the control flowfields were fully laminar. And although evolution to the laminar state generally required over 500,000 time steps to be achieved, statistical data only needed to be collected for 250,000 steps, as the flowfields were devoid of small scale structures.

A. Features of the Time-Mean Flowfields

Shown in Fig. 6 are time-mean skin friction distributions for the forward-facing step cases. In addition to time averaging, these and all other time-mean results were also averaged in the spanwise direction. As reference values, theoretical results for laminar and turbulent flow are also provided in the figure. The laminar distribution corresponds to the Blasius solution, while that for the turbulent distribution represents the result from the momentum integral equation when a 1/7 power law profile is employed⁶⁸ ($C_f = 0.0576 Re_x^{-1/5}$). It is noted that the baseline solution is slightly below the turbulent theoretical value. This was also observed in Ref. 16, where it was pointed out that the theoretical value represents a high Reynolds number equilibrium limit that may not be achieved for this transitional flow. For the control cases, there is large but local increase of the skin friction in the region near the actuator ($x_a = 10.3216$). This behavior is associated with actuator-induced formation of wall-jet-like flow, that subsequently will be recognized in velocity profiles. Downstream, C_f falls dramatically as the flow rapidly returns to a laminar state. The local increase in C_f is smaller for the pulsed case because the actuator is only active for half the time, which is reflected in the time-mean result. Corresponding distributions for the rearward-facing step appear in Fig. 7. It is evident that these results are quite similar to those of the forward-facing step.

The effect of plasma-based control may be quantified by defining a time-mean integrated drag coefficient

Table 2. Integrated drag coefficient

configuration	control	Cd
forward-facing step	baseline	0.0957
	continuous	0.0345
	pulsed	0.0282
rearward-facing step	baseline	0.0952
	continuous	0.0412
	pulsed	0.0330

as

$$Cd = \int_{x=0}^{x=x_d} C_f dx \quad (19)$$

Values of Cd are tabulated in Table 2. Note in Eq. (19), that the integration extends for the entire length of the configuration, including the portion upstream of the steps. Reduction of Cd with control is apparent in the Table. This reduction is slightly lower for the pulsed cases, due to the previously mentioned behavior of C_f near $x = x_a$. These results indicate that drag may be reduced by over 70% when plasma-based control is applied.

Time-mean surface pressure coefficient distributions are presented in Figs. 8 and 9 for the forward-facing and rearward-facing steps respectively. Expansion about the elliptic leading edge is seen in the figures, as well as disruption of the distribution due to the steps. However, there is very little modification of the distributions when control is active. This is an important result, as the lift on an aerodynamic configuration is due mostly to the surface pressure. Thus, the benefit of plasma control with regard to drag reduction, would not seem to be offset by any concurrent loss of lift.

Time-mean streamwise velocity profiles are found in Figs. 10-13. In these figures, the distance from the surface ($y - y_s$) has been normalized by the boundary-layer thickness δ of the baseline solution. It should be mentioned, that in the downstream portion of the domain, the baseline flow is turbulent so that the boundary-layer thickness is substantially larger than that of the control cases. Shown in Fig. 10 are profiles for the forward-facing step at locations $x = 11.0$ and $x = 12.0$, which are just behind the steps and actuators. The control profiles are observed to be much fuller than the baseline case. With continuous control, the profile exhibits classic wall jet behavior. This is not evident for the pulsed case, once again due to the on/off nature of the 50% duty cycle. The figure demonstrates that the basic mechanism for control is transfer of momentum to the bulk flow by the electric field generated by the plasma actuators. This results in velocity profiles with higher energy and altered stability properties, which delay transition to turbulence. It should be noted that the jet-like profiles are inflectional, and excessive actuation might result in an unstable situation that would eventually promote transition.

Displayed in Fig. 11 are velocity profiles for the forward-facing step at $x = 20.0$ and $x = 40.0$, where the baseline flow is turbulent. It is clear that the boundary-layer thickness for the baseline solution is much greater than that of the control cases (recall that δ is taken from the baseline flow). As the control situations have evolved to a laminar state, the wall jet behavior is no longer present. Velocity profiles for the rearward-facing step are given in Figs. 12 and 13. These are observed to be very similar to those of the forward-facing step.

Time-mean velocity profiles, such as those in Figs. 10-13, may be used to compute integral boundary-layer properties. One of the parameters that is often used to assess the state of a boundary layer is the shape factor, defined as the ratio δ^*/θ , where δ^* is the displacement thickness and θ the momentum thickness. Streamwise distributions of this function are plotted in Figs. 14 and 15 for the forward-facing and rearward-facing steps respectively. For comparison, laminar (Blasius) and turbulent (1/7 power law) values of the shape factor also appear. These results reinforce the previously described flowfield behavior, which is fully turbulent in the downstream region for the baseline case, and attains a laminar state when transition has been suppressed by plasma control.

Transition for the baseline flows may be quantified, and compared to control cases by integrating the

Table 3. Mesh spacings in the downstream region

configuration	grid	Δx^+	Δy_s^+	Δz^+	no. pts. in boundary layer
forward-facing step	fine	80.37	0.32	16.74	180
rearward-facing step	fine	78.23	0.31	15.64	276
rearward-facing step	medium	101.12	0.40	20.22	208
rearward-facing step	coarse	139.98	0.56	27.98	138

turbulent kinetic energy in the wall normal direction (y), and plotting the result as a function of streamwise distance. Distributions of the integrated turbulent kinetic energy appear in Figs. 16 and 17 where

$$K_i = \int_{y_s}^{\delta} K dy, \quad \text{and} \quad K = 0.5(\overline{u' u'} + \overline{v' v'} + \overline{w' w'}). \quad (20)$$

In Eq. (20), the integration in y is across the boundary layer, and K has been averaged in the homogeneous spanwise direction (z). After an initial rise at transition, followed by a slight drop in magnitude, K_i for the baseline flows has continuous growth downstream. Levels for the control cases are fairly constant, and of much smaller amplitude. This is in spite of the upstream numerical forcing and unsteady control in the pulsed cases.

B. Numerical Accuracy

In order to assess the effect of grid resolution upon the numerical results, computations for the baseline rearward-facing step case were carried out on three different computational mesh systems. The number of grid points in each system are indicated in Table 1. Time-mean skin friction distributions obtained on each mesh appear in Fig. 18. While it is well known that there exists no concept of grid independence for LES in the absence of explicit filtering,⁶⁹ the trend toward a limit is evident. It is noted that the coarse mesh system contains only 12.8% as many points as that of the fine mesh system, while the medium system has 42.6%. Thus, it is believed that the fine mesh system maintains sufficient resolution for a reliable LES. More evidence of this assertion is furnished in Table 3, which lists mesh spacings in wall units for the turbulent region at $x = 40.0$ for all baseline cases. On the fine mesh systems, spacings in all three spatial directions fall within the commonly accepted range for LES.^{70,71}

C. Features of the Instantaneous Flowfields

Features of the instantaneous flowfields are represented in Figs. 19-26. Illustrated in Fig. 19 are instantaneous planar contours of the spanwise vorticity at the inboard boundary, and planar contours of the u -velocity in the near-wall region for the baseline step flows. In this figure, the normal y -direction has been stretched by a factor of 5.0, and the spanwise z -direction stretched by a factor of 3.0. Hairpin vortices are visible in the vorticity contours, and low-speed streaks can be seen in the near-wall region. These characteristics typify the turbulent nature of the downstream flowfield. Presented in Fig. 20 for the baseline cases are instantaneous planar contours at the inboard boundary and iso-surfaces of the v -velocity. Here once again, the z -direction has been stretched by a factor of 3.0. Iso-surfaces in the upstream portion of the figure define coherent structures which originally evolved from the numerical forcing. The values of the iso-surfaces in the figure are ± 0.001 , which is an order of magnitude greater than that of the forcing. The size and strength of these structures was amplified as they passed over the steps. Distortion due to spanwise instabilities then ensued, eventually leading to a breakdown of the coherence and transition to turbulence, as observed in the downstream portion of the figure. Fine-scale features of the turbulent region for the baseline flows are depicted by instantaneous iso-surfaces of the Q -criterion vortex identification function⁷² in Fig. 21. The Q -criterion has commonly been utilized to represent vortical fluid structures and has been colored by the streamwise velocity in the figure, where the y -direction has been stretched by a factor of 3.0 and the z -direction by a factor of 10.0. In the figure, the iso-surface corresponds to the value $Q = 3.0$.

Figures 22-24 portray temporal evolution of the rearward-facing step flowfield, following activation of the plasma actuator which is applied in the continuous mode. Several instantaneous time frames are displayed in each figure, and demonstrate the re-laminarization process. The flowfield development for the forward-facing step is similar. Nondimensional time levels indicated in the figures are referenced from the initial state at $t = 0.0$, when flow control begins. Found in Fig. 22 are instantaneous planar contours at the midspan location of the spanwise vorticity. The y -coordinate has been stretched by a factor of 5.0 to enhance viewing of the fluid structures. As time progresses, the turbulent flow region can be seen moving downstream, leaving a laminar state behind it. This is due to the momentum addition of the actuator that was noted previously. Shown in Fig. 23 are the same instantaneous time frames, where the flowfield structure is represented by planar contours at the inboard boundary and iso-surfaces of the v -velocity component. The z -coordinate has been stretched by a factor of 10.0 in the figure. At $t = 0.0$ in frame a), coherent structures are observed upstream, which breakdown fairly rapidly. This was illustrated earlier in Fig. 20. When control is initiated, these coherent structures are no longer present. The evolving laminar flow is evident for the planar contours and iso-surfaces in frames b), c), and d). Finally, the re-laminarization is characterized in terms of the Q -criterion in Fig. 24. Here once again, the z -coordinate has been stretched by a factor of 10.0, and the iso-surface is defined by $Q = 0.75$. Evolution of fine-scale structures to laminar flow is apparent in the figure. The average propagation speed of the re-laminarization front is approximate 44.8 ft/sec, which is about one half of the freestream velocity (85.97 ft/sec) at the given flow conditions. The temporal development in Figs. 22-24 is similar for the case of pulsed control.

Appearing in Figs. 25 and 26 are frequency spectra of the turbulent kinetic energy at several streamwise locations, for the forward-facing and rearward-facing steps respectively. For each case, the spectra were collected at a distance from the surface which was equal to one half of the step height ($y - ys = 0.01$), and have been averaged in the homogeneous spanwise direction. At the upstream location ($x = 8.0$), the numerical forcing ($\omega_f = 0.5$ at $x_f = 5.0$) is noticeable in the spectra. In the pulsed control case, the pulsing frequency $\omega_a = 4.0$ and its higher harmonic are also recognized in the figure. This is despite the fact that the pulsing is applied further downstream at $x_a = 10.3216$. The subsonic nature of the boundary layer allows disturbances to propagate upstream. In addition, this behavior may be associated with the circumstance that the pulsing frequency is a higher harmonic of the forcing frequency. Amplitudes of the spectra at this location are very low. Further downstream at $x = 12.0$, there has been a large increase in the turbulent kinetic energy for the baseline cases. The amplification is due to the presence of the steps, leading to transition. All harmonics of the forcing frequency are visible in the baseline cases. At the most downstream location $x = 40.0$, the baseline flow is fully turbulent. Broadband content is apparent in the spectra, and an inertial range is evolving. No broadband content is displayed for the control cases.

VIII. Summary and Conclusions

High-fidelity computations were carried out to simulated the subsonic flow past steps of small height, which were representative of excrescences on aerodynamic surfaces. The calculations were carried out on overset mesh systems, and were able to capture transition and the turbulent flow downstream of the steps. For this purpose, very small amplitude numerical forcing was applied to create perturbations, which were then amplified by the geometric disturbances. A grid sensitivity study indicated that the mesh systems were sufficiently fine to resolve all important features of the turbulent flowfields. Plasma-based flow control was then applied to delay transition. Control computations were facilitated by employing a widely used phenomenological model in order to specify the body force, imparted by the electric field generated by the plasma, to the bulk fluid surrounding the actuators. The body force increased momentum of the fluid, which was the predominant mechanism for control, and resulted in velocity profiles that were able to resist transition. Both continuous and pulsed operation of the plasma-based control was explored, and either mode proved effective, resulting in a reduction of the configuration integrated drag of up to 70%.

Once flow control was initiated, entirely laminar flow could be achieved in approximately 0.12 seconds for the configuration and flow conditions employed in the investigation. The power utilization required by the actuators was obtained by integrating the applied force over the area inscribed by the triangular region depicted in Fig. 2. For the value $D_c = 10.0$, the power per unit span was determined to be 9.24 watts/meter. Although this is a very low requirement level, it is noted that the value corresponds to the power output of the electric field, and not the power input to the actuator. The nondimensional pulsing frequency $\omega_a = 4.0$ of the 50% duty cycle corresponds to 2kHz in dimensional units. An important observation is that this

frequency lies within the operational range of the alternating current cycle commonly employed by plasma actuators. The implication is that such devices are not likely to enhance transition because the alternating current frequency is sufficiently removed from the unstable range. Duty cycles less than 50% may also prove effective, as has been found in other applications of pulsed flow control.^{73,74}

This investigation indicates great potential for the use of plasma-based control to delay excrescence-generated transition and reduce drag of aerodynamic configurations. As mentioned previously, values of D_c less than 10.0 were not considered, but may also be effective. In addition, transition may also be delayed for steps of greater heights than those considered in this study. Thus, the cost of fabrication may be reduced by increasing manufacturing tolerances, at the expense of including plasma actuation in configuration design. And although it may be necessary to conduct trade off studies to determine an optimal balance between such factors, plasma control offers a means to lower drag that may arise during practical operations, such as that due to fatigue, damage, or debris accumulation on aerodynamic surfaces.

Acknowledgments

The work presented here was sponsored by the U. S. Air Force Office of Scientific Research, under a task monitored by D. Smith. Computational resources were supported in part by a grant of supercomputer time from the U. S. Department of Defense Supercomputing Resource Centers at the Stennis Space Center, MS and Wright-Patterson AFB, OH.

References

- ¹Hood, M. J., "The Effects of Surface Waviness and of Rib Stitching on Wing Drag," Technical Note 724, NACA, Aug. 1939.
- ²Fage, A., "The Smallest Size of a Spanwise Surface Corrugation which Affects Boundary-Layer Transition on an Aerofoil," Reports and Memoranda 2120, Aeronautical Research Council, Jan. 1943.
- ³Gregory, N., Walker, W. S., and Johnson, D., "Part I: The Effect on Transition of Isolated Surface Excrescences in the Boundary Layer; Part II: Brief Flight Tests on a *Vampire I* Aircraft to Determine the Effect of Isolated Surface Pimples on Transition," Reports and Memoranda 2779, Aeronautical Research Council, Oct. 1951.
- ⁴Smith, A. M. O. and Clutter, D. W., "The Smallest Height of Roughness Capable of Affecting Boundary-Layer Transition in Low-Speed Flow," Engineering Report ES26803, Douglas Aircraft Company, 1954.
- ⁵Braslow, A. L., "The Effect of Distributed Surface Roughness on Boundary-Layer Transition," AGARD Report 254, North Atlantic Treaty Organization, Jan. 1960.
- ⁶Drake, A., Westphal, R. V., Zuniga, F. A., Kennelly, R. A., and Koga, D. J., "Wing Leading Edge Joint Laminar Flow Tests," Technical Memorandum 4762, NASA, Mar. 1997.
- ⁷Drake, A., Bender, A. M., Solomom, W. D., and Vavra, A. J., "Prediction of Manufacturing Tolerances for Laminar Flow," Technical Report AFRL-VA-WP-TR-2005-3060, Wright-Patterson AFB, OH, Jun. 2005.
- ⁸Wang, Y. X. and Gaster, M., "Effect of Surface Steps on Boundary Layer Transition," *Experiments in Fluids*, Vol. 39, Jun. 2005, pp. 679–686.
- ⁹Bender, A. M. and Drake, A., "Manufacturing Tolerances for Laminar Flow," Technical Report AFRL-VA-WP-TR-2007-3086, Air Force Research Laboratory, Wright-Patterson AFB, OH, Sep. 2006.
- ¹⁰Drake, A. and Bender, A., "Surface Excrescence Transition Study," Technical Report AFRL-RB-WP-TR-2009-3109, Wright-Patterson AFB, OH, Apr. 2009.
- ¹¹McKeon, B. J., Bender, A. M., Westphal, R. V., and Drake, A., "Transition in Incompressible Boundary Layers with Two-Dimensional Excrescences," AIAA Paper 2008-589, Jan 2008.
- ¹²Bender, A. M., Elliot, J. R., Shinagawa, Y., Korntheuer, A. J., Drake, A., Westphal, R. V., Gerashchenko, S., McKeon, B. J., and Yoshioka, S., "An Approach to Measuring Step Excrescence Effects in the presence of a Pressure Gradient," AIAA Paper 2010-373, Jan. 2010.
- ¹³Gerashchenko, S., McKeon, B. J., Westphal, R. V., Bender, A. M., and Drake, A., "Hot-Wire Measurements of the Influence of Surface Steps on Transition in Favorable Pressure Gradient Boundary Layers," AIAA Paper 2010-374, Jan. 2010.
- ¹⁴Drake, A., Bender, A. M. and Korntheuer, A. J., Westphal, R. V., McKeon, B. J., Gerashchenko, S., Rohe, W., and Dale, G., "Step Excrescence Effects for Manufacturing Tolerances on Laminar Flow Wings," AIAA Paper 2010-375, Jan. 2010.
- ¹⁵Bender, A., Harris, C., and Hawkins, B., "Boundary Layer Excrescence Examination Study," Technical Report AFRL-RB-WP-TR-2012-0027, Air Force Research Laboratory, Wright-Patterson AFB, OH, May 2012.
- ¹⁶Rizzetta, D. P. and Visbal, M. R., "Numerical Simulation of Excrescence Generated Transition," AIAA Paper 2013-0079, Jan. 2013.
- ¹⁷Grundmann, S. and Tropea, C., "Experimental Transition Delay Using Glow-Discharge Plasma Actuators," *Experiments in Fluids*, Vol. 42, No. 4, Apr. 2007, pp. 653–657.
- ¹⁸Grundmann, S. and Tropea, C., "Delay of Boundary-Layer Transition Using Plasma Actuators," AIAA Paper 2008-1369, Jan. 2008.
- ¹⁹Seraudie, A., Vermeersch, O., and Arnal, D., "DBD Plasma Actuator Effect on a 2D Model Laminar Boundary Layer. Transition Delay under Ionic Wind Effect." AIAA Paper 2011-3515, Jun. 2011.

²⁰Duchmann, A., Kurz, A., Widmann, A., Grundmann, S., and Tropea, C., "Characterization of Tollmien-Schlichting Wave Damping by DBD Plasma Actuators Using Phase-Locked PIV," AIAA Paper 2012-0903, Jan. 2012.

²¹Kurz, A., Tropea, C., Grundmann, S., Forte, M., Vermeersch, O., Seraudie, A., Arnal, D., Goldin, N., and King, R., "Transition Delay using DBD Plasma Actuators in Direct Frequency Mode," AIAA Paper 2012-2945, Jun. 2012.

²²Duchmann, A., Simon, B., Magin, P., Tropea, C., and Grundmann, S., "In-Flight Transition Delay with DBD Plasma Actuators," AIAA Paper 2013-0900, Jan. 2013.

²³Roth, J. R., "Aerodynamic Flow Acceleration Using Paraelectric and Peristaltic Electrohydrodynamic Effects of a One Atmosphere Uniform Glow Discharge Plasma," *Physics of Plasmas*, Vol. 10, No. 5, May 2003, pp. 2117–2128.

²⁴Roth, J. R., Sin, H., and Madham, R. C. M., "Flow Re-attachment and Acceleration by Paraelectric and Peristaltic Electrohydrodynamic (EHD) Effects," AIAA Paper 2003-0531, Jan. 2003.

²⁵Shyy, W., Jayaraman, B., and Anderson, A., "Modeling of Glow Discharge-Induced Fluid Dynamics," *Journal of Applied Physics*, Vol. 92, No. 11, Dec. 2002, pp. 6434–6443.

²⁶Gaitonde, D. V., Visbal, M. R., and Roy, S., "Control of Flow Past a Wing Section with Plasma-Based Body Forces," AIAA Paper 2005-5302, Jun. 2005.

²⁷Visbal, M. R. and Gaitonde, D. V., "Control of Vortical Flows Using Simulated Plasma Actuators," AIAA Paper 2006-0505, Jan. 2005.

²⁸Visbal, M. R., Gaitonde, D. V., and Roy, S., "Control of Transitional and Turbulent Flows Using Plasma-Based Actuators," AIAA Paper 2006-3230, Jun. 2006.

²⁹Rizzetta, D. P. and Visbal, M. R., "Numerical Investigation of Plasma-Based Flow Control for Transitional Highly Loaded Low-Pressure Turbine," *AIAA Journal*, Vol. 45, No. 10, Oct. 2007, pp. 2554–2564.

³⁰Rizzetta, D. P. and Visbal, M. R., "Plasma-Based Flow Control Strategies for Transitional Highly Loaded Low-Pressure Turbines," *Journal of Fluids Engineering*, Vol. 130, No. 4, Apr. 2008, pp. 041104-1–041104-12.

³¹Rizzetta, D. P. and Visbal, M. R., "Large Eddy Simulation of Plasma-Based Control Strategies for Bluff Body Flow," *AIAA Journal*, Vol. 47, No. 3, Mar. 2009, pp. 717–729.

³²Rizzetta, D. P. and Visbal, M. R., "Effect of Plasma-Based Control on Low-Reynolds Number Flapping Airfoil Performance," AIAA Paper 2011-735, Jan. 2011.

³³Rizzetta, D. P. and Visbal, M. R., "Numerical Investigation of Plasma-Based Control for Low-Reynolds Number Airfoil Flows," *AIAA Journal*, Vol. 49, No. 2, Feb. 2011, pp. 411–425.

³⁴Rizzetta, D. P. and Visbal, M. R., "Plasma Flow Control Simulation of a Low-Reynolds Number Low-Aspect-Ratio Wing," AIAA Paper 2012-1138, Jan. 2012.

³⁵Corke, T. C. and Post, M. L., "Overview of Plasma Flow Control: Concepts, Optimization, and Applications," AIAA Paper 2005-0563, Jan. 2005.

³⁶Beam, R. and Warming, R., "An Implicit Factored Scheme for the Compressible Navier-Stokes Equations," *AIAA Journal*, Vol. 16, No. 4, Apr. 1978, pp. 393–402.

³⁷Gordnier, R. E. and Visbal, M. R., "Numerical Simulation of Delta-Wing Roll," AIAA Paper 93-0554, Jan. 1993.

³⁸Jameson, A., Schmidt, W., and Turkel, E., "Numerical Solutions of the Euler Equations by Finite Volume Methods Using Runge-Kutta Time Stepping Schemes," AIAA Paper 81-1259, Jun. 1981.

³⁹Pulliam, T. H. and Chaussee, D. S., "A Diagonal Form of an Implicit Approximate-Factorization Algorithm," *Journal of Computational Physics*, Vol. 39, No. 2, Feb. 1981, pp. 347–363.

⁴⁰Lele, S. A., "Compact Finite Difference Schemes with Spectral-like Resolution," *Journal of Computational Physics*, Vol. 103, No. 1, Nov. 1992, pp. 16–42.

⁴¹Visbal, M. R. and Gaitonde, D. V., "High-Order-Accurate Methods for Complex Unsteady Subsonic Flows," *AIAA Journal*, Vol. 37, No. 10, Oct. 1999, pp. 1231–1239.

⁴²Gaitonde, D., Shang, J. S., and Young, J. L., "Practical Aspects of High-Order Accurate Finite-Volume Schemes for Electromagnetics," AIAA Paper 97-0363, Jan. 1997.

⁴³Gaitonde, D. and Visbal, M. R., "High-Order Schemes for Navier-Stokes Equations: Algorithm and Implementation into FDL3DI," Technical Report AFRL-VA-WP-TR-1998-3060, Air Force Research Laboratory, Wright-Patterson AFB, OH, Aug. 1998.

⁴⁴Gordnier, R. E., "Computation of Delta-Wing Roll Maneuvers," *Journal of Aircraft*, Vol. 32, No. 3, May 1995, pp. 486–492.

⁴⁵Visbal, M. R., "Computational Study of Vortex Breakdown on a Pitching Delta Wing," AIAA Paper 93-2974, Jul. 1993.

⁴⁶Visbal, M., Gaitonde, D., and Gogineni, S., "Direct Numerical Simulation of a Forced Transitional Plane Wall Jet," AIAA Paper 98-2643, Jun. 1998.

⁴⁷Rizzetta, D. P., Visbal, M. R., and Staneck, M. J., "Numerical Investigation of Synthetic-Jet Flowfields," *AIAA Journal*, Vol. 37, No. 8, Aug. 1999, pp. 919–927.

⁴⁸Rizzetta, D. P. and Visbal, M. R., "Direct Numerical Simulation of Flow Past an Array of Distributed Roughness Elements," *AIAA Journal*, Vol. 45, No. 8, Aug. 2007, pp. 1967–1976.

⁴⁹Rizzetta, D. P. and Visbal, M. R., "Large-Eddy Simulation of Plasma-Based Turbulent Boundary-Layer Separation Control," *AIAA Journal*, Vol. 48, No. 12, Dec. 2010, pp. 2793–2810.

⁵⁰Rizzetta, D. P. and Visbal, M. R., "Numerical Investigation of Transitional Flow Through a Low-Pressure Turbine Cascade," AIAA Paper 2003-3587, Jun. 2003.

⁵¹Rizzetta, D. P., Visbal, M. R., and Blaisdell, G. A., "A Time-Implicit High-Order Compact Differencing and Filtering Scheme for Large-Eddy Simulation," *International Journal for Numerical Methods in Fluids*, Vol. 42, No. 6, Jun. 2003, pp. 665–693.

⁵²Rizzetta, D. P. and Visbal, M. R., "Application of Large-Eddy Simulation to Supersonic Compression Ramps," *AIAA Journal*, Vol. 40, No. 8, Aug. 2002, pp. 1574–1581.

⁵³Rizzetta, D. P. and Visbal, M. R., "Large-Eddy Simulation of Supersonic Cavity Flowfields Including Flow Control," *AIAA Journal*, Vol. 41, No. 8, Aug. 2003, pp. 1452–1462.

⁵⁴Visbal, M. R. and Rizzetta, D. P., "Large-Eddy Simulation on Curvilinear Grids Using Compact Differencing and Filtering Schemes," *Journal of Fluids Engineering*, Vol. 124, No. 4, Dec. 2002, pp. 836–847.

⁵⁵Visbal, M. R., Morgan, P. E., and Rizzetta, D. P., "An Implicit LES Approach Based on High-Order Compact Differencing and Filtering Schemes," *AIAA Paper 2003-4098*, Jun. 2003.

⁵⁶Fureby, C. and Grinstein, F. F., "Monotonically Integrated Large Eddy Simulation," *AIAA Journal*, Vol. 37, No. 5, May 1999, pp. 544–556.

⁵⁷Grinstein, F. F., Margolin, L. G., and Rider, W. J., *Implicit Large Eddy Simulation: Computing Turbulent Fluid Dynamics*, Cambridge University Press, Cambridge, U.K., 2007.

⁵⁸Stoltz, S. and Adams, N. A., "An Approximate Deconvolution Procedure for Large-Eddy Simulation," *Physics of Fluids*, Vol. 11, No. 7, Jul. 1999, pp. 1699–1701.

⁵⁹Mathew, J., Lechner, R., Foysi, H., Sesterhenn, J., and Friedrich, R., "An Explicit Filtering Method for Large Eddy Simulation of Compressible Flows," *Physics of Fluids*, Vol. 15, No. 8, Aug. 2003, pp. 2279–2289.

⁶⁰Visbal, M. R. and Gaitonde, D. V., "Very High-Order Spatially Implicit Schemes for Computational Acoustics on Curvilinear Meshes," *Journal of Computational Acoustics*, Vol. 9, No. 4, Dec. 2001, pp. 1259–1286.

⁶¹Schlichting, H., *Boundary-Layer Theory*, McGraw-Hill, New York, 4th ed., 1960.

⁶²Fasel, H. and Konzelmann, U., "Non-parallel Stability of a Flat-Plate Boundary Layer Using the Complete Navier-Stokes Equations," *Journal of Fluid Mechanics*, Vol. 221, Dec. 1990, pp. 311–347.

⁶³Rai, M. M. and Moin, P., "Direct Numerical Simulation of Transition and Turbulence in a Spatially Evolving Boundary Layer," *Journal of Computational Physics*, Vol. 109, No. 2, Dec. 1993, pp. 169–192.

⁶⁴Rizzetta, D. P. and Visbal, M. R., "Large-eddy Simulation of Supersonic Boundary-layer Flow by a High-order Method," *International Journal of Computational Fluid Dynamics*, Vol. 18, No. 1, Jan. 2004, pp. 15–27.

⁶⁵Rizzetta, D. P. and Visbal, M. R., "Plasma-Based Flow Control Strategies for Transitional Highly Loaded Low-Pressure Turbines," *J Fluids Eng - Trans ASME*, Vol. 130, No. 4, Apr. 2008, pp. 041104:1–041104:12.

⁶⁶Rizzetta, D. P. and Visbal, M. R., "Plasma Flow Control Simulations of a Low-Reynolds Number Low-Aspect Ratio Wing," *Computers and Fluids*, Vol. 70, Nov. 2012, pp. 95–114.

⁶⁷Rizzetta, D. P. and Visbal, M. R., "Plasma Control for a Maneuvering Low-Aspect-Ratio Wing at Low Reynolds Number," *ASME Journal of Fluids Engineering*, Vol. 134, No. 12, Dec. 2012, pp. 121104-1–121104-19.

⁶⁸Schlichting, H., *Boundary-Layer Theory*, McGraw-Hill, New York, 4th ed., 1960.

⁶⁹Ghosal, S., "Mathematical and Physical Constraints on Large-Eddy Simulation of Turbulence," *AIAA Journal*, Vol. 37, No. 4, Apr. 1999, pp. 425–433.

⁷⁰Piomelli, U. and Balaras, E., "Wall-Layer Models for Large-Eddy Simulations," *Annual Review of Fluid Mechanics*, Vol. 34, Jan. 2002, pp. 349–374.

⁷¹Georgiadis, N. J., Rizzetta, D. P., and Fureby, C., "Large-Eddy Simulation: Current Capabilities, Recommended Practices, and Future Research," *AIAA Journal*, Vol. 48, No. 8, Aug. 2010, pp. 1772–1784.

⁷²Jeong, J. and Hussain, F., "On the Identification of a Vortex," *Journal of Fluid Mechanics*, Vol. 285, Feb. 1995, pp. 69–94.

⁷³Bons, J. P., Sondergaard, R., and Rivir, R. B., "Turbine Separation Control Using Pulsed Vortex Generator Jets," *Journal of Turbomachinery*, Vol. 123, No. 2, Apr. 2001, pp. 198–206.

⁷⁴Bons, J. P., Sondergaard, R., and Rivir, R. B., "The Fluid Dynamics of LPT Blade Separation Control Using Pulsed Jets," *Journal of Turbomachinery*, Vol. 124, No. 1, Jan. 2002, pp. 77–85.

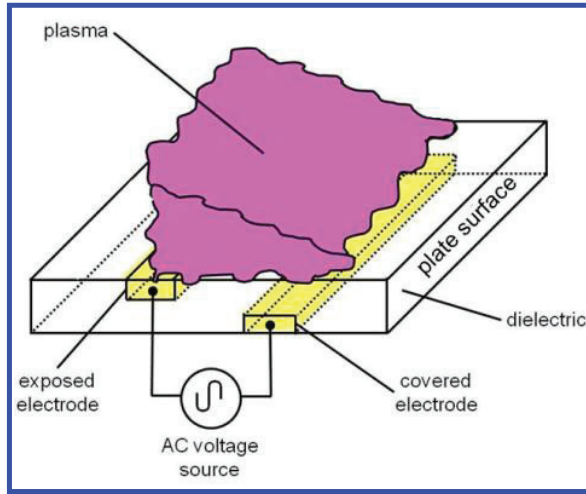


Figure 1. Schematic representation of asymmetric single dielectric-barrier-discharge plasma actuator

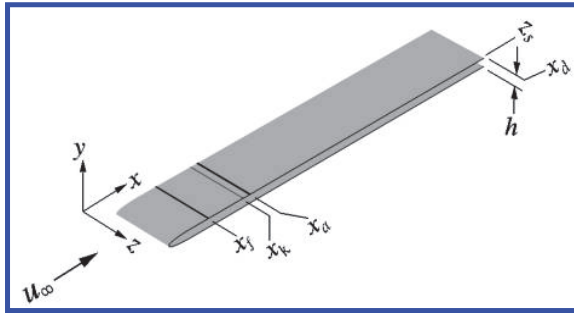


Figure 3. Flat-plate geometry configuration (z-direction stretched by a factor of 10.0).

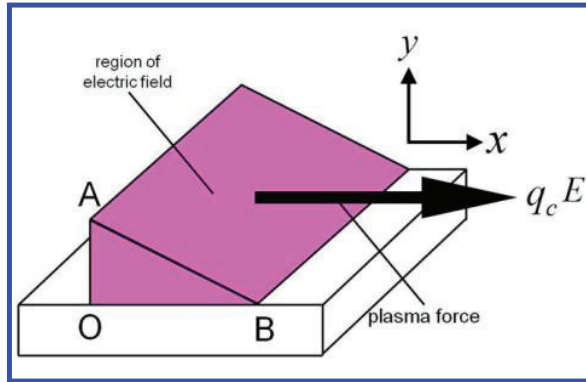


Figure 2. Geometry for the empirical plasma-force model

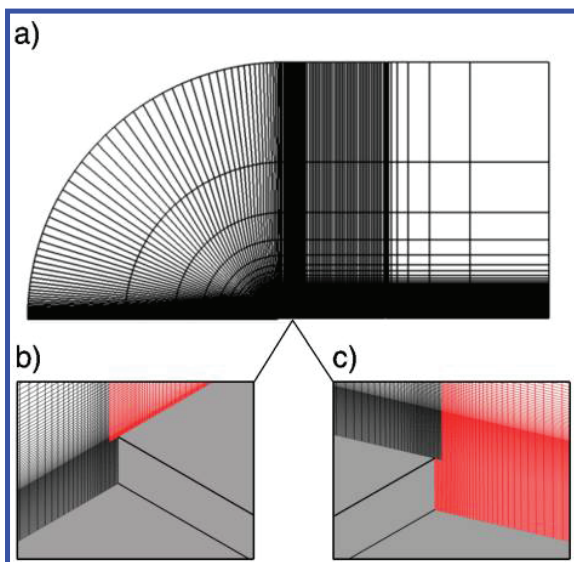


Figure 4. Computational mesh system: a) overall flow-field domain structure, b) overset grid structure for the forward-facing step, c) overset grid structure for the rearward-facing step.

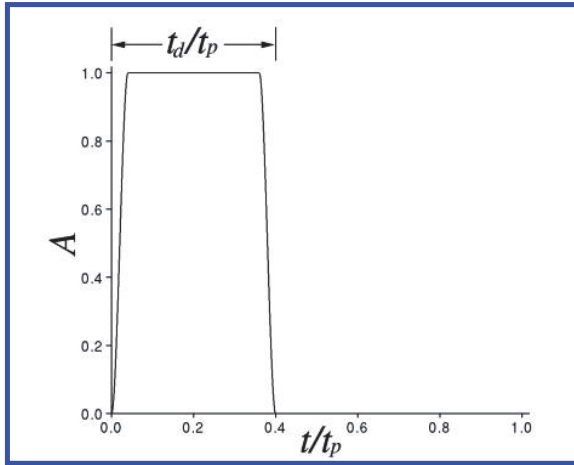


Figure 5. Actuator pulsing amplitude function time history.

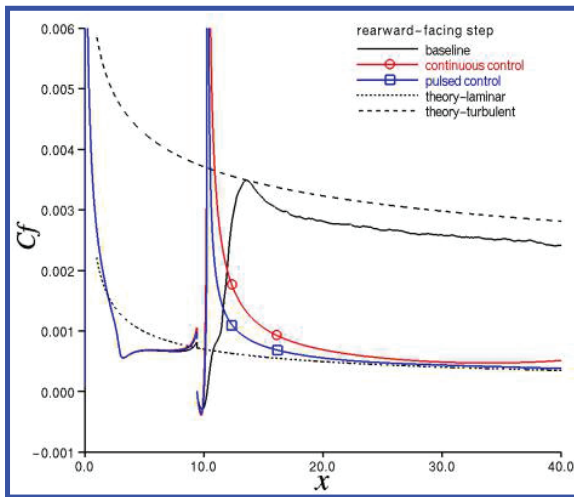


Figure 7. Time-mean skin friction distributions for the rearward-facing step.

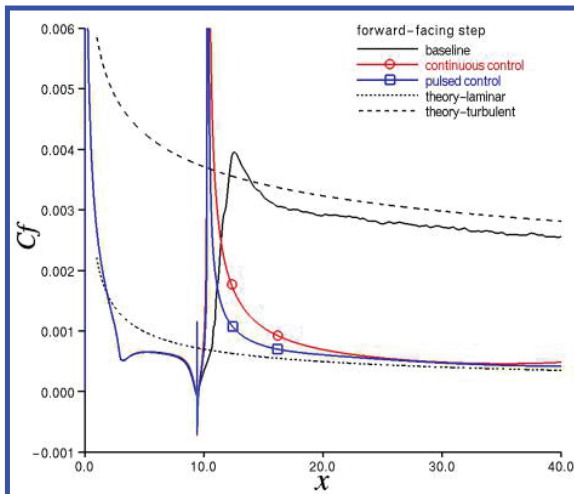


Figure 6. Time-mean skin friction distributions for the forward-facing step.

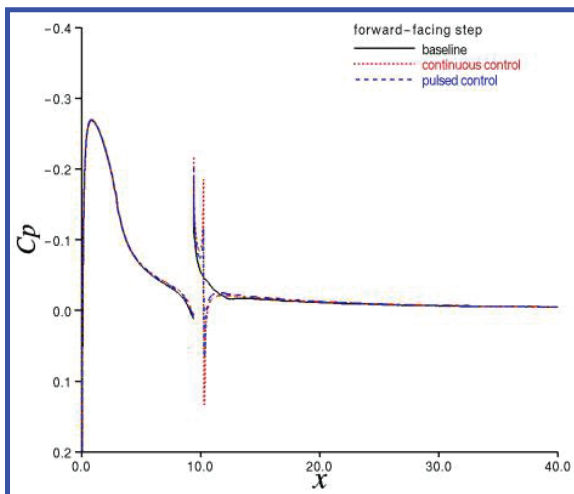


Figure 8. Time-mean surface pressure distributions for the forward-facing step.

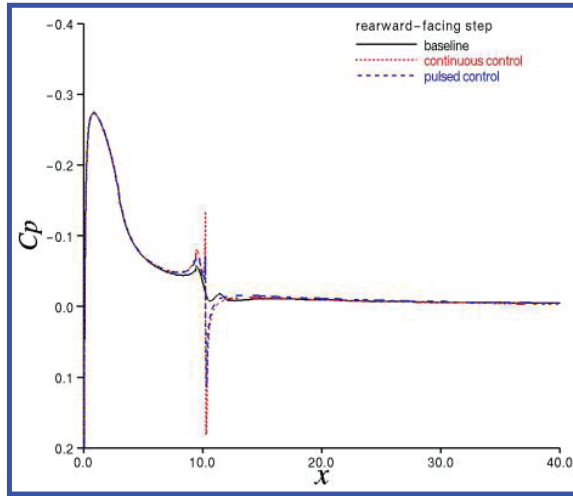


Figure 9. Time-mean surface pressure distributions for the rearward-facing step.

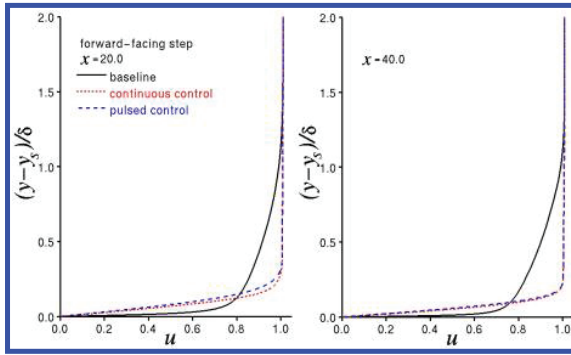


Figure 11. Time-mean streamwise velocity profiles at downstream locations for the forward-facing step.

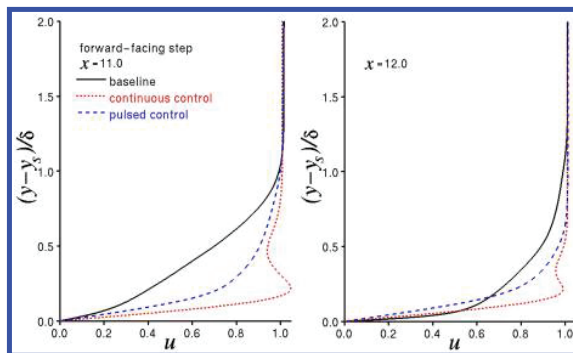


Figure 10. Time-mean streamwise velocity profiles at upstream locations for the forward-facing step.

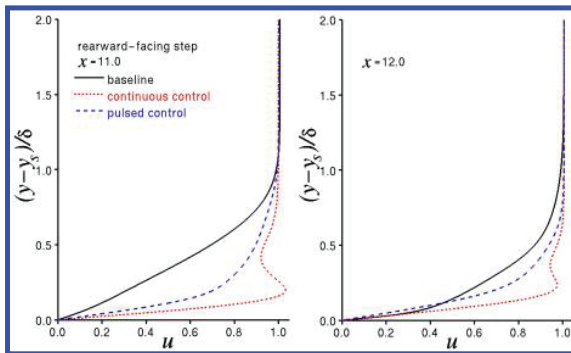


Figure 12. Time-mean streamwise velocity profiles at upstream locations for the rearward-facing step.

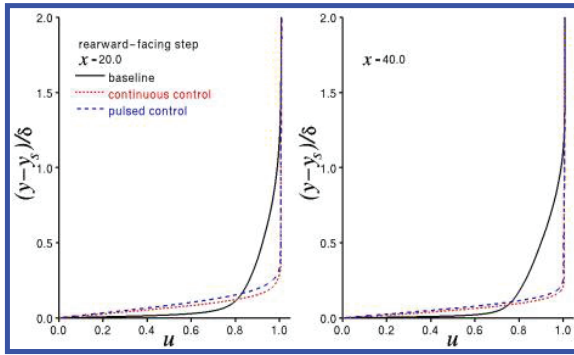


Figure 13. Time-mean streamwise velocity profiles at downstream locations for the rearward-facing step.

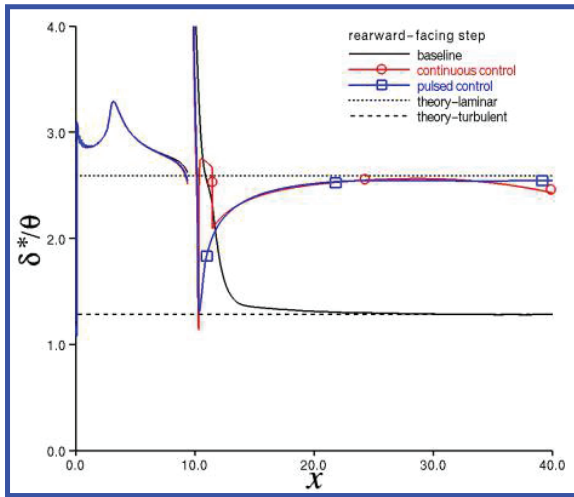


Figure 15. Time-mean shape factor distributions for the rearward-facing step.

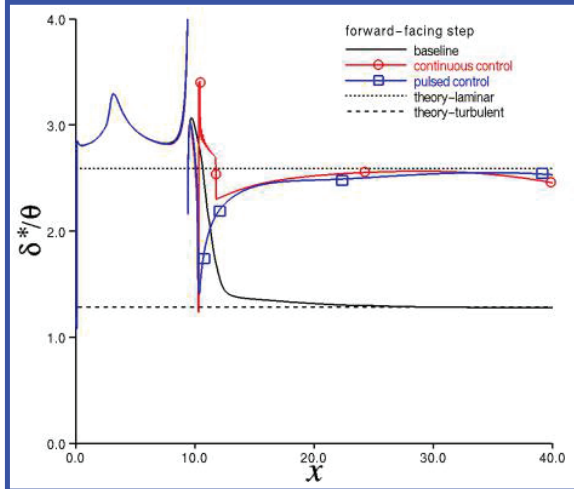


Figure 14. Time-mean shape factor distributions for the forward-facing step.

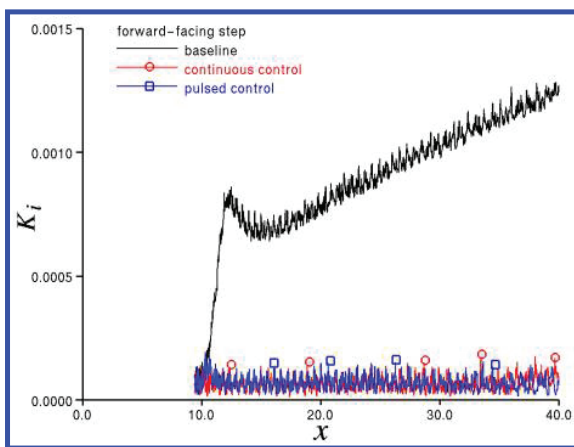


Figure 16. Distributions of the integrated turbulent kinetic energy for the forward-facing step.

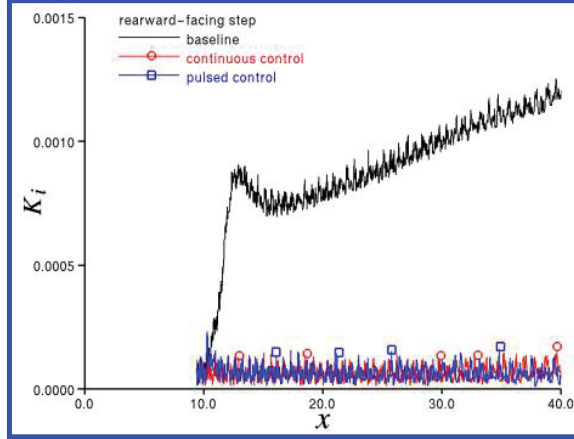


Figure 17. Distributions of the integrated turbulent kinetic energy for the rearward-facing step.

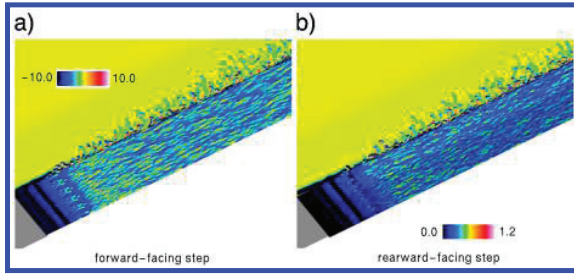


Figure 19. Instantaneous planar contours of the spanwise vorticity at the inboard boundary, and planar contours of the u -velocity in the near-wall region for the baseline cases: a) forward-facing step, b) rearward-facing step (y-direction stretched by a factor of 5.0, z-direction stretched by a factor of 3.0).

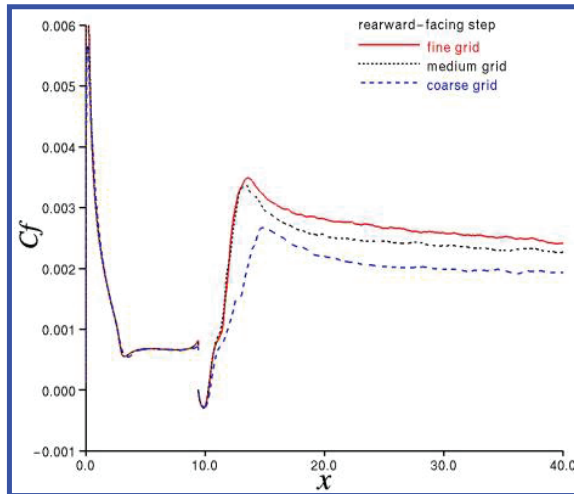


Figure 18. Time-mean skin friction distributions for the baseline rearward-facing step on various mesh systems.

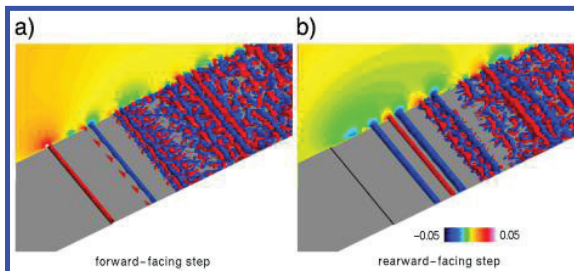


Figure 20. Instantaneous planar contours at the inboard boundary and iso-surfaces of the v -velocity for the baseline cases: a) forward-facing step, b) rearward-facing step (z-direction stretched by a factor of 3.0).

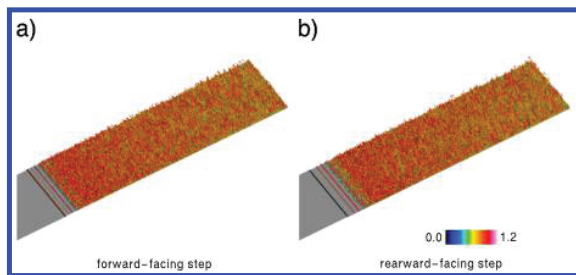


Figure 21. Instantaneous iso-surfaces of the Q -criterion ($Q = 3.0$) colored by the u -velocity for the baseline cases: a) forward-facing step, b) rearward-facing step (y -direction stretched by a factor of 3.0, z -direction stretched by a factor of 10.0).

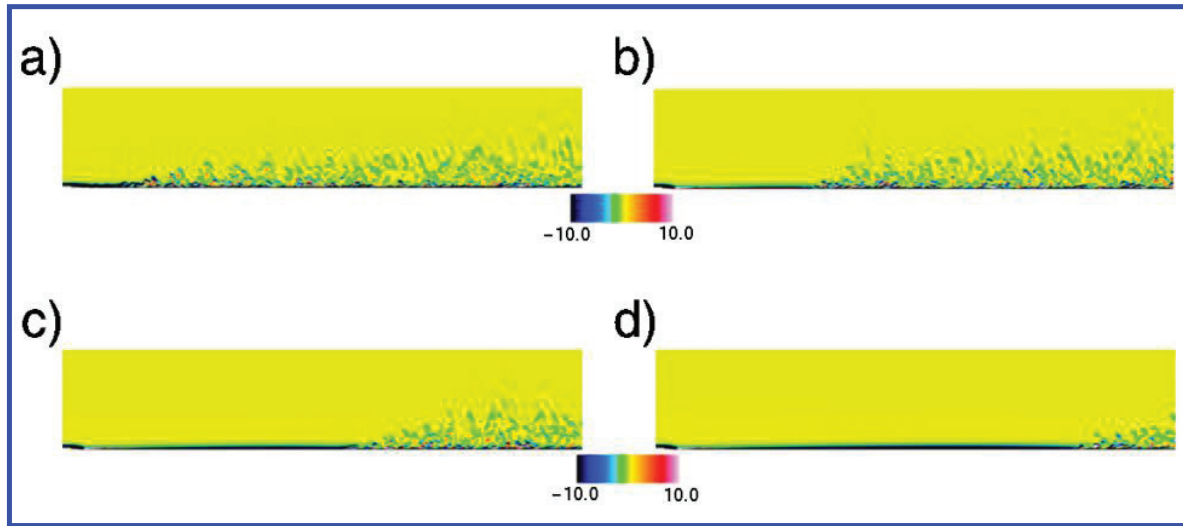


Figure 22. Instantaneous planar contours of the spanwise vorticity at the midspan location for the rearward-facing step with continuous plasma control (y -coordinate stretch by a factor of 5.0): a) $t = 0.0$, b) $t = 19.06$, c) $t = 38.12$, d) $t = 57.18$.

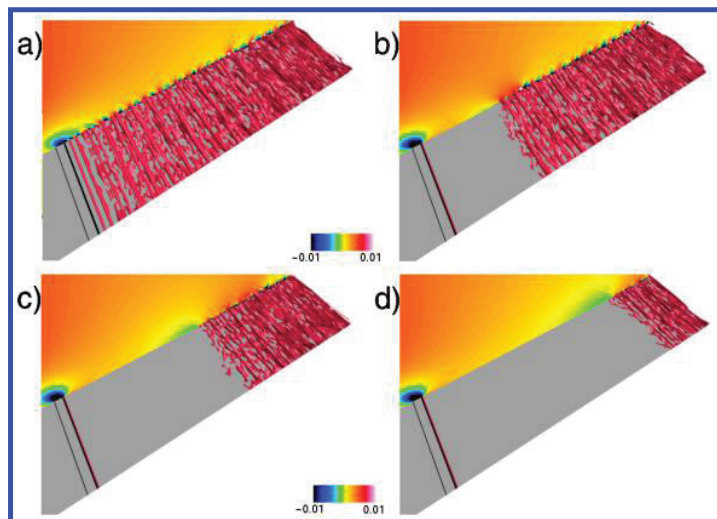


Figure 23. Instantaneous planar contours at the inboard boundary and iso-surfaces of the v -velocity for the rearward-facing step with continuous plasma control (z -coordinate stretch by a factor of 10.0): a) $t = 0.0$, b) $t = 19.06$, c) $t = 38.12$, d) $t = 57.18$.

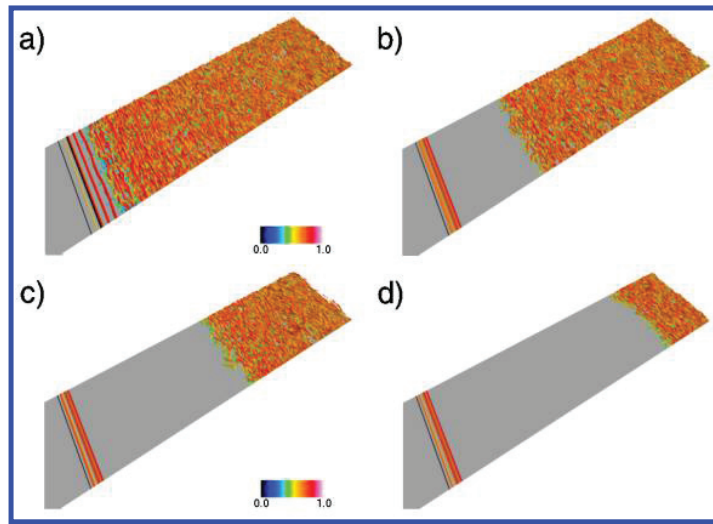


Figure 24. Instantaneous iso-surfaces of the Q -criterion ($Q = 0.75$) colored by u -velocity for the rearward-facing step with continuous plasma control (z -coordinate stretch by a factor of 10.0): a) $t = 0.0$, b) $t = 19.06$, c) $t = 38.12$, d) $t = 57.18$.

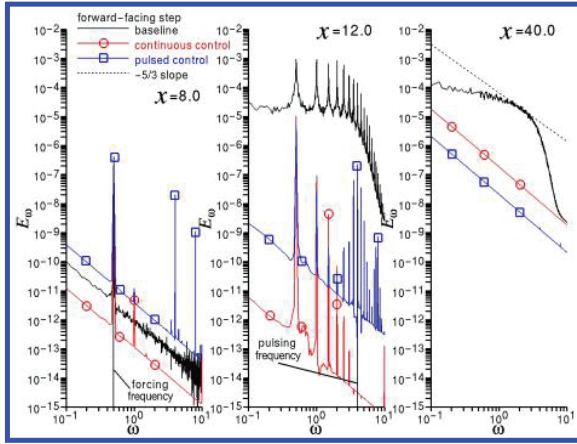


Figure 25. Turbulent kinetic energy frequency spectra for the forward-facing step at several streamwise locations.

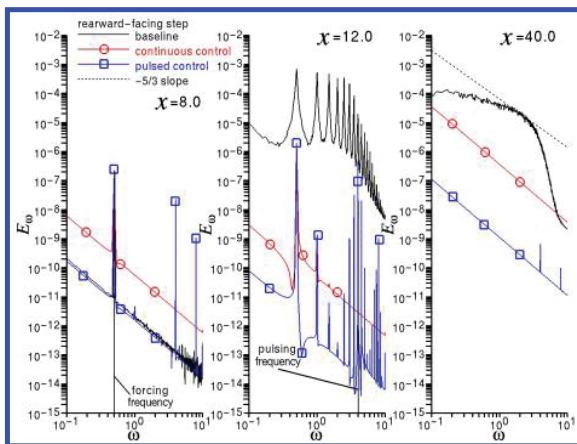


Figure 26. Turbulent kinetic energy frequency spectra for the rearward-facing step at several streamwise locations.

APPENDIX H

Plasma-Based Control of Transition on a Wing with Leading-Edge Excrescence

Donald P. Rizzetta* and Miguel R. Visbal†

Air Force Research Laboratory, Wright-Patterson Air Force Base, Ohio 45433-7512, USA

Large-eddy simulations (LES) are carried out to investigate plasma-based flow control that is used to delay transition generated by excrescence on the leading edge of a wing. The wing airfoil section has a geometry that is representative of modern reconnaissance air vehicles, and has an appreciable region of laminar flow at design conditions. Modification of the leading edge, which can be caused by the accumulation of debris, insect impacts, microscopic ice crystal formation, damage, or structural fatigue, may result in premature transition and an increase in drag. A dielectric barrier discharge (DBD) plasma actuator, located downstream of the excrescence, is employed to mitigate transition, decrease drag, and increase energy efficiency. Numerical solutions are obtained to the Navier-Stokes equations, that were augmented by source terms used to represent the body force imparted by the plasma actuator on the fluid. A simple phenomenological model provided this force resulting from the electric field generated by the plasma. The numerical method is based upon a high-fidelity numerical scheme and an implicit time-marching approach. An overset mesh system is employed to represent excrescence in the leading-edge region. Solutions are generated for both uniform and distributed excrescence geometries, as well as for the clean wing configuration without leading-edge modification. Results are obtained for two different values of the plasma field strength. Features of the computational flowfields are elucidated, and the effectiveness of control is quantified by comparison with baseline results without plasma actuation. It is found that plasma control can re-establish the laminar flow region lost to excrescence-generated transition, and reduce integrated configuration drag by up to 25%.

Nomenclature

c	= airfoil section chord
C_d	= time-mean integrated drag coefficient
C_f	= time-mean skin friction coefficient
C_p	= time-mean surface pressure coefficient
D_c	= plasma scale parameter
e_c	= electron charge, 1.6×10^{-19} coulomb
\mathbf{E}	= nondimensional electric field vector
E	= total specific energy
E_r	= reference electric field magnitude
E_x, E_y, E_z	= nondimensional components of the electric field vector
f	= nondimensional frequency
$\mathbf{F}, \mathbf{G}, \mathbf{H},$	= inviscid vector fluxes
$\mathbf{F}_v, \mathbf{G}_v, \mathbf{H}_v$	= viscous vector fluxes
\mathcal{J}	= Jacobian of the coordinate transformation
k	= spanwise wave number
K	= turbulent kinetic energy spectral amplitude
L_k	= nondimensional streamwise excrescence length

*Senior Research Aerospace Engineer, Aerodynamic Technology Branch, AFRL/RQVA, Associate Fellow AIAA.

†Technical Area Leader, Aerodynamic Technology Branch, AFRL/RQVA, Fellow AIAA.

This material is declared a work of the U.S. Government and is not subject to copyright protection in the United States.

M	= Mach number
n	= nondimensional normal distance from the wing surface
n_k	= nondimensional normal height of the excrescence
p	= nondimensional static pressure
Pr	= Prandtl number, 0.73 for air
q_c	= nondimensional charge density
\mathbf{Q}	= vector of dependent variables
\mathbf{Q}_i	= components of the heat flux vector
Re	= reference Reynolds number, $\rho_\infty u_\infty c / \mu_\infty$
Re_k	= roughness-based Reynolds number, $Re u_t(k) n_k$
R_{11}, R_{22}, R_{33}	= spanwise correlation coefficients of the fluctuating velocity components
s	= nondimensional arc length along the wing surface from the leading edge
s_k	= nondimensional arc length location of the excrescence
\mathbf{S}	= source vector
t	= nondimensional time
T	= nondimensional static temperature
u, v, w	= nondimensional Cartesian velocity components in the x, y, z directions
u_1, u_2, u_3	= u, v, w
u_t	= nondimensional wing tangential velocity component
$u_t(k)$	= u_t evaluated at $s = s_k$ and $n = n_k$ for the clean configuration
U, V, W	= contravariant velocity components
W_k	= nondimensional spanwise elemental-excrescence extent
x, y, z	= nondimensional Cartesian coordinates in the streamwise, vertical, and spanwise directions
x_1, x_2, x_3	= x, y, z
x_a	= nondimensional streamwise actuator location
x_k	= nondimensional streamwise excrescence location
z_s	= nondimensional spanwise extent of the computational domain
γ	= specific heat ratio, 1.4 for air
δ	= nondimensional boundary-layer thickness defined by $u_t = 0.99 u_{te}$
δ_{ij}	= Kronecker delta function
$\delta_{\xi 2}, \delta_{\eta 2}, \delta_{\zeta 2},$	= 2nd-order and 6th-order finite-difference operators in ξ, η, ζ
$\delta_{\xi 6}, \delta_{\eta 6}, \delta_{\zeta 6}$	
$\Delta \mathbf{Q}$	= $\mathbf{Q}^{p+1} - \mathbf{Q}^p$
$\Delta s, \Delta n, \Delta z$	= mesh spacings
Δt	= time step size
λ_k	= nondimensional spanwise inter-element excrescence spacing
μ	= nondimensional molecular viscosity coefficient
ξ, η, ζ	= nondimensional body-fitted computational coordinates
$\xi_t, \xi_x, \xi_y, \xi_z,$	
$\eta_t, \eta_x, \eta_y, \eta_z,$	
$\zeta_t, \zeta_x, \zeta_y, \zeta_z$	
ρ	= nondimensional fluid density
τ_{ij}	= components of the viscous stress tensor
ω	= nondimensional vorticity magnitude

Subscripts

∞	= dimensional reference value
e	= evaluated at boundary-layer edge
s	= evaluated at the wing surface

Superscripts

n	= time level
p	= subiteration level
$\hat{}$	= filtered value

+	= law-of-the-wall variable
'	= fluctuating component
—	= time-mean quantity

I. Introduction

Drag reduction is one of the principal considerations in the design and construction of unmanned air systems (UAS) and high altitude long endurance (HALE) vehicles. Such platforms are primarily used for intelligence, surveillance, and reconnaissance missions, which require long range and/or long endurance operations. Laminar flow configurations for these applications offer a substantial reduction in drag, leading directly to lower fuel consumption, greater energy efficiency, longer range, larger payloads, or increased flight times. Because of these benefits, laminar arrangements are also being considered for new mobility and strike platforms.

There are three main components to consider in the production and deployment of modern laminar flow vehicles. First, the design process must account for flight Reynolds number and sweep angles of high lift systems, and the growth of crossflow disturbances. Second, fabrication of aerodynamic surfaces must honor tolerances required for maintaining laminar flow by minimizing surface steps, skin seams, and three dimensional excrescences. Third, operational effects, resulting in leading-edge modification, must be overcome.

Studies on effects of surface imperfections upon aerodynamic performance have been carried out for many years. Early investigations include the works of Hood,¹ Fage,² Gregory et al.,³ Smith and Clutter,⁴ and Braslow.⁵ Later, flight experiments were conducted by Drake et al.⁶ The advent of long-endurance air vehicles has more recently spawned a current series of experimental studies devoted to the investigation of excrescence effects on transition.⁷⁻¹⁵ Initially, these studies were focussed on zero pressure gradient flows,^{7,9} but the long term goal was an examination of excrescence-generated transition in conditions typical of laminar flow wings.^{10,15} Recent computations of Rizzetta and Visbal¹⁶⁻¹⁸ have demonstrated that it is possible to numerically simulate transition occurring in flows over steps of small heights at moderate roughness-based Reynolds numbers. Predicted locations of transition were found to agree well with the experimental measurements of Drake and Bender.¹⁰

Several experimental works have evidenced the potential of plasma actuation for delaying transition and extending laminar regions on wing-like configurations.¹⁹⁻²⁴ For flat-plate flows, Grundmann and Tropea^{19,20} and Duchmann et al.²² have shown that both continuous and pulsed plasma actuators could delay transition in the presence of zero and adverse pressure gradients. In the experiments of Seraudie et al.²¹ and Kurz et al.,²³ a plasma actuator was embedded near the leading edge of an unswept wing with a low-speed airfoil section. Hot wire anemometry and stability analyses confirmed that transition was delayed when the actuator was operated. Flight experiments were carried out by Duchmann et al.,²⁴ employing a plasma actuator on the pressure side of a laminar flow wing section test article. Microphone and hot wire measurements quantified a measurable, but modest amount of transition delay.

Numerical computations of Rizzetta and Visbal^{17,18} indicated great potential of plasma-based control to delay the onset of transition generated by geometric disturbances. Simulations were conducted for flows past a flat plate configuration with forward-facing and rearward-facing steps at a roughness-based Reynolds number of 1013. This situation was similar to the previous computations of Rizzetta and Visbal¹⁶ and to the experiments of Drake and Bender,^{7,9} and represented mis-aligned panels on aerodynamic surfaces. Plasma-based actuators were then imposed downstream of the steps, and the effect upon transition was determined. It was shown¹⁷ that plasma actuation was able to maintain extensive laminar flow regions downstream of excrescence-sized steps, resulting in configuration drag reduction of more than 70% when minimal power was applied.

The present investigation extends previous efforts¹⁶⁻¹⁸ by considering the flow over a wing at a moderate Reynolds number. The wing airfoil section is representative of modern reconnaissance air vehicles, and has an appreciable region of laminar flow at design conditions. Excrescence-sized geometric disturbances are then imposed in the leading-edge region, creating premature transition and increased drag. Such excrescence can be caused by the accumulation of debris, insect impacts, microscopic ice crystal formation, damage due to general operation and maintenance, or structural fatigue. Large-eddy simulations are then carried out to explore plasma-based flow control that is used to mitigate the excrescence-generated transition. For this purpose, a simple phenomenological model is used to facilitate the representation of a DBD actuator, and

provides the force resulting from electric field generated by the plasma. Coupling of the plasma force to the fluid is achieved by the addition of source terms to the governing equations. High-fidelity solutions are obtained to the Navier-Stokes equations, employing an overset mesh system to describe the wing and excrescence geometries.

In sections that follow, the governing equations, plasma model, numerical method, DNS/LES approach, and details of the computations are described. Results are presented for flow past configurations with both uniform and distributed excrescence. Solutions are compared with plasma control on and off, as well as with the clean wing configuration without leading-edge excrescence. The effect of actuation is quantified in terms of the configuration integrated drag, and features of the computational flowfields are elucidated.

II. The Governing Equations

The governing fluid equations are taken as the unsteady three-dimensional compressible unfiltered Navier-Stokes equations. After introducing a generalized time-dependent curvilinear coordinate transformation to a body-fitted system, the equations are cast in the following nondimensional conservative form

$$\begin{aligned} \frac{\partial}{\partial t} \left(\frac{1}{\mathcal{J}} \mathbf{Q} \right) + \frac{\partial}{\partial \xi} \left(\mathbf{F} - \frac{1}{Re} \mathbf{F}_v \right) + \frac{\partial}{\partial \eta} \left(\mathbf{G} - \frac{1}{Re} \mathbf{G}_v \right) + \\ \frac{\partial}{\partial \zeta} \left(\mathbf{H} - \frac{1}{Re} \mathbf{H}_v \right) = D_c q_c \mathbf{S}. \end{aligned} \quad (1)$$

Here t is the time, ξ, η, ζ the computational coordinates, \mathbf{Q} the vector of dependent variables, $\mathbf{F}, \mathbf{G}, \mathbf{H}$ the inviscid flux vectors, $\mathbf{F}_v, \mathbf{G}_v, \mathbf{H}_v$ the viscous flux vectors, and \mathbf{S} the source vector representing the effect of plasma-induced body forces. The vector of dependent variables is given as

$$\mathbf{Q} = \begin{bmatrix} \rho & \rho u & \rho v & \rho w & \rho E \end{bmatrix}^T \quad (2)$$

the vector fluxes by

$$\begin{aligned} \mathbf{F} = \frac{1}{\mathcal{J}} \begin{bmatrix} \rho U \\ \rho u U + \xi_x p \\ \rho v U + \xi_y p \\ \rho w U + \xi_z p \\ \rho E U + \xi_{x_i} u_i p \end{bmatrix}, \quad \mathbf{G} = \frac{1}{\mathcal{J}} \begin{bmatrix} \rho V \\ \rho u V + \eta_x p \\ \rho v V + \eta_y p \\ \rho w V + \eta_z p \\ \rho E V + \eta_{x_i} u_i p \end{bmatrix}, \\ \mathbf{H} = \frac{1}{\mathcal{J}} \begin{bmatrix} \rho W \\ \rho u W + \zeta_x p \\ \rho v W + \zeta_y p \\ \rho w W + \zeta_z p \\ \rho E W + \zeta_{x_i} u_i p \end{bmatrix} \end{aligned} \quad (3)$$

$$\begin{aligned} \mathbf{F}_v = \frac{1}{\mathcal{J}} \begin{bmatrix} 0 \\ \xi_{x_i} \tau_{i1} \\ \xi_{x_i} \tau_{i2} \\ \xi_{x_i} \tau_{i3} \\ \xi_{x_i} (u_j \tau_{ij} - \mathcal{Q}_i) \end{bmatrix}, \quad \mathbf{G}_v = \frac{1}{\mathcal{J}} \begin{bmatrix} 0 \\ \eta_{x_i} \tau_{i1} \\ \eta_{x_i} \tau_{i2} \\ \eta_{x_i} \tau_{i3} \\ \eta_{x_i} (u_j \tau_{ij} - \mathcal{Q}_i) \end{bmatrix}, \\ \mathbf{H}_v = \frac{1}{\mathcal{J}} \begin{bmatrix} 0 \\ \zeta_{x_i} \tau_{i1} \\ \zeta_{x_i} \tau_{i2} \\ \zeta_{x_i} \tau_{i3} \\ \zeta_{x_i} (u_j \tau_{ij} - \mathcal{Q}_i) \end{bmatrix} \end{aligned} \quad (4)$$

with the source term

$$\mathbf{S} = \frac{1}{\mathcal{J}} \begin{bmatrix} 0 \\ E_x \\ E_y \\ E_z \\ uE_x + vE_y + wE_z \end{bmatrix} \quad (5)$$

and

$$D_c = \frac{\rho_c e_c E_r c}{\rho_\infty u_\infty^2} \quad (6)$$

where

$$U = \xi_t + \xi_{x_i} u_i, \quad V = \eta_t + \eta_{x_i} u_i, \quad W = \zeta_t + \zeta_{x_i} u_i \quad (7)$$

$$E = \frac{T}{\gamma(\gamma-1)M_\infty^2} + \frac{1}{2} (u^2 + v^2 + w^2). \quad (8)$$

In the preceding expressions, u, v, w are the Cartesian velocity components, ρ the density, p the pressure, and T the temperature. All length scales have been nondimensionalized by the airfoil section chord c , and dependent variables have been normalized by reference values except for p which has been nondimensionalized by $\rho_\infty u_\infty^2$. Components of the heat flux vector and stress tensor are expressed as

$$\mathcal{Q}_i = - \left[\frac{1}{(\gamma-1)M_\infty^2} \right] \left(\frac{\mu}{Pr} \right) \frac{\partial \xi_j}{\partial x_i} \frac{\partial T}{\partial \xi_j} \quad (9)$$

$$\tau_{ij} = \mu \left(\frac{\partial \xi_k}{\partial x_j} \frac{\partial u_i}{\partial \xi_k} + \frac{\partial \xi_k}{\partial x_i} \frac{\partial u_j}{\partial \xi_k} - \frac{2}{3} \delta_{ij} \frac{\partial \xi_l}{\partial x_k} \frac{\partial u_k}{\partial \xi_l} \right). \quad (10)$$

The Sutherland law for the molecular viscosity coefficient μ and the perfect gas relationship

$$p = \frac{\rho T}{\gamma M_\infty^2} \quad (11)$$

were also employed, and Stokes' hypothesis for the bulk viscosity coefficient has been invoked.

III. The Empirical Plasma Model

A schematic representation of a typical single asymmetric DBD plasma actuator is depicted in Fig. 1. The actuator consists of two electrodes that are separated by a dielectric insulator, and mounted on a body surface. When an oscillating voltage of sufficient strength is applied across the electrodes, it results in formation of a cold plasma sheet.³¹ The oscillation frequency is typically in the range of 1-15 kHz. For the purposes of numerical computation, it is generally assumed that the bulk fluid cannot respond rapidly to the high frequency alternating voltage, and that the dominant effect of actuation is to impose a time-mean electric field on the external flow. In simulation of control applications, the entire process may be modeled as a steady body-force vector acting on the net fluid adjacent to the actuator, which produces a flow velocity. This body force is obtained from the empirical model of Shyy et al.,²⁷ which has been successfully employed for a number of previous simulations of plasma-controlled flows.²⁸⁻³⁰

The model for the geometric extent of the plasma field generated by such an actuator is indicated in Fig. 2. The triangular region defined by the line segments OA, OB, and AB constitutes the plasma boundary. Outside of this region the electric field is not considered strong enough to ionize the air.²⁷ The peak value of the electric field can be estimated from the applied voltage and the spacing between the electrodes, and is taken as the reference value E_r . Along the segment AB, the electric field diminishes to its threshold value, which was taken as 30 kV/cm.²⁷ The nondimensional electric field is referenced from the threshold value and normalized by E_r . It has its maximum value at point O, and varies linear within OAB such that $0 \leq |E| \leq 1$. The electric body force is equal to $q_c \mathbf{E}$ and provides coupling from the plasma to the fluid, resulting in the source vector \mathbf{S} appearing in Eq. (1), where E_x, E_y, E_z are the components of \mathbf{E} . Some uncertainty exists regarding the direction of the force vector, which was related to the ratio OA/OB in the original work of Shyy et al.²⁷ Within the region OAB, the charge density q_c is taken to be constant. The plasma scale parameter D_c arises from nondimensionalization of the governing equations, and represents the

ratio of the electrical force of the plasma to the inertial force of the fluid. For the purposes of the present computations, it is assumed that the direction of the plasma force is tangential to the actuator surface. Due to empiricism of the formulation, there is ambiguity regarding the value of the scale parameter D_c , which can be increased or decreased to produce more or less force.

DBD actuators are inherently unsteady devices. As mentioned previously, within the context of the empirical model, the body force imposed on the fluid is assumed to be steady owing to the high frequency of the applied voltage. It should be noted that the body force ($q_c \mathbf{E}$) seen in Fig. 2 may be directed in a specific direction by proper orientation of the triangle OAB. In the present applications, this force is acting in the streamwise direction.

IV. Numerical Method

Time-accurate solutions to Eq. (1) were obtained numerically by the implicit approximately-factored finite-difference algorithm of Beam and Warming³³ employing Newton-like subiterations,³⁴ which has evolved as an efficient tool for generating solutions to a wide variety of complex fluid flow problems, and may be written as follows

$$\begin{aligned} & \left[\frac{1}{\mathcal{J}} + \left(\frac{2\Delta t}{3} \right) \delta_{\xi 2} \left(\frac{\partial \mathbf{F}^p}{\partial \mathbf{Q}} - \frac{1}{Re} \frac{\partial \mathbf{F}_v^p}{\partial \mathbf{Q}} \right) \right] \mathcal{J} \times \left[\frac{1}{\mathcal{J}} + \left(\frac{2\Delta t}{3} \right) \delta_{\eta 2} \left(\frac{\partial \mathbf{G}^p}{\partial \mathbf{Q}} - \frac{1}{Re} \frac{\partial \mathbf{G}_v^p}{\partial \mathbf{Q}} \right) \right] \mathcal{J} \times \\ & \left[\frac{1}{\mathcal{J}} + \left(\frac{2\Delta t}{3} \right) \delta_{\zeta 2} \left(\frac{\partial \mathbf{H}^p}{\partial \mathbf{Q}} - \frac{1}{Re} \frac{\partial \mathbf{H}_v^p}{\partial \mathbf{Q}} \right) \right] \Delta \mathbf{Q} = - \left(\frac{2\Delta t}{3} \right) \left[\left(\frac{1}{2\Delta t} \right) \left(\frac{3\mathbf{Q}^p - 4\mathbf{Q}^n + \mathbf{Q}^{n-1}}{\mathcal{J}} \right) \right. \\ & \left. + \delta_{\xi 6} \left(\mathbf{F}^p - \frac{1}{Re} \mathbf{F}_v^p \right) + \delta_{\eta 6} \left(\mathbf{G}^p - \frac{1}{Re} \mathbf{G}_v^p \right) + \delta_{\zeta 6} \left(\mathbf{H}^p - \frac{1}{Re} \mathbf{H}_v^p \right) - D_c q_c \mathbf{S}^p \right]. \end{aligned} \quad (12)$$

In this expression, which is employed to advance the solution in time, \mathbf{Q}^{p+1} is the $p+1$ approximation to \mathbf{Q} at the $n+1$ time level \mathbf{Q}^{n+1} , and $\Delta \mathbf{Q} = \mathbf{Q}^{p+1} - \mathbf{Q}^p$. For $p=1$, $\mathbf{Q}^p = \mathbf{Q}^n$. Second-order-accurate backward-implicit time differencing was used to obtain temporal derivatives.

The implicit segment of the algorithm (left-hand side of Eq. 12) incorporates second-order-accurate centered differencing for all spatial derivatives, and utilizes nonlinear artificial dissipation³⁵ to augment stability. For simplicity, the dissipation terms are not shown in Eq. (12). Efficiency is enhanced by solving this implicit portion of the factorized equations in diagonalized form.³⁶ Temporal accuracy, which can be degraded by use of the diagonal form, is maintained by utilizing subiterations within a time step. This technique has been commonly invoked in order to reduce errors due to factorization, linearization, diagonalization, and explicit application of boundary conditions. It is useful for achieving temporal accuracy on overset zonal mesh systems, and for a domain decomposition implementation on parallel computing platforms. Any deterioration of the solution caused by use of artificial dissipation and by lower-order spatial resolution of implicit operators is also reduced by the procedure. Three subiterations per time step have been applied in the current simulations to preserve second-order temporal accuracy.

The compact difference scheme employed on the right-hand side of Eq. 12 is based upon the pentadiagonal system of Lele,³⁷ and is capable of attaining spectral-like resolution. This is achieved through the use of a centered implicit difference operator with a compact stencil, thereby reducing the associated discretization error. For the present computations, a sixth-order tridiagonal subset of Lele's system is utilized, which is illustrated here in one spatial dimension as

$$\alpha_d \left(\frac{\partial \mathbf{F}}{\partial \xi} \right)_{i-1} + \left(\frac{\partial \mathbf{F}}{\partial \xi} \right)_i + \alpha_d \left(\frac{\partial \mathbf{F}}{\partial \xi} \right)_{i+1} = a \left(\frac{\mathbf{F}_{i+1} - \mathbf{F}_{i-1}}{2} \right) + b \left(\frac{\mathbf{F}_{i+2} - \mathbf{F}_{i-2}}{4} \right) \quad (13)$$

with $\alpha_d = 1/3$, $a = 14/9$, and $b = 1/9$. The scheme has been adapted by Visbal and Gaitonde³⁸ as an implicit iterative time-marching technique, applicable for unsteady vortical flows, and has been used to obtain the spatial derivative of any scalar, flow variable, metric coefficient, or flux component. It is used in conjunction with a low-pass Pade-type non-dispersive spatial filter developed by Gaitonde et al.,³⁹ which has been shown to be superior to the use of explicitly added artificial dissipation for maintaining both stability and accuracy on stretched curvilinear meshes.³⁸ The filter is applied to the solution vector sequentially in each of the three computational directions following each subiteration, and is implemented in one dimension as

$$\alpha_f \hat{\mathbf{Q}}_{i-1} + \hat{\mathbf{Q}}_i + \alpha_f \hat{\mathbf{Q}}_{i+1} = \sum_{n=0}^4 \frac{a_n}{2} (\mathbf{Q}_{i+n} + \mathbf{Q}_{i-n}) \quad (14)$$

where \hat{Q} designates the filtered value of Q . It is noted that the filtering operation is a post processing technique, applied to the evolving solution in order to regularize features that are captured but poorly resolved. Equation 14 represents a one-parameter family of eighth-order filters, where numerical values for the a_n 's may be found in Ref. 40. The filter coefficient α_f is a free adjustable parameter which may be selected for specific applications, where $|\alpha_f| < 0.5$. The value of α_f determines sharpness of the filter cutoff and has been set to 0.40 for the present simulations.

The aforementioned features of the numerical algorithm are embodied in a parallel version of the time-accurate three-dimensional computer code FDL3DI,⁴⁰ which has proven to be reliable for many fluid flow problems. Previous computations of transitional flow past excrescence-size steps^{16–18} which utilized FDL3DI, were found to compare well with experimental measurements, and are closely related to the present work.

V. The DNS/LES Approach

It was shown in the previous results of Rizzetta and Visbal,^{16–18} for excrescence-size step flowfields, that numerical solutions were fully resolved up to the transition location, and therefore corresponded to direct numerical simulations (DNS). Downstream of transition however, the flow was fully turbulent, and the computations reverted to large-eddy simulations. This is also true for the current computations. The aforementioned numerical technique is capable of treating both of these situations. In the LES approach, physical dissipation at length scales smaller than those in the inertial range is not resolved, thereby allowing for less spatial resolution and a savings in computational resources. For nondissipative numerical schemes, without use of subgrid-scale (SGS) models, this leads to an accumulation of energy at high mesh wave numbers, and ultimately to numerical instability. Traditionally, explicitly added SGS models are then employed as a means to dissipate this energy. In the present methodology, the effect of the smallest fluid structures is accounted for by a high-fidelity implicit large-eddy simulation (HFILES) technique, which has been successfully utilized for a number of turbulent and transitional computations. The present HFILES approach was first introduced by Visbal et al.^{41,42} as a formal alternative to conventional methodologies, and is predicated upon the high-order compact differencing and low-pass spatial filtering schemes, without the inclusion of additional SGS modeling. This technique is similar to monotonically integrated large-eddy simulation (MILES)⁴³ and other implicit LES methods⁴⁴ in that it relies upon the numerical solving procedure to provide the dissipation that is typically supplied by conventional SGS models. Unlike those schemes however, here dissipation is contributed by the aforementioned high-order Pade-type low-pass filter only at high spatial wavenumbers where the solution is poorly resolved. This provides a mechanism for the turbulence energy to be dissipated at scales that cannot be accurately represented on a given mesh system, in a fashion similar to subgrid modeling. For purely laminar flows, filtering may be required to maintain numerical stability and preclude a transfer of energy to high-frequency spatial modes due to spurious numerical events. The HFILES methodology thereby permits a seamless transition from large-eddy simulation to direct numerical simulation as the resolution is increased. In the HFILES approach, the unfiltered governing equations may be employed, and the computational expense of evaluating subgrid models, which can be substantial, is avoided. This procedure also enables the unified simulation of flowfields where laminar, transitional, and turbulent regions simultaneously coexist. For the present situation, the range of fluid scales in the transition region is limited and thus are fully resolved by the HFILES formulation. Here, the solution can be considered a direct numerical simulation, which may not be true if lower-order numerical methods are employed.

VI. Details of the Computations

A. The Wing, Excrescence, and Actuator Configurations

The unswept wing configuration to be considered in the simulations is pictured in Fig. 3, where a Cartesian coordinate system is situated with its origin located at the inboard leading edge ($x = y = z = 0.0$). In this orientation, x is the streamwise direction, y the vertical direction, and z the spanwise direction. The extent of the spanwise domain z_s was specified as 10% of the chord. Excrescence was placed at $x = x_k$, which corresponds to a nondimensional arc length of $s = s_k = 0.04$ from the leading edge. A close-up view of the leading-edge region is found in Fig. 4. The non-dimensional excrescence height n_k is 0.00053. This value was chosen to result in a roughness-based Reynolds number of $Re_k \approx 850$. Here $Re_k = Reu_t(k)n_k$ where $u_t(k)$ is the tangential component of velocity evaluated at $s = s_k$ and $n = n_k$ in the undisturbed flow without

Table 1. Computational mesh sizes

configuration	grid size	primary distribution	no. of meshes	total points
clean	fine	(1585 × 407 × 205)	1	132,244,475
clean	medium	(1190 × 305 × 155)	1	56,257,250
clean	coarse	(795 × 204 × 105)	1	17,028,900
uniform excrescence	fine	(1585 × 407 × 205)	6	133,931,625
distributed excrescence	fine	(1585 × 407 × 205)	13	134,098,374

excrescence. It is believed that excrescence with roughness-based Reynolds numbers above 800 should result in transition. The non-dimensional streamwise extent of the excrescence has an arc length of $L_k = 0.002$, such that the length to height ratio $L_k/n_k = 3.7603$. For the distributed-excrescence configuration, six identical elements (rectangular prism shapes) were equally spaced across the span. Each had a non-dimensional spanwise extent $W_k = 0.004905$, and an inter-element spanwise spacing $\lambda_k = 0.01257$. These dimensions produced an elemental width to length ratio $L_k/W_k = 2.4525$, and a spacing to width ratio $\lambda_k/W_k = 2.5627$.

A DBD plasma actuator was situated with point O in Fig. 2 located at $x = x_a$, and $s_a = 0.0531$. This point was just downstream of the separated flow region behind the excrescence in the time-mean flowfield. The normal height of the actuator (OA in Fig. 2) was taken as one half of the local boundary-layer thickness at x_a for the clean configuration, and OB/OA was prescribed as 10.0.

B. Computational Meshes

The computational mesh structure for the clean wing configuration, without excrescence, appears in Fig. 5. Frame a) of the figure exhibits the near surface grid, where the airfoil sectional shape can be seen. This geometry is representative of modern reconnaissance air vehicles, and has an appreciable region of laminar flow. The maximum thickness to chord ratio of the section is 13.6%. Planar contours of the O-grid construct were generated using automated software.⁴⁵ Outer boundaries were stretched to a distance of 100 chords from the airfoil surface, as is evident in frame b) of the figure, where only a fraction of the total mesh points are displayed. The two-dimensional planar grid was then distributed uniformly in the spanwise direction. The mesh exhibited in Fig. 5 consists of $(1585 \times 407 \times 205)$ points in the (ξ, η, ζ) directions respectively, and has a normal spacing at the wing surface of $\Delta n_s = 0.00002$. Computational meshes for the excrescence configurations were constructed from the primary distribution of the clean geometry. Some grid points were removed locally from the clean mesh system, and additional overset meshes were used to described the excrescence geometries. For the clean configuration, several coarser grids were also developed for a resolution study. The total number of points for all meshes appears in Table 1.

C. Boundary Conditions

On solid surfaces, the no slip condition was enforced, along with an adiabatic wall and vanishing normal pressure gradient that were implemented with third-order spatial accuracy. At the farfield outer boundary, freestream conditions were specified for all dependent variables. Grid stretching in the farfield region transfers information to high spatial wave numbers, and it is then dissipated by the low-pass numerical filter.⁴⁶ This technique prevents any spurious reflections, particularly in the outflow area of the computational domain. Periodic conditions were specified at the spanwise boundaries, where a five-grid plane overlap of the mesh systems was employed.

D. Temporal Considerations

The nondimensional time step specified for the calculations was $\Delta t = 0.000025$, which was dictated by accuracy and stability considerations. Numerical flowfields were typically initialized from a previous result (two-dimensional, coarse-mesh, or different value of D_c), and allowed to evolve in time for 100,000 steps in order to attain an equilibrium state. Time-mean and statistical data was then collected for 400,000 time steps, corresponding to 10 flow times over the streamwise length of the wing. All mean results were spatially averaged in the spanwise direction as well as temporally. This was done for all configurations, including

Table 2. Mesh spacings at $x = 0.9$

configuration	grid size	D_c	Δs^+	Δn_s^+	Δz^+
clean	fine	0	35.38	0.71	17.64
clean	medium	0	46.28	0.93	23.14
clean	coarse	0	64.16	1.28	32.08
uniform excrescence	fine	0	28.87	0.58	14.44
uniform excrescence	fine	100	34.68	0.69	17.34
uniform excrescence	fine	200	36.19	0.72	18.10
distributed excrescence	fine	0	28.91	0.58	14.46
distributed excrescence	fine	100	33.81	0.68	16.91
distributed excrescence	fine	200	35.56	0.71	17.78

the distributed-excrescence case, as it is uniform in the spanwise direction downstream of the excrescence location.

E. Flow Conditions

The freestream Mach number M_∞ was set to 0.1, and the Reynolds number based upon freestream conditions and the airfoil chord was specified as $Re = 1,000,000$. The angle of attack is taken as 2.5 deg, which is the wing design condition.

VII. Results

A. The Clean Configuration

For the clean wing configuration, solutions were obtained on all three mesh systems denoted in Table 1. Time-mean results for these calculations are found in Figs. 6-8. Surface pressure coefficient distributions are given in Fig. 6, which illustrate mesh convergence for the fine grid size. Corresponding distributions of the skin friction are provided in Fig. 7, where transition is apparent at $x \approx 0.64$. The figure demonstrates that there is an appreciable extent of laminar flow for the wing at the design condition. Profiles of the wing tangential velocity component at $x = 0.9$ are observed in Fig. 8. These are plotted as a function of the distance from the wing surface, which has been normalized by the local boundary-layer thickness δ . This location ($x = 0.9$) represents a region of the flow which is fully turbulent following transition. Mesh convergence for the fine grid is again apparent. Mesh spacing in wall units at $x = 0.9$ are indicated in Table 2. On all of the grids, results in the three spatial directions fall within the commonly accepted range for large-eddy simulation.^{47,48}

Instantaneous features of the flowfield, obtained on the fine grid, are portrayed in Fig. 9 in terms of surface contours of the vorticity magnitude (top), and an iso-surface of the Q -criterion vortex identification function.⁴⁹ The Q -criterion has commonly been utilized to represent vortical fluid structures, and has been colored by the streamwise velocity in the figure, where the streamwise direction (z) has been stretched by a factor of 1.5. Fine-scale turbulent structures, captured by the simulation downstream of transition, can be observed in the figure.

B. Time-Mean Results for the Excrescence Cases

Some preliminary computations were performed for the uniform excrescence case in order to determine the value of the plasma scale parameter (D_c) which could appreciably delay transition. It was determined that this could be achieved with $D_c = 200$. For comparison, solutions were also obtained with $D_c = 100$. Time-mean surface pressure distributions for the case of spanwise uniform excrescence are shown in Fig. 10. Both control solutions, the baseline, and the clean result are seen in the figure. The important information from the figure, is that plasma control has little impact upon surface pressure, and thus will not degrade lift. Figure 11 displays the corresponding skin friction distributions. In the baseline case, a high level of C_f

Table 3. Integrated drag coefficient

configuration	grid size	D_c	Cd
clean	fine	0	0.00128
clean	medium	0	0.00125
clean	coarse	0	0.00101
uniform excrescence	fine	0	0.00583
uniform excrescence	fine	100	0.00443
uniform excrescence	fine	200	0.00435
distributed excrescence	fine	0	0.00588
distributed excrescence	fine	100	0.00478
distributed excrescence	fine	200	0.00462

occurs immediately downstream of the excrescence location, indicating transition much sooner than for the clean configuration. With plasma control for $D_c = 200$, it is evident that transition is delayed almost to the clean wing location, recovering the extent of laminar flow. When D_c is decreased to a value of 100, there is somewhat less delay, but the applied plasma power is also reduced by 50%. Similar time-mean distributions of surface pressure and skin friction for the distributed excrescence-case appear in Figs. 12 and 13. Although the skin friction is much like the uniform situation, it is apparent in Fig. 13 that control is slightly less effective for distributed excrescence.

In order to quantify control effectiveness, the skin friction was integrated over the airfoil surface to obtain the integrated drag coefficient Cd , where

$$Cd = \oint C_f ds. \quad (15)$$

Integrated drag coefficients for all simulations, including those of the clean case, are tabulated in Table 3. Reduction in Cd with application of plasma actuation is illustrated in the Table. For the uniform-excrescence case and $D_c = 200$, the reduction is more than 25%.

Mesh spacings in wall units at $x = 0.9$ for all excrescence cases are found in Table 2. These are quite similar to the clean-configuration results.

C. Instantaneous Results for the Excrescence Cases

Similar to Fig. 9 for the clean wing, instantaneous results for the baseline and uniform-excrescence cases are provided by Fig. 14 in terms of surface contours of vorticity magnitude and iso-surfaces of the Q -criterion. For the baseline wing, transition is observed to occur just downstream of the excrescence location, as was noted for the skin friction in Fig. 11. Transition with plasma control is demonstrated by the solutions for $D_c = 100$ and $D_c = 200$. Corresponding results for distributed excrescence are presented in Fig. 15, which are seen to be similar.

Fig. 16 portrays temporal evolution of the uniform-excrescence flowfield, following activation of plasma control with $D_c = 200$. Several instantaneous time frames are displayed in the figure, and exhibit the flowfield development. The nondimensional time levels are referenced from the uncontrolled equilibrium state at $t = 0.00$, when plasma actuation is initiated. At $t = 0.56$, control has generated laminar flow to about 50% of the chord. The laminar flow region is extended beyond that of the baseline case at $t = 1.12$, but that was only part of the transient evolution. The new, control equilibrium flowfield, is achieved at $t = 1.68$. Based upon a representative section chord of 1.542 m (5.0 ft) and sea level atmospheric conditions, the total actuation time is approximately 0.73 sec.

A similar flowfield development for termination of control is indicated in Fig. 17, which is also for the uniform-excrescence case with $D_c = 200$. Here, $t = 0.00$ corresponds to the equilibrium state with control on, at which point plasma actuation is terminated. Transition is shown to appear just behind the actuator when $t = 0.20$, and moves downstream. At $t = 0.40$, transition is at about 40% of the chord, and by $t = 0.60$ the flowfield has attained its equilibrium baseline state. Note that the flow evolves to its equilibrium condition in

less than one half of the time as that required when control is initiated. The flowfield evolutions illustrated in Figs. 16 and 17 for uniform excrescence are essentially the same in the distributed-excrescence case.

D. Fluctuating Quantities for the Uniform-Excrescence Case

Fluctuating quantities for the uniform-excrescence configuration appear in Figs. 18-20. These were collected at a normal distance from the wing surface that was approximately equal to one half of the time-mean boundary-layer thickness. Turbulent kinetic energy frequency spectra for the baseline and control ($D_c = 200$) cases are given in Fig. 18, with

$$K = 0.5(u'u' + v'v' + w'w') \quad (16)$$

It is evident at $x = 0.4$ that the baseline flow is already fully turbulent, but the control case has not yet transitioned. Further downstream at $x = 0.9$, the levels of turbulent kinetic energy are similar for both flows, and the inertial range (-5/3 slope) is apparent. In Fig. 19, the turbulent kinetic energy is plotted as a function of the nondimensional spanwise wave number k . Again, similar levels of K for both flows are observed at $x = 0.9$, and the inertial range is captured by the simulations.

One aspect of LES that can preclude correct physical behavior is the length of the homogeneous extent (z -direction). If this distance is not sufficient, the solution may be over constrained due to application of periodic boundary conditions. To determine adequacy of the homogeneous extent, spanwise correlation coefficients of the fluctuating velocity components were computed and are provided for the baseline uniform-excrescence configuration in Fig. 20. The coefficients are defined as

$$R_{ii} = \frac{\overline{u'_{ia} u'_i}}{\sqrt{\overline{u'^2_{ia}}} \sqrt{\overline{u'^2_i}}} \quad (17)$$

where $i = 1, 2, 3$, $u'_1, u'_2, u'_3 = u', v', w'$ and u'_{ia} is evaluated at $z/z_s = 0.5$. A rapid decay in the amplitude of the coefficients away from $z/z_s = 0.5$ signifies that there is no anomalous behavior due to inadequacy of the homogeneous distance.

VIII. Summary and Conclusions

Large-eddy simulations were performed in order to explore the use of plasma-based flow control, that was applied to delay transition produced by excrescence on the leading of a wing. The wing airfoil section had a geometry that is representative of modern reconnaissance air vehicles, and maintained laminar flow for 60% of the chord at design conditions. When excrescence was included at the 4% chord location, transition took place shortly downstream. Plasma-based flow control was then applied just aft of the excrescence position. Simulations of several wing configurations were conducted by obtaining numerical solutions to the Navier-Stokes equations. A high-fidelity scheme was utilized for this purpose, combined with a simple phenomenological model to represent the body force created by the plasma.

Two different representations of excrescence were considered in the investigations, consisting of spanwise-uniform and spanwise-distributed geometries. In addition to baseline computations for each of the excrescence cases, control solutions were obtained for two values of the plasma scale parameter D_c . For the higher of these ($D_c = 200$), it was found that the extent of the laminar flow region could be restored when plasma control was applied, and resulted in a 25% reduction of the integrated configuration drag. At the lower value ($D_c = 100$), control was slightly less effective, but the power requirement was reduced. It was also found that the distributed-excrescence case was somewhat more difficult to control. Although this representation employed a regular size and spacing of excrescence elements, it afforded more realistic approximation of physical circumstances, whereby geometric disturbances may be created through the accumulation of debris, insect impacts, or microscopic ice crystal formation. The investigation indicates that plasma actuation offers a potential to mitigate the repercussions of such events, by providing on demand control without moving parts or mechanical complexity.

Acknowledgments

The work presented here was sponsored by the U. S. Air Force Office of Scientific Research, under a task monitored by D. Smith. Computational resources were supported in part by a grant of supercomputer time

from the U. S. Department of Defense Supercomputing Resource Centers at the Stennis Space Center, MS and Wright-Patterson AFB, OH. The authors are grateful to A. Sullivan, G. R. Dale, and J. R. Martinez for their assistance.

References

- ¹Hood, M. J., "The Effects of Surface Waviness and of Rib Stitching on Wing Drag," Technical Note 724, NACA, Aug. 1939.
- ²Fage, A., "The Smallest Size of a Spanwise Surface Corrugation which Affects Boundary-Layer Transition on an Aerofoil," Reports and Memoranda 2120, Aeronautical Research Council, Jan. 1943.
- ³Gregory, N., Walker, W. S., and Johnson, D., "Part I: The Effect on Transition of Isolated Surface Excrescences in the Boundary Layer; Part II: Brief Flight Tests on a *Vampire I* Aircraft to Determine the Effect of Isolated Surface Pimples on Transition," Reports and Memoranda 2779, Aeronautical Research Council, Oct. 1951.
- ⁴Smith, A. M. O. and Clutter, D. W., "The Smallest Height of Roughness Capable of Affecting Boundary-Layer Transition in Low-Speed Flow," Engineering Report ES26803, Douglas Aircraft Company, 1954.
- ⁵Braslow, A. L., "The Effect of Distributed Surface Roughness on Boundary-Layer Transition," AGARD Report 254, North Atlantic Treaty Organization, Jan. 1960.
- ⁶Drake, A., Westphal, R. V., Zuniga, F. A., Kennelly, R. A., and Koga, D. J., "Wing Leading Edge Joint Laminar Flow Tests," Technical Memorandum 4762, NASA, Mar. 1997.
- ⁷Drake, A., Bender, A. M., Solomom, W. D., and Vavra, A. J., "Prediction of Manufacturing Tolerances for Laminar Flow," Technical Report AFRL-VA-WP-TR-2005-3060, Wright-Patterson AFB, OH, Jun. 2005.
- ⁸Wang, Y. X. and Gaster, M., "Effect of Surface Steps on Boundary Layer Transition," *Experiments in Fluids*, Vol. 39, Jun. 2005, pp. 679–686.
- ⁹Bender, A. M. and Drake, A., "Manufacturing Tolerances for Laminar Flow," Technical Report AFRL-VA-WP-TR-2007-3086, Air Force Research Laboratory, Wright-Patterson AFB, OH, Sep. 2006.
- ¹⁰Drake, A. and Bender, A., "Surface Excrescence Transition Study," Technical Report AFRL-RB-WP-TR-2009-3109, Wright-Patterson AFB, OH, Apr. 2009.
- ¹¹McKeon, B. J., Bender, A. M., Westphal, R. V., and Drake, A., "Transition in Incompressible Boundary Layers with Two-Dimensional Excrescences," AIAA Paper 2008-589, Jan 2008.
- ¹²Bender, A. M., Elliot, J. R., Shinagawa, Y., Korntheuer, A. J., Drake, A., Westphal, R. V., Gerashchenko, S., McKeon, B. J., and Yoshioka, S., "An Approach to Measuring Step Excrescence Effects in the presence of a Pressure Gradient," AIAA Paper 2010-373, Jan. 2010.
- ¹³Gerashchenko, S., McKeon, B. J., Westphal, R. V., Bender, A. M., and Drake, A., "Hot-Wire Measurements of the Influence of Surface Steps on Transition in Favorable Pressure Gradient Boundary Layers," AIAA Paper 2010-374, Jan. 2010.
- ¹⁴Drake, A., Bender, A. M. and Korntheuer, A. J., Westphal, R. V., McKeon, B. J., Gerashchenko, S., Rohe, W., and Dale, G., "Step Excrescence Effects for Manufacturing Tolerances on Laminar Flow Wings," AIAA Paper 2010-375, Jan. 2010.
- ¹⁵Bender, A., Harris, C., and Hawkins, B., "Boundary Layer Excrescence Examination Study," Technical Report AFRL-RB-WP-TR-2012-0027, Air Force Research Laboratory, Wright-Patterson AFB, OH, May 2012.
- ¹⁶Rizzetta, D. P. and Visbal, M. R., "Numerical Simulation of Excrescence Generated Transition," *AIAA Journal*, Vol. 52, No. 2, Feb. 2014, pp. 385–397.
- ¹⁷Rizzetta, D. P. and Visbal, M. R., "Plasma-Based Flow Control for Delay of Excrescence-Generated Transition," AIAA Paper 2014-1272, Jan. 2014.
- ¹⁸Rizzetta, D. P. and Visbal, M. R., "Delay of Finite-Span Excrescence-Induced Transition Using Plasma-Based Control," AIAA Paper 2014-2664, Jun. 2014.
- ¹⁹Grundmann, S. and Tropea, C., "Experimental Transition Delay Using Glow-Discharge Plasma Actuators," *Experiments in Fluids*, Vol. 42, No. 4, Apr. 2007, pp. 653–657.
- ²⁰Grundmann, S. and Tropea, C., "Delay of Boundary-Layer Transition Using Plasma Actuators," AIAA Paper 2008-1369, Jan. 2008.
- ²¹Seraudie, A., Vermeersch, O., and Arnal, D., "DBD Plasma Actuator Effect on a 2D Model Laminar Boundary Layer. Transition Delay under Ionic Wind Effect," AIAA Paper 2011-3515, Jun. 2011.
- ²²Duchmann, A., Kurz, A., Widmann, A., Grundmann, S., and Tropea, C., "Characterization of Tollmien-Schlichting Wave Damping by DBD Plasma Actuators Using Phase-Locked PIV," AIAA Paper 2012-0903, Jan. 2012.
- ²³Kurz, A., Tropea, C., Grundmann, S., Forte, M., Vermeersch, O., Seraudie, A., Arnal, D., Goldin, N., and King, R., "Transition Delay using DBD Plasma Actuators in Direct Frequency Mode," AIAA Paper 2012-2945, Jun. 2012.
- ²⁴Duchmann, A., Simon, B., Magin, P., Tropea, C., and Grundmann, S., "In-Flight Transition Delay with DBD Plasma Actuators," AIAA Paper 2013-0900, Jan. 2013.
- ²⁵Roth, J. R., "Aerodynamic Flow Acceleration Using Paraelectric and Peristaltic Electrohydrodynamic Effects of a One Atmosphere Uniform Glow Discharge Plasma," *Physics of Plasmas*, Vol. 10, No. 5, May 2003, pp. 2117–2128.
- ²⁶Roth, J. R., Sin, H., and Madham, R. C. M., "Flow Re-attachment and Acceleration by Paraelectric and Peristaltic Electrohydrodynamic (EHD) Effects," AIAA Paper 2003-0531, Jan. 2003.
- ²⁷Shyy, W., Jayaraman, B., and Anderson, A., "Modeling of Glow Discharge-Induced Fluid Dynamics," *Journal of Applied Physics*, Vol. 92, No. 11, Dec. 2002, pp. 6434–6443.
- ²⁸Rizzetta, D. P. and Visbal, M. R., "Large Eddy Simulation of Plasma-Based Control Strategies for Bluff Body Flow," *AIAA Journal*, Vol. 47, No. 3, Mar. 2009, pp. 717–729.

²⁹Rizzetta, D. P. and Visbal, M. R., "Numerical Investigation of Plasma-Based Control for Low-Reynolds Number Airfoil Flows," *AIAA Journal*, Vol. 49, No. 2, Feb. 2011, pp. 411–425.

³⁰Rizzetta, D. P. and Visbal, M. R., "Large-Eddy Simulation of Plasma-Based Turbulent Boundary-Layer Separation Control," *AIAA Journal*, Vol. 48, No. 12, Dec. 2010, pp. 2793–2810.

³¹Moreau, E., "Airflow Control by Non-Thermal Plasma Actuators," *Journal of Physics D: Applied Physics*, Vol. 40, No. 3, Feb. 2007, pp. 605–636.

³²Benard, N., Debien, A., and Moreau, E., "Time-Dependent Volume Force Produced by a Non-Thermal Plasma Actuator from Experimental Velocity Field," *Journal of Physics D: Applied Physics*, Vol. 46, No. 24, Jun. 2013, pp. 245201(12pp).

³³Beam, R. and Warming, R., "An Implicit Factored Scheme for the Compressible Navier-Stokes Equations," *AIAA Journal*, Vol. 16, No. 4, Apr. 1978, pp. 393–402.

³⁴Gordnier, R. E. and Visbal, M. R., "Numerical Simulation of Delta-Wing Roll," AIAA Paper 93-0554, Jan. 1993.

³⁵Jameson, A., Schmidt, W., and Turkel, E., "Numerical Solutions of the Euler Equations by Finite Volume Methods Using Runge-Kutta Time Stepping Schemes," AIAA Paper 81-1259, Jun. 1981.

³⁶Pulliam, T. H. and Chaussee, D. S., "A Diagonal Form of an Implicit Approximate-Factorization Algorithm," *Journal of Computational Physics*, Vol. 39, No. 2, Feb. 1981, pp. 347–363.

³⁷Lele, S. A., "Compact Finite Difference Schemes with Spectral-like Resolution," *Journal of Computational Physics*, Vol. 103, No. 1, Nov. 1992, pp. 16–42.

³⁸Visbal, M. R. and Gaitonde, D. V., "High-Order-Accurate Methods for Complex Unsteady Subsonic Flows," *AIAA Journal*, Vol. 37, No. 10, Oct. 1999, pp. 1231–1239.

³⁹Gaitonde, D., Shang, J. S., and Young, J. L., "Practical Aspects of High-Order Accurate Finite-Volume Schemes for Electromagnetics," AIAA Paper 97-0363, Jan. 1997.

⁴⁰Gaitonde, D. and Visbal, M. R., "High-Order Schemes for Navier-Stokes Equations: Algorithm and Implementation into FDL3DI," Technical Report AFRL-VA-WP-TR-1998-3060, Air Force Research Laboratory, Wright-Patterson AFB, OH, Aug. 1998.

⁴¹Visbal, M. R. and Rizzetta, D. P., "Large-Eddy Simulation on Curvilinear Grids Using Compact Differencing and Filtering Schemes," *Journal of Fluids Engineering*, Vol. 124, No. 4, Dec. 2002, pp. 836–847.

⁴²Visbal, M. R., Morgan, P. E., and Rizzetta, D. P., "An Implicit LES Approach Based on High-Order Compact Differencing and Filtering Schemes," AIAA Paper 2003-4098, Jun. 2003.

⁴³Fureby, C. and Grinstein, F. F., "Monotonically Integrated Large Eddy Simulation," *AIAA Journal*, Vol. 37, No. 5, May 1999, pp. 544–556.

⁴⁴Grinstein, F. F., Margolin, L. G., and Rider, W. J., *Implicit Large Eddy Simulation: Computing Turbulent Fluid Dynamics*, Cambridge University Press, Cambridge, U.K., 2007.

⁴⁵Steinbrenner, J. P., Chawner, J. P., and Fouts, C. L., "The GRIDGEN 3D Multiple Block Grid Generation System, Volume II: User's Manual," Technical Report WRDC-TR-90-3022, Wright Research and Development Center, Wright-Patterson AFB, OH, Feb. 1991.

⁴⁶Visbal, M. R. and Gaitonde, D. V., "Very High-Order Spatially Implicit Schemes for Computational Acoustics on Curvilinear Meshes," *Journal of Computational Acoustics*, Vol. 9, No. 4, Dec. 2001, pp. 1259–1286.

⁴⁷Piomelli, U. and Balaras, E., "Wall-Layer Models for Large-Eddy Simulations," *Annual Review of Fluid Mechanics*, Vol. 34, Jan. 2002, pp. 349–374.

⁴⁸Georgiadis, N. J., Rizzetta, D. P., and Fureby, C., "Large-Eddy Simulation: Current Capabilities, Recommended Practices, and Future Research," *AIAA Journal*, Vol. 48, No. 8, Aug. 2010, pp. 1772–1784.

⁴⁹Jeong, J. and Hussain, F., "On the Identification of a Vortex," *Journal of Fluid Mechanics*, Vol. 285, Feb. 1995, pp. 69–94.

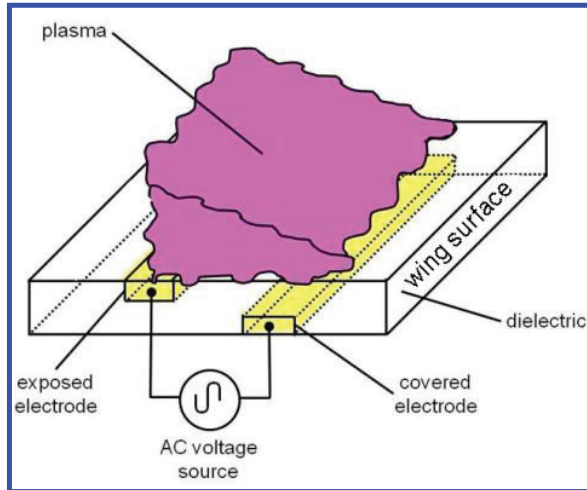


Figure 1. Schematic representation of asymmetric single dielectric-barrier-discharge plasma actuator.

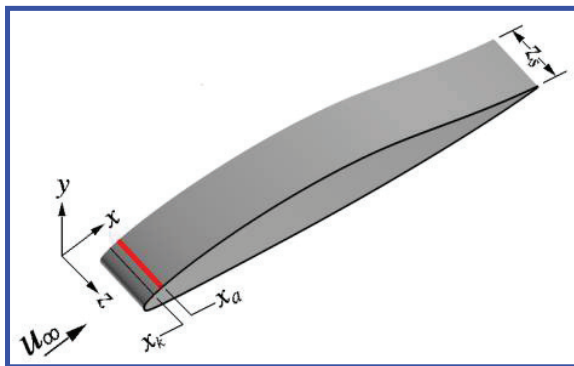


Figure 3. Wing configuration (z coordinate stretch by factor of 1.5).

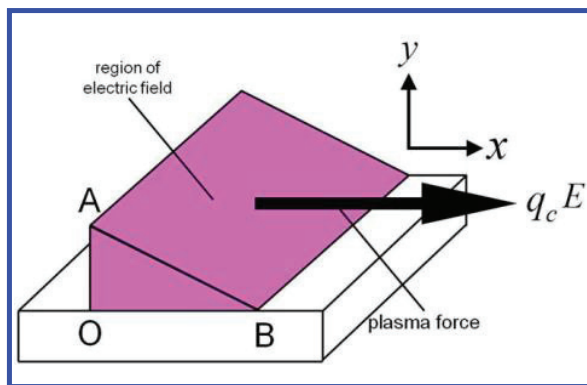


Figure 2. Geometry for the empirical plasma-force model.

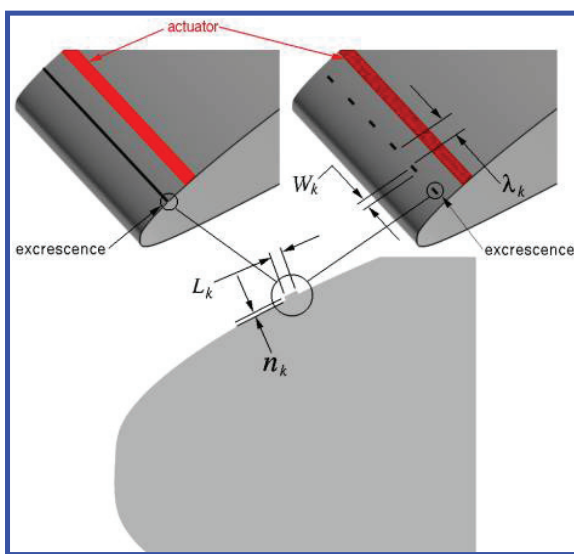


Figure 4. Wing leading edge excrescence configurations.

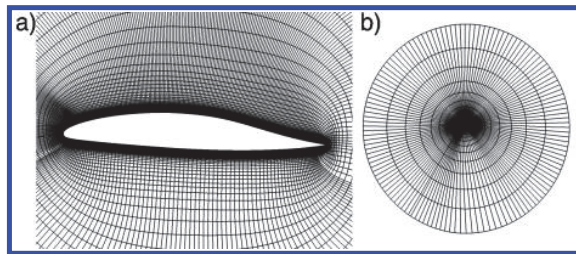


Figure 5. Computational mesh: a) near-surface region, b) farfield region.

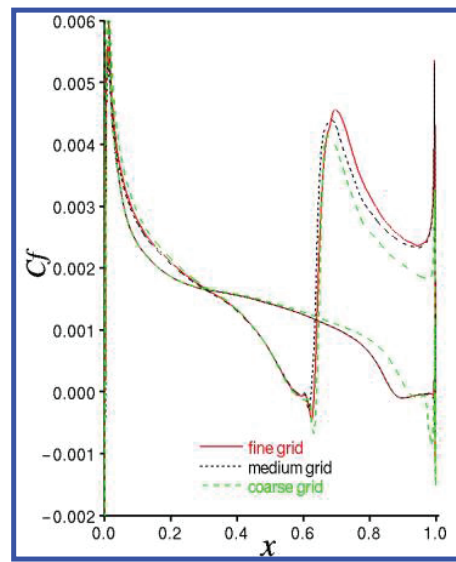


Figure 7. Time-mean skin friction distributions for the clean configuration.

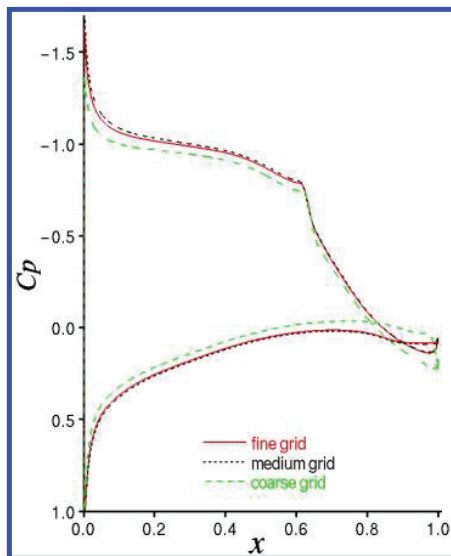


Figure 6. Time-mean surface pressure distributions for the clean configuration.

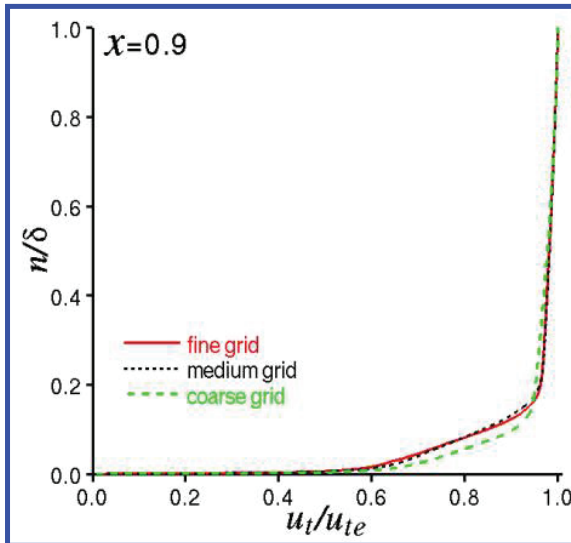


Figure 8. Time-mean velocity profiles for the clean configuration.

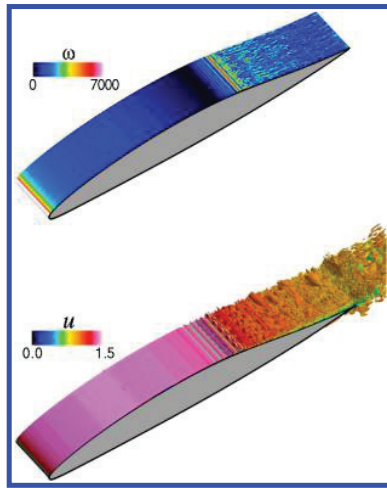


Figure 9. Instantaneous surface contours of vorticity magnitude (top) and iso-surface of the Q -criterion ($Q=0.01$) colored by u velocity (bottom) for the clean configuration (z coordinate stretch by factor of 1.5).

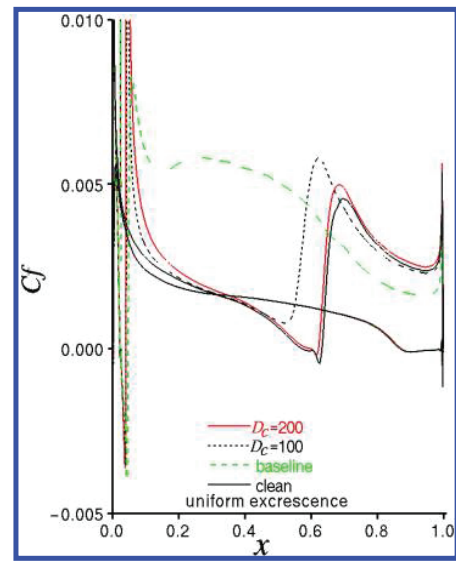


Figure 11. Time-mean skin friction distributions for the uniform-excrescence configuration.

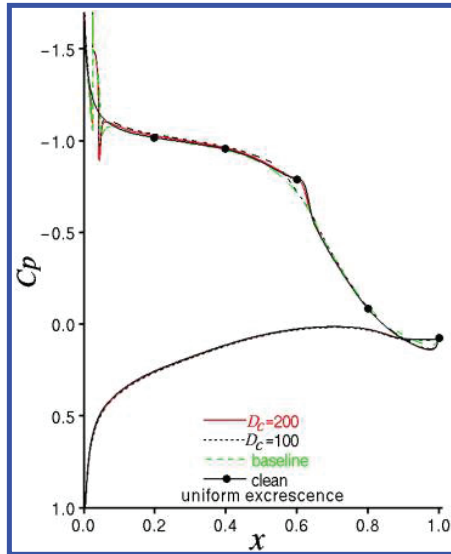


Figure 10. Time-mean surface pressure distributions for the uniform-excrescence configuration.

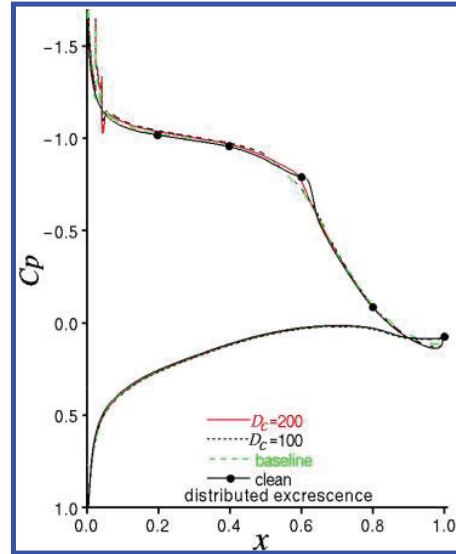


Figure 12. Time-mean surface pressure distributions for the distributed-excrescence configuration.

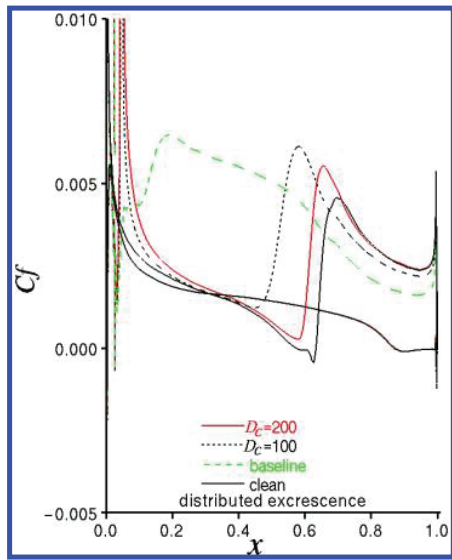


Figure 13. Time-mean skin friction distributions for the distributed-excrescence configuration.

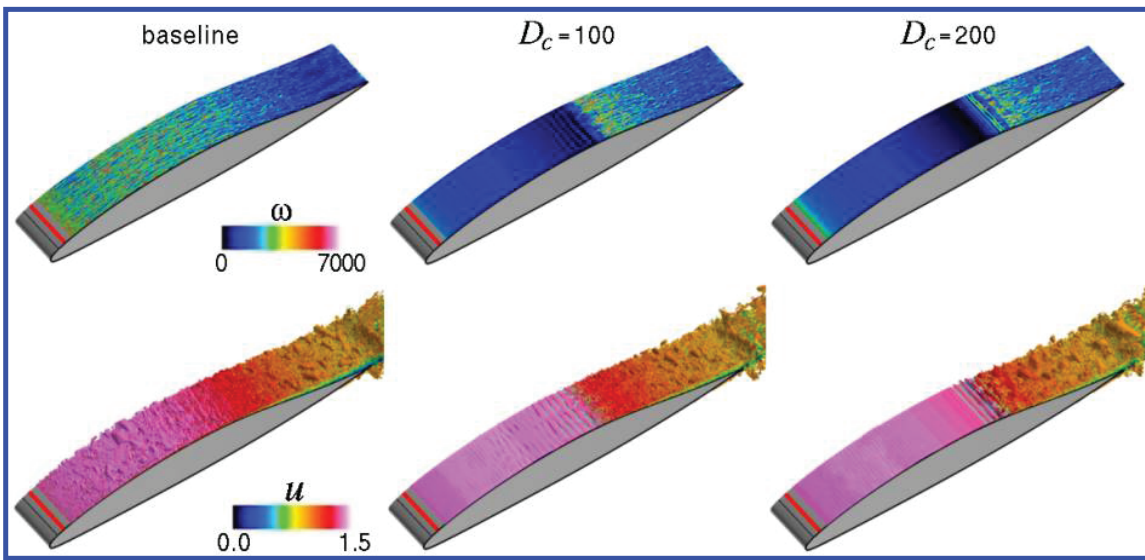


Figure 14. Instantaneous surface contours of vorticity magnitude and iso-surfaces of the Q -criterion ($Q=0.01$) colored by u velocity for the uniform-excrescence configuration (z coordinate stretch by factor of 1.5).

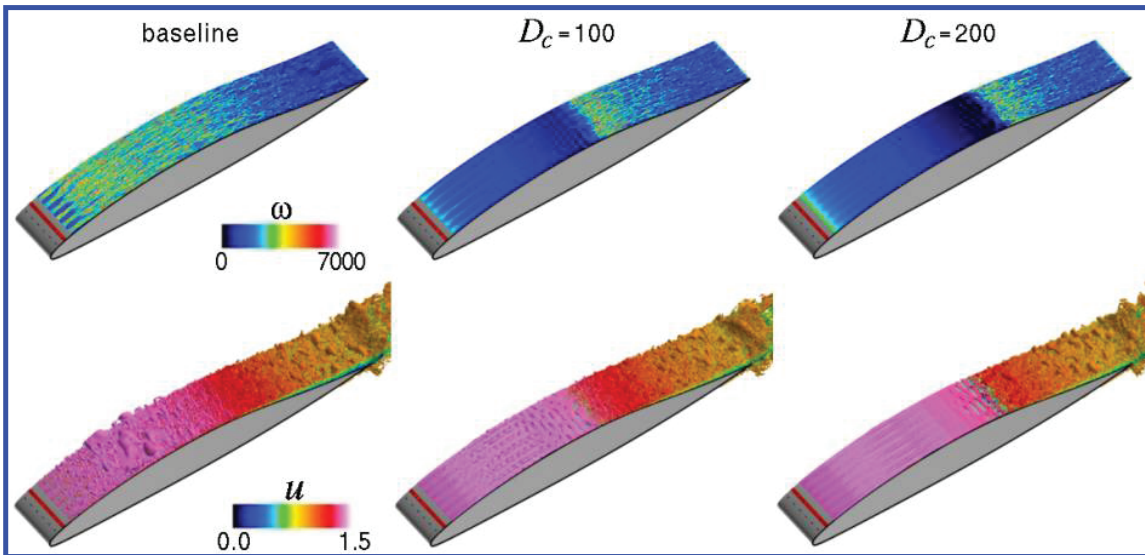


Figure 15. Instantaneous surface contours of vorticity magnitude and iso-surfaces of the Q -criterion ($Q=0.01$) colored by u velocity for the distributed-excrescence configuration (z coordinate stretch by factor of 1.5).

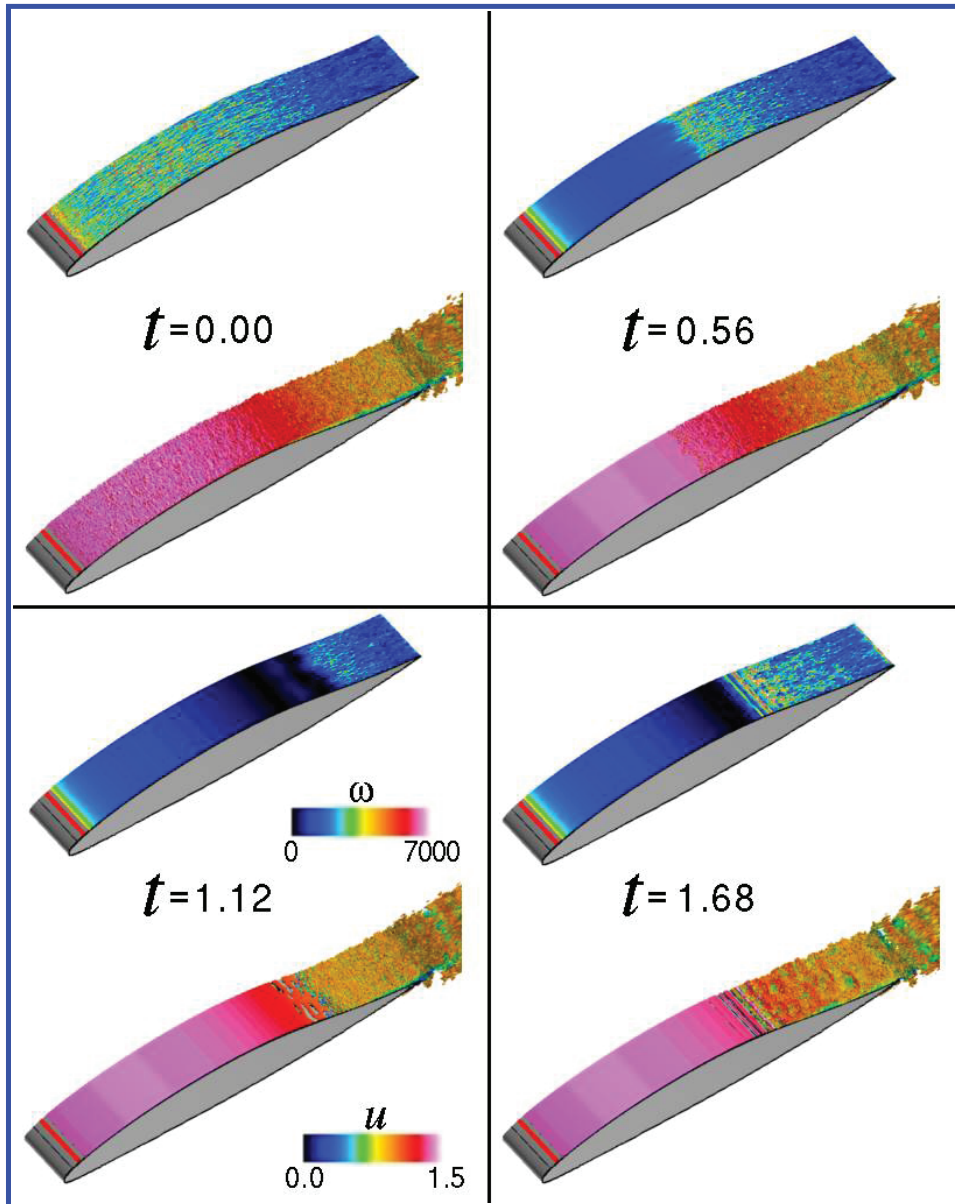


Figure 16. Instantaneous surface contours of vorticity magnitude and iso-surfaces of the Q -criterion ($Q=0.01$) colored by u velocity for the uniform-ex crescence configuration with $D_c = 200$, where $t = 0.00$ corresponds to the onset of actuation (z coordinate stretch by factor of 1.5).

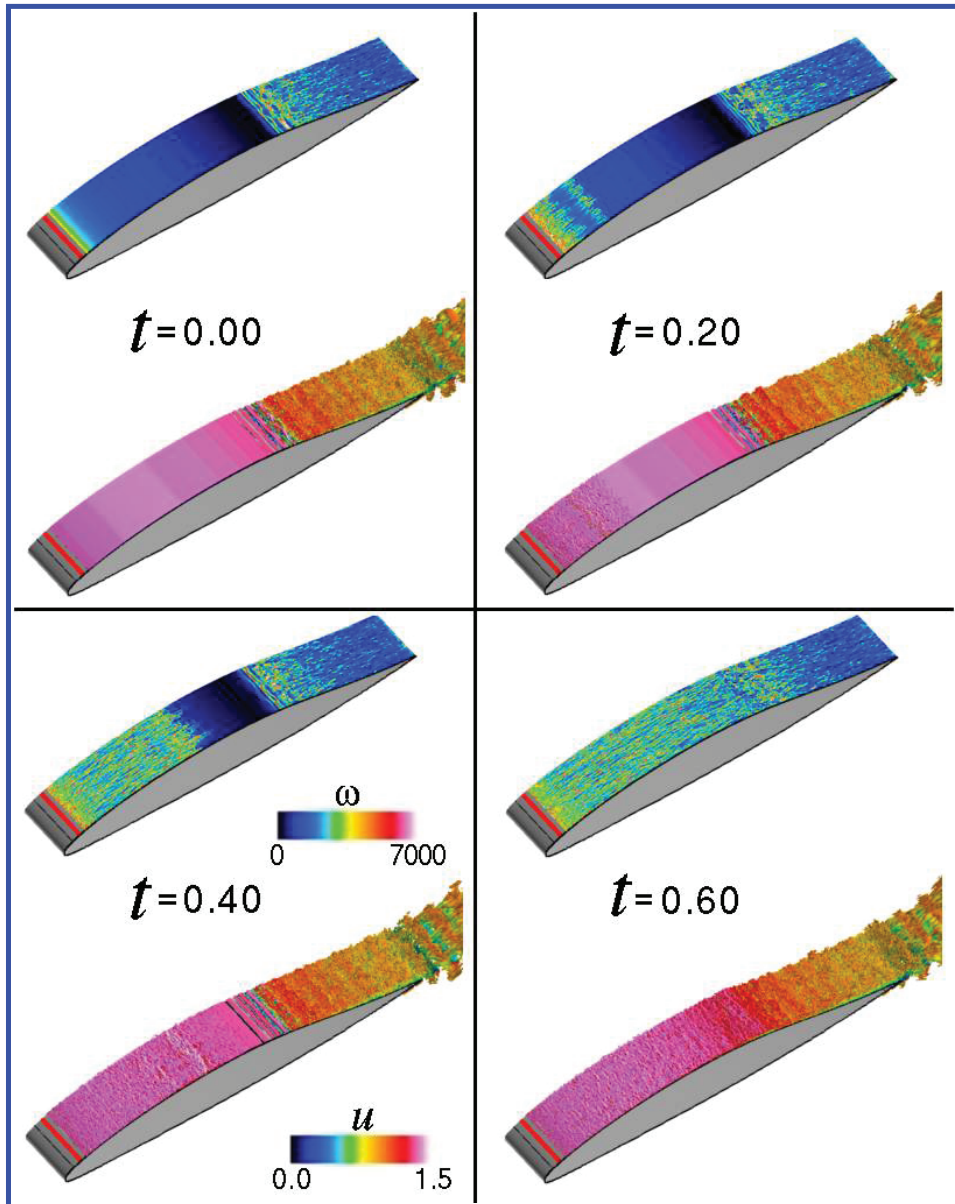


Figure 17. Instantaneous surface contours of vorticity magnitude and iso-surfaces of the Q -criterion ($Q=0.01$) colored by u velocity for the uniform-excrescence configuration with $D_c = 200$, where $t = 0.00$ corresponds to the termination of actuation (z coordinate stretch by factor of 1.5).

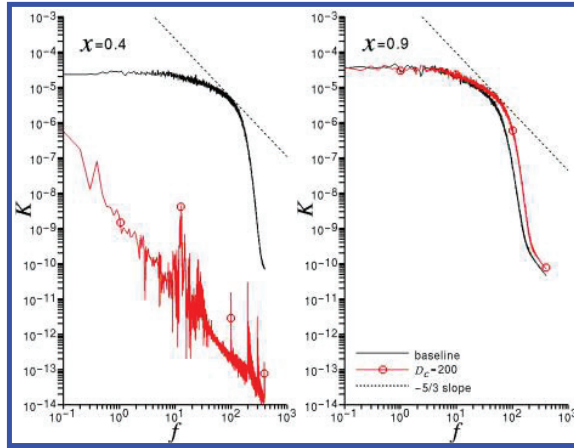


Figure 18. Turbulent kinetic energy frequency spectra for the uniform-excrescence configuration.

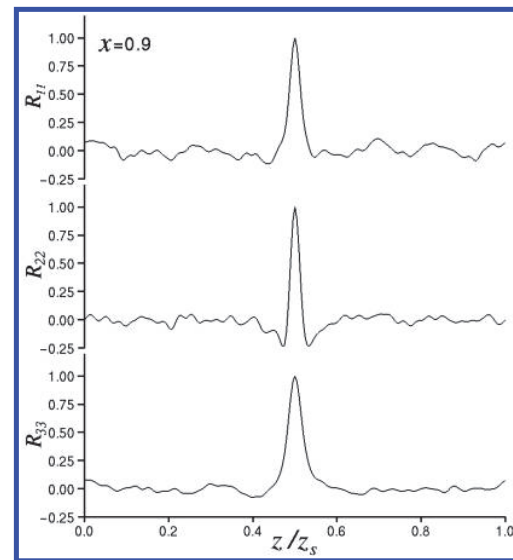


Figure 20. Spanwise correlation coefficients of the fluctuating velocity components for the baseline uniform-excrescence configuration.

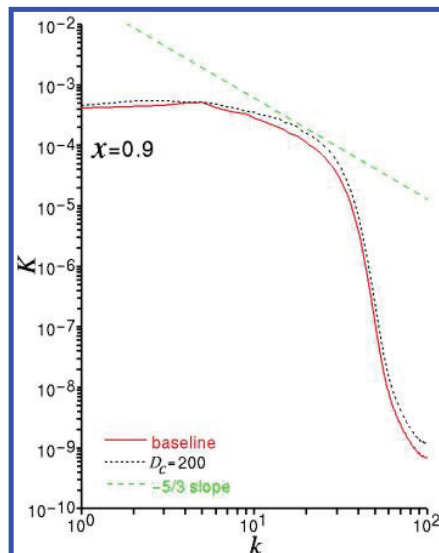


Figure 19. Turbulent kinetic energy spanwise wave number spectra for the uniform-excrescence configuration.